**Interaction Dynamics
of High Reynolds Number Magnetized Plasma Flow
on the CTIX Plasma Accelerator**

by

Stephen James Howard

B.A. Bennington College, Vermont 1999

A dissertation submitted in partial satisfaction of the
requirements for the degree of
Doctor of Philosophy

in

Engineering - Applied Science

in the

GRADUATE DIVISION
of the
UNIVERSITY OF CALIFORNIA, DAVIS

Approved:

....

....

....

Spring 2006

Interaction Dynamics

of High Reynolds Number Magnetized Plasma Flow

on the CTIX Plasma Accelerator

Interaction Dynamics of High Reynolds Number

Magnetized Plasma Flow on the CTIX Plasma Accelerator

Abstract

The Compact Toroid Injection eXperiment, (CTIX), is a coaxial railgun that forms and accelerates magnetized plasma rings called compact toroids (CT's). CTIX consists of a pair of cylindrical coaxial electrodes with the region between them kept at high vacuum (2 m long, 15 cm outer diameter). Hydrogen is typically the dominant constituent of the CT plasma, however helium can also be used. The railgun effect that accelerates the CT can be accounted for by the Lorentz $\mathbf{j} \times \mathbf{B}$ force density created by the power input from a capacitor bank of roughly a Giga-Watt peak. The final velocity of the CT can be as high as 300 km/s, with an acceleration of about 3 billion times Earth's gravity. The compact toroid is able to withstand these forces because of a large internal magnetic field of about 1 Tesla.

Understanding the nature of high speed flow of a magnetized plasma has been the primary challenge of this work. In this dissertation we will explore a sequence of fundamental questions regarding the plasma physics of CTIX. First we will go over some new results about the structure and dynamics of the compact toroid's magnetic field, and its electrical resistivity.

Then we will present the results from a sequence of key experiments involving reconnection/compression and thermalization of the plasma during interaction of the CT with target magnetic fields of various geometries. Next, we look at the Doppler shift of a spectral line of the He II ion as a measurement of plasma velocity, and to gain insight into the ionization physics of helium in our plasma. These preliminary experiments provide the background for our primary experimental tool for investigating turbulence, a technique called Gas Puff Imaging (GPI) in which a cloud of helium can be used to enhance plasma brightness, allowing plasma density fluctuations to be imaged. We will conclude with an analysis of the images that show coherent density waves, as well as the transition to turbulence during the interaction with a wire target perturbation.

To Nissa and Meera,

and to the years ahead.

Acknowledgments

Above and beyond the daily teamwork that I have relied upon during every phase of this project, I would like to thank the members of the CTIX group for their special contributions that have made this experiment, as well as my graduate experience, truly excellent. First, I would like to thank Prof. David Hwang for his encouragement and enthusiasm for the research we have done together. His creative vision has moved mountains, as well as plasmas, and I want to thank him for all that he has done to help me.

I want to express my deep gratitude and respect for Robert Horton for his prolific generation of ideas, innovations and practical implementations, from which I have learned so much.

In the same way, I want to thank Russ Evans for all that he has taught me about the inner workings of computers. He has been the bedrock of our group and has provided balance and humor throughout the years.

I also want to thank Sam Brockington for all of his hard work; from 12 hour vacuum openings, to rebuilding the experiment at the new facility, he has been a source of optimism and progress. I would also like to thank Alex Graf for building such a fine spectrometer and being so flexible about how we used it.

I want to thank my mother and father, Anne and Dennis, for proofreading my sequence of drafts. Their loving support has been a great help to me.

And to my wife Nissa, I want to thank you for your patience and flexibility through all those sleepless nights. And to Meera, my daughter, thank you for your spirit that makes it all worthwhile.

Contents

Appendices

List of Figures

List of Tables

Chapter 1

Introduction

1.1 Overview of study

My work has dealt with a sequence of basic plasma physics questions that range over a wide territory of subject matter. The common aim of these questions is to better understand the nature of high speed flow of a magnetized plasma. One important aspect of this work is the physics of turbulent flow states. The device that makes this investigation feasible is the CTIX plasma accelerator. However, our great success at designing and operating this accelerator has been founded on only a very rudimentary model of the plasma physics involved. Like early hominids, not understanding combustion chemistry hasn't stopped us from rubbing two sticks together and making fire.

As I have endeavored to do something new and useful with CTIX, I have been repeatedly confronted with fundamental questions regarding the plasma physics that makes it all work in the first place. I have tried to answer these questions as they have become experimentally accessible, and I have attempted to synthesize our results into improved models of what is actually going on inside the plasma. The individual results I have produced are interesting in themselves, in that they advance our understanding of the inner workings of CTIX-like plasma accelerators; but as a

collection I hope that they serve a more general purpose by providing a better understanding of the range of possible initial conditions and plasma parameters that give rise to fundamentally interesting phenomena such as magnetohydrodynamic (MHD) turbulence. In addition, I have tried to develop a useful framework of well posed questions that will serve to guide future progress.

I have organized my results in a sequence from chapter 2 to chapter 6 in a way that logically establishes the key prerequisites for an MHD turbulence experiment. Chapter 2 examines the structure and dynamics of the compact toroid's magnetic field. Next, in chapter 3 I develop some important results about the electrical resistivity of the plasma. This information is critical for properly analyzing the Reconnection/Compression experiments described in chapter 4. Together this work provides the initial conditions for the wire target turbulence experiments discussed in chapter 9. The resistivity measurements are of key importance in the estimation of the magnetic Reynolds number of the plasma flow, which we will use to characterize the flow conditions in our turbulence experiments.

Chapter 5 describes measurement of the electron temperature of the plasma and looks at the dynamics of energy conversion during the process of interaction with a transverse magnetic field. The knowledge about the electron temperature helps to construct an accurate model of the ionization of helium under our range of conditions. Helium enters the equation because of its ability to emit light brightly when bombarded with plasma electrons. This optical emission provides several diagnostic opportunities. The first is explored in chapter 6. Using a high resolution spectrometer we were able to measure the Doppler shift of a spectral line of He II ions. In doing so we measured the velocity of the plasma in previously inaccessible locations in the vessel.

Several of these preliminary results are combined in chapter 7 where I calculate values of the Reynolds numbers that occur in the CTIX plasma flow. The dimensionless Reynolds numbers play a vital role in determining the properties of a fluid flow, and our results provide some evidence of the existence of certain turbulent phenomena occurring at large Reynolds numbers.

From chapter 8 on we direct our attention to the experiments in the drift section of CTIX

where conditions are suitable for exploring MHD turbulence. Chapter 8 discusses our primary tool for investigating turbulence, a technique called Gas Puff Imaging (GPI) in which a cloud of neutral helium can be used to image plasma density fluctuations. Chapter 9 introduces a wire target that was used in a set of experiments to act as a magnetic perturbation to the plasma flow, and presents the analysis of images that show coherent and incoherent density waves that are created in the presence of the wire target perturbation.

Proposed future work and and a variety of technical details are included as appendices.

1.2 Structure of CTIX device

The Compact Toroid Injection eXperiment, (CTIX), is a coaxial railgun that forms and accelerates magnetized plasma rings called compact toroids (CT's). CTIX consists of a pair of cylindrical coaxial electrodes with the region between them kept at high vacuum. The outer conductor vessel is 2.5 m in length and 15.24 cm in diameter. The electrodes are connected to high voltage 50 μF capacitors and metglass passive timing delay inductors that together form the rail gun circuit. The electrically conductive CT plasma forms a sliding short between the inner and outer electrodes, and completes the path for current to flow down the center conductor, across the plasma, and back along the outer conductor. The railgun effect that accelerates the CT can be accounted for by the Lorentz $\mathbf{j} \times \mathbf{B}$ force density, where $\mathbf{j}$ is the current density driven by the external circuit, and $\mathbf{B}$ is the magnetic field created by the current flowing in circuit, (primarily down the center conductor). There are separate capacitor banks for the formation and accelerator sections that can be charged to different voltages. The final velocity of the CT can range from $V_{CT} = 5cm/\mu s$ up to $V_{CT} = 25cm/\mu s$. V_{CT} can be adjusted within this range by changing the applied accelerator voltage. The mass of the injected hydrogen CT is typically in the range of a few micrograms.[1]

The center electrode has a larger diameter in the formation region, has a step down in diameter, and then a tapered section, and finally it has a long, slightly thinner straight section
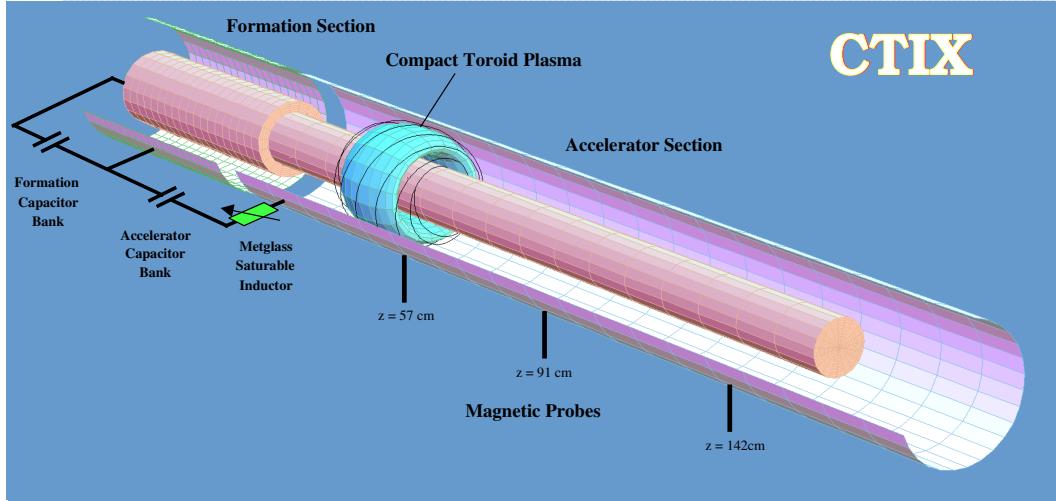
Figure 1.1: 3D view of CTIX showing magnetic probe positions and circuit schematic

where most of the CT acceleration occurs. The outer electrode has a corresponding tapered section at the junction between the formation and acceleration regions. Some of these details are not included in the graphical rendering of CTIX displayed in figure 1.1.

Originally, the center electrode was electroplated with gold to minimize surface effects from the raw stainless being exposed to the plasma. However, after years of operation, the sustained direct impact of massive high current discharges at gigawatt power levels has resulted in most of the gold plate on the middle 10 cm of the formation section center conductor becoming completely removed via ablative processes and deposited elsewhere in the vessel. Droplets of gold, typically having diameters less than 2 mm, are occasionally found toward the end of the accelerator, and in the drift and target chambers. These have apparently been accelerated during a plasma discharge and seem to have cooled in mid flight because of their resulting tear-drop shape. It is unknown how these droplets affect the electrodynamics of the acceleration discharge.

Also, some regions near the step down edge on the center conductor (z = 20 cm) have accumulated the gold deposits as a highly textured surface that looks like cracked stucco or peeling paint. We don't know exactly what effect this surface has on the formation process, but all evidence

suggests that either it does not matter at all, or it actually improves the formation of high density compact toroids.

The possibility that this surface texture could be beneficial is interesting, and not inconceivable. Electric fields will be significantly stronger at the tips of the gold flakes than elsewhere in the bulk volume. Positive contributions to the formation process might be accounted for simply by an enhanced secondary electron generation at the surface, or some kind of hollow-cathode effect, in which the small flat spaces between the flaking gold layer and the vessel wall act to create very efficient fast ionization of the plasma in a large number of little pockets distributed over a large surface area. Additionally, such an unusual formation boundary condition might partially account for the fact that the neutral gas break-down event is held off for such a long time (several ms) while the seed magnetic field decays until it is at just the right magnitude and field geometry, and then break-down spontaneously occurs. It is also possible that such a rough surface on the boundary of the newly forming plasma could modify the fluid velocity field such as by exciting high k turbulence for example, which ultimately results in the mysteriously efficient fast dynamo effect that is responsible for the creation of the large internal magnetic field of every single compact toroid we generate on CTIX.

The observations of extended hold-off of break-down, and unusually high magnetic flux amplification factor (~ 200) that occur during the plasma formation are two of the most basic features on the CTIX device [2]. They are definitely in need of further explanation, and the effects of a non-trivial boundary condition should be an important element to consider in future work on the subject.

CTIX was situated to be able to inject its CT's into the Davis Diverted Torus (DDT), which was a small toroidal device that was built in order to investigate basic tokamak physics. It was composed of a stainless steel toroidal vacuum vessel, major radius of 44 cm, minor radius 14 cm, which is surrounded by 7 toroidal field coils, as well as a variety of poloidal field coils, an Ohmic core, and a set of pre-ionization coils. DDT originally operated in a pulsed mode where a tokamak-like

plasma was heated and confined. The DDT toroidal field coils had a radius of 40 cm and produced about 3 Gauss per Amp at the center of the minor axis of the vacuum vessel. They were water-cooled and have achieved a maximum field of 600 Gauss in steady-state mode.
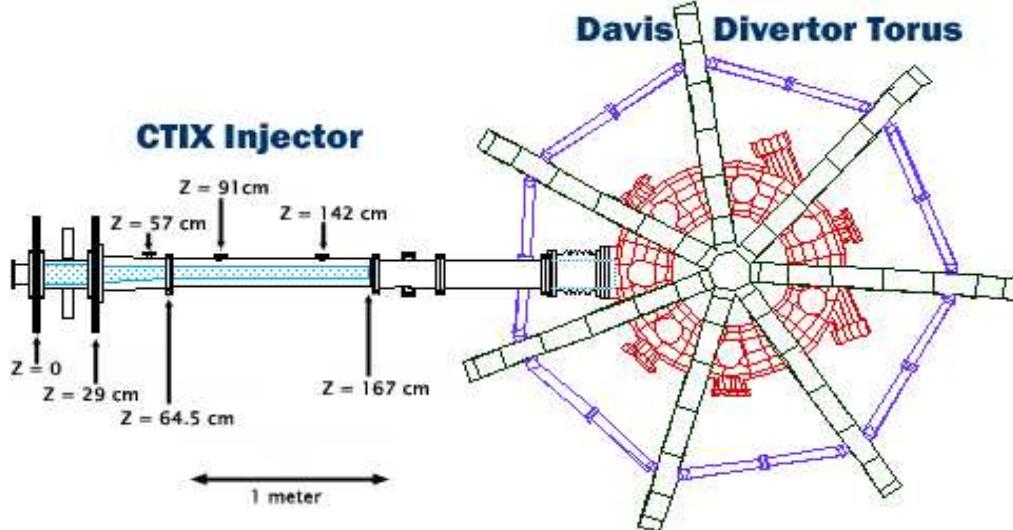
Figure 1.2: Top view of the CTIX-DDT facility

However, as the focus of experiments shifted toward CTIX we ceased the full-power pulsed mode and only operated DDT with smaller currents in a steady-state mode. In this mode a tokamak-like plasma is not possible or desired. Instead, we injected the CT into the vacuum field of DDT so that we could observe the interaction of the CT and the external toroidal field. The presence of tokamak plasma would have made the diagnostic situation more difficult in certain ways, mostly because once reconnection has occurred there is no easy way to distinguish between the tokamak plasma and the CT. Without the tokamak plasma getting in the way of our diagnostics, we can look at zeroth order stopping effects, as well as post-reconnection dispersion and thermalization since the only plasma in the device is that which originated in the CT. For a more detailed description of the phenomenon of magnetic reconnection see chapter 4.[3],[4]

Future work at a new experimental facility* will be conducted with CTIX injecting directly into a smaller diagnostic chamber, with DDT removed from the system. This will significantly

decrease the total volume of the vacuum vessel and allow higher repetition rate because of the shorter pump-out time. Also the new design will greatly improve diagnostic access and usability of the system.

1.3 Concept of a compact toroid plasma

A compact toroid is a magnetized plasma ring formed within a conducting vessel of coaxial geometry. The term "compact" is used because traditionally these plasmas tend to be formed between coaxial electrodes having only a modest outer radius of about 10 cm.[5]

It has a strong interior magnetic field with a special geometry that has closed flux surfaces, resulting in plasma particles being trapped on the field lines for much longer than the escape time due to the particle's thermal velocity. Also, this magnetic field is self-generated by the currents flowing within the plasma ring. In this way the compact toroid is self-confined in a stable geometry
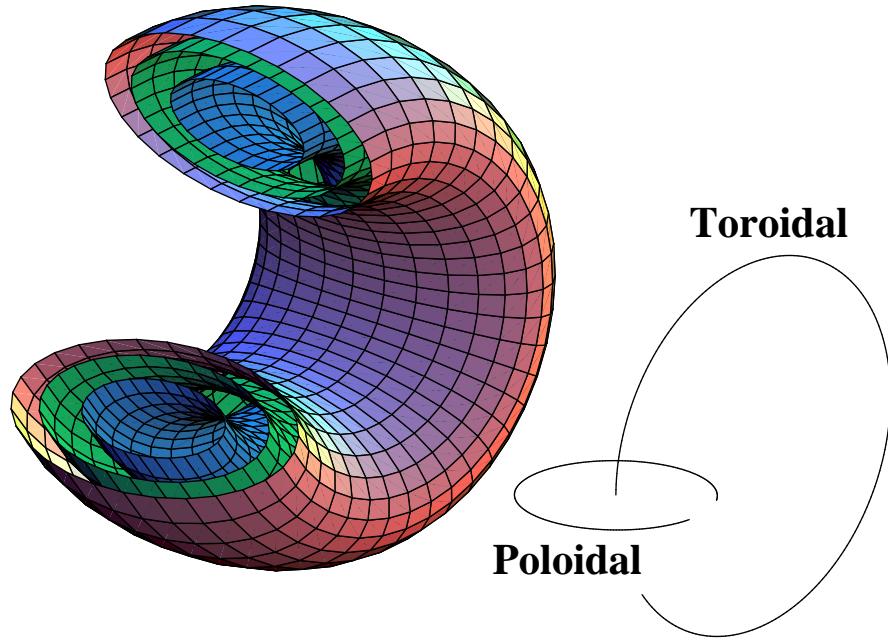
Figure 1.3: Visualization of magnetic flux surfaces within a compact toroid

that persists until the internal currents resistively die down or particles escape as certain non-trivial phenomena eventually dominate.

This special magnetic field geometry has comparable poloidal and toroidal components at each point within the plasma. Field lines wrap around toroidal surfaces called flux surfaces, in this way field lines can be grouped by what flux surface they lie on, and the entire magnetic field constitutes a set of nested tori of flux surfaces.

The fields are maintained by associated toroidal and poloidal plasma currents. Its magnetic geometry is much like a spheromak, the distinction between them is primarily that a compact torus is being accelerated by a large railgun current, whereas a spheromak is formed at rest with respect to the laboratory. Also, spheromaks are formed in large, roughly spherical vessels, while the coaxial vessel allows the compact toroids to have almost any aspect ratio, and can range from doughnut shapes to long, cigar shapes.

Measured surface magnetic fields at the edge of the CT are large $B \sim 1$ kGauss to 5 kGauss and internal magnetic fields are expected to be a factor of 3 to 10 times larger.

A more detailed account of the theory of the magnetic equilibrium of compact toroids and spheromaks will be presented in chapter 2. The CT has a long lifetime of over 1 ms, and is able to hold itself together under some rather large forces. The compact toroids formed on CTIX can be characterzed according to two parameters, the thermal beta, and the kinetic beta.

$$\beta_{thermal} = \frac{P_{thermal}}{B^2/2\mu_0}, \qquad \beta_{kinetic} = \frac{\rho v^2}{B^2/\mu_0}$$

The thermal beta is the ratio of the hydrodynamic thermal pressure to the magnetic pressure, while the kinetic beta is the ratio of kinetic energy density to magnetic energy density. Part of what makes an accelerated compact toroid plasma special is that it has a low thermal beta, yet a high kinetic beta, $\beta_{thermal} \ll 1$, yet $\beta_{kinetic} \sim 1$. This is important because it means that magnetic effects will dominate many pure hydrodynamic effects, yet there is an abundant source of kinetic energy that can drive plasma phenomenon into the non-linear range.

There is a large toroidal magnetic field behind the CT, initially generated by the railgun current flowing in the center conductor. This field becomes spatially uniform and steadily decays as the column of magnetized plasma behind the CT expands. During this expansion magnetic energy is converted into the kinetic energy of the plasma, thereby driving the acceleration of the compact toroid, which rides at the leading edge of the expanding column.

As it leaves the accelerator, CT plasma is relatively dense with $n = 10^{14}$ particles per cm^3 and of modest temperature $T_e = T_i = 50eV \sim 580,000°$K.

The total visible emission of the plasma has been measured to have a peak value of about 10^{17} photons/$(cm^3 \cdot sec)$. This is enough for many amplified or high-sensitivity optical detectors to get a good signal, if they have long enough exposure ($\sim 1 - 10 \ \mu s$), and integrate over a wide enough wavelength range. However, for certain challenging measurements such as high-speed, high-resolution spectroscopy, and fast imaging through optical filters, special techniques are required to increase either plasma brightness or detector sensitivity. The CT plasma and is optically thin in the visible range (i.e., it is transparent to its own light).

1.4   Timescales within the life of a CTIX plasma

The innovative aspect of the CTIX design is that it is capable of sustained operation with a maximum firing rate of 0.2 Hz, (1 shot every 5 seconds). We will often refer to the firing rate of CTIX as its rep rate or repetition rate. When we were taking data the rep rate was typically 0.05 Hz (1 shot every 20 seconds) so that the vacuum vessel could be fully pumped back down to base pressure between shots.

The standard firing rate is sufficiently fast to be able to take 1000 shots a day. If the pumping rate was significantly increased (or injected gas volume was decreased), in principle the repetition rate could be increased to 1 kHz if the capacitors could be maintained at high voltage.
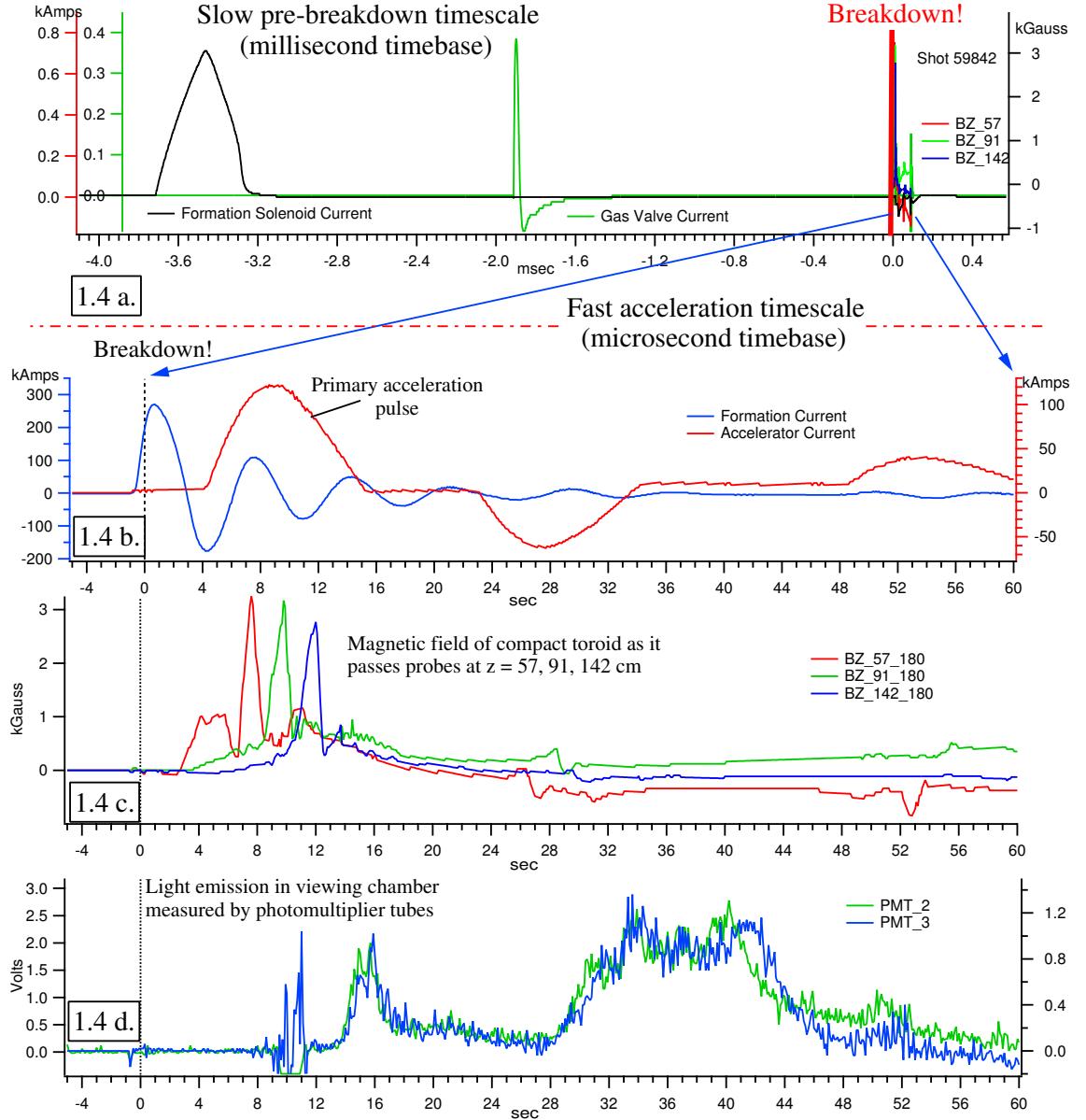
Figure 1.4: Timescales during a CTIX acceleration discharge

CTIX's rapid fire ability is due to the fact that it is passively switched [1]. The only thing we actively control on CTIX is the gas valve trigger pulse that causes a puff of gas to be let into the formation section, already energized to a steady high voltage of about 10 kV. Then at some randomly occurring time later, the gas ionizes due to the formation potential, thereby completing

the formation circuit.

After a fixed delay of about 4 μs that allows the magnetized plasma to expand into the acceleration region and relax into a CT geometry, the accelerator circuit then fires, and accelerates the CT to its injection velocity.

The whole system is passively dependent on the event of the gas break-down, which means that CTIX can fire any number of times in quick succession at whatever rate you can successfully send in distinct pulses of gas. One limitation is that presently the capacitors loose their charge after only one firing cycle. Recharging the capacitor bank takes about 3 seconds when the system is running in a fully automated mode. So, in principle we could fire once every 3 second with the present machine. However, in practice we run at a much slower firing rate to accommodate several other factors. First, the data acquisition system (CAMAC + LabView) typically requires about 5 seconds to record all the data. And second, as previously mentioned, the pumping rate of our present vacuum system is only fast enough to allow a repetition rate of one shot every 20 seconds. Any faster than this and the gas pressure will steadily rise over the course of a run. If the electrodes are energized when the base pressure is too high (above 10^{-4} Torr), premature arcing will occur that can damage the device.

The basic operations of CT formation and acceleration have been demonstrated to operate very robustly, with a nearly failure-free production of compact toroids over the course of more than 60,000 firings of CTIX. Although CTIX almost never fails to produce and accelerate viable CT's, there is a noticeable amount of random variation of CT properties from one shot to another. With all experimentally controllable settings of the device held fixed, important observables such as plasma density, CT magnetic field shape and strength, and CT final velocity, will jump around randomly within some finite range. These fluctuations are attributed to uncontrollable variations in the initial conditions during the CT formation process.

For example, the formation gas valve sometimes lets in a little more hydrogen then average, sometimes less, resulting in a correspondingly greater or lesser CT plasma density. Another

uncontrollable event is the ionization of the neutral hydrogen (called the breakdown), which will occur at a randomly occurring time, that can vary as much a several milliseconds.

The time of breakdown is likely to depend on a variety of system parameters in a complex way. It is expected that the peak density of neutral hydrogen should play an important role, the strength and geometry of the formation magnetic field that acts to bend the trajectories of free charged particles, and it most critically depends on the spontaneous creation of enough free electrons (possibly via cosmic rays) to trigger the needed runaway cascade of electron impact ionization. Overall, there are many more questions than answers regarding the details of the formation process.

1.5   Typical CTIX plasma parameters

Typical CTIX Parameters			
Quantity	*Units*	*Low*	*High*
Density $n_e = n_i$	[cm^{-3}]	10^{14}	10^{15}
Electron Temperature	[eV]	10	80
Peak magnetic field	[kGauss]	1	10
Electron collision rate	[MHz]	4	900
Debye Length λ_D	[cm]	7×10^{-5}	7×10^{-4}
Electron gyroradius	[cm]	7×10^{-4}	0.2
Fluid Reynolds number $V_{CT}L/\nu$		100	2×10^4
Magnetic Reynolds number $V_{CT}L/D_M$		10	10^4

Table 1.1: Typical range of CTIX plasma paramters

1.6   Overview of diagnostics on CTIX

1.6.1   Probe diagnostics

Along CTIX there are a number of **magnetic field probes**. Each is capable of resolving poloidal and toroidal components of the magnetic field at the outer edges of the CT. These different components are recorded on separate digitizer channels. We have three magnetic probes situated along the length of the accelerator at 57 cm, 91 cm, and 142 cm from the gas valve. The B_z probe

signals are used on a daily basis to see the existence of the CT and to get a quick estimate of its average velocity and acceleration using time-of-flight kinematics. Details of the magnetic probes will be discussed next, in chapter 2. We also use magnetic probes throughout the drift section and DDT.[1],[6]

A simple measurement of plasma density can be made with **Langmuir probes**, consisting of a thin coaxial line that has its center conductor protruding at the probe tip, this allows the metal to be in direct contact with the plasma. By charging the probe tip to a bias voltage relative to the plasma, either electron current or ion current will be collected by the wire. Some temperature information can be acquired by observing how the current varies when the bias voltage is scanned over a range.[7]

Operated in a similar manner, we have another kind of plasma probe called an **energy analyzer probe** (EAP). It uses a set of fine metal grids to repel charged particles, yet allowing a high-energy subset of the population to be collected by a plate in the back of the probe assembly. It is designed to measure the energy distribution function of the plasma, and therefore the temperature, by way of scanning the bias voltages applied to the repeller grids [8],[9]. More details of the energy analyzer probe will be discussed in chapter 5.

1.6.2 Optical diagnostics

One of our most complex diagnostics is our set of three laser **interferometers** that measure the electron density of the plasma by detecting changes in the index of refraction. This is done using a long coherence-length He Ne laser, whose beam is split into two sub-beams, one that passes through the plasma, and a second reference path of the same length as the first that only passes through air. These two beams are mixed back together, and the result is that phase of the combined light will undergo constructive and destructive interference by an amount that depends on the difference in refractive index along the two paths. [1]

A heterodyne mixing technique is used to efficiently extract the phase information from
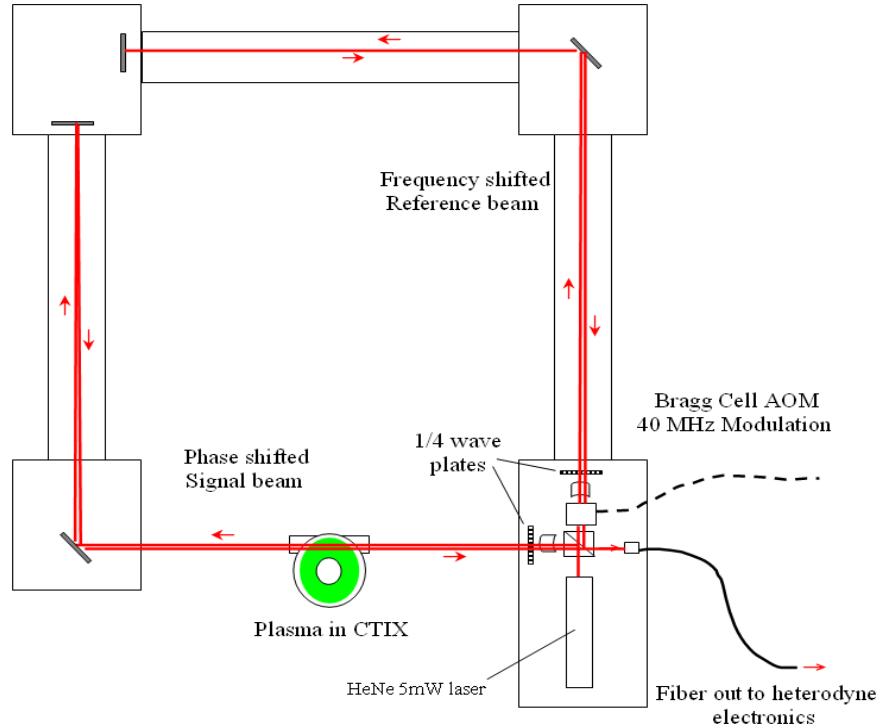
Figure 1.5: Schematic of He Ne laser heterodyne interferometer

fast time-domain measurements of the laser intensity. A key feature in our system is that the plasma passing through the interferometer laser chord results in a very rapid change in phase, which can easily be distinguished from much slower modulations due to mechanical oscillations of the interferometer support structure (shown in fig. 1.5). We have three such interferometers, positioned at the optical ports at z = 57, 91, 142 cm.

A very attractive alternative to the interferometer is the **laser deflectometer**, which also accomplishes electron density measurements, but it does so by detecting microscopic deflections of a laser beam passing through the density gradients that exist within our finite sized plasma. It uses a low cost diode laser, and a four quadrant laser spot detector in combination with a custom-made amplifier circuit to measure the laser deflection as a function of time. Special care needs to be

given when designing the frequency response of the circuit to make in insensitive to low frequency mechanical vibrations, as well as very high frequency electrical noise. In addition to low cost, it has the advantage that it is relatively easy to align, and is well suited to detecting small-scale structures that have steep density gradients, such as would occur in shock waves, and possibly in turbulence. The deflectometer is currently being developed by Samuel Brockington as part of his Ph.D. project.[10]

The plasma actively emits visible light, and there is a lot that we can do with this fact [11]. One route is to measure the time dependence of the emission within some range of wavelengths, and localized along a narrow chord in the plasma using **optically filtered photomultiplier tubes (PMT)** [12]. The plasma light is collimated using a pair of small adjustable apertures mounted at the ends of a long tube. Before the light can be detected by the PMT, it must first pass through an optical bandpass filter, allowing only a small range of wavelengths through. The PMT is needed because its high sensitivity and dynamic range allows detection of the very small fraction of plasma light that makes it through the apertures and narrow filters. This has been very useful in quantifying individual atomic processes within the plasma. The use of the filtered PMT assemblies to measure the excitation of singly ionized helium will be discussed in chapter 6.

We can also take digital photographs of the plasma using a variety of **high speed imaging devices**, including a high-sensitivity CCD, a micro-channel plate intensified CCD, and a fast framing Imacon tube. These can also be used to view the plasma light through optical filters in order to distinguish different atomic processes. Fast imaging is primarily useful in revealing the existence of global structures within the plasma that would have gone unnoticed using only point measurements.

Lastly, we can use **spectrometers** to quantify how plasma light is distributed in wavelength space. Typically the visible plasma spectrum is dominated by line emission from atomic and molecular transitions. We have used two different spectrometers on CTIX, that differed in spectral resolution and sensitivity [13], [14]. The details of these will be discussed in chapter 6.

1.6.3 System monitors

A number of current and voltage monitors are used to diagnose what is going on within the CTIX accelerator circuit. These included the current applied to operate the formation gas valve, and formation solenoid. We routinely measure the voltages across the formation and accelerator gaps, as well as the currents flowing in the formation and acceleration electrodes. Figure 1.4 shows the waveforms generated by some of the primary system diagnostics.

The vacuum pressure within the vessel is continuously monitored using low pressure ion gauges that can operate below 10^{-4} Torr, as well as Convectron gauges the are sensitive above 1 milliTorr. The higher pressure gauges are part of a vacuum interlock system that will close gate valves to protect the turbo-pump if the pressure somehow climbed too high. Typical base pressure is about 5×10^{-7} Torr.

1.6.4 Data acquisition

The primary architecture for handling time-domain diagnostic data consists of 10 CAMAC crates controlling fast analog-to-digital converters (digitizers) located inside the experimental area, which are connected by a fiber optic serial highway to the main control room computer via a GPIB card. The data from up to about 120 digitizer channels is stored to disk immediately after each shot, with a total read time of about 5 seconds or less, depending on the number of channels being stored. A variety of different digitizer modules are used, and typically we run at a sampling rate of 10 to 100 MHz (1 digital sampling every 100 ns or 10 ns).

The data acquisition system software, with integrated accelerator system controls and data viewing was implemented in the form of a custom made user interface designed in LabView. The binary files recorded by LabView can be read and processed using a separate data analysis program, also implemented in LabView, or they can be converted into delimited text files suitable for reading into a spreadsheet application, or other analysis programs such as Igor, Mathematica, Matlab, etc.

Image and spectral data are handled in a more decentralized manner than the time data.

Each camera has its own dedicated acquisition computer, with data and control commands being exchanged between them using a proprietary data line (either fiber optic, copper bus, or BNC) and a corresponding data acquisition card installed on computer.

* Exodus As briefly mentioned already, the CTIX-DDT facility has been taken apart, carried by truck, forklift and tired backs, and reassembled about 3/4 of a mile away. Somehow we lost DDT along the way. Moving to the new experimental facility located in the UCD Hertz Hall building, and departing from our historic venue in B435 of LLNL, began in November of 2004, with experimental operations ceasing on September 1st, 2005, and complete vacancy of the premises by September 30th, 2005. First plasma in the new location was made on March 2nd, 2006.

Chapter 2

Compact toroid

magnetic field geometry,

experiment and theory

2.1 Force-free magnetic field model

Let us begin by examining the basic constraints imposed on a self-confined magnetized plasma ring existing within a cylindrically symmetric conducting vessel. The coaxial geometry of CTIX will require that we apply the following boundary conditions at both the inner and outer walls. It is natural to work in a cylindrical coordinate system (r,θ, z).

The time varying part of the magnetic field $\mathbf{B}$ of the compact toroid must satisfy the boundary conditions

$$\mathbf{n} \cdot \mathbf{B} = 0 \qquad \mathbf{n} \times \mathbf{B} = \mu_0 \mathbf{K} \qquad (2.1)$$

where $\mathbf{K}$ is the surface current density. To satisfy the first condition, B_r must vanish at the wall. From the second condition we see that B_z is nonzero if there is a surface current K_θ in the azimuthal

direction, and B_θ is nonzero if there is a current K_z in the axial or z direction.

Thus measurements of B_z and B_θ at the wall as a function of axial position and time (z, t) will let us know the state of the magnetic field and the current density at the boundary of the plasma.
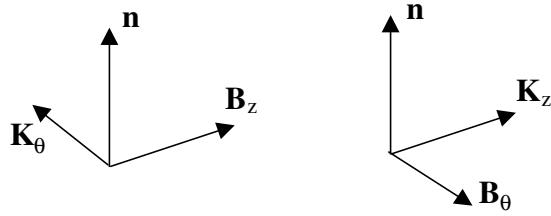
Figure 2.1: Relationship between surface current and magnetic field components

Much work has been done on the theory of force-free equilibrium of plasmas in cylindrical, toroidal, and coaxial geometries [5],[15], [16],[17],[18]. The relaxation of a magnetized plasma to a state of minimum magnetic energy, while global helicity is preserved, results in the Woltjer-Taylor force-free equilibrium ($\mathbf{j} \times \mathbf{B} = \nabla P = 0$) given by

$$\nabla \times \mathbf{B} = \lambda \mathbf{B} \tag{2.2}$$

where the constant $\lambda = \mu_0 j / B$. Within a conducting vessel of coaxial geometry, and with the added assumption of zero axial surface current, $K_z = 0$, an axisymmetric solution exists that is separable and is expressible in terms of Bessel functions according to

$$B_r = B_0 \frac{k_z}{\lambda} \cos\left[k_z(z - z_0)\right][J_1(k_r r) + f Y_1(k_r r)] \tag{2.3}$$

$$B_z = -B_0 \frac{k_r}{\lambda} \sin\left[k_z(z - z_0)\right][J_0(k_r r) + f Y_0(k_r r)] \tag{2.4}$$

$$B_\theta = -B_0 \sin\left[k_z(z - z_0)\right][J_1(k_r r) + f Y_1(k_r r)] \tag{2.5}$$

where $k_r^2 + k_z^2 \equiv \lambda^2$ relates the radial and axial wavenumbers to the magnetic eigenvalue λ. Here,

$J_n(x)$ and $Y_n(x)$ are Bessel functions of the first and second kind, order n, respectively.
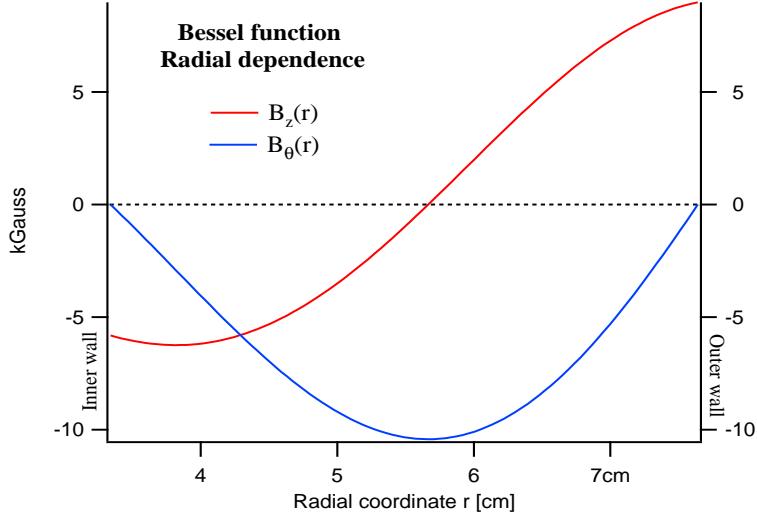
Figure 2.2: Plot showing the radial dependence of Bessel function solution of the magnetic field.

To match the first boundary condition, values of k_r and f must be found such that $B_r(r, z) = 0$ at the inner and outer walls, $r = r_1$ and $r = r_2$ respectively. The radial term is zero when

$$f = -J_1(k_r r_1)/Y_1(k_r r_1) = -J_1(k_r r_2)/Y_1(k_r r_2)$$

and so k_r must satisfy

$$J_1(k_r r_1)Y_1(k_r r_2) - J_1(k_r r_2)Y_1(k_r r_1) = 0$$

For the CTIX vessel, $r_1 = 3.34\ cm$ and $r_2 = 7.62\ cm$ in the acceleration section and so $k_r = 75.18\ m^{-1}$. In order for $B_z = 0$ at $z = z_0$ and $z = z_0 + \Delta z$, $k_z = m\pi/\Delta z$. The axial extent of the compact toroid within CTIX tends to be about $\Delta z = 1$ meter and should be dominated by m =1 mode, which implies that $k_z = 3\ m^{-1}$. Using these values the Taylor state eigenvalue should be $\lambda = 75.24\ m^{-1}$. From this result we would also conclude that the ratio of the current density to magnetic field is

$$j/B = \lambda/\mu_0 = 5.98 \times 10^7\ H$$

where $H = 1$ Henry $= C^2/kg \ m^2$.

This means that for a modest CT surface field of 0.1 Tesla we would have a current density of about 6×10^6 Amps/ m^2 or 60 kA/cm^2. This is in rough agreement with other estimates based on experimental data.

One paper on this general topic is a 1993 paper discussing the MARAUDER plasma accelerator and their experiments [19]. Their paper tackles the issue of MHD equilibrium for compact toroids, and presents a combination of analytical results, simulation and experimental results. Overall it is a very useful review of many relevant topics, and is the only published account I have been able to find that gives an analytic solution of $\nabla \times \mathbf{B} = \lambda \mathbf{B}$ in a coaxial geometry.

Despite their thoroughness, they made a few problematic mistakes in their presentation of the theory of force-free equilibria that are worth notice. The least of the errors was a simple typo, they gave the magnetic helicity as $\mathbf{A} \times \mathbf{B}$, when it should be $\mathbf{A} \cdot \mathbf{B}$ [1].

In the same section they made a more confounding mistake by writing down a believable-looking yet incorrect solution for the magnetic field of a force-free state $\nabla \times \mathbf{B} = \lambda \mathbf{B}$ in a coaxial geometry. Lastly, they listed a key reference that seemingly does not exist, even after much effort investigating a very wide margin of possibility for typographic or factual error.

As it relates to my present discussion, relying on the correctness of their published formulas caused some difficulty when I first attempted to make quantitative comparisons between theory and our experiment. The effect is that their formula gives a much larger B_z than B_θ inside the CT, whereas experiment showed that the two components are roughly equal (within a factor of 2). Their formula for B_z had a coefficient (k_r^2/k_z^2), but when the curl is taken and field components are compared, I found that B_z should just depend on (k_r/k_z), not squared. The corrected formulas listed above (2.3 - 2.5) actually satisfy $\nabla \times \mathbf{B} = \lambda \mathbf{B}$, while their counterparts in the 1993 paper did not. When this is corrected, the ratio of B_θ/B_z approaches unity within the CT, basically in agreement with experiments.

---

[1] See Appendix A for a discussion of Helicity of a force-free state

A further point of refinement can be made, which will be examined more closely in section 2.2, if the bending of the field lines near the probe port hole is taken into account. This bending results in an effective depth of the probe measurements that is approximately 0.5 cm into the interior of the plasma. The Taylor state model predicts that at this depth, the magnitude of B_θ should be very close to $1/2$ of the value of B_z. It also makes a much broader prediction that throughout volume of the CT, the ratio B_θ/B_z should be only a function of radial position simply because the z dependence divides out.

When compared to our experiments, this first prediction that our probes should measure $B_\theta = \frac{1}{2}B_z$ turns out to be reasonable accurate when considering the peak value of B_z at the center axial position of the CT. On the majority of shots we observe a noticeable dip in the B_θ signal that is coincident with the CT center, whose amplitude is very close to $1/2$ the peak value of B_z. My interpretation is that this central dip in B_θ is due to Taylor state fields.

However, the behavior of B_θ elsewhere in the CT is in complete disagreement with the second prediction of the Taylor state model: that the ratio B_θ/B_z is not a function of z. Our measurements show a significant ramping up of B_θ, going from zero at the leading edge of the CT to about $1/2$ to $3/4$ of the value of $B_z(t_{peak})$, by the time the back edge of the CT has passed the probe. Then when the probe crosses over into the pushing field, B_θ increases until it is near the value of the peak of B_z. (See fig 2.6 and 2.9).

This linear ramp-up of B_θ inside the CT is not accounted for by the Taylor state, and some kind of modification to the simple force-free state is required.

Many interesting questions remain that involve exactly how the CT magnetic geometry varies away from a true force-free Taylor equilibrium when it is being strongly accelerated. We will briefly examine one possible modification to this theory, after asking some hard questions about the physics that underlies our magnetic probes, in order to get them up to the task of testing these various theories.

2.2 Magnetic field measurements

The measurements of the axial and toroidal magnetic field components are done with special magnetic probes, each component is measured with its own 1 cm × 1 cm square loop coil of several turns. The two loops are wound at right angles to each other through small holes at the tip of a long plastic rod (see figure 2.3).

The magnetic probe operates like any standard Faraday inductive pick-up coil. As the net magnetic flux through the loop changes when the magnetized plasma flows around it, a corresponding current is induced in the wire that is proportional to the time derivative of the instantaneous magnetic field at the loop. This current is put through a passive RF integrator that effectively takes the time integral of the signal, and the output signal is digitized.

This recorded signal has some further numerical corrections applied to it in order to compensate for an inherent droop effect of the integrator circuit. The final product is a well calibrated measure of the magnetic field strength as a function of time at the position of the loop.

In order to make a quantitative comparison between theory and our experimental measurements of the magnetic field, we need to split a few technical hairs. In particular, the exact shape of the vacuum vessel in the vicinity of the probes will play a critical role in formulating a correct interpretation of the experimental signals. The results of this analysis will be essential in determining the systematic errors involved with our magnetic measurements, needed in later chapters for placing constraints on estimated plasma resistivity and fluid velocity fields.

2.2.1 Probe port geometry

Each magnetic probe is inserted into a special port that consists of a 0.874 inch hole in the stainless steel outer conductor, with a stainless tube (0.874 inch inner diameter) welded to the hole and extending radially outward (about 1 inch) to a flange that makes an o-ring vacuum seal with a 1/2 inch diameter ceramic tube. The ceramic tube is 6 inches long with one closed end that

is inserted into the vessel so that the tip of the ceramic tube is approximately flush with the inner surface of the outer conductor. The other end of the ceramic tube is open to the air, and a plastic rod with the magnetic probe coils at its end is then inserted fully into the ceramic tube so that the coils are as close to the plasma as possible (see figure B.6 in appendix B for more details).

The ceramic tube acts in three ways: 1) as high voltage insulator to protect the probe coils from the ~ 10 kV potential of the outer conductor, 2) as a vacuum seal and vessel wall that separates the atmospheric pressure from the 10^{-6} Torr vacuum inside CTIX, and 3) as a dielectric boundary that lets the magnetic field at the edge of the plasma enter the probe coil and be detected.

Thus the probe coils are actually inside a finite-sized conducting cylindrical well, approximately 0.874 inches in diameter and 0.765 inches deep. The boundary conditions are significantly different than if the port was not there. As the magnetized plasma flows by a port, it dips into the annular gap between the outside of the ceramic tube and the inside of the stainless steel. Even if plasma flow effects are ignored, the edge magnetic field will expand to fill the conducting well of the port and there will be a gradient in the field as components change to match the boundary conditions. So the result of the measurement depends strongly on the precise depth of the probe position inside the port well.

The radial position of the probes have been carefully measured. Here we list the difference between the tip of the probe coil and the inner surface of the outer conductor, measured in inches, $\Delta r = (r_{outer} - r_{probe\ tip})$

$$\Delta r_{57} = -0.151'', \qquad \Delta r_{91} = +0.0125'', \qquad \Delta r_{142} = +0.0075''.$$

Here, we took into account the thickness of the wire used for the coil (0.0625"), so that the "probe tip" really corresponds to the top position of inner area of the coil, not the tip of the wire surface. Deciding how to split these hairs is not easy, but the small scale of the system we are considering requires that we make precise definitions, sometimes without any good intuitive guidance from simple idealizations.

2.2.2 Effective depth of probes

One key characterization that is needed to properly interpret the magnetic measurements is the calculation of the effective depth of the experimental magnetic measurements. The idea is that because of the well geometry of the port, the probes are effectively measuring the fields at some point in the interior of the plasma, some small but not exactly zero distance away from the outer wall.

This would help reconcile the fact that the analytic Bessel function solution to the Woltjer-Taylor force-free equation has zero B_θ at the walls, while our probe measurements show it to be non-zero. If we accept that the probe is not actually measuring exactly "at the wall" but rather at the effective depth into the interior, then the question of consistency is relaxed. The comparison between model and experiment would then become a quantitative comparison of the ratio of field components at the effective depth.

A reasonable approximation can made by considering the magnetostatic problem with an ideal conductor in the shape of the magnetic probe port. This ignores any plasma dynamics that
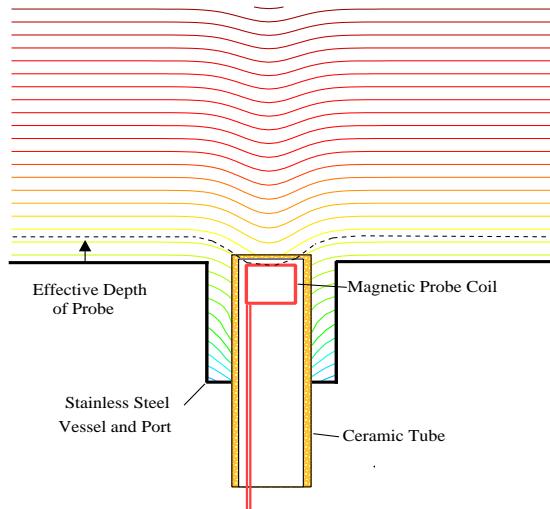
Figure 2.3: Sketch of magnetic probe port and the effect it would have on a uniform field. See appendix B for a more detailed drawing of the probe port.

might affect the measurement, but in the case of a low beta plasma, like our CT, the magnetic field is boss. And although we consider a magnetostatic problem, this isn't such a bad approximation given that the relevant MHD transit timescales are many orders of magnitude slower than the speed-of-light transit timescale for the probe port system. Still, we hope to greatly improve upon these preliminary estimates in the future, and in part, I am documenting the details of my work here in order to provide a starting point for future work, including some 3-D MHD simulations proposed for the near future.

2.2.3 2-D Magnetostatic field computation

We want to find the geometric effect on field lines near the port, given that the field is uniform at infinity. There will exist some field line that intersects the tip of the probe coil. If we follow this field line away from the port sufficiently far, it will level off uniformly. The effective depth of the probe would then be defined as the distance from the wall of this field line when it is far from the port. Additional calibration factors due to field expansion must also be taken into account. The effect is that the measured field is very strongly dependent on the exact radial position of the probes. The interior fields of the CT are several times larger than what we would expect without these additional calibration factors. After certain brief theoretical considerations have been made, we will compare predicted and measured calibration factors.

In order to tackle these issues I considered a variety of approaches. The mathematical details of these methods are presented in Appendix B. However, there are several key results from these methods that are relevant to the current topic and should be summarized.

Because the diameter of the probe coil is relatively small compared with the diameter of the port hole, an accurate 2-D approximation can be made for the magnetic fields near the central plane of the probe port well. I have found that field expansion effects should be more faithfully recreated by a 2-D solution of the right cross-section geometry than a 3-D solution of the wrong cross-section geometry. For example, there exists a standard, fully analytic result for the magnetic

field near a plane with a circular hole in it. This is attractive because it has some features that are qualitatively similar to our probe port; however, the key difference is that in this simple case the field is allowed to expand out infinitely into the void beneath the plane, instead of just into the finite sized well that we actually have. This means that the calibration factor $\frac{B_\infty}{\langle B \rangle_{probe}}$ due to field diminishment caused by expansion, would be somewhat less in the hole geometry than for a finite well. Also, each field line that enters the hole will go deeper than it will in the case of a finite well. Thus for a given probe position, the resulting effective depth will be noticeably larger for the simple hole than it would be for the finite well.

There is also one significant practical simplification that we should use to our advantage. The magnetic field vectors themselves are not really important to find the effective depth and expansion factor. Really we just need to know the shape of the flux surfaces on which the magnetic field lines reside. The simplifications arises from the fact that the magnetostatic potential ϕ_M is the harmonic dual of the electrostatic potential ϕ_E. To go from a potential function to its harmonic dual, we just have to interchange the role of equipotentials and flux surfaces, and the resulting potential will still satisfy the Laplace equation, but with the dual boundary condition.[20]

The magnetostatic potential satisfies the Neumann boundary condition at the surface of the conductor, while the electrostatic potential for the same conductor geometry satisfies the Dirichlet boundary condition. Therefore, we can find the flux surfaces of the magnetic field by actually computing the equipotential surfaces of the dual electrostatic potential problem. This is an advantage because Dirchelet boundary conditions are intrinsically simpler in that you don't have to evaluate derivatives to apply them, and they lend themselves to numerical solution by iterative relaxation methods.

Once the flux surfaces have been evaluated using your method of choice, the effective depth can be found by tracking field lines away from the well and then finding how high above the wall they are after going several hole-radii away from the well. Field expansion ratios can be calculated by comparing the distance between two neighboring field lines, when they are far from the well, vs

when they are at the center of the well.

Here we are using the fact that the magnitude of the magnetic field is proportional to the density of field lines, which gives us the ratio of the far field to its corresponding value of the distorted near field. To measure the average flux through the probe coil, we just choose one field line that passes through the upper tip of the coil, and a second that passes through the lower tip of the coil. If the distance between these two field lines far from the probe well is δz and the height of the probe coil is Δz_{coil} then the calibration factor due to field expansion is $C_{exp} = \frac{\Delta z_{coil}}{\delta z}$.

Following the procedure outlined above, I have implemented a simple 2-D Gauss-Seidel method to find the flux surfaces of the magnetic field in the region near the probe port, and then I evaluated the calibration factor and effective depth as a function of probe position and hole diameter. (see appendix B for details). [21, pp. 47-50]
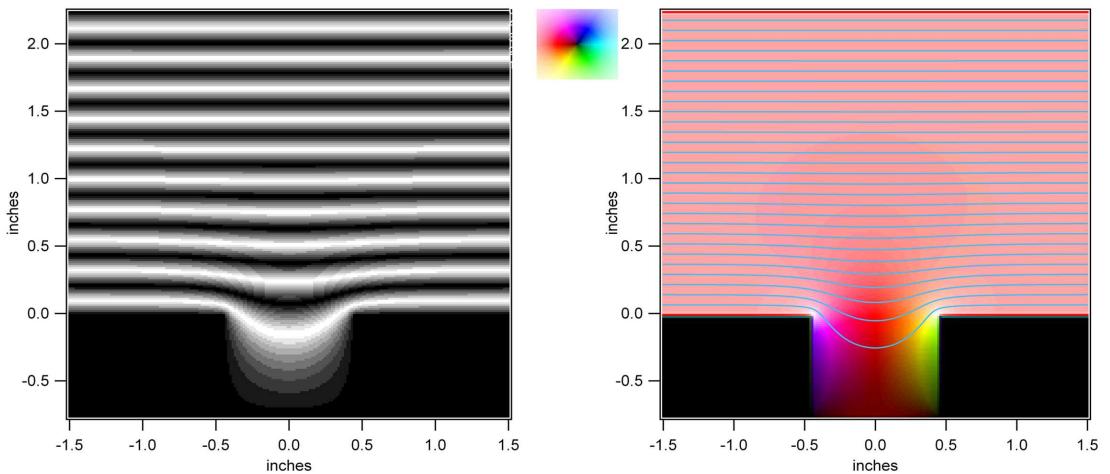
Figure 2.4: 2-D Relaxation simulation result of magnetic field near a conducting port well. Image on left uses a cyclic gray-scale to visualize flux surfaces. Image on right represents the magnetic field vectors using a color-wheel type coloring of the complex plane, which corresponds to the (y, z) directions in physical space. Red indicates a vector pointing directly in the -y direction, while other colors represent vectors at other directions as indicated by the color legend in top left. Vector magnitude is represented by a color's brightness, with black for the zero vector.

The result of the magnetic field computation is shown in fig 2.4, using two different visualizations. On the left, the potential function has been displayed in a cyclic gray-scale to visually identify level sets of the potential, which correspond to magnetic flux surfaces (and also field lines).

On the right, the magnetic vector field has been displayed in a novel color-based vector representation, which is described in appendix F. Also, a set of field lines have been overlaid to guide the eye.
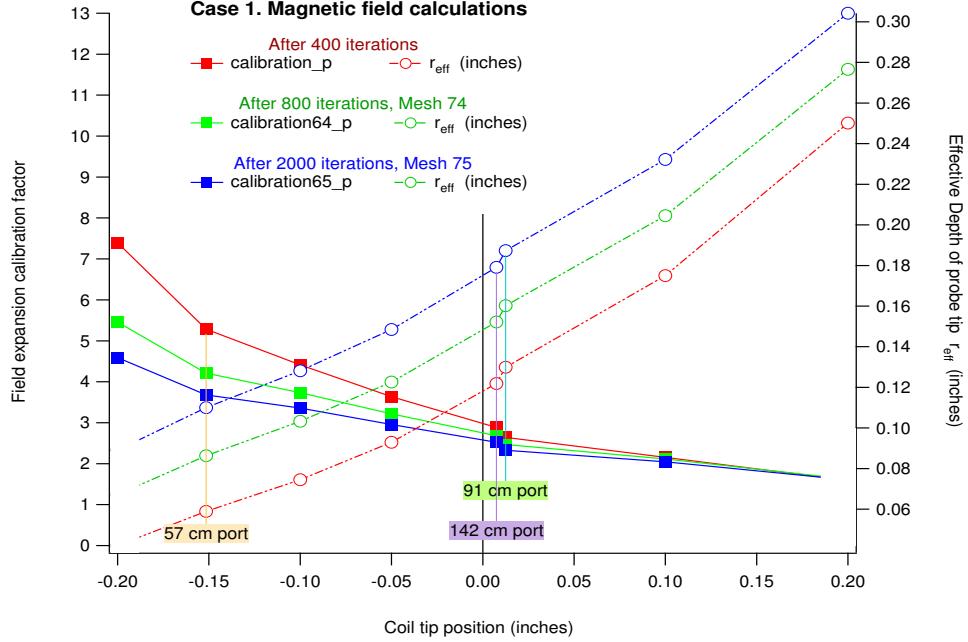
Figure 2.5: Probe position dependent trends in the expansion factor (left) and the effective depth of measurement (right) for magnetic field expansion into full volume of well. Position zero corresponds to the probe coil tip being flush with the inner edge of the port hole.

This is a nice result, but we should try to test its predictions against some real probe data. This can be done using an independent consideration regarding actual magnetic measurements that leads to a relative calibration between the primary set of magnetic probes. Our goal is to test if the relative difference in probe tip position is in agreement with the resulting difference in probe measurements.

2.2.4 Comparison to experimentally determined relative corrections

The basis of this comparison relies on the observation that for late times ($t > 14\mu s$) during the acceleration process, the B_θ pushing field behind the CT relaxes toward an equilibrium state

Case 1.		Calibration factors
C_{57}	=	3.67827
C_{91}	=	2.52267
C_{142}	=	2.32853
Effective depth of probes (inches)		
ρ_{57}	=	0.11045"
ρ_{91}	=	0.17906"
ρ_{142}	=	0.18732"

Table 2.1: Case 1. Calibration factor (C) due to field expansion and effective depth (ρ) for each magnetic probe, using the results after 2000 iterations in the case of the field expanding into the full volume of the probe well.

that is nearly uniform as a function of z.

This effect is clearly seen in the time signals for the toroidal magnetic field component B_θ, and it very closely agrees with the simple kinematic model of a uniform magnetic slab that is decreasing in field strength due only to its uniform expansion.
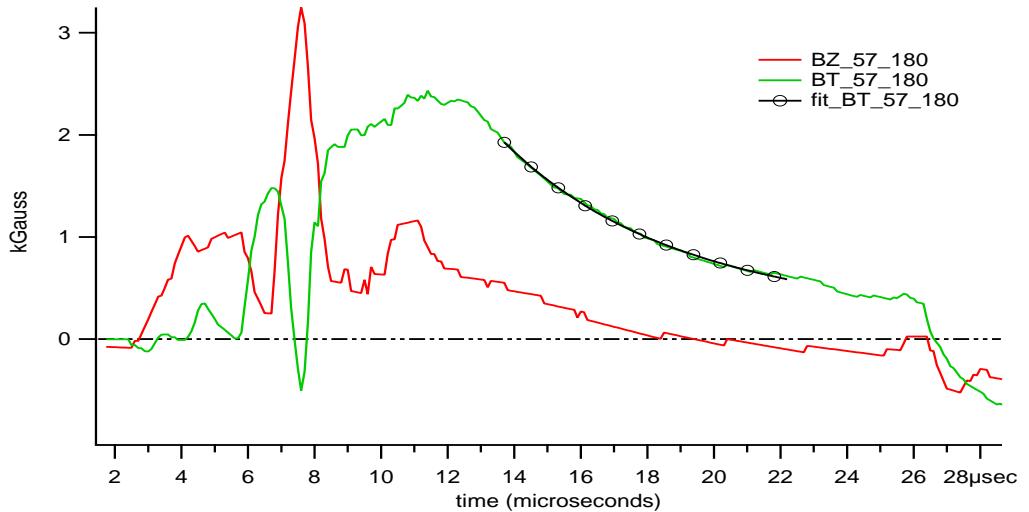
Figure 2.6: B_z and B_θ signals at z = 57 cm as a function of time. The fit to the expansion model is shown as a black curve.

The formula used to fit the expansion of $B_\theta(t)$ is

$$f(t) = \frac{f_0 \Delta z_0}{\Delta z_0 + \Delta v \ (t - t_0) + \frac{1}{2}\Delta a \ (t - t_0)^2} \tag{2.6}$$

We hold constant t_0, which is the starting time for the region of the curve that is being fitted, and also hold constant the initial signal level $f_0 = f(t_0)$, and the initial axial extent of the slab $\Delta z_0 = z_{probe}$. The free parameters for the fit are the difference in velocity and acceleration between the front and back of the slab, Δv and Δa.

In order to compare total calibration factors we just need to look at the ratio of the post-CT B_θ signals as measured by different probes at the same time. If these ratios equal 1, then there is no problem with the relative calibration between probes. Any difference between the probes can be compared to predictions of the field expansion analysis given above.

When we look at the actual B_θ data, there is a small but systematic discrepancy between the measurements at the three locations. This could mean that there exists a highly reproducible non-uniformity of $B_\theta(z,t)$ that depends on z in an exactly fixed way, or that previous calibration factors for the probes were slightly off by differing amounts.

The average value (over 60 shots) of ratios of the three possible pairs of probes are:

$$\frac{B_\theta[57]}{B_\theta[91]} = 1.02529 \pm 0.10296, \quad \frac{B_\theta[57]}{B_\theta[142]} = 1.21117 \pm 0.17172, \quad \frac{B_\theta[91]}{B_\theta[142]} = 1.19293. \tag{2.7}$$

This shows that $B_\theta[57]$ and $B_\theta[91]$ are nearly balanced, while $B_\theta[142]$ is about 20% diminished relative to the other two probes. Comparison with the data in table 2.1, shows a clear discrepency. If the only unaccounted relative difference between the probes was due to the depth-dependent field expansion effect, then we would expect the probes at 91 and 142 to be almost exactly balanced (because they are inserted at nearly the same depth), while the probe at 57 cm would have a reduced signal compared to the other two (because is is more recessed into the well). Using the computed values for the field expansion calibration factors we would expect that the signal ratios would be

$$\frac{B_\theta[57]}{B_\theta[91]} = 0.68583, \quad \frac{B_\theta[57]}{B_\theta[142]} = 0.63305, \quad \frac{B_\theta[91]}{B_\theta[142]} = 0.91903. \tag{2.8}$$

The disagreement between (2.7) and (2.8) could be due to a variety of reasons. There could be errors in my 2-D approximations, or in the accuracy of the probe calibrations the we have been using. Or, the existing probe calibration may be actually better than anticipated and it has already taken these relative scalings into account, implicitly by the nature of the original calibration process.

An alternative way of reconciling this issue is to consider that during the CTIX discharge there might be a stationary plasma surrounding the probe, acting as conductive filling that excludes the magnetic field of the passing CT. The field of the compact torus would only expand into the interior of the ceramic tube itself, which is the same for all the probes. In this case, the details of precisely how far the probe is recessed into, or protruding out of a larger port hole, would be unimportant. Effectively, all the probes would have the same exact geometry for the conducting well; one made of the plasma surrounding the ceramic tube, not the stainless steel vessel. To calculate the effective depth and field expansion calibration factors, we would use a well with the same diameter as the ceramic (0.5") and measure the conditions at a position that is recessed into the well a distance equal to the thickness of the ceramic wall at the probe tip. Figure 2.7 shows the results of the analysis in this case with stagnant plasma in the annular gap around the probe (call this Case 2).

Case 2.	Calibration factor	
$C_{expansion}$	$=$	4.20797
Effective depth of probes (inches)		
ρ_{eff}	$=$	0.07919"

Table 2.2: Calibration factor (C) due to field expansion and effective depth (ρ), which are the same for all the magnetic probe in the case of the field expanding only into the smaller volume of the ceramic tube. We use the results after 2000 iterations.

Over the course of these considerations we have found that value of the effective depth of any of the probes should be between 0.079" and 0.187" (2 mm to 4.7 mm), while the additional calibration factor due to field expansion should be between 2.3 and 4.2. However, the precise values within these ranges are still too indeterminate given the existing data from experiment and
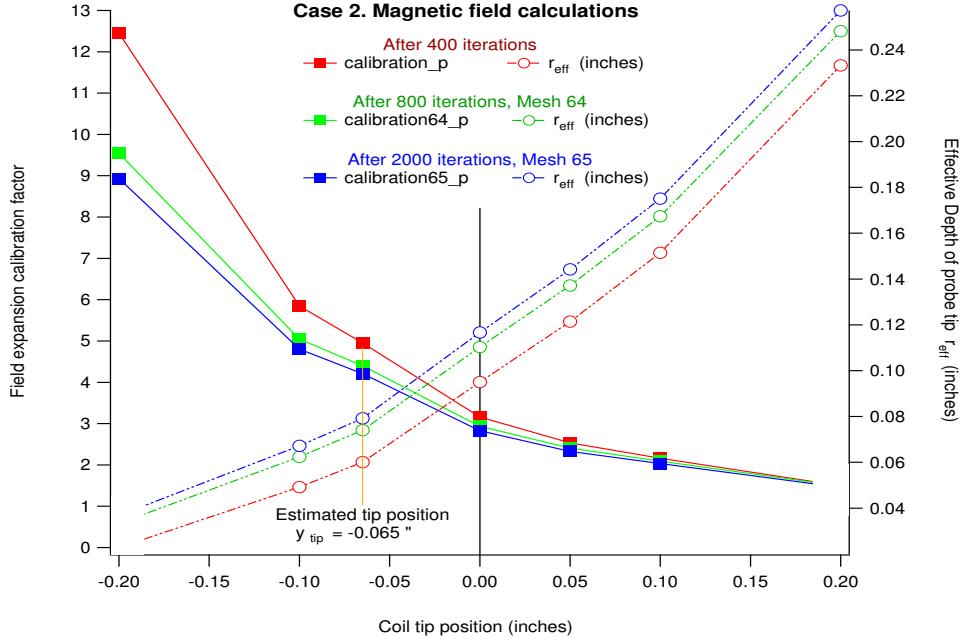
Figure 2.7: Probe position dependent trends in expansion factor (left) and effective depth of measurement (right) for magnetic field expansion into only partial volume of well due to field exclusion by stagnant plasma. Position zero corresponds to the outer surface of the ceramic probe sleeve.

simulations. Direct experimental measurements of these constants should be done soon, and this could be complemented by some better 3-D simulation, possibly including plasma effects. For now, we can let this range of values serve as error bars on our subsequent estimates.

As it relates to our primary question of how the compact toroid magnetic field can be modeled, the effective depth is the critical variable for comparison with experiment. Our estimates for the effective depth can now be used to quantitatively compare the ratio $\frac{B_\theta}{B_z}$ between theory and experimental measurements. Using the Bessel function solution of $\nabla \times \mathbf{B} = \lambda \mathbf{B}$ in a coaxial geometry with $r_1 = 3.34$ cm and $r_2 = 7.62$ cm we can evaluate the magnetic field components at any specified depth. We find that

$$(\rho_{eff} = 2mm) \; \rightarrow \; \left| \frac{B_\theta}{B_z} \right| = 0.1379, \qquad (\rho_{eff} = 4.7mm) \; \rightarrow \; \left| \frac{B_\theta}{B_z} \right| = 0.3818 \qquad (2.9)$$

2.2.5 Conclusions

Based on our preliminary observation that most CTs have a central dip in B_θ equal to about 1/2 the peak of B_z, we can now say with some certainty that the Bessel function model is in moderate agreement with our measurements, provided that the true effective depth is at, or above, the upper end or the believable range. However, if the physically real ρ_{eff} is as small as 2 mm, then this is not the case; the measured B_θ would be about 4 times too large to be accounted for by the Bessel function model. On the other hand, if we could stretch our errors enough to let $\rho_{eff} = 6\ mm$ be considered reasonable, then we would have a perfect match between theory and experiment.

Further progress can be made toward quantifying this comparison. In addition to the improvements that are possible with understanding the magnetic expansion effects in the vicinity of the well, we can also better quantify this "dip-to-peak" ratio in actual data and gather the statistics of this quantity over a large data set. Clearly, this is a task that would be best postponed until there ample time to do it properly (when some future student feels compelled to take up the cause). In the meanwhile, we can trust that there is truth in idea of the CT existing in some sort of minimum energy state, and rely upon this idea as an approximation if it helps to make a difficult problem more tractable.

Next, we will introduce a very useful "quasi-tomographic" method, which I call Lagrangian interpolation, whose purpose is to squeeze as much information out of sequence of three probe measurement as is humanly possible. We will use this method on several occasions throughout this study, for both visualization and deduction.

2.3 Lagrangian interpolation of probe signals

In order to bridge the gap between theory and experiment there is much progress that can be made simply by improving our understanding of existing experimental data. Here we present a method of reconstructing the approximate spatial dependence of the magnetic field within the

plasma, using the data collected from three magnetic field probes as the plasma rushes past them during the acceleration process. The result is an accurate estimation of the magnetic components B_z and B_θ as a function of axial position at each instant in time. These lend themselves to being turned into nice little movies of the CT going down the accelerator, making it easy to visualize the spatial structure of the magnetic fields.[2]

More importantly, once we know how these magnetic field components depend on (z, t) we can take derivatives with respect to space and time, allowing the full repertoire of electrodynamics to be applied. We can then develop certain quantities that have been derived from our experimental data, and compare them to theoretical predictions.

I call this method *Lagrangian interpolation* because it follows the trajectories of fluid elements through the system, and performs an interpolation of the field quantity using the measured values at the points where a trajectory crosses the probe locations, doing so along the path of each trajectory. This interpolation relies on first making an estimation of the velocity field throughout the system, usually based on the apparent time-of-flight kinematics of the magnetic pulses. A more detailed account of the method is presented in appendix C. Here we will examine those specific results relevant to resolving the issue of the magnetic geometry of the compact toroid.

One way to estimate the flow field on CTIX is to track one very distinct feature as it travels down the pipe, and then apply the same relative kinematics to the rest of the fluid elements in the system. We have found that the most stable such feature on the CTIX waveforms is the back edge of CT. This is the junction point between the CT and the pushing field, and we can reliably define the arrival of this point as being the time when the B_z signal of a given probe crosses the half-maximum level on the trailing edge. The high accuracy of this method is due to the very reproducible and cleanly steep slope that occurs at the CT back edge on virtually every shot.

In this way we can find the times that the CT back edge passes by the three accelerator probes, t_{57}, t_{91}, t_{142}. These immediately allow us to find the average velocities due to the transit

---

[2]Magnetic field movies can be downloaded from our website http://ctix.das.ucdavis.edu

times between the probes

$$\bar{\text{v}}_{57-91} = \frac{91 - 57}{t_{91} - t_{57}}, \qquad \bar{\text{v}}_{91-142} = \frac{142 - 91}{t_{142} - t_{91}}.$$

Then from the change in velocity we can find the average acceleration of the back edge

$$\bar{\text{a}} = \frac{2(\bar{\text{v}}_{91-142} - \bar{\text{v}}_{57-91})}{(t_{142} - t_{57})}.$$

We can subsequently infer an initial velocity and initial position,

$$\text{v}_0 = \bar{\text{v}}_{57-91} - \bar{\text{a}}\frac{(t_{57} + t_{91})}{2}$$

$$z_0 = 57 - \text{v}_0 t_{57} - \frac{1}{2}\,\bar{\text{a}}\,t_{57}^2$$

This is based on the assumption that the CT back moves with constant acceleration

$$z_{CT}(t) = z_0 - \text{v}_0 t - \frac{1}{2}\,\bar{\text{a}}\,t^2.$$

For positive values of acceleration there will always be a minimum z- position, z_{min}, that the CT never goes below, according to this simple description.

$$z_{min} = z_0 - \frac{\text{v}_0^2}{2\,\bar{\text{a}}}$$

This is also the point on the trajectory where $\text{v}(t) = 0$. The problem is that for early times, before the fluid element has reached z_{min} according to this description taken literally, it would have a negative velocity, which is unphysical for our system. Instead we will only apply these uniformly accelerated models to the region above z_{min}, and during times of positive velocity.

If we work with a simple model in which all the fluid elements have the same acceleration throughout time and space, they will all have the same z_{min}, but they would pass through it at different times. Based on this, we arrive at a velocity field of the form

$$\text{v}(z,t) = \sqrt{2\,\bar{\text{a}}\,(z - z_{min})} \tag{2.10}$$

Notice that this depends on space but not on time. We can think of this like a Taylor series approximation which is most accurate near the central point, and decreases in accuracy as you move

away. In this same way, this velocity field will be most accurate in the neighborhood of the CT back edge. But long after the CT has passed by, the acceleration dynamics will certainly change, and this approximation will no longer be a good one.

Some modification to this velocity field must be done to make it fit certain basic physical constraints. For the case where $z_{min} > 0$ we clearly need a different way to handle the velocity in the region $z < z_{min}$. Since this will always occur in the region before the first probe at $z = 57$ cm, where there is a scarcity of real velocity information, the most pragmatic approach is to set the velocity equal to a constant value that matches the accelerated velocity curve at some point $z_{fit} > z_{min}$. For instance, we have found good results by defining the position of the fit $z_{fit} \equiv \min \left(\frac{3}{2} z_{min}, \ 57cm\right)$, then defining the velocity in a piece-wise fashion.

$$\mathrm{v}(z,t) = \begin{cases} \sqrt{2 \ \bar{\mathrm{a}} \ (z - z_{min})} & \text{if } z > z_{fit} \\ \sqrt{2 \ \bar{\mathrm{a}} \ (z_{fit} - z_{min})} & \text{if } z \leq z_{fit} \end{cases} \tag{2.11}$$

An additional modification is needed because we begin recording the signal about 12 μs before the shot begins, and then there is a period of about 4 μs before the accelerator back fires, during which time the velocity field is driven only by the formation bank. This leads to a natural division of the time domain into three parts. 1) Before the formation back fires, the velocity should be zero everywhere. 2) Once the formation current begins to flow, the velocity field should be determined by the kinematics of the leading edge of the CT, where we detect the first early rise above the zero level of B_z. 3) Lastly, once the accelerator current turns on we can use a velocity field like (2.11), based on the motion of the CT back edge.

This is not the only possible velocity field that can be extrapolated from the kinematics of the back edge of the CT. However, when it is applied to actual data it seems to give the best agreement with our expectations of how the magnetic fields should behave globally. For instance, velocity models that go to zero as $z \rightarrow 0$ will produce a quite unphysical "precognition" effect near the origin, where there is a build up of fluid trajectories that results in an axially compressed version of the future wave pattern that seems to be "waiting in the wings" until it hears its cue and makes

its debut passing by the first probe and out onto the theater of our observation. Instead of this, some moderately large initial velocity is needed to be in agreement with the fact that there is a high rate of magnetic flux input from the external circuit, as well as an ongoing formation of new plasma by ionization of the steady flux of neutrals from the slowly closing gas valve. In this way, velocity fields like (2.11) are good because they are qualitatively consistent with these facts, and therefore prevent the fluid elements from "hanging out backstage" too much.
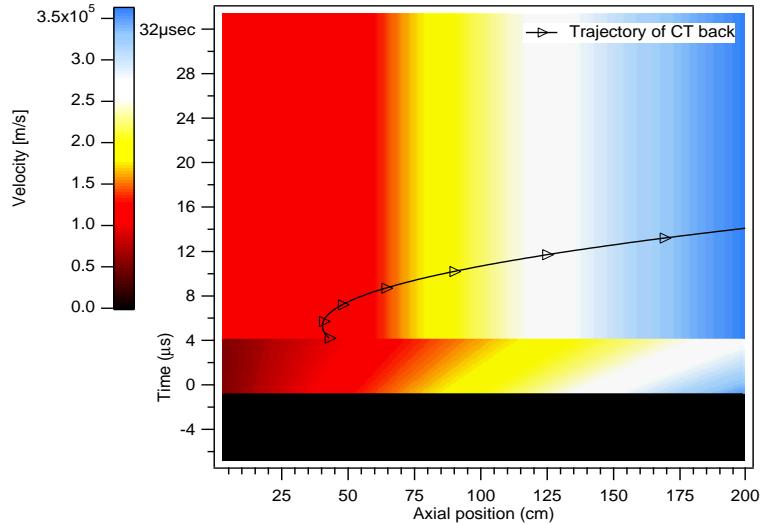
Figure 2.8: The estimated velocity field on the (z,t) domain. The trajectory of the CT back is shown as a black curve.

Once we have a reasonable estimation of the fluid velocity field, we can interpolate the real probe signals across the trajectories, filling the whole (z, t) domain with values of the field components. We can then sample this 2-D array of interpolated values along slices of constant time, and see the shape of the fields as a function of z, at any instant of time. Typically we performed this interpolation using 200 points in the z direction, one point per cm, and 1024 points in the time direction at a rate of 0.1 μs per point, taken from the scaling of the raw time signals.

Shown in figures 2.9 to 2.14 on the following few pages, is the resulting interpolation of the z and θ components of the magnetic field at several instants in time. Before computing the interpolation, we applied the calibration factors discussed in the previous section to the probe signals.

The safest approach is to use the relative calibration determined from comparison of the experimental ratios of B_θ in the expanding pushing field, and combine that with an absolute expansion factor determined from the magnetostatic simulation. These factors had values of:

$$C_{57} = \frac{4.2}{1.211} = 3.4682, \qquad C_{91} = \frac{4.2}{1.1929} = 3.5207, \qquad C_{142} = \frac{4.2}{1.0} = 4.2$$
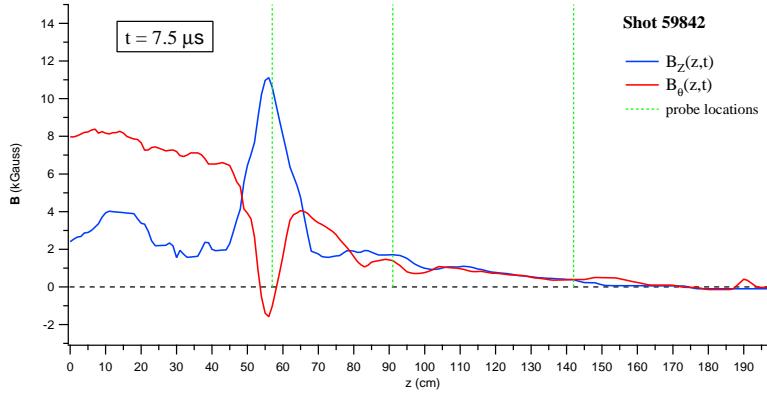
Figure 2.9: $\mathbf{B}_\theta$ and $\mathbf{B}_z$ as a function of axial position at time t $= 7.5$ μs for shot 59842.
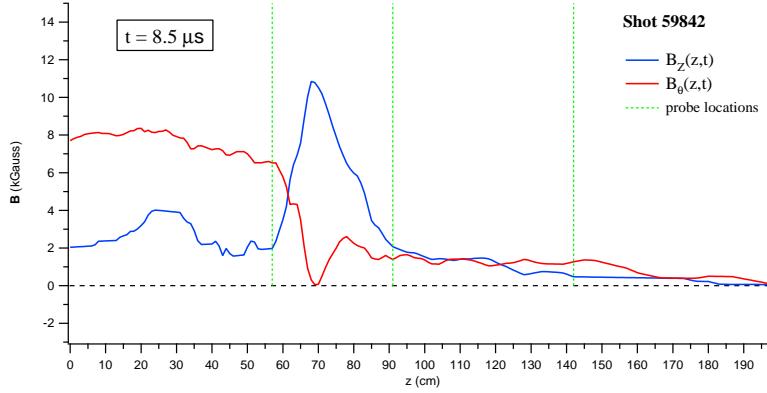
Figure 2.10: $\mathbf{B}_\theta$ and $\mathbf{B}_z$ as a function of axial position at time t $= 8.5$ μs for shot 59842.

As can be clearly seen in these figures, the axial dependence of the magnetic fields is clearly more complicated than the simplistic $\sin\left(k_z(z - z_0)\right)$ and $\cos\left(k_z(z - z_0)\right)$ of the force-free Bessel function model. However, there is some evidence to support that the radial dependence of
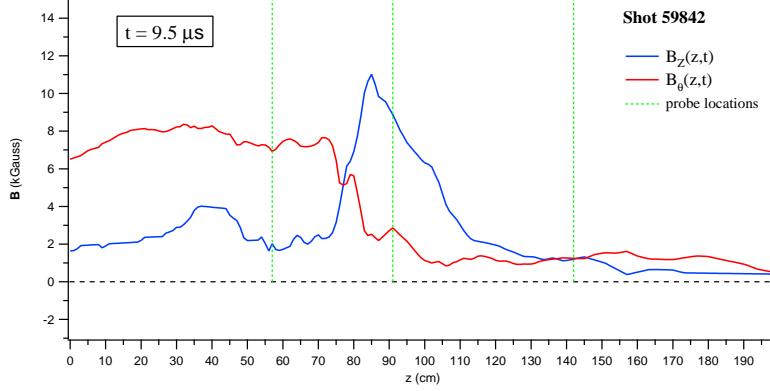
Figure 2.11: $\mathbf{B}_\theta$ and $\mathbf{B}_z$ as a function of axial position at time t $= 9.5\ \mu s$ for shot 59842.
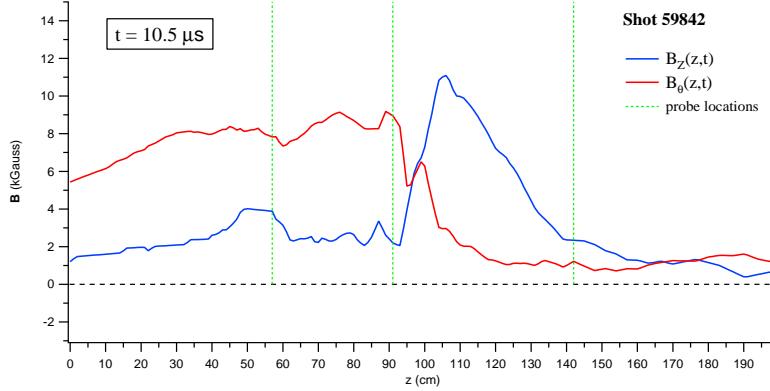
Figure 2.12: $\mathbf{B}_\theta$ and $\mathbf{B}_z$ as a function of axial position at time t $= 10.5\ \mu s$ for shot 59842.

the fields is reasonably well described by the Bessel function model. We may combine the two if we assume that the field is separable in terms of radial and axial dependence. Doing so will at least allow us to make a comparison between experiment and a minimally modified version of the Taylor state equilibrium.

In the following discussion we will use this Bessel function combination so frequently that it is notationally useful to define

$$F_i(x) \equiv [J_i(x) + fY_i(x)], \qquad i \in \{0, 1, 2, \ldots\}. \tag{2.12}$$
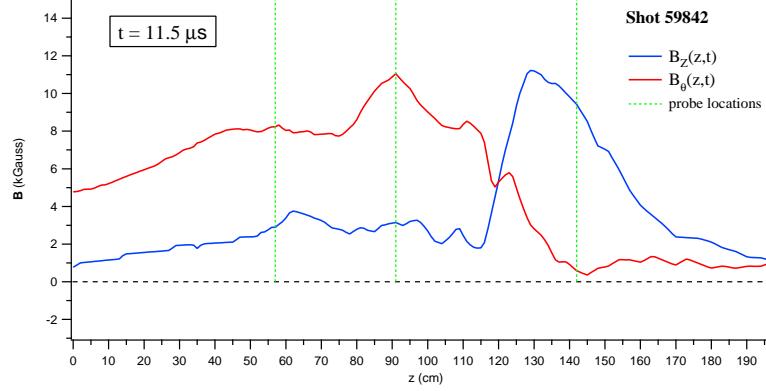
Figure 2.13: $\mathbf{B}_\theta$ and $\mathbf{B}_z$ as a function of axial position at time t $= 11.5$ μs for shot 59842.
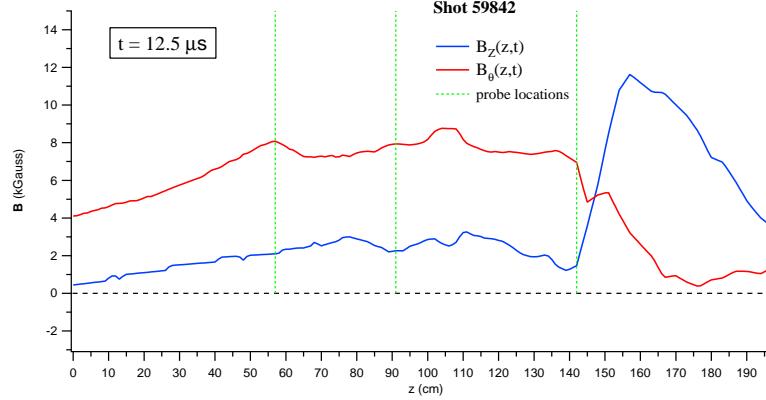
Figure 2.14: $\mathbf{B}_\theta$ and $\mathbf{B}_z$ as a function of axial position at time t $= 12.5$ μs for shot 59842.

This merger requires having a good estimation of the effective depth of the probe measurements. The z-component of the field would then vary throughout the full domain of the system according to

$$B_z(r, z, t) = B_z(z, t) \frac{F_0(k_r r)}{F_0(k_r r_{\text{eff}})} \qquad (2.13)$$

where $B_z(z, t)$ is the interpolated probe signal as a function of axial position and time, and r_{eff} is the effective radial location of the probe measurement. All other terms are the same as have been used previously. The form of this is necessary to match the probe signals $B_z(r_{\text{eff}}, z, t) = B_z(z, t)$.

Likewise, the θ-component has the form

$$B_\theta(r,z,t) = B_\theta(z,t)\frac{F_1(k_r r)}{F_1(k_r r_{\mathrm{eff}})} \tag{2.14}$$

We can use this radial dependence and the non-existence of magnetic monopoles ($\nabla \cdot \mathbf{B} = 0$) to evaluate the r-component of $\mathbf{B}$.

$$B_r(r,z,t) = -\frac{\partial B_z(z,t)}{\partial z}\frac{\frac{1}{r}\int r F_0(k_r r)dr}{F_0(k_r r_{\mathrm{eff}})} \tag{2.15}$$

$$= -\frac{\partial B_z(z,t)}{\partial z}\frac{1}{k_r}\frac{F_1(k_r r)}{F_0(k_r r_{\mathrm{eff}})} \tag{2.16}$$
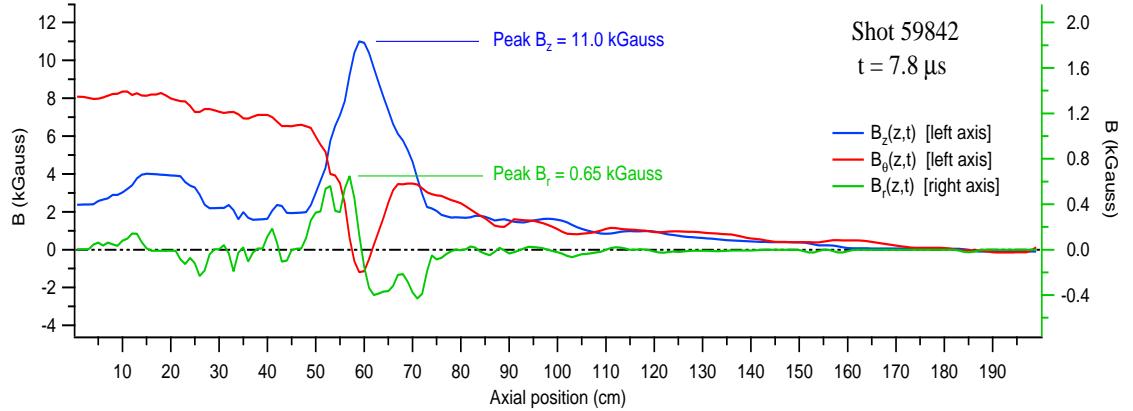
Figure 2.15: plot of B_r, B_z, B_θ at a single time.

We can evaluate Ampere's equation $\nabla \times \mathbf{B} = \mu_0 \mathbf{j}$ in cylindrical coordinates with assumed axisymmetry ($\frac{\partial}{\partial \theta} \equiv 0$). The resulting components of $\mathbf{j}$ are:

$$j_r = -\frac{1}{\mu_0}\frac{\partial B_\theta}{\partial z} \tag{2.17}$$

$$j_\theta = \frac{1}{\mu_0}\left(\frac{\partial B_r}{\partial z} - \frac{\partial B_z}{\partial r}\right) \tag{2.18}$$

$$j_z = \frac{1}{\mu_0 r}\frac{\partial\, r B_\theta}{\partial r} \tag{2.19}$$

Notice that both j_r and j_z depend only on B_θ, while j_θ depends on both B_r and B_z.
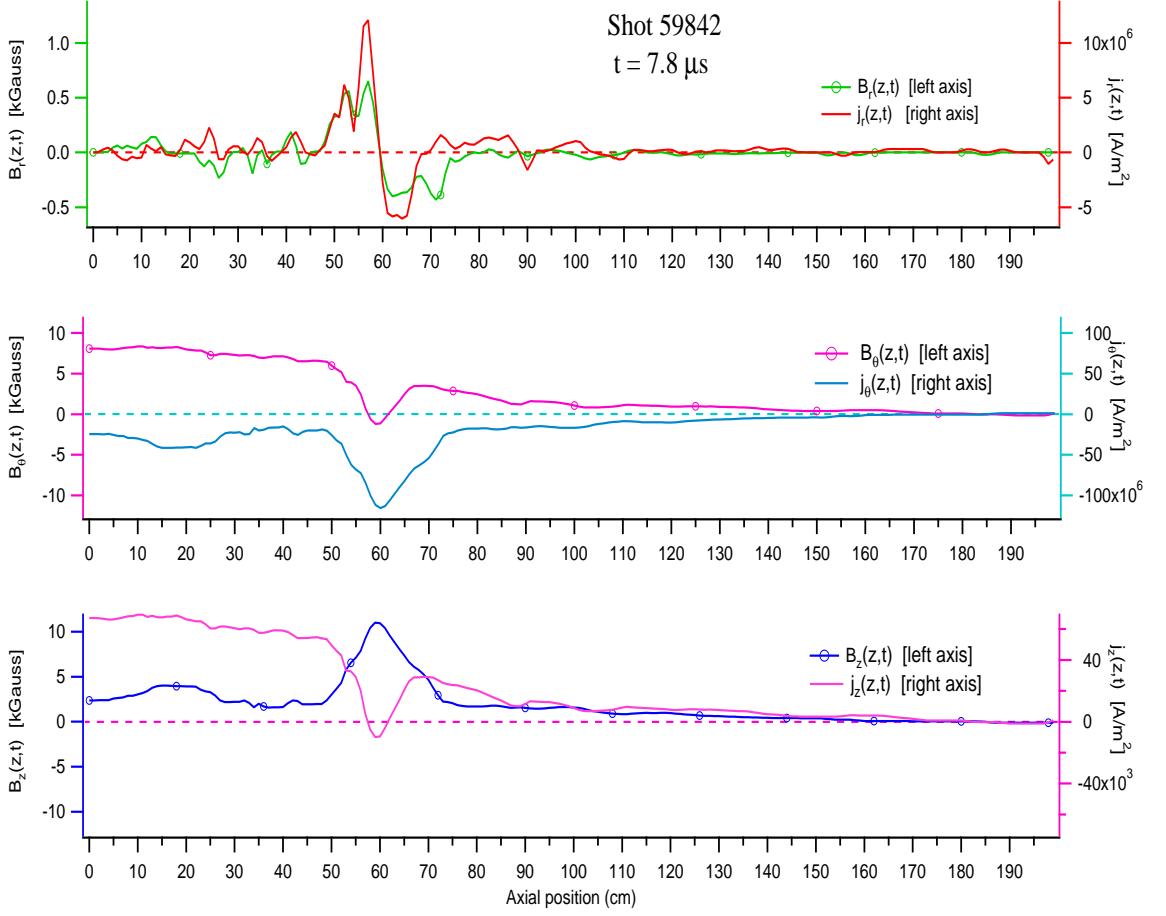
Figure 2.16: Trio of overlay plots, j_r and B_r, j_z and B_z, j_θ and B_θ at a single time.

We find that at the effective depth of the probe, the following generalization appears to hold. The radial current density has a nearly constant proportionality with the radial magnetic field component, $j_r \propto B_r$, in agreement with $\mathbf{j} \times \mathbf{B} = 0$. Yet the other two components appear to be cross-wise related, $j_z \propto B_\theta$, and $j_\theta \propto -B_z$. This leads to a significant deviation away from a force free state.

The proportionality between j_r and B_r, is interesting and significant because they are derived from independent experimental measurements. The radial current density j_r comes from $B_\theta(z,t)$, while B_r comes from $B_z(z,t)$ using the assumption of the Bessel function radial dependence

only to fix the magnitude of the signal, its z-dependence is determined purely from $B_z(z,t)$. So this is a true symmetry inherent in the actual magnetic field configuration, and not some artifact of the reconstruction.

On the other hand, the relations between the z and θ components arises from an actual lack of symmetry between the z and θ magnetic fields. We must conclude that $\mathbf{j} \times \mathbf{B} \neq 0$ within the CT, and that this departure has a noticeable effect on the magnetic equilibrium. This effect is really nothing more than what we have known all along, that the CT is being dramatically accelerated by a large rail-gun Lorentz force density equal to $\mathbf{j} \times \mathbf{B}$. The uncertainty up to this point has always been that we were unsure of exactly where in the system $\mathbf{j} \times \mathbf{B}$ has nonzero values, and to what extent we can apply the standard model of force-free equilibrium.

2.4 The Hall term, $\mathbf{j} \times \mathbf{B}$

Based on the Lagrangian interpolation of the probe signals we can calculate the $\mathbf{j} \times \mathbf{B}$ vector throughout the system. Shown in figure 2.17 is the magnitude of $\mathbf{j} \times \mathbf{B}$, as well as the resulting angle between $\mathbf{j}$ and $\mathbf{B}$, both calculated from the data taken on shot 59842.
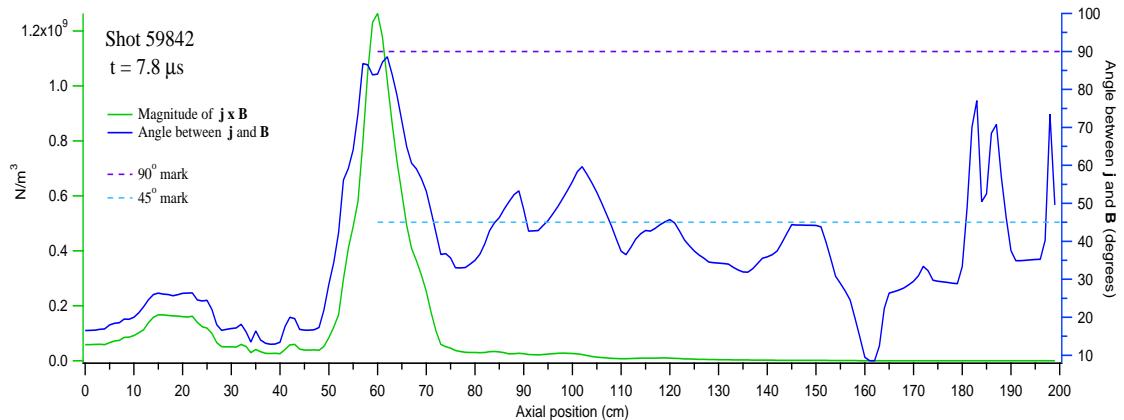
Figure 2.17: The magnitude of $\mathbf{j} \times \mathbf{B}$ and the angle between $\mathbf{j}$ and $\mathbf{B}$, shown as a function of axial position at time t = 7.8 μs for shot 59842.

The primary qualitative observation is that $\mathbf{j} \times \mathbf{B}$ is large throughout the whole CT, and

not limited to just the interface with the pushing field. The plasma may be in some relaxed minimum energy state, but is not anything close to force-free. We see that within the center of the CT, the current is approximately at right angles to the magnetic field, while at the edges the angle drops down to about 45°.

We can break down the $\mathbf{j} \times \mathbf{B}$ vector into (r, θ, z) components, and consider their individual effects.
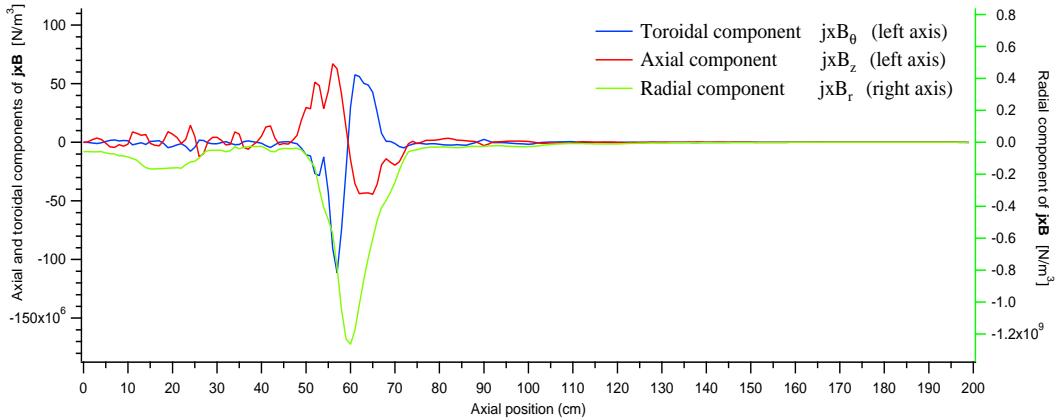
Figure 2.18: The radial, toroidal, and axial components of the $\mathbf{j} \times \mathbf{B}$ vector, shown as a function of axial position at time t = 7.8 μs for shot 59842.

We see that most of $\mathbf{j} \times \mathbf{B}$ is due to a component in the negative radial direction. This should be in agreement with the standard MHD equilibrium condition $\mathbf{j} \times \mathbf{B} = \nabla P$, where P is the hydrodynamic pressure of the plasma. Due to the large radial gradients in density, the pressure gradient at the outer wall should also be directed inward, in the -r direction. Exact quantitative comparison between this value of $(\mathbf{j} \times \mathbf{B})_r$ and reasonable estimations of $(\nabla P)_r$, still remain to be done. It is hopeful that their equivalence may serve as an independent constraint on the calibration factors used in the magnetic measurements. [22]

We may also be able to relate the volume integral of $(\mathbf{j} \times \mathbf{B})_z$ with the net force on the CT that results in its acceleration in the axial direction. Ball-park estimations of these quantities show promising agreement. It is interesting to note that $(\mathbf{j} \times \mathbf{B})_z$ has a strong positive peak at the back

edge of the CT, while it has a lesser negative peak at the front edge. This is what is responsible for the CT maintaining its shape as it travels. The net axial force on the CT should correspond to the pressure differential across the CT.

The most surprising result is the effect of a nonzero $(\mathbf{j} \times \mathbf{B})_\theta$, which should result in toroidal spin-up of plasma. The apparent front-to-back sign reversal of $(\mathbf{j} \times \mathbf{B})_\theta$ would imply that the front edge is counter-rotating relative to the back edge, with a strong axial shear in the toroidal velocity field. The fact that $(\mathbf{j} \times \mathbf{B})_\theta$ is comparable in magnitude to $(\mathbf{j} \times \mathbf{B})_z$ would seem to imply that the toroidal component of the velocity may be as large as the axial velocity of the CT (5 to 30 cm/μs).

Anticipating this possibility, we did make an attempt to measure this toroidal effect via Doppler measurements of the He II ion line at 4686 Å, using the high resolution spectrometer described in chapter 6. We did this by acquiring the light from the z = 57 cm optical ports at $60°$ and $300°$, using multiple fibers inputs imaged on the same intensified CCD at the dispersion plane of the spectrometer. One fiber collected light in the $+ \theta$ direction, while a second fiber collected light in the $- \theta$ direction. Any difference in the center wavelengths of the line profiles should be due to a net toroidal rotation of the ions. The preliminary measurements of toroidal rotation were null, $v_\theta < 1 cm/\mu s$, but this may have been due to the relatively long exposure times (2 to 5 μs) needed to overcome problems with low light levels in this spectrometer configuration. Long exposures would result in a blending of the positive Doppler shift at the front edge of the CT with the negative shift due to the back edge. On average, over a few μs, there would be zero net toroidal rotation observed. In order to accurately measure a differential Doppler shift like that predicted by this result for $(\mathbf{j} \times \mathbf{B})_\theta$, the measurements would need to have exposure times of less than 0.5 μs, preferably as short as 0.1 μs in order to resolve a change in velocity across the length of the CT.

Now going back to our original question, "How do we describe the magnetic equilibrium of a compact toroid?", we find that all of these considerations lend their support to the validity of a more recent theory that is a generalization of Taylor's relaxation idea, but includes the effect of a non-zero Hall term $(\mathbf{j} \times \mathbf{B})$ in the formula for resistivity of the plasma (Ohm's Law). This is

ultimately part of an entire field of study often called Hall Magnetohydrodynamics (HMHD), which can yield quite different descriptions of the same phenomena treated by regular MHD (which ignores the Hall term), simply due to this change in the character of the resistivity of the plasma.

The idea first proposed by Turner [23], is that magnetic relaxation can still occur, but when the Hall term is included in Ohm's law, a different quantity that he calls the *hybrid helicity* becomes an invariant of the system. The conservation of the both the magnetic helicity and the hybrid helicity will constrain the magnetic field so that it can never fall all the way down to the Taylor state, but instead reach a different equilibrium which is not force-free. There are actually several distinct generalizations to the Taylor relaxation theory [24],[25],[26],[27], but Turner's idea is overall the simplest, and most applicable the CTIX plasma.

The derivation of an equation for this HMHD minimum energy state will require us to consider the velocity field on equal footing with the magnetic field. In fact we consider the vorticity of the flow, and the cyclotron-normalized magnetic field.

$$\omega = \nabla \times \mathbf{v}, \qquad \omega_c \equiv \frac{e\mathbf{B}}{mc}$$

We can then define a hybrid vorticity according to

$$\mathbf{\Omega} = \omega + \omega_c$$

and this evolves in time via

$$\frac{\partial \mathbf{\Omega}}{\partial t} = \nabla \times (\mathbf{v} \times \mathbf{\Omega})$$

If we note that $\mathbf{\Omega}$ is expressible in terms of a vector potential $\mathbf{V}$

$$\mathbf{\Omega} = \nabla \times \mathbf{V}$$

and consider a solenoidal form of $\mathbf{V}$, (i.e., $\nabla \cdot \mathbf{V} = 0$), we can see that

$$\mathbf{V} = \mathbf{v} + \frac{e\mathbf{A}}{mc} + \nabla \chi$$

where $\mathbf{A}$ is a particular instance of the magnetic vector potential, and χ is an arbitrary scalar function that satisfies Laplace's equation $\nabla^2 \chi = 0$. The hybrid helicity is defined as the volume

integral of the dot product between $\boldsymbol{\Omega}$ and $\mathbf{V}$

$$H_{hybrid} \equiv \int \mathbf{V} \cdot \boldsymbol{\Omega} \; d^3x$$

It can be shown that this is an invariant of an ideal MHD fluid with a non-zero Hall term.

A two-parameter Lagrange multiplier analysis can be performed to solve the variation problem in which total energy is minimized while the system is constrained by both the magnetic and hybrid helicities being held constant. The result is that each of the Lagrange multipliers serve as eignevalues of a pair of (coupled) minimum energy equations,

$$\nabla \times \omega_c = (\tilde{\lambda}_1 + \tilde{\lambda}_2)\omega_c + \tilde{\lambda}_2 \omega \qquad (2.20)$$

$$\nabla \times (\omega + \omega_c) = \frac{\omega}{\tilde{\lambda}_2} \qquad (2.21)$$

where $\tilde{\lambda}_1, \tilde{\lambda}_2$ are the multipliers after having been normalized, $\tilde{\lambda}_i = \frac{c}{\omega_p}\lambda_i$. The solution to this system of equations for ω and ω_c is what we call the Hall minimum energy state.

In the future, we would like to find an exact solution to these equations for the coaxial geometry and compare them to our experiment. Additionally, the main features of this theory provide good motivation to attempt improved measurements of the velocity and magnetic field profiles by experimental means.

Chapter 3

Determination of plasma resistivity

Of all the properties of the compact toroid plasma, it is the electrical resistivity that provides the most fundamental characterization of its nature as a magnetofluid. Resistivity measures a material's intrinsic tendency to block the flow of electric current, by way of some energy dissipation mechanism. For a conductive fluid, the resistivity determines how electric and magnetic fields will couple to the velocity field of the fluid. The resistivity also plays a central role in determining the value of the magnetic Reynolds number used to characterize the nature of turbulence in a magnetofluid, as discussed in chapter 7. Yet despite this important role, the resistivity and related magnetic diffusion coefficients remain poorly understood in many systems. For most of our estimates we will rely on standard formulas, despite uncertainties about their applicability. We will also explore some methods to improve our approximations using actual measurements.

3.1 Collisional Spitzer resistivity

One of the longest standing results in plasma physics is Spitzer's formula for the resistivity of a magnetized plasma [28],[29]. It is derived by analyzing the dissipative energy loss (drag) due to long range collisions mediated by the electrostatic Coulomb force between charged particles. The

resulting formula is dominantly dependent on electron temperature T_e,

$$\eta_\perp = 1.03 \times 10^{-4} \ T_e^{-3/2} \ Z \ \ln \Lambda \qquad [\Omega \cdot m] \tag{3.1}$$

Where Z is the effective charge state of the plasma, which is very nearly 1 for our hydrogen CT's, and the term $\ln \Lambda$ is the called the Coulomb logarithm, which is defined as the natural log of the ratio of the maximum interaction distance ($r_{\max}$) over the minimum interaction distance ($r_{\min}$, also called the impact parameter), averaged over a Maxwellian distribution,

$$\ln \Lambda = \ln \left(\frac{\langle r_{\max} \rangle}{\langle r_{\min} \rangle} \right) \ \simeq \ \ln \left(12\pi n_e \lambda_D^3 \right) \ = \ 24 - \ln \left(n_e^{1/2} \ T_e^{-1} \right) \quad \text{for } T_e \leq 10 \text{ eV} \tag{3.2}$$

The maximum and minimum interaction distances are related to the Debye length, λ_D of the plasma, which is the length over which static electric fields are shielded out by free charges in the plasma. $\lambda_D = \sqrt{kT/4\pi n_e e^2}$

The presence of a magnetic field acts to impede the flow of charged particles (and hence electric current) in the direction perpendicular to the field. This is manifested as a directional dependence of the resistivity, with the plasma being more resistive in the cross field direction. Under normal conditions there is a simple proportionality between the transverse and parallel values, $\eta_\perp = 1.96 \ \eta_\parallel$.

The underlying assumptions that make Spitzer's derivation possible are:

1) The plasma is in a steady state (all quantities are constant in time).

2) The magnetic field is uniform in space.

3) The electrons are well magnetized, i.e., the gyroradius is less than the mean free path $\rho_e \ll \lambda_{\mathrm{mfp}}$.

4) The electron motion is dominated by collisions, $\lambda_{\mathrm{mfp}} \ll L_{\mathrm{system}}$.

5) The electric field is small enough that only small departures away from Maxwellian electron distributions will occur, $E\lambda_{\mathrm{mfp}} < T_e$.

6) Collisions between electrons and neutrals can be ignored.

We can consider the validity of each of these assumptions. The steady state assumption (1) is rather hard to apply in any global sense to our experiment given the rapid acceleration that
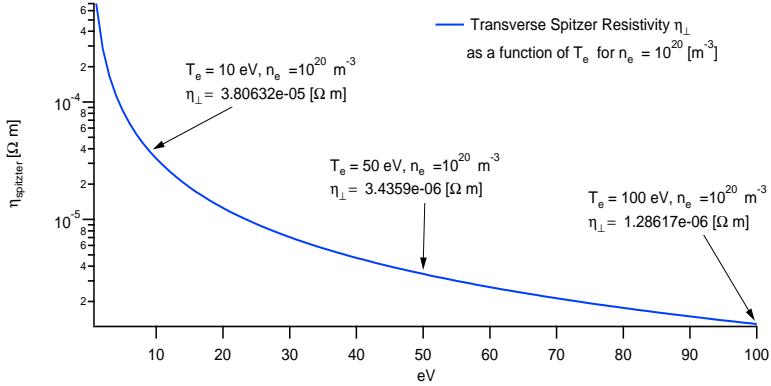
Figure 3.1: The transverse Spitzer resistivity and its dependence on electron temperature.
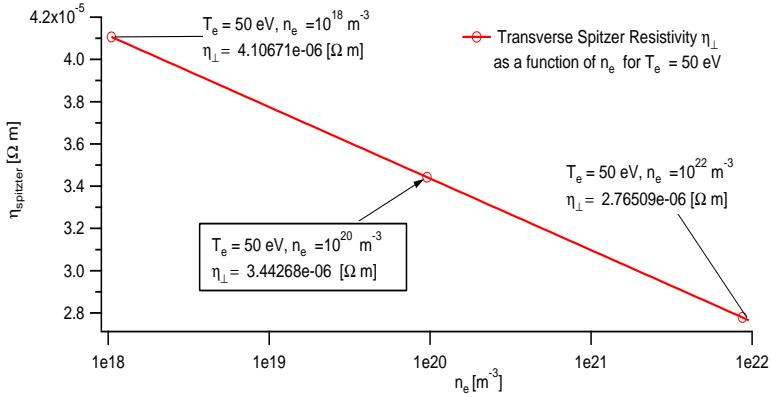
Figure 3.2: The weak but non-vanishing dependence of transverse Spitzer resistivity on plasma density. We see that $\eta_\perp$ only changes by less than a factor of 2, when n_e varies over 4 orders of magnitude, due to the weak dependence of the Coulomb logarithm on density.

is occurring. However, on the scale of a microsecond or two, and from the perspective of a frame that is comoving with the plasma, there is some local steadiness to the plasma's behavior, and this will be good enough for us. With regards to (2), clearly the magnetic field inside the CT is not uniform, and under many circumstances the finite gradients in **B** will create radical departures away from the conditions needed for the Spitzer model to work. Such as the case of magnetic reconnection (discussed in chapter 4), where we may need to consider more comprehensive models of the resistivity. However, there has been some recent experimental verification of the Spitzer value
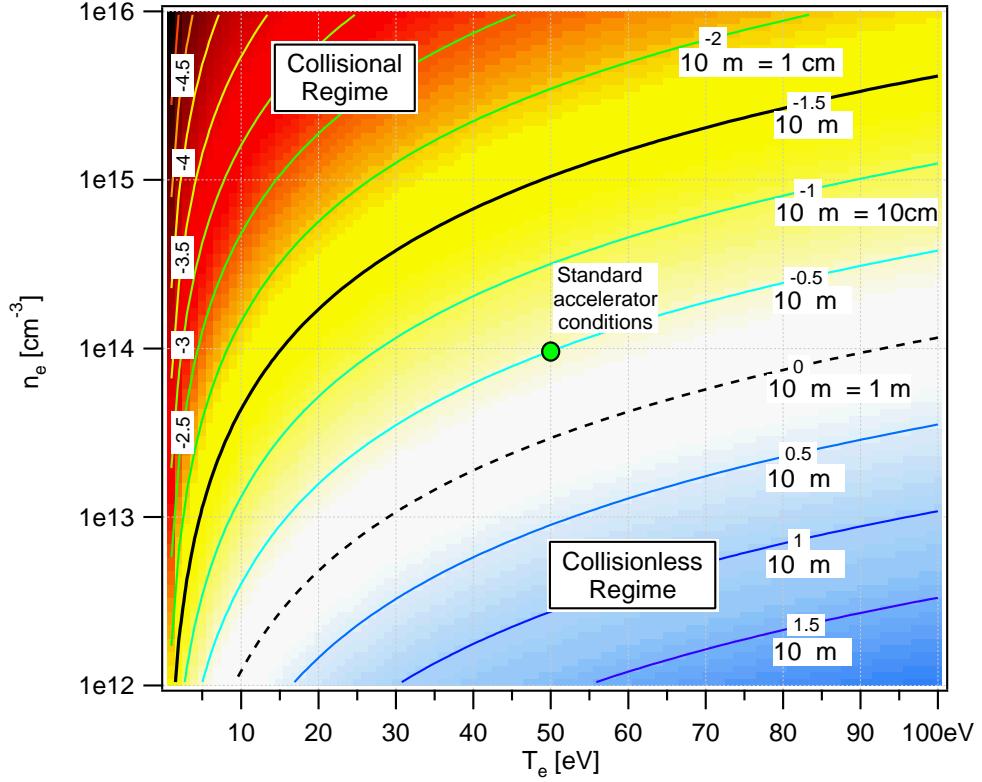
Figure 3.3: The electron mean free path as a function of electron temperature and density.

of the transverse resistivity within the reconnection region of a collisional plasma. [cite MRX paper]

As mentioned in the introduction (table 1.1) the electron gyroradius is at most a few millimeters, while the mean free path at typical parameters can be much longer, $3\ cm < \lambda_{\mathrm{mfp}} < 1\ m$. This ensures that assumption (3) will hold.

For the CT plasma, the assumption (4) that the electron drag is dominated by collisions is just on the edge of validity. Essentially, we can regard a plasma as being dominated by collisions when the mean free path is significantly smaller than the size of the system. By inspecting figure 3.3, we can see that for compact toroids that fall toward the colder, denser end of the spectrum, the collisionality assumption will hold well. But for compact toroids that happen to be relatively hot and diffuse, the mean free path can easily exceed 1 meter.

Assumption (5) depends on the electric field within the plasma, and it is uncertain exactly how large this is on CTIX. This may hold over most of the system, yet be violated in localized pockets where E is large, such as near a reconnective current sheet or plasma sheath. The validity of assumption (6) is also conditional. When interacting with a dense neutral gas puff, electron-neutral collisions might become important. Otherwise it is a fairly safe assumption to make.

Overall, the questionable validity of the Spitzer model on CTIX implies that its resistivity formula is best used as a lower bound for the resistivity of the plasma. When the full menagerie of phenomena are taken into account, the effective resistivity can only be increased about this standard value.

3.2   Theory of magnetic analysis

The results established in chapter 2 have given us the ability to reconstruct the approximate spatial and temporal dependence of the magnetic field within the CTIX accelerator. This can now be put to use as a tool to explore some fundamental physics.

How does the magnetic field evolve in space and time? How does that evolution constrain the effective electrical resistivity of the plasma? How does that measured value of resistivity compare with standard theoretical predictions. If the magnetic field and plasma velocity field are known functions of space and time then, in principle, the effective resistivity of the plasma can be deduced using the MHD evolution equation for $\mathbf{B}$

$$\partial_t \mathbf{B} - \nabla \times (\mathbf{v} \times \mathbf{B}) = \frac{\eta}{\mu_0} \nabla^2 \mathbf{B} \tag{3.3}$$

Where η is the electrical resistivity of the fluid. Alternatively, we could more directly find the resistivity using a generalized Ohm's law.[1]

$$\mathbf{E} + \mathbf{v} \times \mathbf{B} = \eta \mathbf{j} \tag{3.4}$$

---

[1]For the simplicity of presentation we are temporarily neglecting the Hall term and pressure gradient term $\frac{1}{e \, n_e}(\mathbf{j} \times \mathbf{B} - \nabla P)$, but we can add them back in at any point.

It is clear that these are equivalent to each other since the curl of (3.4) equals (3.3).

To find the resistivity we would need to evaluate the given combinations of the known quantities, being careful not to mix-up vector components, and solve for η.

But first we must take notice of the vector nature of the above equations. In truth η is not really just a number. In the presence of a strong magnetic field its true properties are best described as a tensor that takes into account the difference of plasma conductivity in the direction parallel to the magnetic field, as compared to its value in the direction perpendicular to the field. This tensor can be expressed in terms of just two scalars, the parallel resistivity $\eta_\parallel$, and the transverse resistivity $\eta_\perp$.

To describe this, let us choose a coordinate system $\{\mathbf{e}_1, \mathbf{e}_2, \mathbf{e}_3\}$ that is locally aligned with the magnetic field vector, [2] in such a way that $\mathbf{B} = B\mathbf{e}_3 = (0, 0, B)$. The subsequent choice of the orientation of $\{\mathbf{e}_1, \mathbf{e}_2\}$ is completely arbitrary, and can be made however is most convenient.

In this coordinate system Ohm's law becomes

$$E_3 = \eta_\parallel \, j_3, \qquad E_2 - \mathrm{v}_1 B = \eta_\perp \, j_2, \qquad E_1 + \mathrm{v}_2 B = \eta_\perp \, j_1 \tag{3.5}$$

If we define an effective electric field $\tilde{\mathbf{E}} = \mathbf{E} + \mathbf{v} \times \mathbf{B}$ in order to simplify our notation, then we have the standard form for the resistivity tensor.

$$\begin{pmatrix} \tilde{E}_1 \\ \tilde{E}_2 \\ \tilde{E}_3 \end{pmatrix} = \begin{pmatrix} \eta_\perp & 0 & 0 \\ 0 & \eta_\perp & 0 \\ 0 & 0 & \eta_\parallel \end{pmatrix} \cdot \begin{pmatrix} j_1 \\ j_2 \\ j_3 \end{pmatrix} \tag{3.6}$$

One practical difficulty is that we really need to write our equations with respect to the laboratory-framed cylindrical coordinates (r, θ, z), in terms of which all our measurements have been made. The most straight-forward method is to use Euler angles (α, β, γ) (with standard x-

---

[2]In general, there may not exist any one global definition that provides a single continuous coordinate system that covers the entire volume without being multivalued somewhere. To deal with this problem in a fully rigorous way, a set of many coordinate systems might be needed that cover the space in overlapping patches, along with the functions that smoothly relate them to each other (i.e., the calculus of manifolds [30]). This level of rigor is clearly beyond the scope of this discussion, and we will simply keep in mind the local nature of the above transformations as we try to get some testable results.

convention) [31],[32], where β is the angle in space between the local direction of the magnetic field ($\mathbf{e}_3$), and the z-axis of CTIX. The angles (α, γ) are determined by your previous choice of $\{\mathbf{e}_1, \mathbf{e}_2\}$.

Thus, the orientation of the local magnetic field relative to the lab-frame determines a transformation $(r, \theta, z) \rightarrow (e_1, e_2, e_3)$, which we formulate in terms of the Euler angles.

For example, if we are able to measure the (r, θ, z) components of the effective electric field in the lab frame, we can apply a transformation to get the magnetically aligned components of $\tilde{\mathbf{E}}$,

$$
\begin{pmatrix} \tilde{E}_1 \\ \tilde{E}_2 \\ \tilde{E}_3 \end{pmatrix} = \begin{pmatrix} \cos\gamma\cos\alpha - \cos\beta\sin\alpha\sin\gamma & \cos\gamma\sin\alpha + \cos\beta\cos\alpha\sin\gamma & \sin\gamma\sin\beta \\ -\sin\gamma\cos\alpha - \cos\beta\sin\alpha\cos\gamma & -\sin\gamma\sin\alpha + \cos\beta\cos\alpha\cos\gamma & \cos\gamma\sin\beta \\ \sin\beta\sin\alpha & -\sin\beta\cos\alpha & \cos\beta \end{pmatrix} \cdot \begin{pmatrix} \tilde{E}_r \\ \tilde{E}_\theta \\ \tilde{E}_z \end{pmatrix}
$$
$$(3.7)$$

and then use (3.6) to find the resitivity.

In the regions near the wall where B_r is negligible, especially at the peak in B_z and in the trailing plasma, a practical simplification can be applied. Here, the magnetic field vector resides only in the two dimensional (z, θ) plane, therefore $\alpha, \gamma = 0$, and the transformation depends only on one angle, β.

$$
\begin{pmatrix} \tilde{E}_1 \\ \tilde{E}_2 \\ \tilde{E}_3 \end{pmatrix} = \begin{pmatrix} 1 & 0 & 0 \\ 0 & \cos\beta & \sin\beta \\ 0 & -\sin\beta & \cos\beta \end{pmatrix} \cdot \begin{pmatrix} \tilde{E}_r \\ \tilde{E}_\theta \\ \tilde{E}_z \end{pmatrix}
$$
$$(3.8)$$

Applying this transformation to both $\mathbf{j}$ and $\tilde{\mathbf{E}}$ we have the following relations

$$\tilde{E}_1 = \tilde{E}_r \qquad j_1 = j_r \tag{3.9}$$

$$\tilde{E}_2 = \cos\beta \ \tilde{E}_\theta + \sin\beta \ \tilde{E}_z \qquad j_2 = \cos\beta \ j_\theta + \sin\beta \ j_z \tag{3.10}$$

$$\tilde{E}_3 = -\sin\beta \ \tilde{E}_\theta + \cos\beta \ \tilde{E}_z \qquad j_3 = -\sin\beta \ j_\theta + \cos\beta \ j_z \tag{3.11}$$

Overall, these relations lead to two distinct formulas for $\eta_\perp$, and one formula for $\eta_\parallel$. Let us examine the simplest of these first, equation (3.9). Recalling (3.6) immediately gives us an expression for the transverse resistivity.

3.2.1 Method 1.

$$\eta_\perp = \frac{\tilde{E}_r}{j_r} = \frac{E_r + v_\theta B_z - v_z B_\theta}{j_r} \tag{3.12}$$

This should hold even with the inclusion of the Hall and pressure terms in Ohm's law, because (as mentioned in section 2.4) the radial pressure gradient is expected to exactly cancel the radial $\mathbf{j} \times \mathbf{B}$ force.

In this expression, the different terms are known with different levels of precision. The axial velocity of the plasma v_z is very precisely measured using a robust time-of-flight analysis. The values of the magnetic components B_z, and B_θ are also well calibrated, and our analysis has shown that we can make firm upper bounds on the error of these diagnostics.

Next in line is the radial component of the current density j_r, which can be estimated using Ampere's Law, and our Lagrangian reconstruction of B_θ, according to

$$j_r = -\frac{1}{\mu_0} \frac{\partial B_\theta}{\partial z} \tag{3.13}$$

The reconstructed axial variation of $B_\theta(z, t)$ is most accurate in the neighborhood of the probe, and so this is where we will evaluate the entire expression for $\eta_\perp$.

As a check of our math, we can also establish some general upper and lower bounds on the magnitude of the radial current density. We can do this by taking the measured total current flowing down the center conductor and dividing it by an estimated cross section area equal to the surface area of the region where radial conduction through the plasma is occuring, $j_r \sim I/A_{estimate}$. In order to be in qualitative agreement with the basic nature of the CTIX discharge, the overall axial extent of this region of return current should be in the range $5 \ cm \ < \Delta z \ < 50 \ cm$, and so $A_{estimate} = 2\pi r_2 \Delta z$ should be between about $478 \ cm^2$ and $2394 \ cm^2$. Using a typical value of peak accelerator current of 120 kAmps, we find that we can conservatively limit the radial current density to be in the range: $50 \ Amps/cm^2 \ < \ j_r \ < \ 500 \ Amps/cm^2$. Or restated in SI units this is: $5 \times 10^4 \ Amps/m^2 \ < \ j_r \ < \ 5 \times 10^6 \ Amps/m^2$. If our reconstructed value of j_r fell outside of these

limits, then we would know there was some kind of error.

Alternatively, if we use a more educated estimate of the area that supports radial current, based on the axial extent of the region where $B_\theta(z, t)$ has a slope in the z-direction, then we could make an independent evaluation of the average j_r using the measured accelerator current. The results of these two methods can be compared, and their difference would be a good indication of the uncertainties inherent in the measurement.

We have quite a different situation when it comes to evaluating the toroidal velocity v_θ, which is entirely unmeasured. Theoretical estimations based on $(\mathbf{j} \times \mathbf{B})_\theta$ are attractive but not sufficiently well understood to produce results with any precision. Essentially, v_θ will be considered almost as a free parameter.

The radial electric field E_r has a similar level of uncertainty. Despite this, there are some relatively accessible ways to estimate its value. We can make a simple estimate based on the voltage difference between the inner and outer electrodes (at radii r_1 and r_2), in a vacuum the radial electric field is

$$E_r(r) = \frac{V_{acc}}{r \ln(r_2/r_1)}$$

One problem is that the voltage V_{acc} is a non-trivial function of position and time during the CTIX discharge. In the future we might use a good circuit model to estimate $V_{acc}(z, t)$, but for now we are limited to making a back of the envelope estimation, and then evaluate the vacuum expression for E_r at the outer radius.

Using data from the accelerator voltage monitor, on shot 59842, V_{acc} was about 1.3 kV at the time of peak current, as measured at the gap between the formation and acceleration sections (z = 20 cm), we find that the vacuum expression gives $E = 2.23 \times 10^4$ V/m. Let us refer to this value of the electric field as E_{vacuum}, which will be considered later in the calculation of possible values for $\eta_\perp$. We can use this measured value of V_{acc} for all values of axial position at the instant of the peak accelerator current because at the peak $dI/dt = 0$, and so the inductive voltage drop along the accelerator will be zero. At other times when dI/dt is large, axial voltage differentials will

be significant and we would need a circuit model to estimate the voltage across the plasma.

Alternatively, electric fields can exist within the plasma if they are induced by dynamic, spatially nonuniform magnetic fields. We can use Faraday's law to find the line integral of E_r in terms of the time derivative of B_θ. The derivation here is motivated by the analysis used on the MRX resistivity experiments [33]. We can equate the closed line integral of the electric field with minus the rate of change of magnetic flux through a loop C having a surface S.

$$\oint_C \mathbf{E} \cdot \mathbf{dl} = -\frac{d}{dt} \int_S \mathbf{B} \cdot \mathbf{n} \, da \tag{3.14}$$

For a rectangular integration loop in the (z, r) plane that lies outside the conducting walls on three of its sides, and with its fourth side traversing radially through the plasma from the inner wall to the outer wall, we can find the average value of radial electric field along that fourth side. Assuming a cylindrically diverging form for the radial electric field $E_r(r, z, t) = \frac{r_{\text{eff}}}{r} E_r(z, t)$,

$$r_{\text{eff}} \ln(r_2/r_1) \langle E_r(z, t) \rangle_{ave} = \int_{r_1}^{r_2} \mathbf{E} \cdot \mathbf{dl} = -\frac{d}{dt} \int_0^z \int_{r_1}^{r_2} B_\theta(r, z', t) \, dr \, dz' \tag{3.15}$$

While we do have a reasonably accurate estimation of the axial dependence of the B_θ using the Lagrangian interpolation, its radial dependence behind the CT is a matter of some speculation. Some reasonable candidates for radial forms that we might try are 1) the Bessel function solution to the force-free state, and 2) the vacuum field due to the current in the center electrode, $\sim 1/r$.

We can go ahead and evaluate these possible functions, if we assume that the field is separable,

$$B_\theta(r, z) = B_\theta(z) \frac{R_\theta(r)}{R_\theta(r_{\text{eff}})},$$

where $B_\theta(z)$ is the interpolated probe signal, $R_\theta(r)$ is the assumed radial profile, and r_{eff} is the effective radial position of the magnetic probe measurements.

In the case of $R_\theta(r) = \frac{1}{r}$, we have a complete cancellation of the radial terms resulting in,

$$\langle E_r(z, t) \rangle_{ave} = -\frac{d}{dt} \int_0^z B_\theta(z', t) \, dz' \tag{3.16}$$

And in the case of the coaxial Bessel function $R_\theta(r) = F_1(k_r r)$, defined in equ. (2.12), we have

$$\langle E_r(z,t)\rangle_{ave} = \frac{F_0(k_r r_2) - F_0(k_r r_1)}{k_r r_{\text{eff}} \ln(r_2/r_1) F_1(k_r r_{\text{eff}})} \frac{d}{dt} \int_0^z B_\theta(z',t)\ dz' \tag{3.17}$$

This wild looking radial term actually boils down to just a simple proportionality factor.

$$\langle E_r(z,t)\rangle_{[\text{Bessel}]} = 1.564\ \langle E_r(z,t)\rangle_{[1/r]}.$$

Numerical evaluation of this integral yields values quite similar to the result of the vacuum estimation,

$$\langle E_r(z,t)\rangle_{[1/r]} = 2.570 \times 10^4\ V/m \tag{3.18}$$

$$\langle E_r(z,t)\rangle_{[\text{Bessel}]} = 4.019 \times 10^4\ V/m \tag{3.19}$$

These were evaluated without any of the field expansion calibration factors described in chapter 2. If they are used the results for E_r are proportionately larger (by a factor of 3 or 4).

One final constraint is that any physical value of resistivity must be a positive number. This matters because each of the terms in formula (3.12), could in principle be positive or negative. So if j_r is negative at some point, then $(E_r + v_\theta B_z - v_z B_\theta)$ must also be negative at that point, so that the ratio is positive. Actually, this is probably the most solid constraint we have in this problem.

We can now put all of these factors together, using values derived from data on CTIX shot 59842 at the time of peak B_z ($t = 9.8\ \mu s$), at the z = 91 cm probe. First, based on the Lagrangian interpolation, the radial current density is positive, since B_θ has a negative axial slope at that time, and it has a value of $j_r = 2.2617 \times 10^6\ A/m^2$, well within the range established earlier. We have a precise value of $v_z B_\theta = 1.8796 \times 10^4\ N/C$, yet an almost completely undetermined value of $v_\theta B_z$. Lastly, we have a radial electric field that is probably in between $E_{vacuum} = 2.23 \times 10^4\ V/m$ and $\langle E_r \rangle_{[\text{Bessel}]} = 4.019 \times 10^4\ V/m$.

If we consider the simple case where $v_\theta = 0$ and use the smaller value of E_{vacuum} then we find that the corresponding resistivity is $\boxed{\eta_\perp = 1.549 \times 10^{-3}\ \Omega \cdot m}$. This is about a factor of 40

times larger than the Spitzer value of the resistivity at $T_e = 10 \ eV$, and exactly equal to the Spitzer value for $T_e = 0.5245 \ eV$, although this is implausibly too cold for our plasma.

We could also consider what limiting value of v_θ would be needed to set $\eta_\perp = 0$ with the other parameters held constant. The result is that a value of $v_\theta = -1.10589 \ cm/\mu s$ would agree with zero resistivity. This is a quite reasonable value for a possible toroidal velocity, it is so small in fact that it would be experimentally challenging to measure it accurately. This means only that the real value of $\eta_\perp$ could be anything between the $v_\theta = 0$ estimate and the Spitzer value. Our estimate would give exactly the Spitzer value of $\eta_\perp$ at $T_e = 10 \ eV$ if the toroidal velocity is equal to $-1.0772 \ cm/\mu s$. Basically, any velocity near $1 \ cm/\mu s$ in the negative toroidal direction would result in agreement with the value of the Spitzer resistivity for some reasonable plasma temperature.

We see from this exploration the inherent difficulty with taking the difference of two similar large numbers, especially when the uncertainty of some of the quantities are larger than the difference we are trying to determine.

3.2.2   Method 2.

As mentioned earlier, there is a second way to find $\eta_\perp$ using equation (3.10). Solving for $\eta_\perp$ yields the result

$$\eta_\perp = \frac{\tilde{E}_\theta \left(1 + \frac{\tilde{E}_z}{\tilde{E}_\theta} \tan \beta\right)}{j_\theta \left(1 + \frac{j_z}{j_\theta} \tan \beta\right)} \tag{3.20}$$

where the components of the effective electric field are $\tilde{E}_\theta = E_\theta + v_z B_r$ and $\tilde{E}_z = E_z - v_\theta B_r$. However, we are only examining the regions where $B_r \sim 0$ and so these simplify $\tilde{E}_\theta = E_\theta$, $\tilde{E}_z = E_z$.

Also according to the definition of β, $\tan \beta = \frac{B_\theta}{B_z}$. It follows that

$$\eta_\perp = \frac{E_\theta \left(1 + \frac{E_z B_\theta}{E_\theta B_z}\right)}{j_\theta \left(1 + \frac{j_z B_\theta}{j_\theta B_z}\right)} \tag{3.21}$$

This formula has the great advantage of not containing the toroidal velocity, and all of its associated troubles. And when we use real data to evaluate these ratios, the formula simplifies further. At the peak of B_z, we have $\frac{B_\theta}{B_z} = 0.28$, and $\frac{j_z}{j_\theta} = -2.15 \times 10^{-4}$, resulting in a very small value

of $\frac{j_z B_\theta}{j_\theta B_z} = -6.235 \times 10^{-5}$. This is clearly insignificant compared to unity, and so the denominator of equ. (3.21) reduces to simply j_θ. Likewise, it is physically implausible that the ratio $\frac{E_z}{E_\theta}$ could be much larger than $\frac{j_z}{j_\theta}$, and so it must also be negligible. Thus we have a very simple formula for the transverse resistivity,

$$\eta_\perp = \frac{E_\theta}{j_\theta} \tag{3.22}$$

From here we can again use Faraday's law, now to find E_θ in terms of the time derivative of B_z. We can equate the closed line integral around a toroidal loop of the electric field with minus the rate of change of magnetic flux through that loop. If we rely on the assumption of approximate axisymmetry then the line integral is exactly proportional to E_θ, and Faraday's law reduces to

$$E_\theta(r,z,t) = \frac{-1}{r}\frac{d}{dt}\int_{r_1}^{r} r'\ B_z(r',z,t)\ dr' \tag{3.23}$$

where r_1 is the radius of the inner conductor and r the radial location where E_θ is being measured. We can use the Bessel function coaxial radial dependence to evaluate this integral. We have find that

$$E_\theta(r,z,t) = -\frac{\partial B_z(z,t)}{\partial t}\left[\frac{1}{k_r}\frac{F_1(k_r r)}{F_0(k_r r_{\text{eff}})}\right] \tag{3.24}$$

Numerically evaluating this expression for our example shot (59842), gives a nice result

$$\eta_\perp = \frac{-8.3125 \times 10^3\ V/m}{-1.0535 \times 10^8\ A/m^2} = 7.89 \times 10^{-5}\ \Omega \cdot m \tag{3.25}$$

which is only a factor of 2 larger than the $T_e = 10\ eV$ Spitzer value.

Hopefully these exercises have improved our intuition about the compact toroid plasma, as well as established a higher level of confidence in the applicability of Spitzer model to our system.

Chapter 4

Reconnection and compression

experiments

Reconnection within magnetized plasma occurs when two separate regions of magnetic field come in contact in such a way that the magnetic fields of the two regions are oppositely directed in the vicinity of the interface surface (separatrix) [34],[35]. A change of the topology of the magnetic field then occurs in which the separate field lines merge at the reconnection zone, and become a single larger field line that now connects the two regions [36].[1] Reconnection of magnetic fields in a conducting fluid is only possible if the field is able to diffuse relative to the fluid. However, due to the high conductivity of laboratory and astrophysical plasmas, classical resistive diffusion rates are far too slow to account for the incredibly rapid rates of field line merging observed in actual reconnection processes such as the tearing mode instability within tokamaks. The challenge is to explain these anomalously fast diffusion rates occurring within a wide class of laboratory and astrophysical plasmas.[37] [38]

Reconnection has been identified as an important mechanism in a variety of processes

---

[1]However, the notion that field lines are indistinguishable from one another leads to a subtle fact, that the time-evolution of a single field line is not uniquely defined. See appendix D.

throughout the full extent of the CTIX accelerator system. It plays a critical role in the dynamo formation process of the CT, it limits the acceleration timescale, and is important when considering injection/refueling into a tokamak type reactor.

During the formation of a compact toroid, magnetic reconnection occurring on a small scale (possibly via microturbulence) allows internal flux cancellation and enables the plasma to relax into a minimum energy configuration.

Next, it is a larger scale reconnection process in the radial direction that allows the CT to pinch off at its back edge, forming a closed magnetic topology, just like blowing a soap bubble. [39]

Then, during the acceleration the system consisting of the pushing field, the CT, and the radial current sheet at the junction between them can be modeled as a region where right-angle reconnection occurs. Across this separatrix, the field difference is actively maintained by the radial current driven between the electrodes by the accelerator circuit. However, current sheet does broaden during the shot as it resistively diffuses away from it central plane.

Reconnection across this interface may also play a role in the blow-by acceleration instability [40]. When the pushing magnetic field significantly exceeds the strength of the internal magnetic field of the CT, the current sheet junction between the two fields can destabilize near the inner conductor, where the the pushing field is the largest and the CT field is weakest. When this happens, the pushing field can "blow-by" the CT, and the result is poor accelerator efficiency. Onset of this instability may be due to reconnective flux cancellation of the larger B_θ eating up the smaller B_{CT}. This can occur at a rate on the order of the Alfven transit time. Further analysis is needed to determine if this mechanism could maintain a positive growth rate for long enough to significantly alter the CT magnetic geometry. The blow-by effect can also be explained in terms of a Rayleigh-Taylor instability between the relatively heavy CT, and the lighter pushing field. Reconnection could add to this effect, and complicate the magnetic structure that would occur during this kind of blow-by event.

Lastly, reconnection provides a very efficient method for the deposition of a fuel plasma

into the center of a reactor field [41],[42],[43]. This is the primary engineering application of CTIX, and there is still much to be understood about this process [3],[44],[4]. As discussed in chapter 5, we have found that during this kind of reconnection the plasma will thermalize, and the electron energy distribution function will become modified away from a simple Maxwellian equilibrium.
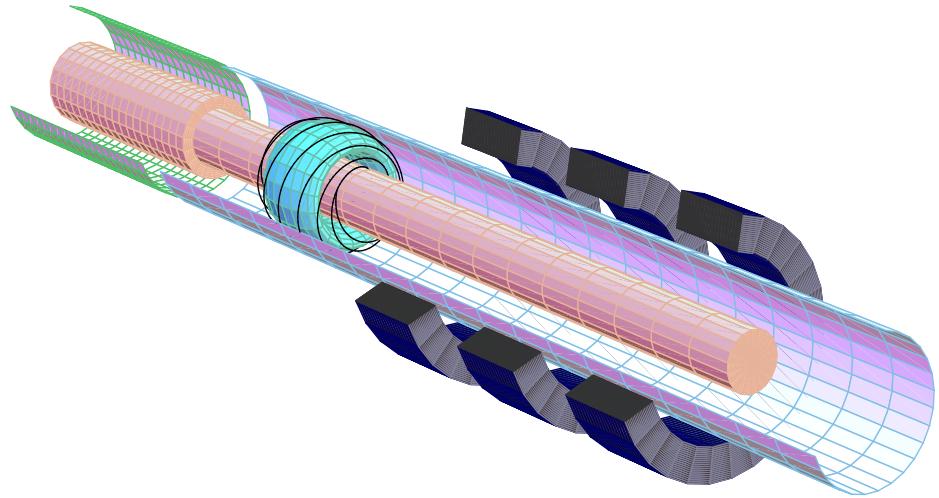
Figure 4.1: 3D Rendering of axial field coils on CTIX .

This chapter presents the results of a series of experiments that studied the interaction dynamics that occur when an accelerated compact toroid is injected into a solenoidal target magnetic field, which can be aligned either parallel or anti-parallel to the internal field of CT at its leading edge. Depending on the alignment direction, basic resistive MHD predicts that the interaction should result, respectively, in either compression or reconnection of the two fields. The results of the three independent diagnostics provide consistent and complementary new information about the MHD interaction physics within the CT plasma.

4.1 Experimental overview

Four external magnetic field coils have been installed on the CTIX accelerator for the purpose of applying magnetic perturbations to CT within the accelerator region. The coils are solenoids that are concentric with the center axis of the accelerator and produce an axisymmetric **B** field that is directed along the axis of CTIX near the middle of the coils, but also has a radial component near the ends of the coils. Because the magnetic field produced by the coils is primarily directed axially, we refer to these coils as "axial field coils".
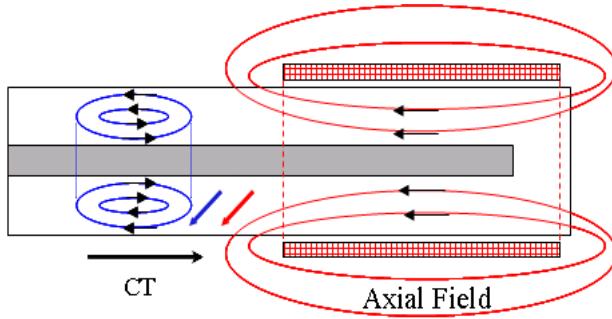
Figure 4.2: Parallel axial field results in a compression effect.
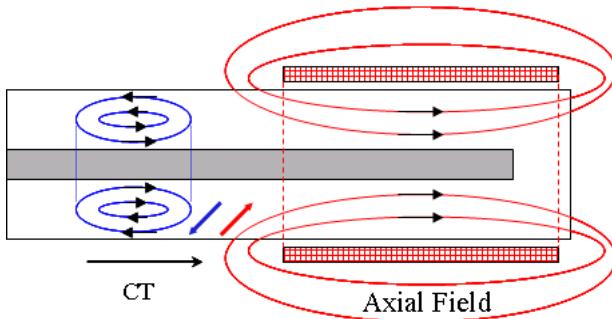
Figure 4.3: Anti-parallel axial field results in magnetic reconnection of the two fields.

The direction of the external magnetic field produced by these coils can be aligned either parallel or anti-parallel to the internal field of CT at its leading edge. Depending on the alignment

direction, basic resistive MHD predicts that the interaction should result in reconnection of the two fields for the case of anti-parallel alignment, or a compression effect in the case of parallel alignment.

These effects have been measured on CTIX using the three magnetic field probes located along the accelerator, a laser interferometer chord to measure plasma density at the 142 cm position on the accelerator, and also by using a fast framing camera that records a sequence of 12 images of the plasma along an axial line of sight. Using these images, the spatial and temporal dependence of the visible light emission of the CT during the interaction is compared to its emission intensity without the external field. The results from the framing camera data are consistent with the independent measurements of plasma density and magnetic field. Overall, we observe that magnetic field strength, plasma density, and acceleration kinematics of the CT are modified by when we apply an external magnetic field, by an amount that depends on the strength and polarity of the external field. Figures 4.2 and 4.3 show side views of the external axial coils and fields in the two geometries.

4.2   Description of external coils

The four axial field coils are located at z = 65 cm, z = 100 cm, z = 120 cm, and z = 148 cm, as measured from the start of the formation section to the start of each coil. The coils are composed of 25 turns of 2 cm diameter welding cable. Each coil is 15.24 cm long and has an inner diameter of 20.32 cm, and produces 1.85 Gauss per Amp at coil center.

Insulating acrylic support spools encircle the 16 cm outer diameter accelerator section of CTIX. The spools are suspended by an independent support structure that carries the weight of the coils and also maintains a 2 cm gap between the inner diameter of the acrylic spool and the OD of the stainless steel accelerator. This gap is needed because the accelerator section is charged to high voltage (up to 15 kV) and can heat up to as high as $140°$ F as a result of repeatedly carrying high pulsed current loads (120 kA for $\sim 20~\mu s$) during shot runs that can last many hours.

The welding cables have been wound around the spools to form the coils, and connected

in series to a variable DC power supply. Each coil can be individually connected or disconnected from the circuit to produce a variety of field geometries. Only 3 of the coils were used for the reconnection/compression experiments, those being the coils at z = 100 cm, 120 cm and 148 cm. The coil at z = 65 cm was disconnected because early tests indicated that it disrupted the CT formation process when run at high current.

Typically we cycled the power applied to the axial coils so that they would not not overheat. They would be ramped up to full current over the course of one second, reaching a flat-top about 2 seconds before the shot, then ramped down starting about one second after the shot. In total there was a 3 second window for the shot to occur in, which was always long enough. For 20-second shot cycles, the on-time was about 1/5 th of the cycle period.

4.3   Magnetic fields during reconnection and compression

The external fields generated by the axial field coils are relatively small compared to the peak field of the CT, yet they have a noticeable effect on the plasma. The peak field of the CT is a high as 12 kGauss, while the strongest external fields we applied were only 400 Gauss near the center, a ratio of about 30:1.

First, let us consider the effect that the external field has on the strength of the internal field of the compact toroid plasma as the two fields are driven into each other. The results gathered from the data set consisting of (x?) shots are displayed in figure 4.4.

The applied axial magnetic field (B_{AF}) was scanned from - 400 Gauss to + 400 Gauss, and we plotted the resulting average value of the peak B_z field at each setting along with error bars representing the variance of the data at each setting. Reconnection occurs for negative values of B_{AF}, while magnetic compression occurs for positive values. The data shown in figure 4.4 does not include any of the proposed calibration factors discusses in chapter 2, and so is probably an underestimate of the true values.
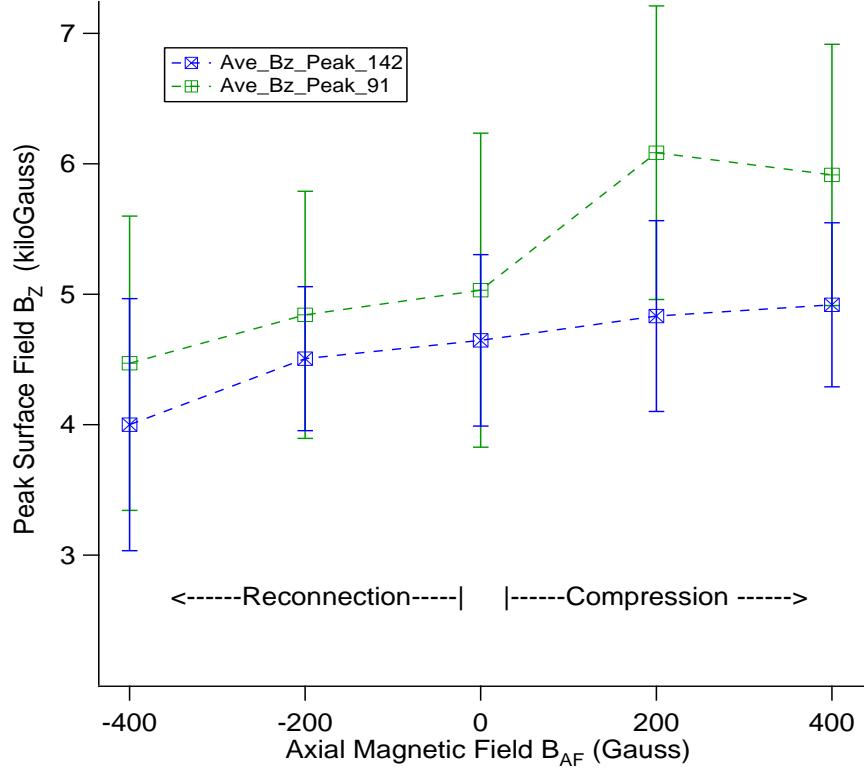
Figure 4.4: Effect of external field on peak B_z of CT
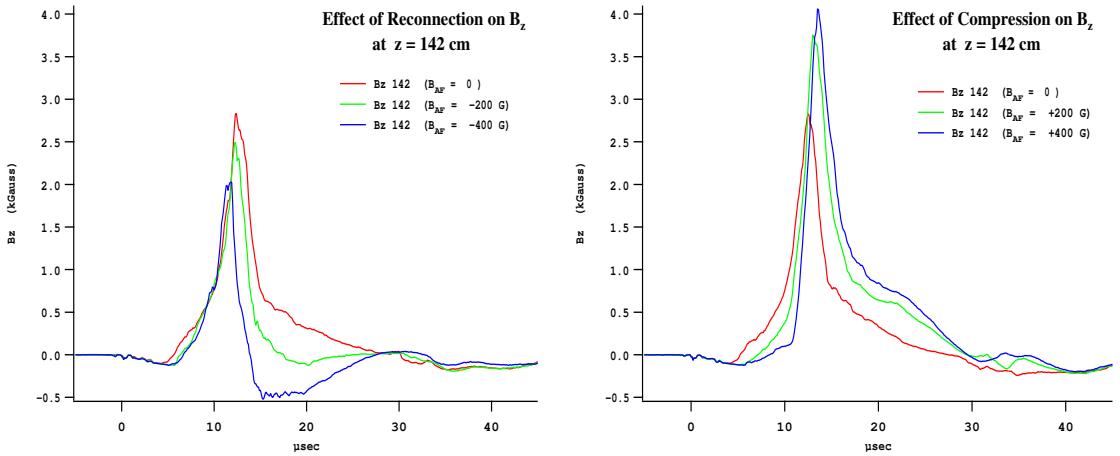
Figure 4.5: Effect of external field on B_z at z = 142 cm

When the axial field is aligned anti-parallel to the internal field of the CT (when B_{AF} is negative) we observe a significant decrease in the peak value of the B_z field as it propagates into the axial field. This is consistent with magnetic flux cancellation that should occur during the process of magnetic reconnection. The amount of reconnective flux cancellation that is observed in our experiment is directly proportional to the strength of the applied external field, given the same initial CT field strength.

Conversely, when the axial field is aligned parallel to the internal field of the CT, the peak value of B_z is observed to increase as the CT enters axial field. This is consistent with magnetic flux amplification due to a compression of the magnetic field in the axial direction.
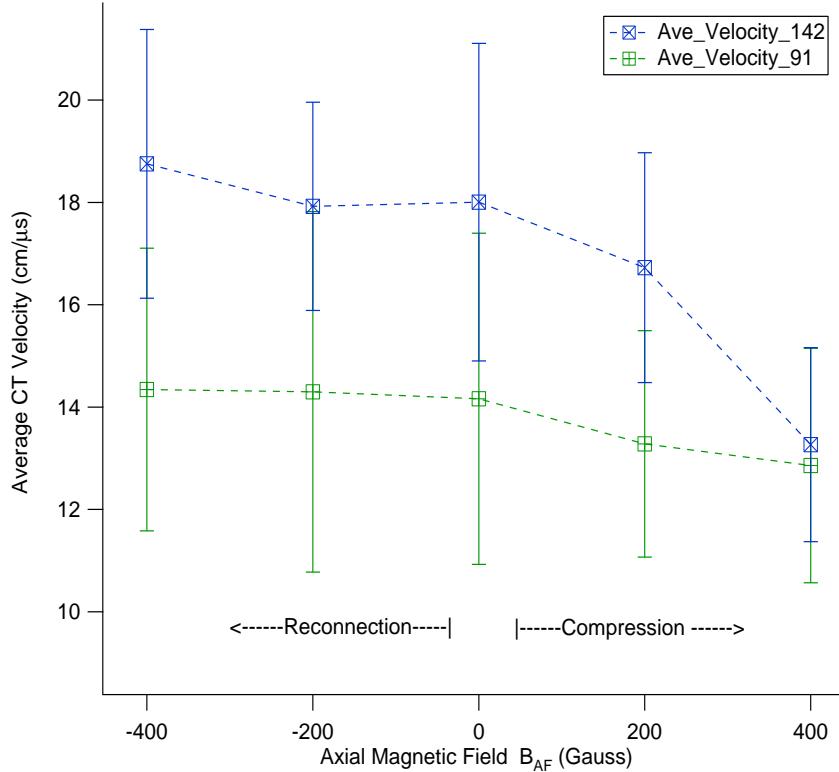
Figure 4.6: Effect of external field on CT velocity

The magnetic probe signals can also be used to measure the time-of-flight kinematics of

the CT. In figure 4.6, we plot the average velocity of the CT as a function of applied axial magnetic field. Here the average velocity "at 91 cm" can be more precisely defined as the average velocity of the CT from 57 cm to 91 cm, $\bar{v}_{91} = (91 - 57)/(t_{91} - t_{57})$, while $\bar{v}_{142} = (142 - 91)/(t_{142} - t_{91})$.

In the case of the reconnection field geometry (anti-parallel $B_{AF} < 0$) we observe an increase in the acceleration of the CT that is directly related to the applied external field. This means that as reconnection occurs the magnetic energy of the CT is converted into kinetic energy of the plasma's forward motion.

When compression occurs, it does so at the expense of the forward acceleration. Dynamically, an opposing external force is required to compress the plasma and embedded fields. The time-of-flight analysis shows dramatic decrease in rate of acceleration, down to zero acceleration when $B_{AF} = +400G$.

Some insight regarding the interaction dynamics can be gained by examining the axial dependence of the magnetic field under these different circumstances (using Lagrangian interpolation).

The closed magnetic structure of the CT results in a localized pulse in the B_z signals that propagates down the accelerator. Under normal operation ($B_{AF} = 0$), probe signals show B_z fields that remain approximately constant in size and shape as the CT is accelerated. When the axial field is applied, noticeable changes in CT shape occur.

The toroidal component B_θ is affected in an unusual way by the reconnection process. During reconnection, the BT component of the CT advances into the external field, ahead of the region where Bz is localized, which is normally considered to be the front edge of the CT. This effect can be understood if the 3D nature of the reconnection is taken into account. Since it is the poloidal components of the CT and external field that are undergoing reconnection, the toroidal component of the CT field (and the associated poloidal current density) is unconstrained in the reconnection zone and can freely expand into the region ahead of the CT. bringing some diffuse plasma with it.

When thinking about the interaction dynamics it is important to remember that the external field lines pass through the walls of the vessel, and they are securely pinned to the wall as the
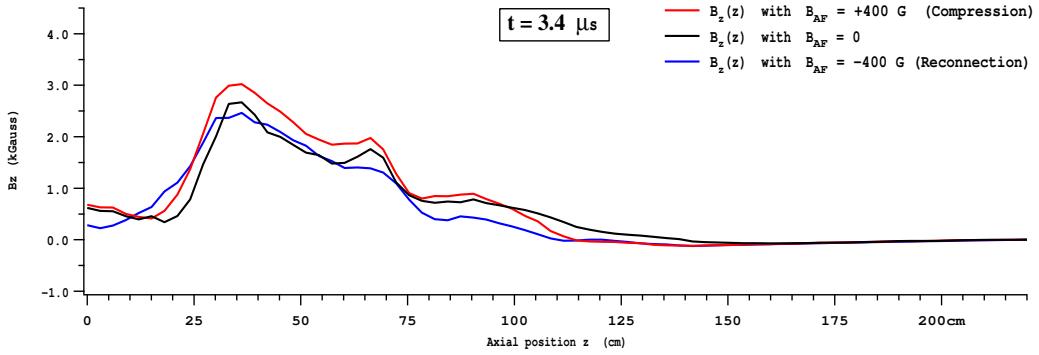
Figure 4.7: Effect of external field on CT at t = 3.4 μs
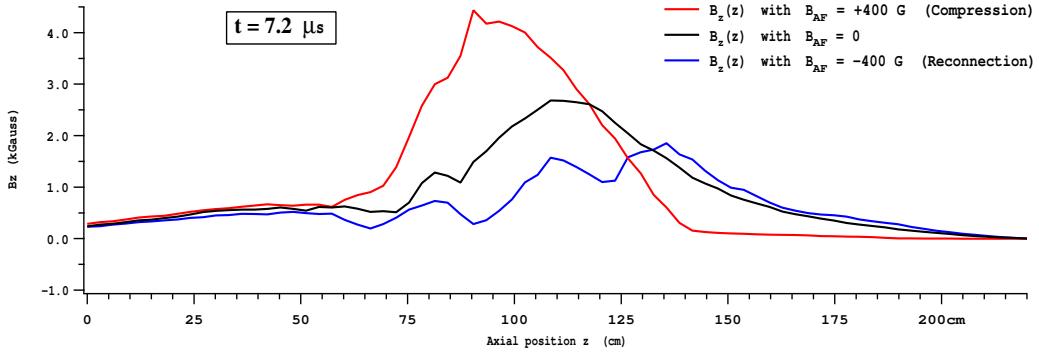
Figure 4.8: Effect of external field on CT at t = 7.2 μs
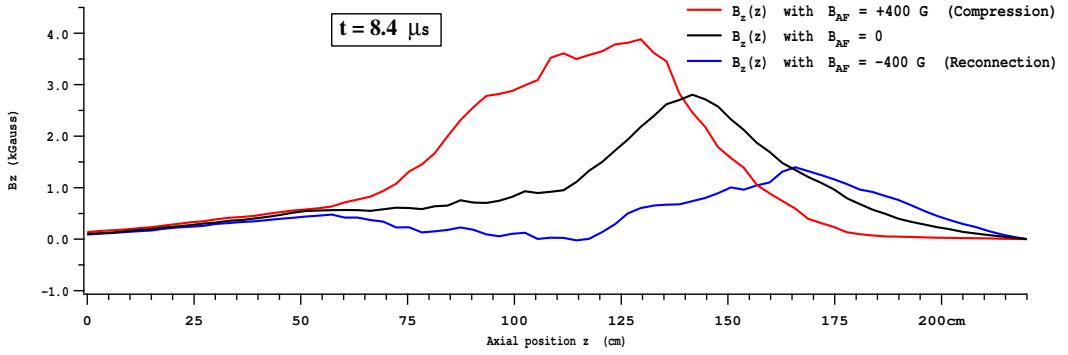
Figure 4.9: Effect of external field on CT at t = 8.4 μs

CT passes because of the wall's high conductivity. As mentioned in chapter 2, the time varying part of **B** must not have any component that is normal to the wall. However there can be a DC magnetic field (constant in time) that intersects the wall at any angle, such as the external field created by the axial field coils in this experiment. As the internal field of the CT interacts with the external field, this DC component which intersects the wall must remain, while new time-varying fields are created in superposition with the original.

4.4 Interferometric measurement of density increase

For this experiment we used the He Ne laser interferometer to measure the time evolution of line averaged electron density at the z= 142 cm port position on the accelerator. The processed interferometer data is shown in figure 4.10. The signals from each data set were averaged together, and the result was smoothed with a moving average filter to eliminate high frequency noise.
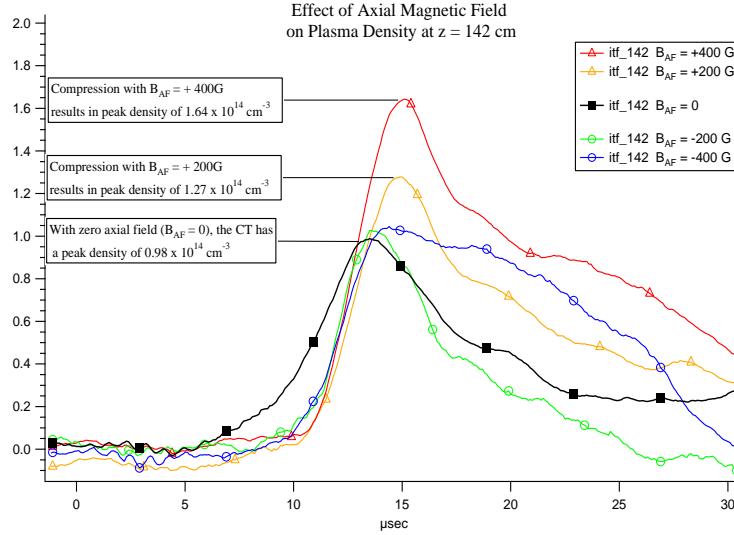
Figure 4.10: Effect of external field on electron density of CT, as measured by the interferometer chord at z = 142 cm

There are several effect that are evident in this data. Most clearly, we have a direct observation of the magnetic compression effect in which the line averaged electron density as measured

at z= 142 cm position is greatly increased (by a factor of 1.6 for $B_{AF} = 400$ Gauss), and the arrival time of the peak density is delayed. These are both in agreement with the idea that there is a force acting in the -z direction, due to the applied external field. We also see that this density build up scales in a nearly linear fashion with the strength of the applied external field, when running in the polarity that causes compression.

We also see that there is almost no effect on the value of peak density when running with the external field polarity that causes reconnection. It remains the same as with no axial field applied, however, the signal length does seem to be stretched out for the case of $B_{AF} = $ -400 Gauss. In this case, it seems that the reconnection effect was strong enough to keep some of the plasma back in the accelerator. While at the lower setting, the density profile was mostly unaffected.

One last observation can be made. It seems that with all the external field configurations, the leading edge of plasma density comes a few microseconds later with axial field on, than with no field at all. It is unclear exactly why this would be so. This leading edge has lower density, and weaker internal fields, and would be more strongly effected by the external fields. It seems that in both the reconnection and compression geometries, the interaction at the leading edge causes either a delay or a diminishment of plasma density at the 142 cm position.

It is possible that these are actually opposite dynamical effects that result in the same final measurement. In the reconnection case, a very high rate of acceleration might occur for the low mass leading edge, resulting in an early diminishment of plasma density because it has greatly expanded while being swept far ahead of the CT center. On the other hand, the compressional case would result in simply a delay of the arrival of the density, and when it does come it has been built up to a higher peak value.

4.5 Optical measurement of reconnection and compression

The fast framing camera diagnostic is particularly useful because it can give us information about the radial distribution of plasma and how it changes with time. The Imacon 790 camera we used can take a sequence of 12 images of the CT during the interaction. It has an adjustable frame-rate that can varied in fixed increments from one frame every 2 μs to frame every $0.25\mu s$. Using these images, the light emission intensity of the CT during the interaction can be compared to its emission intensity without the external field. For the reconnection experiments the framing camera is particularly useful because it simultaneously provides a time history of the axial position of the CT, as well as the radial and angular variation in light emission.
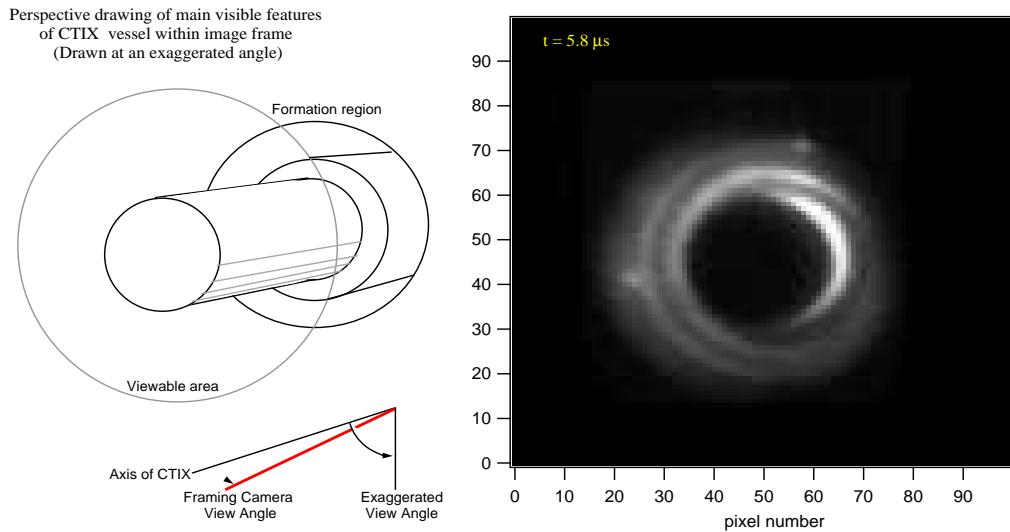
Figure 4.11: Diagram of CTIX vessel structure seen in framing camera image, and grey-scale image of framing camera output at t = 5.8 μs.

For this study we used an exposure of 400 ns, with an inter-frame time of 2 μs. Visible light emission is primarily from impurities in the trailing plasma, and so the framing camera is able to image the plasma sheath in the transition region between the CT field and the purely toroidal field behind the CT that is caused by the railgun acceleration current.

Neutral atoms cannot be co-moving with the CT because they are not directly acted on by

the accelerating fields. However, they may be scraped off the wall as the CT goes by. Once ionized, the story is different, and impurity ions can follow behind the CT for a period of time.

The framing camera is well suited for measuring the level of angular variations in plasma density and current density in the CT, as an indicator of the quality of the equilibrium. The line of sight bounces off of an internal front surface mirror, then through a glass vacuum window, and then via a sequence of external alignment mirrors, and into the f 4 zoom lens mounted onto the framing unit. The output phosphor plate of the Imacon is viewed by a 384×576 pixel CCD camera that makes a digital image of the shot.

Some care needs to be given to properly consider the line of sight used by the framing camera, and what parts of the vessel are within the frame of the image. The view is looking down the barrel of the accelerator, but is slightly off-axis (fig. 4.11). We can clearly see the circular end of the center conductor, situtated at the center of the image and taking up about 1/3 rd of the total diameter. Because the line of sight is slightly tilted, we can also see some of the side of center conductor shaft. The larger diameter of the formation section center electrode is also visible, especially at early times when the formation region is brightest. Some of the outer wall can be seen on one side. Most of the structure we see in the image is due to the plasma hugging the wall, and being affected by the edges of the vessel. The plasma near the wall has a higher impurity content and so it emits more visible light than the cleaner, fully ionized core.

One feature (which has advantages and disadvantages) is that all the light is integrated axially along each line of sight. On one hand, this is good because it means that we can see all the way back to inside of the formation section. On the other hand, it is bad because it can be hard (or sometimes impossible) to determine what axial position the light is coming from, whether it is axially localized and moving toward the camera, or spread out uniformly along the entire line of sight.

The radial variation in vessel geometry does provide some help with this issue. The clearest example of this is the diagnostic opportunity provided by the right angle cylindrical edge of the center

conductor end. At early times in the discharge the surface at the electrode's end appears dark, simply because no light-emitting plasma has made it down the accelerator that far. When plasma begins to come off the end the accelerator, it will normally fill in the region in front of the end of the center conductor, and begin to light it up. Thus we can be certain that when we see light from in front of the end-disk of the center conductor, that plasma has passed that point, about z = 165 cm.

A similar right-angle radial step occurs at the end of the formation section, which also allows us to see when the plasma is entirely in the formation region, and then watch as it flows out to fill in the region in front of the step.

The overall result of inspecting such features is that the images taken during the reconnection experiment demonstrate a reduced amount of light from in front of center conductor. Whereas during the compression experiment, we saw an increase in light emission from back in the accelerator region.
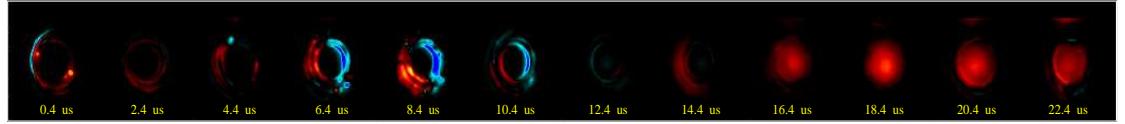
Figure 4.12: Effect of reconnection with axial field on light emission from CT
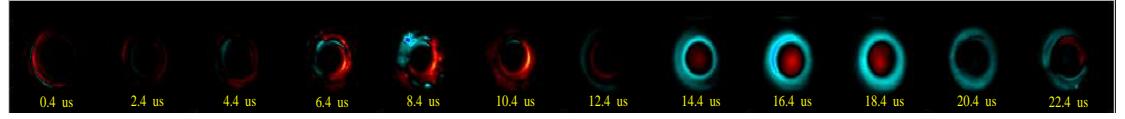
Figure 4.13: Compression effect of axial field on light emission from CT

We have compared the average of 20 images taken with no axial magnetic field to the average of 20 images taken when the CT is injected into an axial field of - 400 Gauss (in the anti-parallel direction). We have also compared the average image taken with no axial magnetic field to

the average image taken when the CT is injected into an axial field of $+$ 400 Gauss (in the parallel direction). In the time-sequence of images in figure 4.12, the red pixels show where the plasma was brighter with the axial magnetic field turned off, and the blue pixels show where the plasma was brighter with the axial magnetic field turned on. For black pixels there was no difference in plasma brightness.

When the CT is fired into an anti-parallel magnetic field, we observe a decrease in light emission from the region in front of the center electrode, implying plasma is prevented from filling in this central region. After reconnection, the expected mechanism for plasma fill-in of the region in front of center conductor is cross-field diffusion. Less plasma is seen in this region for $B_{AF} = -400G$ than for $B_{AF} = 0$. These framing camera images have demonstrated the efficient trapping of CT plasma on the external field lines, and have provided information about the radial dependence of reconnection effects.

When the CT is fired into a parallel magnetic field, we first observe an increase in light emission from the region between the center electrode and the outer electrode, implying that the plasma density and corresponding luminosity greatly increase before the CT is able to leave the accelerator section. This effect is seen in figure 4.13 as the bright ring of blue pixels beginning at 14.4 μs. For $B_{AF} = +400G$ it appears that most of CT plasma does not leave the end of the center conductor. During the compressional interaction its brightness increases due to the increase in density. And consequently, there is a delay while the internal field increase due to axial compression and the trailing plasma is prevented from getting past the compression interaction region. Thus it also make sense at later times during the discharge that there is less center electrode fill-in when compression is occurring.

It is very satisfying that the conclusions based on the framing camera data are consistent with the data taken on the same set of shots from surface magnetic probes that and the interferometric measurements of plasma density.

4.6   Model of two interacting magnetic fields

When the Compact Toroid enters an axially directed magnetic field, there is either an attractive force or a repulsive force of interaction between the two fields. In certain simple ways, this is just like two magnets being brought together along the axis of their poles. Whether the interaction is attractive or repulsive depends on the polarity of the external axial field relative to the internal field of the CT plasma.

For these experiments, the magnetic polarity of the CT is fixed, as it is determined by the electrical polarity of the CT formation circuit and formation seed field, while the externally imposed magnetic field can be easily varied in polarity and strength by adjusting the DC power supply, with no consequence on the quality of the compact toroid formation.

To understand this qualitative effect of either attraction or repulsion, it is simplest to consider the poloidal component of the internal field (the component which is created by toroidal plasma currents), since its geometry is analogous to the field of a simple permanent magnet. In standard operation the CT is accelerated with the North end of its poloidal field at the leading edge, so that the poloidal magnetic field vector (near the center axis) points in the direction of motion, which we call the positive z direction.

Then if we were to apply, via a solenoid, an external axial field with its North pole pointing backward toward the oncoming CT, we would expect the two fields to repel each other (North repels North). With the addition of this repulsion force, the acceleration of the CT would be decreased as it enters the external solenoid.

On the other hand, if we had oriented the external field so that its South pole was facing the CT's North pole as it approached, then the CT will be attracted toward the external solenoid (South attracts North). In this configuration the linear acceleration of the CT will be enhanced above the normal value caused by the rail gun circuit alone.

While this simple intuitive model of magnets attracting or repelling one another is correct

on a basic level, and does predict the approximate outcome of actual experiments, it leaves out many important and complicating subtleties.

The first detail that must be considered is that a compact toroid is a plasma, not a rigid body. It is a conducting fluid with a nearly frozen-in magnetic field, and is capable of compression and expansion, as well as vortex-like and complicated shear flow patterns.

When the CT is accelerated into a repulsive target field we would expect that the CT will be compressed in the z direction since it is being pushed on from both ends, from behind by the pushing field of the accelerator and in front by the repulsive axial field. The CT density and internal field will increase until some sort of pressure balance is reached. Although this compression is relatively straightforward, there are some interesting effects that are possible. Radial variation of the external field can provide a weak spot for the CT to squeeze through. If the external field is high enough reflection of the CT may occur.

A very different process occurs when the CT is propelled into an attractive field. In that case, the full complexity of the plasma shows itself during the process of magnetic reconnection. This is a topological change in the structure of the magnetic field in which the effective rate of diffusion of magnetic field lines relative to fluid elements typically exceed what would be expected based on the bulk resistivity of the plasma.

The two separate magnetic fields merge as the outermost field lines of the compact toroid reconnect with adjacent field lines of the external field; each pair of closed lines becomes a single longer field line that encircles the still distinct inner field lines that have yet to reconnect. This is accompanied by (or mediated by) a layer of strong electric current at the surface of reconnection [45]. The key condition for reconnection is that the magnetic field changes sign in at least one component as the surface of interaction is crossed.

Overall, the most interesting complications come about when considering the geometry of the internal and external magnetic fields and the boundary conditions that the conducting walls of the vessel apply to the plasma and fields.
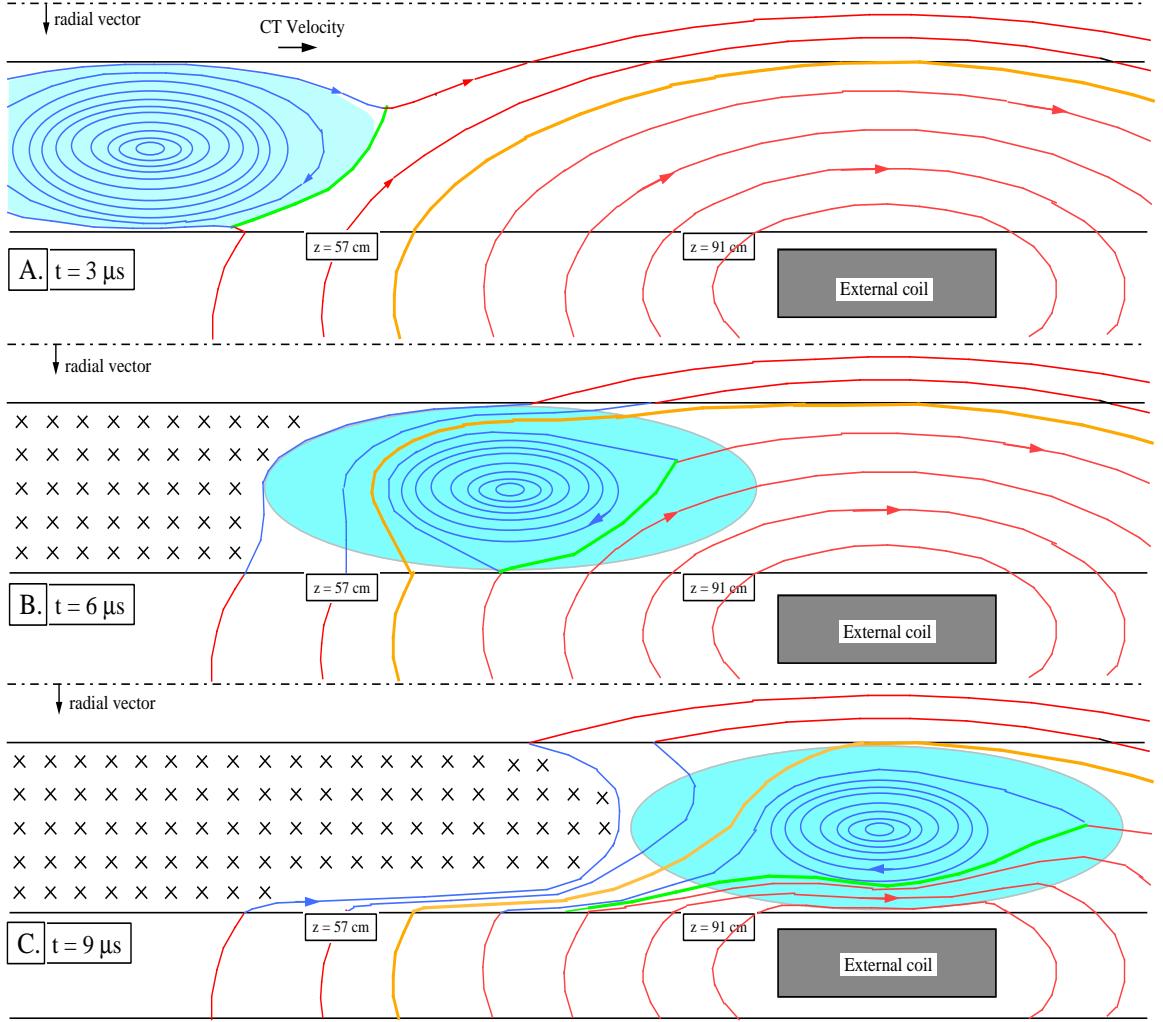
Figure 4.14: Sketch of flux surfaces during reconnection at three times A. t = 3 μs, B. t = 6 μs, C. t = 9 μs. Red field lines are members of the external field from the axial coils, before they have reconnected with the CT field, which is depicted in blue. The green curve in each figure shows the location of the reconnective current sheet at the separatrix between the opposing fields. The current in this sheet would be flowing in the toroidal direction, coming out of the page [45]. Behind the CT the toroidal pushing field is shown as a set of × marks indicating a magnetic vector going into the page. The thick orange field line is the last field line that intersects the both the inner and outer wall. The smaller field lines that are nested inside the orange curve will only intersect the outer wall. The large turquoise ellipse represents the approximate location of the original plasma of the CT as time passes.

Shown in figure 4.14 is a sketch that illustrates the qualitative behavior and geometry of

reconnection of the CT with the axial field. Certain features are disproportionate, such as the ratio

of internal CT magnetic flux to external flux, and the drawing is not to scale. It approximately maintains a divergence free **B** field while satisfying the nontrivial boundary condition that force the external field lines to be pinned to the wall on the experimental timescales. This leads to several effects, the most obvious is that the field lines that do intersect the wall will at certain times become compressed against the wall, greatly increasing the magnetic flux density (**B**) until it matches the strength of the larger internal fields.

Given an internal field that is larger than the external field, there will be a final flux surface of the CT that will undergo reconnection with the external field. Reconnection will proceed rapidly while there is opposing flux in the direction of CT motion, and will diminish to a negligible rate by the time that the current sheet has tilted to lie almost entirely in the (z, θ) surface. After the last flux surface has reconnected, the core of the CT will essentially "slip past" any remaining opposing external flux until it comes out the other end of the coils, where is will meet with a parallel field that interacts compressively. This is depicted in frame C. of figure 4.14.

To preserve the divergence-free nature of **B** (equivalently, by Gauss's Law) the contact angle between the field lines and the wall on the post-reconnection side of the CT, (the back side) must obey

$$\tan \theta_{\text{contact}} = \frac{B_{AF}(\text{wall})}{B_{CT}(\text{wall})} \tag{4.1}$$

which will lead to very small values of θ_{contact} due to the small ratio between B_{AF} and B_{CT}. This is constrained by the fact that $B_{AF}(\text{wall})$ must maintain the same value as it had before the plasma discharge began. On the other hand, $B_{CT}(\text{wall})$ will be evolving in time as the CT passes by.

This simple geometric model correctly predicts the interesting feature of negative B_z measured by the probes after the CT has passed by (see fig. 4.5), which is the result of the radial compression of the remnants of the anti-parallel external axial field, as shown in fig. 4.14 C. in the region between z = 57 cm and z = 91 cm.

The best conceptual picture for the reconnective increase in the acceleration of the CT is that ultimately, the presence of an anti-parallel field is simply a catalyst to unlock the large amount

of stored internal magnetic energy of the CT. The gain in kinetic energy of the CT comes mostly from the magnetic energy stored in the outer layers of its volume that are shed as it reconnects.

This fraction of its total volume can be estimated very roughly using a few approximations. In the future this could be turned into a more precise calculation. The idea is that the magnetic energy lost due to reconnection should be equal to the gain in kinetic energy of the CT. If we use the approximation that without reconnection, the total magnetic energy of the CT is roughly equal to the total kinetic energy, then we can express the energy balance in terms of a propotional change in energy. Stated in this way, we see that the mass of the CT divides out,

$$\frac{\Delta U_m(\text{reconnect})}{U_m(\text{total})} = \frac{\Delta KE(\text{reconnect})}{KE(\text{total})} = \frac{v_R^2 - v_O^2}{v_O^2} \tag{4.2}$$

We can simplify the magnetic energy ratio if we assume a nearly uniform distribution of energy density,

$$\frac{\Delta U_m(\text{reconnect})}{U_m(\text{total})} = \frac{\int_{\Delta V_{\text{shell}}} B^2 \, dV}{\int_{V_{\text{total}}} B^2 \, dV} = \frac{\Delta V_{\text{shell}}}{V_{\text{total}}} \tag{4.3}$$

where ΔV_{shell} is the volume of the outer region of the CT that attaches to the axial field during reconnection and V_{total} is the total volume of the CT. Then the fraction of the CT volume that gets sloughed off can be calculated from the measured final velocity in the case of reconnection ($v_R \sim 19 \; cm/\mu s$), and that without ($v_O \sim 18 \; cm/\mu s$).

$$\frac{\Delta V_{\text{shell}}}{V_{\text{total}}} = \frac{19^2 - 18^2}{18^2} \simeq 0.1 \tag{4.4}$$

In other words, approximately the outer 10% of the CT will be separated from the core during reconnection with an external magnetic field of 400 Gauss. Alternatively, we can say that 90% of the CT makes it all the way through the reconnection process intact.

Given that this magnetic energy is released in a finite period of time, we can estimate the average rate of flux annihilation [34], [35], [46]. The total process is at most about 5 μs in duration and the total magnetic energy of the CT is about 500 J, which means that the outer 50 J of magnetic energy was liberated from the CT, resulting in about 10 J/μs or 10 megaWatts of reconnection power.

Chapter 5

Temperature measurements

5.1 Particle velocity and energy

In this chapter we will discuss measurements of the electron energy distribution function of the plasma. By taking the first moment of this energy distribution we arrive at the average thermal energy of the electron population, which is proportional to the electron temperature of the plasma for a Maxwellian equilibrium, $\langle E_{thermal} \rangle = \frac{1}{2}nKT_e$. Here n is the number of degrees of freedom that the plasma electrons can move in, which is 3 for our system, and $K = 1.38 \times 10^{-23} \text{J}/^\circ\text{K}$ is Boltzmann's constant, and so KT has units of energy. Because the electron and ion populations are distinct interpenetrating fluids, it is possible for them to not be in thermal equilibrium with each other and exist with different energy distribution functions, and different temperatures.

When thinking about the kinetic energy of the plasma particles it is important to distinguish between their drift and thermal velocity components. The drift velocity of the plasma is defined to be the average velocity of all the particles with a macroscopic fluid element, relative to the rest frame of the laboratory. In other words, the drift velocity is the fluid flow velocity of the plasma. It may vary with position, since the fluid elements may be flowing along the streamlines of some non-uniform velocity field.

In the CTIX accelerator, the plasma drift velocity is dominantly in the direction of the axial acceleration, although there may be some smaller toroidal or poloidal component of the velocity of individual fluid elements. On the largest scale, however, if we average over all the particles in a thick annular slice at a given axial position, any poloidal rotation of the fluid will average to zero over the cross section, while toroidal rotations may exist but are expected to be much smaller than the dominant axial velocity. This is what we often call the CT velocity, and it is what we can measure with time-of-flight analysis of sequential magnetic probe signals, or with Doppler spectroscopy under certain conditions.

The thermal velocity component of any particle is simply the velocity vector that remains when we subtract the drift velocity from the particle's velocity relative to the lab frame. In this way, a particle's velocity vector is the vector sum of its thermal velocity component, and the drift velocity of the fluid.

$$\mathbf{v}_{particle} = \mathbf{v}_{drift} + \mathbf{v}_{thermal}$$

This thermal velocity will vary randomly in direction and magnitude as we go from particle to particle. We can characterize this random variation by the distribution function of the thermal velocity. We will also separately take account of the drift energy, and the thermal energy of each particle,

$$E_{drift} = \frac{1}{2}m\mathbf{v}_{drift}^2 \ , \qquad E_{thermal} = \frac{1}{2}m\mathbf{v}_{thermal}^2$$

where m is the mass of the particle.

5.2 Thermalization of electrons

A thermalization effect occurs when a compact toroid is injected into the vacuum magnetic field of the Davis Diverted Torus. Experiments were conducted in which the CT was injected transversely ($\perp$) into magnetic fields of 105, 150, and 180 Gauss, each defining a distinct data set [8]. Due simply to the net motion of the CT the ions have a drift kinetic energy in the range of

100 eV to 200 eV. The electrons, in contrast, gain little kinetic energy from the net motion of the plasma, owing to their much smaller mass (1/1856 of the mass of a proton); the net drift contributes no more than 0.1 eV to the electrons, which is insignificant compared to the electron thermal energy of 10 eV or greater.

During the process of collision and reconnection with the magnetic field of DDT the initial velocity field cannot stay directed axially. As the center of mass of the CT is brought to rest, the original directed kinetic energy is converted into thermal energy as the anisotropy of the particle velocity field is lost to a more isotropic velocity field in which entropy is maximized. While this basic concept provides a general description of thermalization, it leaves many questions unanswered. A more complete and predictive model would need to delineate the mechanisms that enable the conversion of particle energy to field energy and vice versa, as well as coupling between particles, such as the energy transfer from the ions to the electrons. These mechanisms could include kinetic effects, possibly via collisions, wave growth instabilities, and kinetic damping. Fluid effects could also be important, such as a turbulent cascade of fluid energy down to microscopic dissipative scales, shock heating, and magnetic reconnection. The theory behind these issues is far too extensive to tackle within this dissertation. However, the basics can be outlined, and several new experimental findings can be reported, which may help future work toward confirming existing theories, or guiding the invention of better theories.

The fundamental concept needed to describe the process of thermalization is the distribution function of the thermal energy of the particles; we will notate the energy distribution by $f_E(E)$. The energy distribution function $f_E(E)$ expresses the electron population density as a function of energy. If it is normalized to unity (the convention that I usually prefer), then $f_E(E)$ also represents the probability that any single electron will be found to have a thermal energy in the neighborhood of the energy E.

And of course there are other relevant particle distribution functions. For example $f_E(E)$ is related to the speed distribution by $f_E(E) = J f_v(v(E))$ where v is the speed, or magnitude of

the velocity of a particle, and J is the Jacobian of the transformation $v \to E(v) = \frac{1}{2}mv^2$. Then $J = |dv(E)/dE| = |(2mE)^{-1/2}|$. [47]

Maxwellian equilibrium   For reference purposes I would like to include some relevant formulas here [28],[48]. The velocity distribution function for a Maxwellian equilibrium of temperature T , with n spatial degrees of freedom, normalized to unity is

$$f(\mathbf{v}) = \left(\frac{m}{2\pi kT}\right)^{\frac{n}{2}} e^{-\frac{m|\mathbf{v}|^2}{2kT}} \tag{5.1}$$

where the n components of $\mathbf{v}$ range over the domain from $-\infty$ to ∞, and T is in units of degrees Kelvin, with $[kT] =$ Joules. Although the velocity distribution depends only on the speed $v = |\mathbf{v}|$, it is critical to remember that the distribution function for the speed v of a particle (i.e., the speed distribution) is not the same as the velocity distribution. The Maxwellian speed distribution function in the case of $n = 3$ is

$$f_v(v) = \frac{4}{\sqrt{\pi}} \left(\frac{m}{2kT}\right)^{\frac{3}{2}} v^2 \, e^{-\frac{mv^2}{2kT}} \tag{5.2}$$

where the domain of $f_v(v)$ is $0 \le v < \infty$. From the speed distribution we can write down the energy distribution function for a Maxwellian system $(n = 3)$,

$$f_E(E) = 2\pi^{-\frac{1}{2}}(kT)^{-\frac{3}{2}} \, \sqrt{E} \, e^{-\frac{E}{kT}} \tag{5.3}$$

where the energy is, of course, always positive; $0 \le E < \infty$, and we usually work with the more convenient units of $[E] = [kT] =$ eV. Note that $f_E(E)$ has dimensions of E^{-1}.

On the CTIX device, we have successfully measured electron energy using a pair of electrostatic energy analyzers [**?**]. We found that immediately before the collision/reconnection the electron thermal energy was approximately 30 eV to 40 eV and afterward the thermal energy increases to greater than 70 eV. Ion thermal energy is also expected to increase during the collision, however experimental verification of this effect remains incomplete. An attempt was made to repeat the energy measurement on the ion population using a larger 4-grid Ion Analyzer Probe, based off of a

previous design [49]. This was ultimately not successful. The measurement of ion thermal energy is more challenging due to the larger diameter ion Larmor orbits and certain plasma sheath effects.

A note on distribution functions   A quick comment should be included here regarding a difference of terminology. The function that physicists call a distribution function (as I have been using it above), is the same thing that mathematicians somewhat more precisely refer to as a probability density function (or pdf). The math nomenclature does a better job of conveying the meaning of the function because the integral of a pdf over a given interval results in the probability that the continuous random variable will take on a value within the limits of integration. In this way the value of the pdf at any given point represents the density of probability of random occurrence near that point. It reminds us that we need to integrate the pdf to get a value that is actually a probability. To add to this confusion, mathematicians have given the name 'distribution function' yet another definition, F(X) which is the integral from $-\infty$ to X of the pdf f(x). The mathematician's distribution function measures the probability of the event that the random variable will take on a value less than X. This will never be what I mean when I refer to the distribution function of some variable. I will always use 'distribution function' as the physicists do, equating it with the mathematician's pdf. And since my audience is primarily composed of physicists, I will follow their convention and mainly speak in terms of distribution functions.

5.3   Experimental overview

In our experiments we measured the electron energy distribution before and after it interacts with the DDT target magnetic field using electrostatic energy analyzer probes (EAP) in a variety of configurations. For all of these experiments we measured the initial velocity of the CT as it entered the injection region, as well as the final velocity of the reconnected plasma as it propagated along the field lines of DDT.

We wanted to know how the initial and final states scale with injection energy, and so we

repeated the same measurements for three different accelerator settings, CTIX accelerator voltage at 9.5 kV, 12 kV, and 15 kV. For this sequence of data sets, we adjusted the strength of the tokamak field to follow the increased accelerator voltage, ($B_{DDT} = 105$, 150, and 180 G). We did this with the intention of maintaining the CT stopping condition. As we will see, because of some accelerator inefficiency, the CT injection velocity did not depend on V_{acc} according to a simple, monotonically increasing function, as we naively expected. Instead, the velocity peaked near 12 kV, and then fell off as the applied accelerator voltage was further increased. The result is that we explored a much broader variety of stopping conditions than we originally planned.

We can characterize the stopping condition in terms of a zeroth order energy balance, between the CT kinetic energy density and the external magnetic energy density of DDT. The compact toroid will be able to go all the way through the field and hit the back wall if

$$\frac{1}{2}\rho v_{CT}^2 > \frac{1}{2\mu_0}B_{DDT}^2 \tag{5.4}$$

For known values of CT velocity and external magnetic field strength, this results in a limit on the particle density of the CT. The CT will not be stopped by the field if the density n is greater than the zeroth order stopping density,

$$\text{If } n > n_{stop} = \frac{B_{DDT}^2}{\mu_0 \, m_p \, v_{CT}^2}, \text{ then the CT will not be stopped by } B. \tag{5.5}$$

where m_p is the mass of a proton, and the mass density used in (5.4) is $\rho = n \, m_p$.

Table 5.1: Stopping conditions for injection into DDT

$\mathbf{V}_{acc}$	$\mathbf{B}_{DDT}$	$\mathbf{V}_{CT}$	n_{stop}
9.5 kV	105 G	13.65 $cm/\mu s$	$2.81 \times 10^{12} \ cm^{-3}$
12 kV	150 G	18.4 $cm/\mu s$	$3.16 \times 10^{12} \ cm^{-3}$
15 kV	180 G	12.14 $cm/\mu s$	$1.04 \times 10^{13} \ cm^{-3}$

In table 5.1 we see that the 9.5 kV data set had the lowest stopping density, in other words it made it the easiest for $n > n_{stop}$ to occur. While in the 15 kV data set the CT's were the most strongly stopped. For example, if the CT density was 3.0×10^{12} (which is possible given

the expansion in the drift section and DDT), then the 105 G field of the 9.5 kV data set would be insufficient to stop its CT's, the 150 G field of the 12 kV data set would have just barely stopped its CT's, and the 180 G field of the 15 kV data set would have been very good at stopping its CT's.

The details of the design and operation of gridded electrostatic energy analyzer probes is presented below, which includes an analysis of simulated data to arrive at an estimate of the experimental error, as well as some statistical results regarding the systematic error due to the analysis algorithm.

5.4   EAP construction

The probe tip is a hollow cylindrical assembly, 2 cm in diameter, made from anodized aluminum with a moderately large 1 cm diameter aperture to let plasma inside. Within the probe tip are the following components: two circular grids, (the ion repeller grid and control grid), and a circular collector plate. They are stacked together in a sandwich configuration with mica spacers to insulate them from each other and from the case of the probe tip. The probe tip is supported by a 28" long stainless steel shaft which slides through an o-ring vacuum seal to allow the probe to be inserted into the vacuum vessel over a range of depths.

The two grids are tungsten mesh of high transparency, and the collector is tantalum. The two grids and the collector each have a thin nickel wire spot-welded to them that runs back through the shaft and connects to the electronics that operate the probe. By way of these wires the grids can be charged to different potentials and a current can be drawn from the collector plate, and recorded by a digitizer. We will ultimately derive the electron energy distribution function from measurements of how the electron current drawn by the collector plate depends on the applied repeller grid voltage.

For our experiments the energy analyzer probe tip was positioned at the center of the vacuum vessel with the aperture oriented toward the incoming plasma to have the best opportunity to intercept a good signal. For the injection experiments involving collision/reconnection on DDT
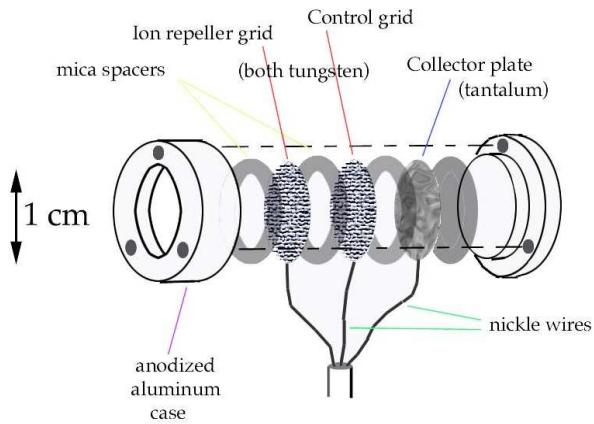
Figure 5.1: Exploded view of EAP showing grids and collector plate

target field, the EAP was mounted on the top port 90° from the injection point on DDT; then for the pre-injection measurements, the probe was positioned in the drift section.

5.5   Grid biasing

The functionality of the energy analyzer probe is achieved primarily by charging the control grid to a negative potential with respect to ground. This potential on a probe is often referred to as the bias voltage or simply the bias. Negatively charged electrons that initially enter the aperture of the probe will feel a repulsive force from this grid. The electric field of the control grid can be thought of as an electrostatic hill standing between the electrons in plasma and the collector plate. This hill will act to separate those electrons which are fast enough to make it over the hill from those which are too slow to get over the hill. All of the electrons that do make it over this hill are then promptly absorbed into the metal collector plate, causing an AC-coupled negative current to flow across a bias capacitor and then back to the digitizer.

The magnitude of this current is directly proportional the total number of electrons in the
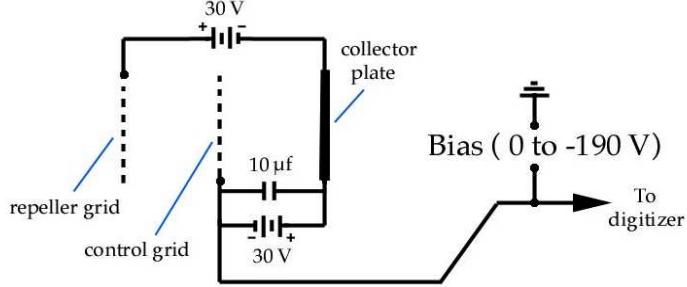
Figure 5.2: Schematic of EAP biasing circuit

vicinity of the probe which had enough energy to make it over the hill. In Fig. 5.3 we have shown

the collector current as a function of time over the course of a typical shot.
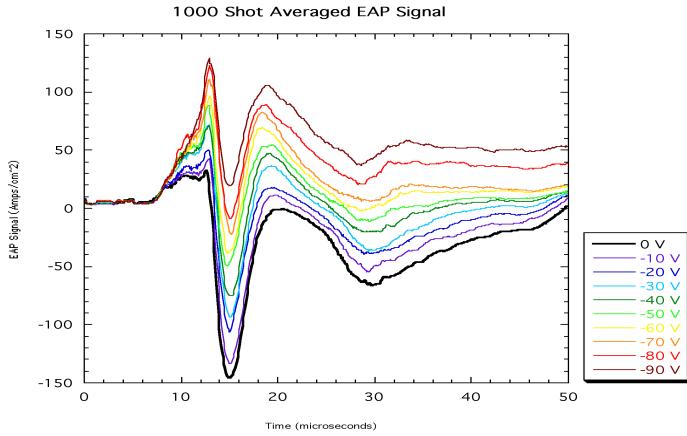
Figure 5.3: Time dependence EAP collector current, parameterized by control bias voltage. As the negative bias is increased, a larger electron fraction is repelled. The first strong negative peak in the signal corresponds to the arrival time of the compact toroid.

Now, as we vary the bias voltage applied to the control grid, we will repel a variable amount

of electrons in a manner that is energy dependent. At a larger negative bias, more electrons are

repelled by the control grid, letting only the very fastest electrons get to the collector plate, hence a

small current is drawn. When we decrease the magnitude of the bias, very few electrons are repelled

hence a very large current. At zero bias, all the electrons can get by and so the current has leveled off to a maximum value.

The other grid in the probe, the ion repeller grid, is situated to be the first to encounter incoming plasma and is charged positive in order to prevent ions from entering the interior of the probe. In the simplest possible biasing circuit, the positive bias on the ion repeller grid is accomplished using a high impedance battery that provides a DC voltage yet blocks the fast signals caused by interaction with the transient plasma.

For example, let us examine the collector current as a function of time as shown in figure 5.3. It shows the raw EAP data taken for the pre-injection experiment. Each of the 10 colored line-plots in the 1000 shot average is the point-by-point time-dependent average of the 100 shots that were all taken at the same bias voltage. The important features are first, the strong negative peak that occurs at the time of CT arrival, and second, the weaker negative pulse that is due to the trailing plasma eventually getting to the probe. The lowest of the curves (the black curve) was taken with electron repeller bias voltage set to zero and you can see that both the CT and the trailing plasma cause electron current to be collected by the probe. When we increase bias voltage to the -90 V (brown curve at top), it is clear that almost all electrons have been repelled.

5.6 Relation between $I(V)$ and $f_E(E)$

Everything that I have already described about the operational mechanism of the EAP, and how it can be used to measure the electron temperature of a plasma can be succinctly summarized in the following integral relationship between $I(V)$ and $f_E(E)$. Because the electron energy distribution $f_E(E)$ measures the probability density of electrons in each infinitesimal slice of energy space, we can express the collector current $I(V)$ as an integral of the electron energy distribution.

$$I(V) = q \cdot \Gamma \int_{qV}^{\infty} f_E(E)dE \qquad (5.6)$$

Here, q is the charge of an electron, it works as the conversion factor between V in Volts and E in electron-Volts. This integral counts all of the electrons which have an energy above (qV), which are collected as electron current by the EAP when the bias voltage is V. Randomness enters our measurements primarily from the electron flux rate $\Gamma = n_e \mathrm{v}_e A_{collector}$ which varies from shot to shot with an approximately Gauss-normal distribution. Here n_e is the electron number density, v_e is the average electron speed (dominated by thermal motion), and $A_{collector}$ is the area of the collector plate. The physical source of this variation is mostly due to irreproducibility in the total gas output of the formation gas valve, and also partly due to spatial variations in plasma density and how that density intercepts the probe. Now, it is the current that is experimentally measured, initially as the set of data points making up the I-V scatter plot, one (I, V) point per CTIX shot. We first need to extract an approximation of the function $I(V)$ from the raw data by some averaging or curve fitting procedure. Once we have the measured $I(V)$, we can solve equation 5.6 for the unknown $f_E(E)$ by differentiating both sides.

$$f_E(E) = \frac{1}{q\Gamma} \frac{dI(V)}{dV}\bigg|_{\frac{E}{q}} \tag{5.7}$$

We also see that $V = E/q$ is the bias voltage which is able to repel an electron of energy E.

Lastly, the average thermal energy is computed by taking the first moment of the energy distribution function.

$$\langle E_{thermal} \rangle = \int_0^\infty E f_E(E) dE$$

So the experimental task is to find a feasible way to measure the I-V curve with the EAP so that we can differentiate it to get the local electron energy distribution function. In our setup we do not try to measure the energy distribution of the plasma for each individual shot because the desired plasma conditions in the vicinity of EAP are so transient. The plasma wave passes over the probe for only a few microseconds and then is gone. While it is physically possible to sweep the bias over a few hundred volts at a MHz rate, we believe that the cost and inherent difficulties in implementing and operating such a system would overshadow any benefits for measuring the fast plasmas on our experiment.
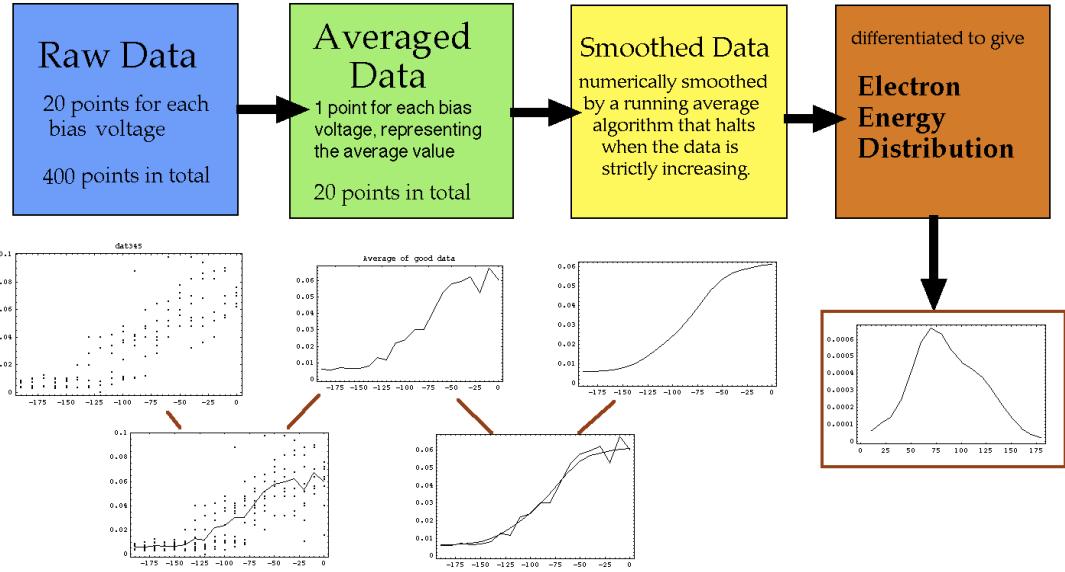
Figure 5.4: Analysis method using moving-window smoothing

It is more experimentally feasible to build up the I-V curve point by point, one point for each shot. To make this pointillistic composite of the I-V curve we collected 20 shots per bias voltage setting, with a total of 20 settings from 0 volts to -190 volts in increments of -10 volts. This gave a total of 400 shots per data set in the original post-reconnection measurement of electron temperature.

We were careful not to take all 20 shots for a single bias voltage at once. We broke up the bias settings into even and odd multiples of -10 V. We would first go sequentially through the even set, with 10 shots at each setting, then do a round on the odd set with 10 shots per bias setting. Then we repeat this to get the second 200 out of 400.

The reason for dividing the scan into a several repetitive cycles was to separate out any systematic trends in system performance from the real electron temperature effect. For example, it might be a problem if all the low bias voltage shots were taken at the beginning of the day, and all the high voltage shots at the end of the day. There would be no way of knowing that as the device

warmed up over the course of the day, variation in the gain of the electronics or in the performance of the accelerator was the real source of the observed trends in the data. However, based on the comparison of these divided data sets, we found that there was no measurable systematic variation in the performance of the EAP diagnostic over the course of several weeks of runtime.

5.7   Analysis methods

Method 1: Two Parameter Nonlinear Fit to a Maxwellian form I(V) Curve. This method assumes that plasma is in thermal equilibrium with an effective number of degrees of freedom that must be chosen by the user. The fitting function returns a temperature and a normalization factor. The idea is that if the electrons had a Maxwellian distribution, then the $I(V)$ curve for the EAP should obey some analytically expressible formula. If we evaluate equation (5.6) using the Mawellian energy distribution given in (5.3), then we find

$$I_{Maxwell}(V) = 1 + \frac{2}{\sqrt{\pi}}\sqrt{\frac{qV}{KT}}e^{-\frac{qV}{KT}} - Erf\left(\sqrt{\frac{qV}{KT}}\right) \qquad (5.8)$$

Method 2: Non-analytical Free Fitting Method. Using no analytical assumptions about the form of the Energy Distribution Function, this method is able to reconstruct deviations from thermal equilibrium that may exist within the plasma. The raw data is averaged, smoothed and then differentiated numerically to yield a discretized plot of the energy distribution function. Both methods have been implemented and compared.

5.8 Experimental results

5.8.1 Post-injection Experiment
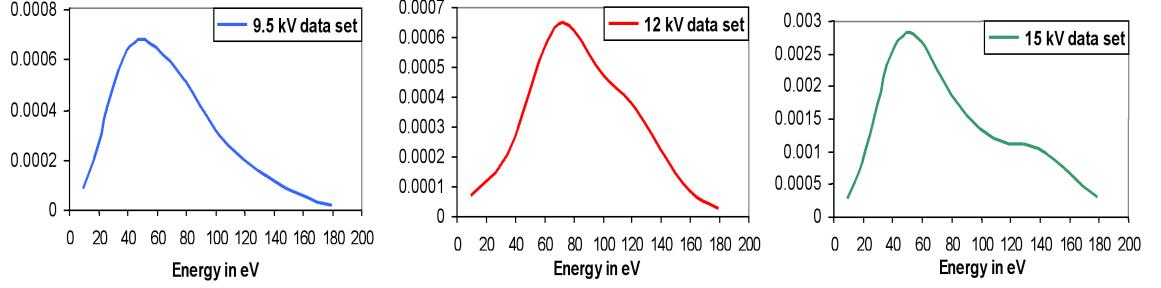
Figure 5.5: Reconstructed electron energy distribution functions.

Table 5.2: Summary of results from the post-injection data sets

$\mathbf{V_{acc}} = \mathbf{9.5}$ **kV**, $\mathbf{B_{DDT}} = \mathbf{105}$ **G**	*Pre-injection*	*Post-reconnection*
Fluid velocity	13.65 $cm/\mu s$	5.95 $cm/\mu s$
Net Ion Kinetic Energy	97.2 eV	18.5 eV
Electron Thermal Energy	unmeasured	**70.1 eV**

$\mathbf{V_{acc}} = \mathbf{12}$ **kV**, $\mathbf{B_{DDT}} = \mathbf{150}$ **G**	*Pre-injection*	*Post-reconnection*
Fluid velocity	18.4 $cm/\mu s$	14.95 $cm/\mu s$
Net Ion Kinetic Energy	176.7 eV	116.6 eV
Electron Thermal Energy	unmeasured	**86.4 eV**

| $\mathbf{V_{acc}} = \mathbf{15}$ **kV**, $\mathbf{B_{DDT}} = \mathbf{180}$ **G**	*Pre-injection*	*Post-reconnection*
Fluid velocity	12.14 $cm/\mu s$	10.26 $cm/\mu s$
Net Ion Kinetic Energy	76.9 eV	54.9 eV
Electron Thermal Energy	unmeasured	**80.3 eV**

5.8.2 Pre-injection Experiment
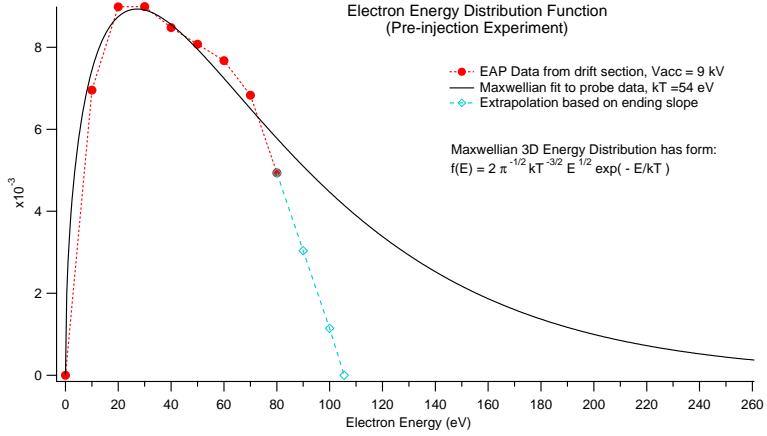
Figure 5.6: Pre-injection electron energy distribution function, red curve is the reconstruction using a free-form analysis, black curve is the Maxwellian fit to the 1000 points of raw data.

Method 1: Free Fit

Average thermal energy $\langle E_{thermal} \rangle_{ave} = 43$ eV

The error due to data set statistics is $\sigma^2_{\text{Thermal Energy}} = \pm 2.02788 \; eV$

The error due to smoothing is $\sigma^2_{\text{Smoothing}} = \pm 2 \; eV$

Method 2: Maxwellian Fit

(fit to raw I-V data) 33.47 eV $\leq \; \langle E_{thermal} \rangle_{ave} \leq 54$ eV (Maxwellian fit to Free-fit distr.)
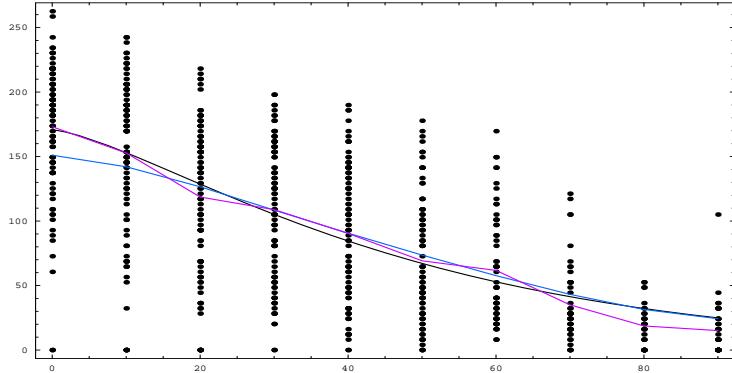

Figure 5.7: 1000 shots of raw data {•} with average-value curve {violet}, iteratively smoothed curve {black}, and Maxwellian fitted I-V curve {blue}. The x-axis measures the absolute value of the EAP bias voltage, and the y-axis measures the resulting EAP collector current (arbitrary scale).

5.9   Error analysis of simulated data

We will now closely examine two test cases, one simulation done with a Maxwellian input distribution and one done with non-Maxwellian input distribution. The Maxwellian energy distribution used for this test is shown in the left frame of figure 5.8. It has an average thermal energy of 1.4 (arbitrary units). To simulate the EAP diagnostic, we integrate the a priori known energy distribution analytically to create the ideal I-V curve. Then we generate a set of simulated "measured I-V data points" that are randomly scattered around the ideal I-V curve.

More precisely, for each bias setting, we generate 20 normal-random numbers which have the same standard deviation as the real data set and we use these numbers as the vertical distance of the data points away from the ideal I-V curve. To do this we just multiplied the 20 normal-random numbers by the height of the ideal I-V curve to get the scatter of points in right relative frame above and below the ideal curve. The final simulated data set has 400 points in it, just like the actual data set collected for the post-injection thermalization experiment.

Then as the last step, we performed the free-fit analysis on the simulated data in order to create reconstructed version of the energy distribution (shown in right frame of figure 5.8).
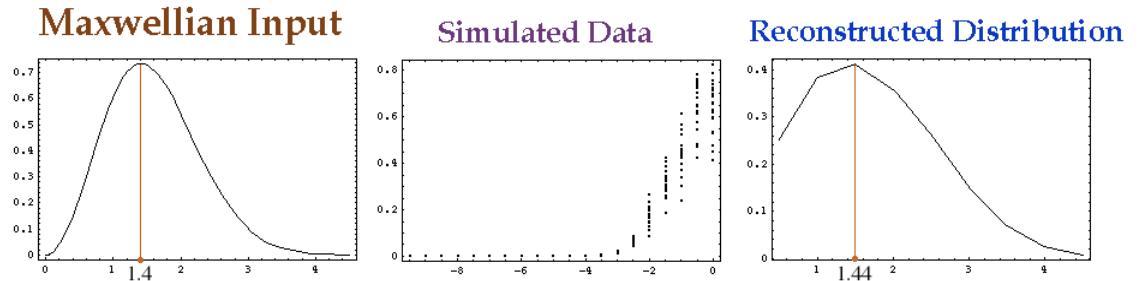

Figure 5.8: Comparison of reconstructed and original energy distributions for a Maxwellian original.

This test should reveal the trustworthiness of the free-fit method for our data's size and statistics. If the reconstructed distribution is wildly different from the original in the simulation, then we would have to expect that the experimentally measured distribution would also be wildly

different from the idealized, physically real distribution.

On the other hand, if the input and output distributions were very similar, and this similarity held for a wide range of input curves then we would be guaranteed an equivalent level of similarity between our measured energy distribution and the actual energy distribution of the plasma. We could then accept the experimentally reconstructed energy distributions as being "real" and well measured.

Shown in the right frame of figure 5.8 is the energy distribution reconstructed from the simulated data. It has close to the same average thermal energy of 1.44, which differs from the average value of the original by about 3%. The distribution's shape has spread out quite a bit due to the effects of randomization in creating the simulated data. However, this is not an error in the average-smooth-differentiate algorithm because when simulations were done with 2000 data points in the set, we reconstructed the proper shape of the distribution quite well.

As the number of data points shrinks, the reconstructed distribution becomes correspondingly more round in shape. Also, it was observed that no simulated sets produced humps where they were none to begin with. In this way all of the Maxwellian reconstructions were easily identified as being Maxwellian.
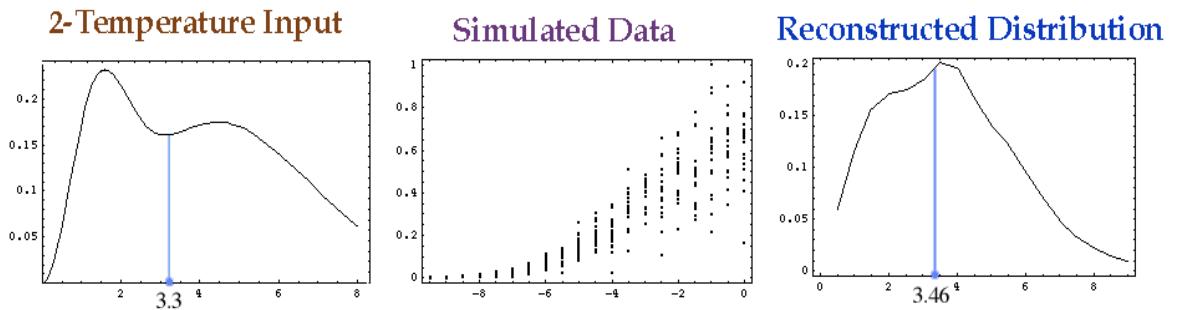

Figure 5.9: Comparison of reconstructed and original energy distributions for a two-temperature original.

For comparison, we also tried using a non-Maxwellian distribution as the input for the simulation. Here we have the original distribution (left frame of figure 5.9), and its average thermal

energy is 3.3. Using the same simulation algorithm as before, we create the "measured" I-V data set as shown in the center frame. Again we applied the free-fit analysis to this simulated data set and found a reconstructed energy distribution.

While its shape is quite different from the original, its average thermal energy is still very close, 3.46 which is within 4.8% of the original. Many other functional forms were tried as the input for the simulation. Similar results were obtained for all simulations using the same statistics as our actual data sets. In all but a few of these runs (there were some very unphysical cases that caused some trouble), the average value of thermal energy was correctly reconstructed to within 5% of the original.

5.10   Statistical error analysis

The main result from the simulation work was that the average value of thermal energy had a relatively small total error for the size of data sets we are working with. In this section we take this result a step further by deriving an exact relationship between the data set dimensions and the resulting error in the average thermal energy of the plasma.

We consider a situation where the probe current $I(V)$ has been measured n_V times at the k bias voltage settings, where in general, n_V could take different values at different bias voltages, hence the V index is used to denote this possible dependence. A non-constant n_V could easily occur in a real life experimental data set, where system failures of one sort or another could require that data from certain shots be excluded from the dataset. The result would be a slightly patchy scan of the parameter space,where more good data was gathered for some voltage settings than for others.

To get the energy distribution the data is averaged, smoothed until it is a well-behaved monotonic function, and finally differentiated to yield the energy distribution (refer to figure 5.4 for a diagram of analysis process).

For now, we will ignore the smoothing step, which doesn't lend itself to the analytic treat-

ment being considered here.

The variable Γ was observed to be normally distributed about the mean density. Because each $I(V)$ measurement depends on the random variable Γ and a monotonic function of V, the variance of the I data at V obeys

$$\sigma^2(V) = \sigma^2(0) \cdot \int_{qV}^{\infty} f_E(E) dE \tag{5.9}$$

Note that the variance at $V = 0$ should be equivalent to the variance that describes how the electron flux rate Γ is randomly distributed (i.e., $\sigma^2(0) \equiv \sigma_\Gamma^2$).

As mentioned earlier, the random variation in $I(V)$ is due almost entirely to fluctuations in Γ, while the stable dependence on voltage is due entirely to the integral of $f_E(E)$, and so the variance will decrease with increasing $|V|$.

This condition is useful as an indicator of whether or not the probe is really working. If $\sigma^2(V)$ doesn't decrease with increasing $|V|$ then there is a problem with the probe. Error bars for the values of the $I(V)$ curve at each voltage can then be estimated from the measured $\sigma^2(V)$ and the number of data points n_V at that energy. For each voltage setting, the variance of the average value of the (n_V) probe current measurements is related to the variance of the measurements themselves, according to

$$\sigma_{ave}^2(V) = \frac{\sigma^2(V)}{n_V} \tag{5.10}$$

Of more importance to this study is an upper bound on the error of the average thermal energy, quantified by the variance first moment of $f_E(E)$. We used moment generating functions to make the transformation from the variances of the individual measurements to the variance of the error in the average thermal energy. The resulting total variance is just the sum of the variances of the average value at each voltage $V_1, V_2, \ldots, V_k$.

$$\sigma_{thermal\ error}^2 = \frac{\sigma^2(V_1)}{n_{V_1}} + \frac{\sigma^2(V_2)}{n_{V_2}} + \cdots + \frac{\sigma^2(V_k)}{n_{V_k}} \tag{5.11}$$

The key feature in this expression is that the error will tend to grow linearly with k (where k is the number of bias voltage settings in the scan, also the number of terms in this sum). It must be noted

that it does not work to try to minimize the error by taking k =1, since your choice of that single voltage setting will dominate the final answer. Enough voltage settings must be included in order to have a minimum amount of energy resolution to consider the final result a reasonable approximation to the distribution function. With that in mind, k should be at least 10, and then n must be chosen to be large enough to bring down the error. (k =10, n=200 are good values to plan an experiment around).

5.11   Conclusions

The simulation has shown the limitation of accuracy of our experimental method when only 400 data points are taken. The exact shape of the distribution cannot be trusted, except that if it has some lumps, it is very unlikely to be from a Maxwellian plasma. If it has no lumps, the physically real energy distribution still has a chance of being non-Maxwellian. On the other hand we can put more confidence in the average thermal energy of the distribution.

The simulation has shown that the free-fit analysis method we used on the 400 data points from the post-injection experiment is fairly robust with respect to this average value, and we can expect that with our real data we have correctly reconstructed the average thermal energy of the plasma to within 5%.

We tried to improve upon these statistics when doing the follow-up experiment in the pre-injection region, by having only 10 bias voltage settings, with 100 shots at each voltage, which according to (5.11) we would expect the variance of the average thermal energy to be about 1/10th of the variance of the raw data at a single voltage setting. This seemed like a significant improvement to the previous variance estimate for the post-injection experiment with 20 bias voltage settings, and 20 shots per voltage, which would have yielded an average thermal energy with exactly the same variance as the raw data. According to these estimates (applied somewhat naively), we expected that measurement of the average thermal energy in the pre-injection study would be 10 times more

precise than the earlier study of the post-injection conditions.

The problem with these estimates is that they don't take into account any effect of the choice of bias voltages for your EAP scan. If the scan window is too small or in the wrong region, then the average thermal energy will end up being reconstructed very near the mid-point of the energy scan window. For instance, you might naively conclude that the average thermal energy of the electrons was 200 eV, if you had only scanned from 100 V to 300 V. In the case of the pre-injection study, although we had superficially better statistics we chose to scan the EAP voltage only in the range from 0 V to 90 V, and ended up with 43 eV as our answer for the average thermal energy (very close to the half-way point at 45 eV). This result probably would have been higher if we had scanned up to 200 V like we did in the post-injection experiment. For this reason, it seems most reasonable to use the upper estimate on electron temperature given by the Maxwellian fit shown in figure 5.6, of $T_e = 54$ eV, for the value used in other chapters.

Some further insight can be gained by comparing the results of the post-injection study to the time-of-flight data from the magnetic probes in the accelerator and Langmuir probes in DDT. We find that the final electron thermal energy is comparable to final ion kinetic energy. This implies that electrons and ions may have gone through some process of equilibration during the collision.

It is also informative to compare the magnetic stopping conditions with the resulting energy distribution functions of the post-injection experiment. There is a direct relationship between how strongly the CT is stopped by the field, how much ion kinetic energy is lost during the collision with DDT field, and the resulting shape of the final energy distribution. As mentioned in section 5.3, the conditions used in the 15 kV dataset resulted in the strongest stopping condition (see table 5.1), it had the smallest drop in ion kinetic energy ($\Delta KE = 22$ eV, a 28% loss of ion KE, see table 5.2), and had a non-Maxwellian double-hump shaped energy distribution that had the most clear high energy tail. The 12 kV data set had the second strongest stopping condition, the second smallest ion kinetic energy loss ($\Delta KE = 60.1$ eV, a 34% drop in KE), and a non-Maxwellian distribution with one dominant hump about halfway between the two humps of the 15 kV distribution. Lastly, the

9.5 kV set had the weakest stopping condition, the largest drop in ion kinetic energy ($\Delta KE = 78.7$ eV, a loss of 80.9% of its original energy), and an energy distibution that was the most Maxwellian of the trio.

These relationships lead us to the idea that when the magnetic stopping condition is strong, less thermalization of the original ion kinetic energy occurs because a strong target magnetic field is able to redirect the plasma flow without slowing it down. As the stopping condition is weakened, an intermediate regime occurs where thermalization increases, and less of the plasma flow is smoothly redirected into a path that is tangent to the target field. Then, if the stopping condition falls below some critical value, the injected plasma is able to pass entirely through the target field and come to a dead stop by colliding with the back wall of the target vessel. This results a very efficient thermalization of the plasma that very rapidly evolves into a Maxwellian equilibrium.

Chapter 6

Spectroscopic measurements of ion velocity

6.1 Previous low resolution spectroscopy

One of our standard instruments has been general purpose visible survey spectrometer. It can measure the entire visible spectrum 300 nm to 670 nm on a single exposure of a gated/intensified linear detector array (1024 pixels). This allows diagnosis of the light emitted by impurity species within the plasma. Two modes of operation are possible. We can integrate over the entire shot, or gate the spectrometer to measure light from a small time interval within the shot. Time evolution of spectrum during the acceleration process can be built up over a sequence of shots in the gated mode by stepping the delay time of the start of the spectrometer gate pulse relative to the time of CT plasma formation. The spectrometer can view the plasma axially via an internal mirror, or transversely through glass window ports. Focusing optics are required for time-gated operation in order to collect enough light into the fiber optic bundle to make detectable light signal at the diffraction plane.
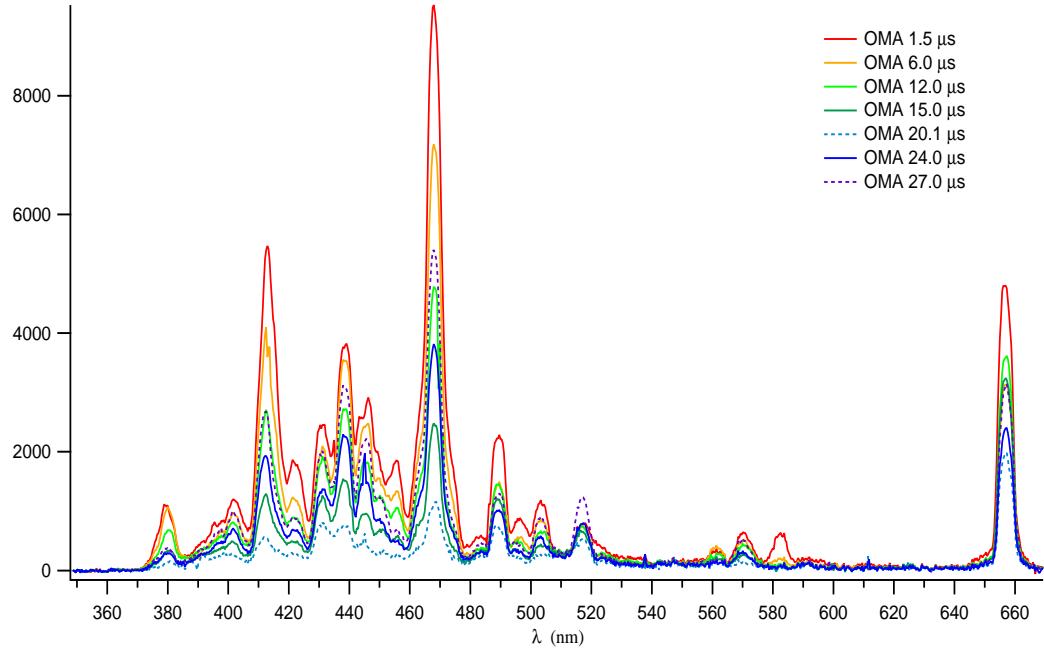
Figure 6.1: Time sequence of low resolution spectra.

6.2 High resolution visible spectrometer

A transmission grating spectrometer appropriate for visible light (3500 Å to 6800 Å) was built by Alex Graf[1] in collaboration with EBIT group and was used to study the plasma created by the CTIX machine. The fast time resolution and high spectral resolution are possible due to special LLNL fabricated transmission gratings, which the design is based around.

The transmission grating is circular with a diameter 150 mm, groove spacing of 3944.5 +/- 0.5 Å. Due to its large diameter this grating allows faster integration times, it has an f/3 which is much greater than the f/10 in a conventional spectrometer. It has a demonstrated spectral resolution, $\lambda/\Delta\lambda$, of up to 14500 for a wavelength of 5790.7 Å while using a 50 μm slit (fig. 6.2 and 6.3). The optics within the spectrometer allow for off axis ($\pm$ 1 cm) input light. [13]

My part in the spectrometer project was primarily the development of practical imple-

---

[1]Graduate student in UCD Physics Dept.

Optical parameters
Slit width = 50 μm
Resolution $\Delta\lambda = 0.3$Å to 0.8Å
Range of λ : 3650Å to 6750Å
Dispersion = 11.4504 Å/mm
or 0.14648 Å per pixel

Transmission Grating:
2535 lines per mm
150 mm diameter

Lenses
Focal length = 50 cm
f = 3.8, 130 mm diameter

CCD
Pixel size 12.8 x 12.8 μm
Gating time: 0.5 μs to 5 μs

Center Wavelength
$\lambda = d(\sin\alpha + \sin\beta)$
d = 3945 Å

Input fiber optics

Slit

Lens

α

Lens

Transmission Grating

β

Detector

Figure 6.2: Operational schematic of high resolution spectrometer

1. Transmission grating
2. Achromat lenses
3. Detector
4. Input fiber optic
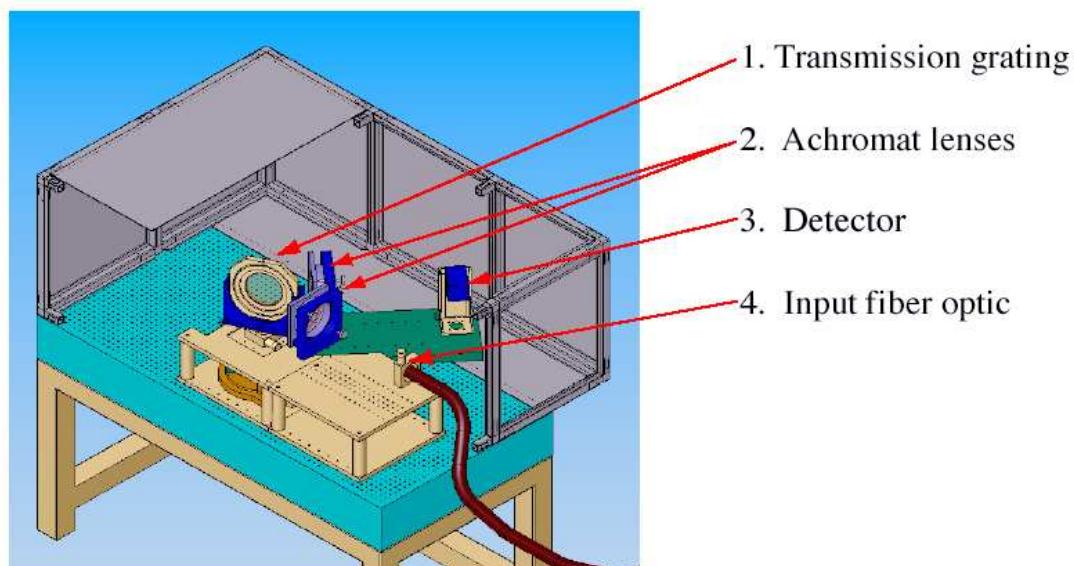
Figure 6.3: Rendered 3-D cut-away view of high resolution spectrometer

mentations of fast detector arrangements suitable for viewing the CTIX plasma. We constructed a sequence of custom-made adjustable supports for mounting any available fast CCD camera that we had at our disposal into the interior of the spectrometer so that it could record the spectrum image at the dispersion plane. All together, we took data using a sequence of 5 distinct detectors in as many months of run time.
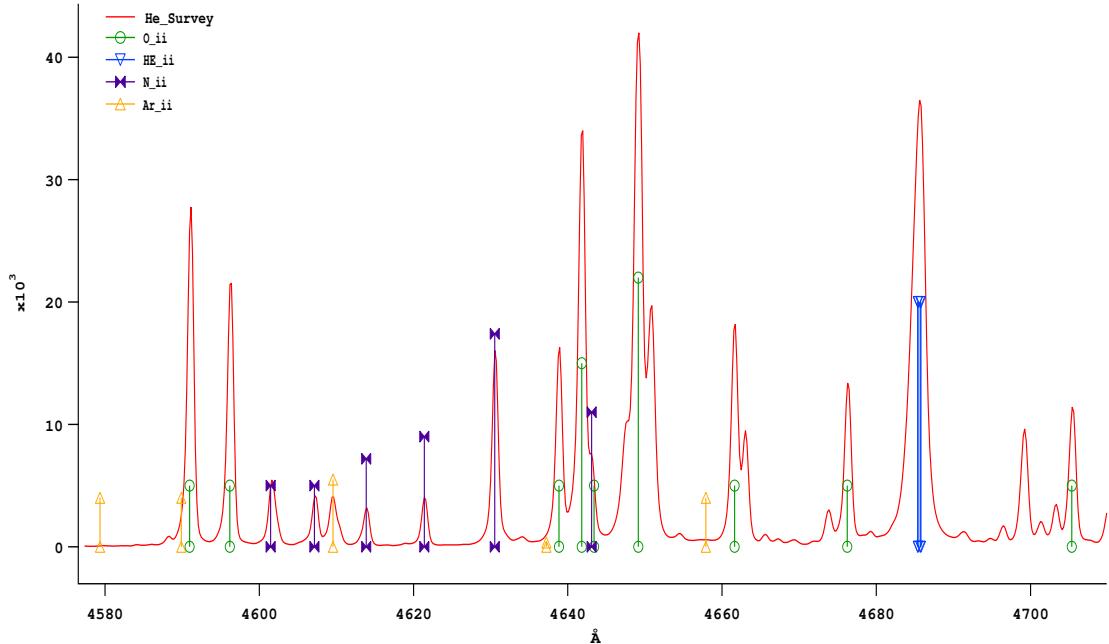

Figure 6.4: Survey spectrum of helium plasma near He II line

The first experimental task that we completed was a time integrated impurity survey of the light from a helium CT plasma. The spectral resolution is far superior to that of the former device allowing a proper separation and identification of the many features present. This high-resolution survey spectrum spanned most of the visible wavelengths from 3500 Å to 6800 Å. This spectrum was compiled from about 50 individual spectra, and it mapped out the location and relative intensities of hundreds of impurity lines, as well as the primary helium and hydrogen lines. Next we selected one of the brighter spectral lines for further study. The best candidate was the line transition at

4686 Å of singly charged helium (He II). [50]

The largest shift expected for a 200 km/s CT is around 4 Å well within the spectral bandwidth of typically 150 Å, while the smallest shift we can detect is at least ~ 0.4 Å (less if the light is sufficiently bright).
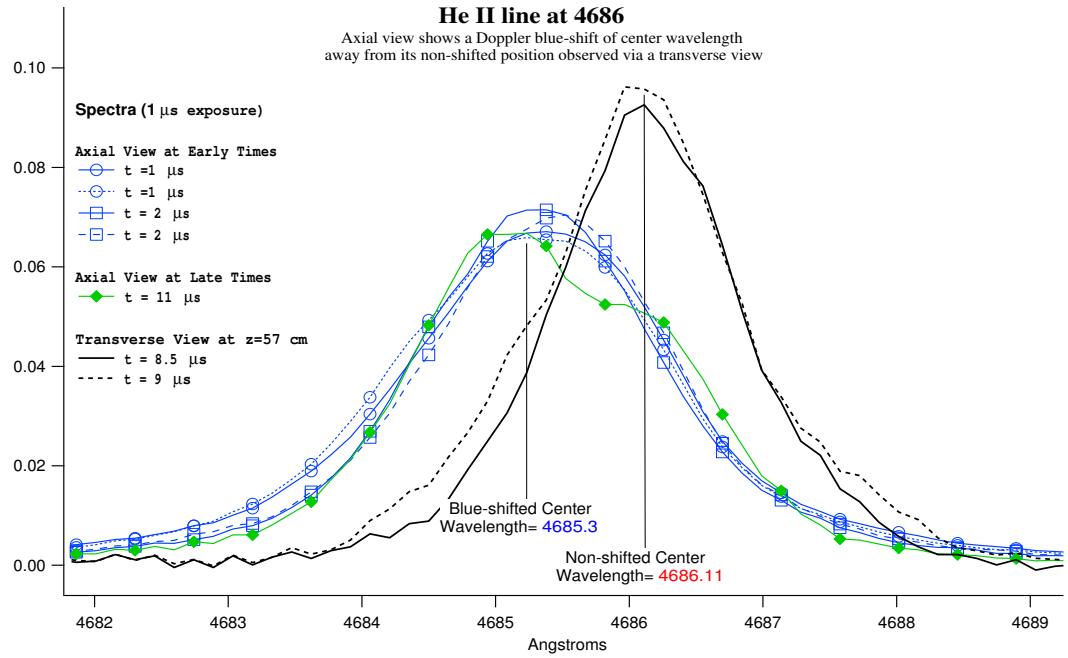

Figure 6.5: Doppler shift of helium II line at $\lambda = 4686$ Å

We measured Doppler shifts of this line using an axial line of sight, where the plasma is rapidly moving toward the point of observation. We compared this to spectra that were taken along three different transverse chords that are orthogonal to the direction of plasma motion and so experience no Doppler shift. The spectra along all four of these lines of sight were recorded using a time gating method that mapped out the time evolution of the spectral lines and their Doppler shifts in 1 microsecond increments from the moment of plasma breakdown until 30 microseconds after breakdown. During this period the CT plasma is accelerated from 0 to 200 km/s.

The resulting time evolution of Doppler measured plasma velocity was a bit of a surprise

at first. Using time gating of the CCD we are able to watch the evolution of ion velocity using the measured Doppler shift at each time step (see fig 6.6). He II ion velocity peaks very early at 1.5 μs, with a maximum of $\sim$50 km/s and then dwindles to only 10 km/s during most of the acceleration of the compact toroid. A second peak of $\sim$72 km/s occurs at 14 μs, which is coincident with the moment when the CT leave the end of the accelerator, at this time a re-strike occurs at z = (0 to 20 cm) due to the ringing of the railgun circuit.

We never saw the plasma reach anything close to the peak velocity of 200 km/s as measured by the time of flight between magnetic probes, and we would like to know why.

After completing a subsequent experimental and analytical investigation, we found a satisfactory explanation for this effect, which relies on new evidence of a dramatic variation of ion density as a function of position and time that can be accurately modeled within a simple framework.

6.3   Measurement of average Doppler velocity

We are looking at a comparison between the transverse spectra and the axial spectra of the line emission of He II (Z=1) at λ = 4686 Å.

The transverse spectra have no detectable shift, while the axial spectra show a Doppler blue-shift because the plasma is moving rapidly toward the input fiber. The apparent wavelength of the blue-shifted light is:

$$\lambda = \lambda_0(1 - v/c)$$

where v/c is the ratio of the ion velocity to the speed of light, which is always less than 10^{-4} for the CTIX plasma. Experimentally however, we cannot measure the Doppler shift of individual ions. In our setup, the light from nearly all the ions in the entire volume of plasma is collected by the axial line-of-sight fiber optic. The measured shift in center wavelength is actually a weighted average of the Doppler shift throughout the vessel. And so we can only infer an average fluid velocity based on this average Doppler shifted wavelength.[51],[52]

$$\mathrm{v}_{ave}(t) = c\left(1 - \frac{\lambda_{ave}(t)}{\lambda_0}\right) \tag{6.1}$$

where $\lambda_{ave}(t)$ is the experimental average of Doppler shifted center wavelength as measured by the axial line of sight and λ_0 is the unshifted center wavelength of the line emission as determined by the transverse measurements. $\lambda_{ave}(t)$ is found by taking the first moment of the measured line profile.

$$\lambda_{ave}(t) = \frac{1}{N_I(t)} \int_{\lambda_0 - \Delta}^{\lambda_0 + \Delta} \lambda I(\lambda, t) d\lambda$$

where the normalization of a single line of the spectrum at each instant in time is given by

$$N_I(t) = \int_{\lambda_0 - \Delta}^{\lambda_0 + \Delta} I(\lambda, t) d\lambda$$

Here, $I(\lambda, t)$ is the output signal of the spectrometer when viewing the axial line of sight, calibrated for wavelength but with intensity in arbitrary units. The range of the integration, $\pm\Delta$ away from the center wavelength, is just large enough to include all of the line profile, without including any neighboring lines. If we assume a Gaussian line shape for emission from an infinitesimal fluid element we can approximate the spectrum as the integral over the axial coordinate z over the length of the accelerator L

$$I(\lambda, t) = \frac{1}{\sigma\sqrt{\pi}} \int_0^L I(z, t) e^{-(\lambda - \lambda_0(1 - v(z,t)/c))^2/\sigma^2} dz \tag{6.2}$$

where $I(z, t)$ is the intensity of emission at the center wavelength from the fluid element at position z and time t, and σ is the line width. Here $v(z, t)$ denotes the actual fluid velocity of the plasma, which varies in time and position throughout the accelerator. The velocity function of the plasma is not known for all (z, t) but it is strongly constrained by measurements of the average velocity determined by the time of flight between signals of magnetic probes at three axial positions along the acceleration section.

Also, the results of 2-D MHD simulation of the accelerator dynamics of CTIX provide accurate approximations to $v(z,t)$. However, one of the goals of this spectroscopic work is to find an independent measure of $v(z,t)$ that can be compared to other results as a check of accuracy. Using the above expression for $I(\lambda, t)$ we can evaluate $v_{ave}(t)$. After some simplification we find

$$v_{ave}(t) = \frac{1}{N_I(t)} \int_0^L I(z,t)v(z,t)dz \tag{6.3}$$

The emission intensity $I(z,t)$ is of key importance. We have endeavored to measure it as directly as possible with the use of narrow bandpass filtered photomultiplier tube measurements made simultaneously at several positions along the length of the accelerator. These measurements can be analyzed using the Lagrangian interpolation technique, in synthesis with the magnetic field data. Additionally, our understanding of the basic ionization and excitation mechanisms can be used to make a simple predictive model of the accelerated helium ions in our system. Ultimately we would like to compare the average velocity evolution measured via Doppler spectroscopy to the results from the two other independent methods, the PMT-Magnetic composite of $I(z,t)$ the yields $v_{ave}(t)$, and a purely theoretic approach.

In the light of this possible cross-comparison of methods, the geometric complication of the axial integrated data is ultimately a good thing since it means that the Doppler measurements provide some constraints on a model of ion density field $n_i(z,t)$, which up to this point had been uncharted on the CTIX device.

6.4 Ion velocity evolution

Using time gating of the CCD we are able to watch the evolution of the average ion velocity using the measured Doppler shift at each 1 μs time-step.

This analysis shows that He II ion velocity peaks very early at 1.5 μs, with a maximum of $\sim$ 50 km/s and then dwindles to only 10 km/s during most of the acceleration of the compact
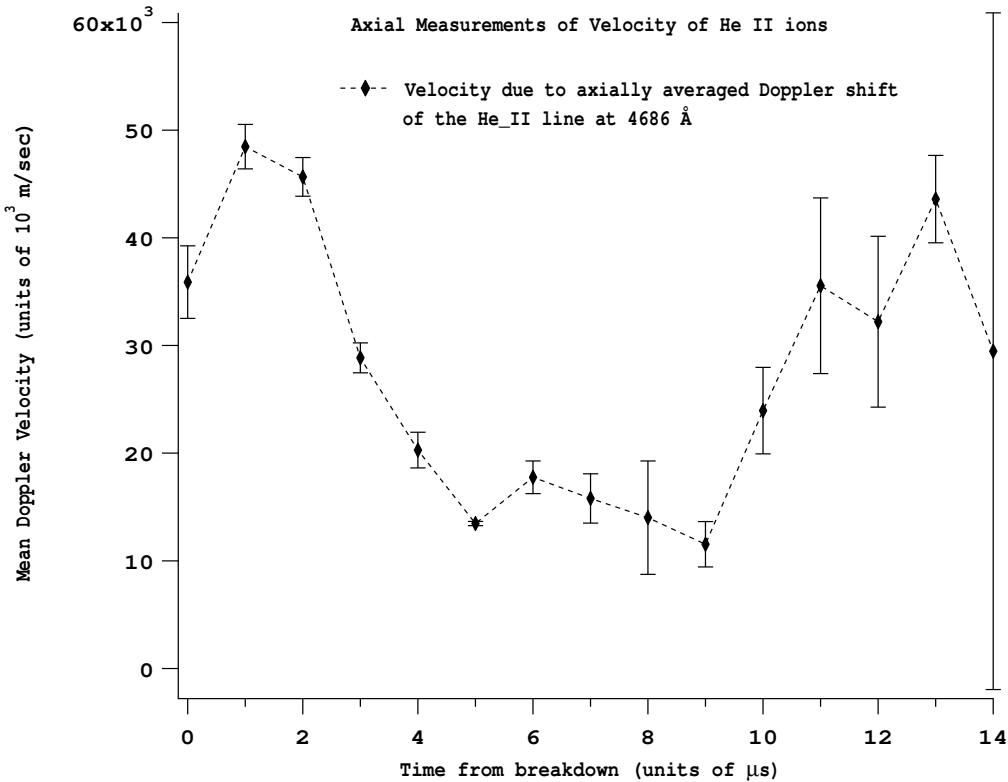
Figure 6.6: Average Doppler velocity as a function of time.

toroid. This unusual result requires some further explanation. Careful examination of the transverse data show that the He II state becomes extinct as it propagates down the accelerator. Very little is observed at the $z = 91$ cm, and absolutely none at all is seen at $z = 142$ cm. A second peak of ~ 72 km/s occurs at 14 μs, which is coincident with the moment that the CT becomes fully detached from the end of the accelerator, at this time a re-strike occurs in the formation section ($0 < z < 20cm$) due to the ringing of the rail-gun circuit. Error bars in figure 6.6 represent the standard deviation of the measured average velocity at each time step. There were 10 data points per time step.

It is clear that the maximum velocity measured by the Doppler spectrometer is much less than the CT velocity of 200 km/s as measured by the magnetic probes. The reason for this

discrepancy is all in equation 6.1. We have come to understand that because the electron temperature is sufficiently hot, the population of He II does not last more than a few microseconds during the discharge before it becomes fully ionized. Also, He II is limited in space to the region close to the formation section, because by the time the He II ions get to the end of the accelerator they have had enough time to turn entirely into α particles (see ionization diagram 6.12 on page 120).

And so the Doppler spectrometer using the axial line of sight to view the plasma will never see He II ions moving at the maximum plasma velocity. It can only observe them early on in the acceleration process, when velocities are small. The helium ions do in fact get up to the high speeds of 200 km/s or higher, we just can't see them once they loose their last electron. This is a very reasonable interpretation of the data, however it is important to carefully compare the timescales involved in the ionization and acceleration processes and make sure the numbers work out. In the next section we investigate several models and compare them to experimental results.

6.5 Fast visible emission measurements

When a charge state is being depleted during the acceleration process, there will be some diminishment of its light emission with increasing axial position. Fast silicon photodiodes with low-noise RF amplifiers were used to make the first preliminary measurements of this effect, by looking at the visible light emissions from the CTIX plasma. The light output of the three accelerator ports, as well as the axial line of sight were monitored in this way.

Optical band-pass filters were used to isolate the light from distinct impurity species and find its evolution as a function of axial position and time. The most general observation we can take away from the photodiode measurements is that across the spectrum, all visible emission was decreasing exponentially with increasing axial position. We believe this is primarily due to thermal electron impact ionization.

I was involved in the task of using the results from the high resolution survey spectrum

to select a set of optical bandpass filters that allowed light from a limited region (10 nm wide) of the plasma spectrum to be measured by amplified silicon photodiodes. A summer student, Michael Rogers[2] constructed three amplified photodiode assemblies with moderate width (10 nm) optical bandpass filters and measured the time evolution of light at the three diagnostic windows along the accelerator section. The visible emission was measured at wavelengths of 465 nm (includes He II, OII, NII), 435 nm (includes OII) and 655nm (includes Hα line). For comparison, the total visible light emission was measured without the use of filters.

Using time-of-flight analysis on these measurements, we could find a difference in the rate of acceleration between the trajectory of peak magnetic field of the CT, and trajectory of the peak light signal, for each spectral filter. We could also compare the kinematic results between the measurements using different filters, in order to determine if some impurities were lagging behind the others. This measurement served as a simple test of the hypothesized centrifuge effect where ions of different mass become separated in space due to a difference in acceleration. And most importantly, the measurement of the decay of ion luminosity as a function of axial position gave us the ability to track the time evolution of atomic processes such as ionization, and accumulation of neutrals due to scrape-off from the wall.

As the CT moves down the accelerator it emits less and less light. Fast photodiode measurements show an exponential decrease of: Total visible light Emission near 465 nm (includes He II, OII, NII) Emission near 435 nm(includes Oxygen II) Emission near 655nm (includes H a line)

These measurements gave some circumstantial evidence that the ionization model I proposed was correct. However, they had the problem that the filters took in light from a variety of different line transitions, and so it was not possible to isolate exactly what the He II line at 468.6 nm was doing.

To improve upon these encouraging results, we purchased a set of custom made optical band-pass filters with very narrow transmission range. These made it possible to isolate the light

---

[2]Undergraduate in Physics at UC Santa Cruz, visiting us as part of the National Undergraduate Fellowship for Plasma Research, Princeton Plasma Physics Lab.
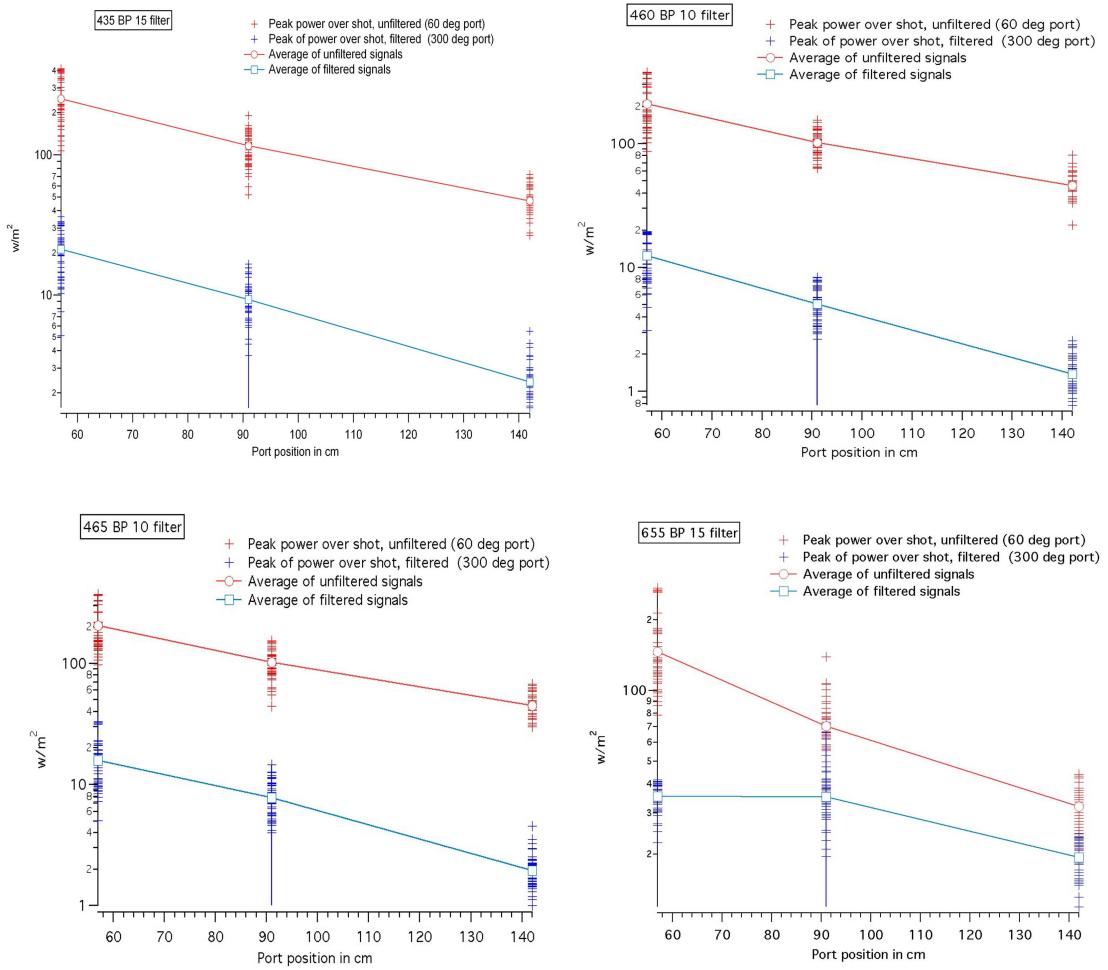
Figure 6.7: Log of peak radiated power of filtered light (blue) and unfiltered light (red) as a function of axial position, for filters centered at 435 nm, 460 nm, 465 nm, 655 nm.

coming from a single line transition. And with the right detectors we were able to record the magnitude of an individual line emission continuously in time.

Once I began working with the narrow filters, I ran into a number of technical complications that we had not encountered with the wide filters. Initially I had simply plugged the narrow filters into the original photodiode housing, but that suffered from the serious problem that light plasma could enter the filter at all angles from 0 degrees to as much as 30 degrees off normal incidence.
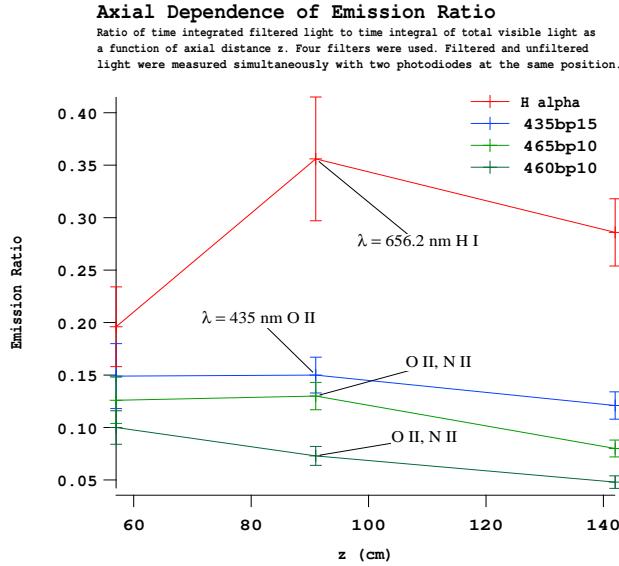
Figure 6.8: Fractional distribution of power between wavelength ranges as a function of axial position, for filters centered at 435 nm, 460 nm, 465 nm, 655 nm.
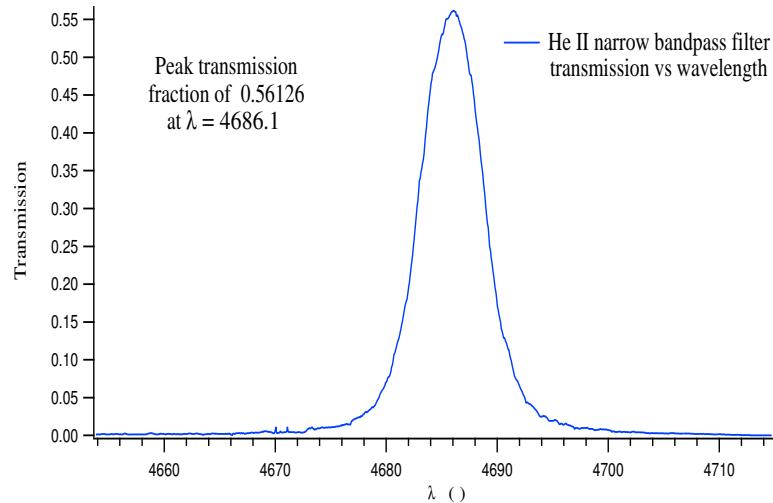
Figure 6.9: Transmission curve of narrow bandpass He II filter.

The critical effect is that the center wavelength of the transmission curve becomes shifted with increasing angle. So non-helium light from neighboring spectral lines could still get through the filter if they enter at some significant angle. To solve this, I first quantified this effect and found

that there is a shift of the center wavelength by approximately 0.1 nm per degree away from normal.
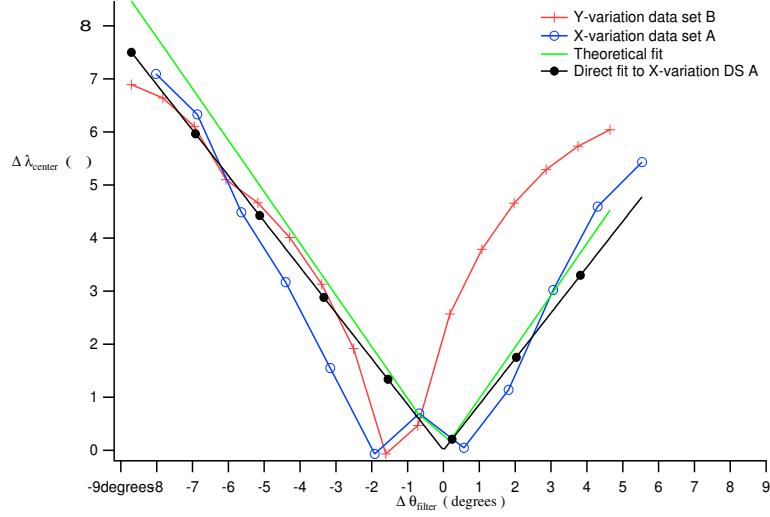
Figure 6.10: Effect of tilt-induced wavelength shift, plotted here in terms of Å per degree.

The shift in the center wavelength of the filter as a function of incidence angle is given by,

$$\Delta\lambda(\theta) = \lambda_\perp \left[\left(1 - \frac{\sin\theta}{m^2} \right)^{-1/2} - 1 \right] \tag{6.4}$$

where $\lambda_\perp$ is the center wavelength of the bandpass region at normal incidence. Using the measured rate of wavelength shift, the filter must have an effective index of refraction of m = 6.88.

Based on the survey spectra there were neighboring oxygen lines about 0.5 nm on either side of the He II line so we would need to limit the angular acceptance to well below 5 degrees. This has been accomplished with the construction of 9 cm diameter collimator tubes that have a pair of adjustable apertures separated by 55 cm, and internal baffles that block internal reflections off of the tube wall.

The narrow bandpass filters are mounted in micrometer adjustable universal-joint swivel mounts that allow precise alignment of the plane of the filter, in order to orient them exactly perpendicular to the axis of the aperture pair. The apertures can be varied in size to optimize the trade-off between angular acceptance and light signal level.

Photomultiplier Collimator Assembly

Micrometer adjustable
universal swivel mount
for filter

Iris variable
aperture

Fixed
aperture

Fixed
aperture

Iris variable
aperture

PMT

Incoming light

Flexible opaque
black fabric enclosure

L = 54.61 cm
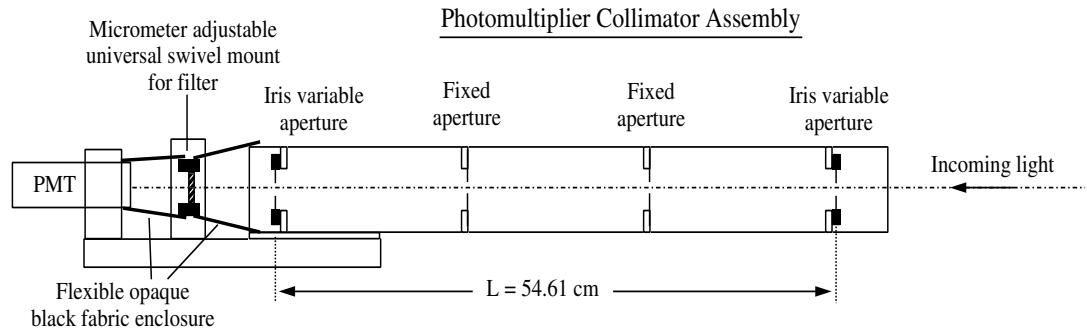
Figure 6.11: Drawing of collimated PMT assembly

Under typical plasma conditions the angular acceptance can be limited to less than half a degree, while still allowing good light signal. However, many orders of magnitude of the plasma light are thrown away when using the combination of the collimator and the narrow bandpass filter. The resulting light signal was far too dim to be detected by the original silicon photodiode and amplifier circuit. A much more appropriate choice of detector is a photomultiplier tube (PMT). They have nanosecond response times and can be sensitive enough to count single photons. We happened to have an old RCA model 8852 PMT and I was able to borrow two more of the same model from the SSPX group (Sustained Spheromak Physics eXperiment) [12].

6.6   Ionization model

At the instant of plasma formation there is already a large cloud of moderately high density neutral helium filling the formation section and diffusing lightly out into the accelerator section. Once a small population of energetic electrons becomes liberated within the static electric field, ionization of the neutral helium proceeds rapidly and the electron and ion densities rise primarily through the process of single electron impact ionization.
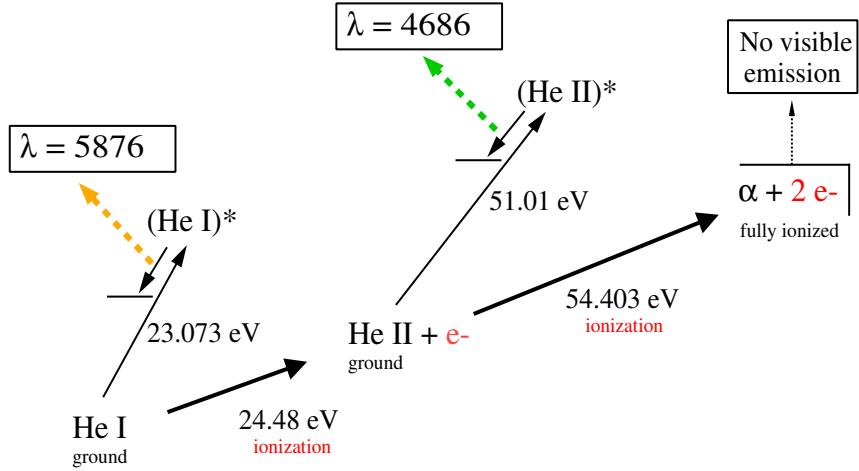
Figure 6.12: Helium ionization and excitation process

Figure 6.12 diagrams the excitation and ionization process that occurs in the CTIX helium plasma. Note that the excitation and ionization energies are comparable. This leads to the general effect that if the plasma electron population is hot enough to cause visible line emission from a species, then it also has enough energy to ionize that species into the next higher charge state.

As discussed in chapter 5, electron probe measurements show an electron temperature of $T_e = 54$ eV within the accelerator. This is high enough to rapidly burn through neutrals and singly charged ions leaving only an α particle plasma that does not emit in the visible.

In this section we will model the evolution of the charge state populations once ionization has begun, given known cross sections. First we will consider the case where the ionization is occurring within a dense cloud of neutral helium, such as in the formation section. Secondly, we examine the case when the neutral (He I) density is zero, but there is a population of He II, which subsequently evolves into a population of fully ionized helium without replenishment from the neutrals. This case should describe what happens at the leading edge of the CT plasma where a population of singly charged ions has been accelerated out of the neutral cloud, and will evolve on its own from then on.

In both of these models we begin with the following assumptions:

- Constant electron temperature → Constant ionization cross sections

- Closed system → No particles enter or leave the system.

- Ignore vessel geometry effects → Zero-dimensional + time

- Ignore recombination, double impact ionization, and photo ionization.

Recombination rates are small ($a \sim 10^{-14} cm^3 s^{-1}$) and so will be ignored on the fast timescales in the formation. In fact, ions will not recombine before the experiment is over ($25\mu s$) because the lifetime of ions (before they recombine) is $1/(a\ n_e) \sim 1$ second. Because of this, the ionization fraction of the plasma is a monotonically increasing function of time.

The rate of double ionization due to electron impact is more than an order of magnitude smaller than for single ionization, and does not have a significant effect on the lifetime of the He II in the CTIX plasma. First, He II can only lose one more electron before it is fully ionized, so double ionization does not affect He II at all once it has formed. Second, the small effect that does exist acts primarily to slightly reduce the maximum value of He II density that is obtained during the evolution by allowing a small fraction of the Helium neutrals to bypass the He II state and go straight to the fully ionized state. This does not significantly affect the lifetime of the He II population, and so double electron impact ionization will be ignored.

There is a wealth of theoretical and experimental data about single impact ionization that we can use. In particular, the most useful results available in the literature are stated in terms of total ionization cross sections. For helium, there is excellent agreement between the theory and experimental data.[53],[54],[55],[56]

To understand the necessary terminology we need to consider the basic physical process that occurs during ionization [57],[56]. Suppose that we have an atom and a swarm of thermal electrons. There will be some finite probability of the event that the atom is hit by an incident electron of energy E_i, _and_ it subsequently becomes ionized and emits an electron with an exit energy of ϵ. The probabililty of this very specific event is determined by the *differential cross section* $\sigma(\epsilon, E_i)$. There
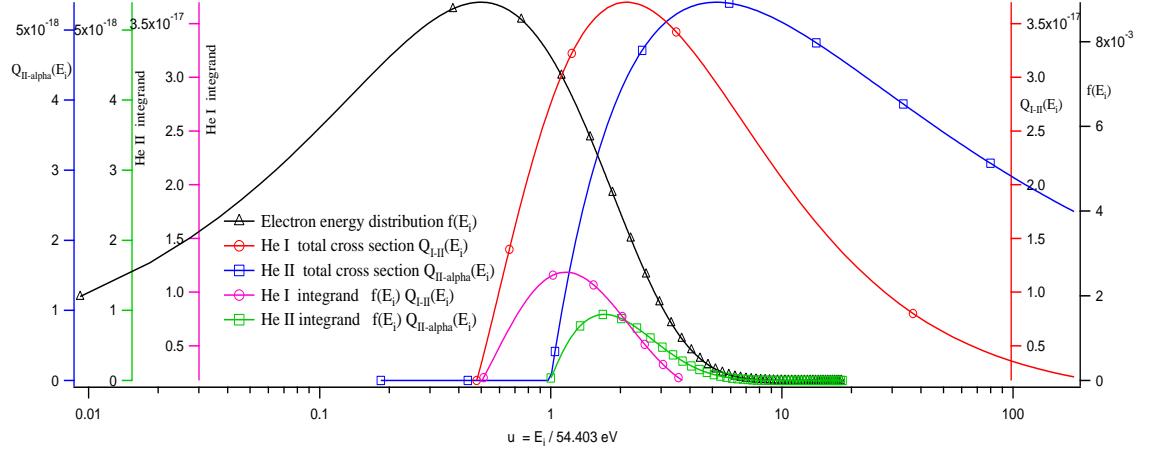
Figure 6.13: Ionization cross sections as a function of electron energy and the energy distribution function for incident electrons in a 54 eV plasma.

is a minimum input energy called the ionization energy I, below which the differential cross section is zero, $\sigma(\epsilon, |E_i < I|) = 0$. The *total cross section* measures the integral of the differential cross section over all possible ejection energies ϵ, that is $\sigma_T(E_i) = \int \sigma(\epsilon, E_i)d\epsilon$. The resulting total cross section depends on the incident electron energy, in a mono-energetic fashion. On the other hand, in a plasma there is a distribution of electron energies, with a spread in their ability to ionize the atoms. Therefore, the total cross section will need to be further integrated against the electron energy distribution function of the plasma in order to find the actual, or effective cross section for the ionization reaction within a plasma of a known temperature.

$$\sigma_{\text{eff}} = \int_0^\infty \sigma_T(u) f_e(u) du \tag{6.5}$$

Here $u = E_i/I$ is used to ensure that the $f_e(u)du$ is dimensionless. The integrands of the effective ionization cross section for He I and He II are shown in figure 6.13, (magenta and green, respectively).

In this way we can numerically evaluate these integrals over $f_e(u)$, to find the the effective cross sections for the ionization of neutral He I $\rightarrow$ He II, and from He II $\rightarrow$ a fully ionized state,

which we will call σ_0 and σ_i respectively. They have the values of:

$$\sigma_0 \;\; = \;\; 2.352 \times 10^{-17} \; cm^2 \tag{6.6}$$

$$\sigma_i \;\; = \;\; 2.029 \times 10^{-18} \; cm^2 \tag{6.7}$$

Now, for the ion evolution equations we need to work with a slightly different quantity called the *ionization rate*, which is dependent on the effective cross section and the electron average thermal velocity, $S = \sigma_{\text{eff}} \cdot v_{\text{th}}$. For our plasma these work out to be:

$$S_0 \;\; = \;\; \sigma_0 v_{\text{th}} \;\; = \;\; 1.254 \times 10^{-8} \; cm^3/s \tag{6.8}$$

$$S_i \;\; = \;\; \sigma_i v_{\text{th}} \;\; = \;\; 1.082 \times 10^{-9} \; cm^3/s \tag{6.9}$$

We see that the ionization rate of the neutral helium is about 10 times higher than the ionization rate of the He II ions. More precisely, this ratio is $K = S_i/S_0 = 0.086$. These are the values we will use through the rest of this discussion.

Formation Region Model In the formation region, where the neutral density is high, the evolution of $n_0(t)$ and $n_i(t)$ are coupled through two first order nonlinear ODE's and an algebraic equation for $n_e(t)$. The density functions can be formulated in terms of the constant $N = n_0(-\infty)$ which is the number density of neutrals before any ionization takes place.

At time $t = 0$ the initial conditions are $n_0(0) = N(1 - \epsilon)$, $n_i(0) = n_e(0) = N\epsilon$ where ϵ is a number much less than one. This model is closed in that no particles enter or leave the volume. However, if we assume that the ionization rates S_0 and S_i (for neutrals and singly charged ions respectively) to be constant in time then some large amount of energy must enter the system to keep the electron temperature constant.

If it is desired, the doubly charged ion density (α-particle density) can be easily accounted for using conservation of nucleons once $n_0(t)$ and $n_i(t)$ are found. The evolution equations are:

$$\frac{dn_0}{dt} = -S_0 n_e n_0 \qquad \frac{dn_i}{dt} = -S_i n_e n_i + S_0 n_e n_0 \qquad n_e(t) = 2N - 2n_0(t) - n_i(t)$$

We can rephrase this system in terms of dimensionless variables

$$\tau = tS_0N = t/t_0 \quad K = S_i/S_0 \quad \alpha(\tau) = n_0(t)/N \quad \beta(\tau) = n_i(t)/N \quad \gamma(\tau) = n_e(t)/N$$

The evolution equations for α, β, γ are

$$\frac{d\alpha}{d\tau} = -\alpha\gamma \qquad \frac{d\beta}{d\tau} = -K\beta\gamma + \alpha\gamma \qquad \gamma = 2 - 2\alpha - \beta$$

These have initial conditions $\alpha(0) = 1 - \epsilon, \ \beta(0) = \gamma(0) = \epsilon \ll 1$

If you solve for γ and then combine the two ODE's you can find the path in (α, β) phase space by solving

$$\frac{d\beta}{d\alpha} = (K\frac{\beta}{\alpha} - 1)$$

Provided that $K \neq 1$ then the curve $\beta(\alpha)$ is given by

$$\beta = \frac{1}{1-K}(\alpha^K - \alpha) \tag{6.10}$$

The evolution of the system can then be fully described in terms of a single variable $\psi = \alpha^{-1}$

$$\frac{d\psi}{d\tau} = -\frac{1}{\alpha^2}\frac{d\alpha}{d\tau} = \frac{\gamma}{\alpha}$$

$$\frac{d\psi}{d\tau} = 2\psi - \frac{1}{1-K}\psi^{1-K} - (2 - \frac{1}{1-K}) \tag{6.11}$$

We do not know if a general closed form solution exists for this equation, and so we have mainly worked with numerical solutions instead. However there is a special case, when K = 1/2, in which equation 6.11 can be transformed into a linear equation and solved exactly.

$$\text{For } K = 1/2, \quad \psi(\tau) = (Ae^\tau + 1)^2 \ \text{ where } A = \sqrt{\frac{1}{1-\epsilon}} - 1$$

This corresponds to a density evolution of

$$n_0(t) \ = \ N(Ae^{S_0Nt} + 1)^{-2} \tag{6.12}$$

$$n_i(t) \ = \ 2NAe^{S_0Nt}(Ae^{S_0Nt} + 1)^{-2} \tag{6.13}$$

This is too far from the case of K = 0.086 to be of any practical use on our actual helium plasmas, but it does serve as a simple test of any implementation of a general numerical solution to the full problem.
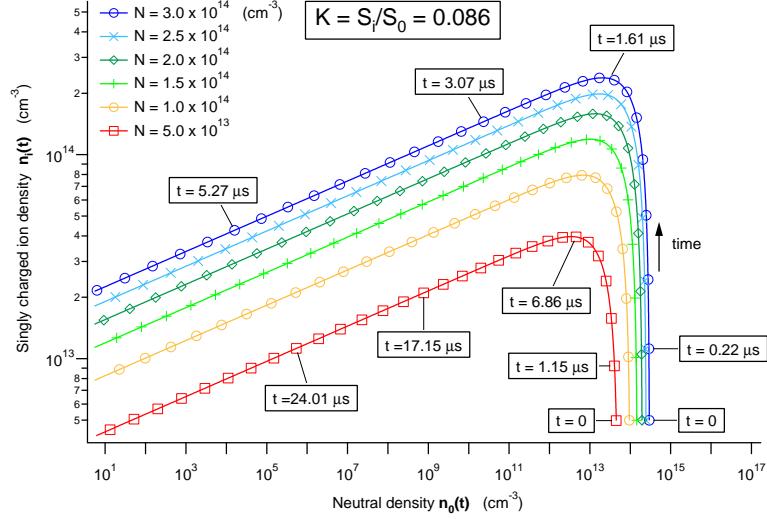
Figure 6.14: Log-Log plot of system evolution in (n_0, n_i) phase space, for K = 0.086, showing the dependence on initial neutral density. The six curves plot the solutions for N = {0.5, 1.0, 1.5, 2.0, 2.5, 3.0 × 10^{14} cm^{-3}}. Notice how the higher density system evolves significantly faster along its trajectory than does the low density system. These curves are a dimensional version of equ. (6.10)
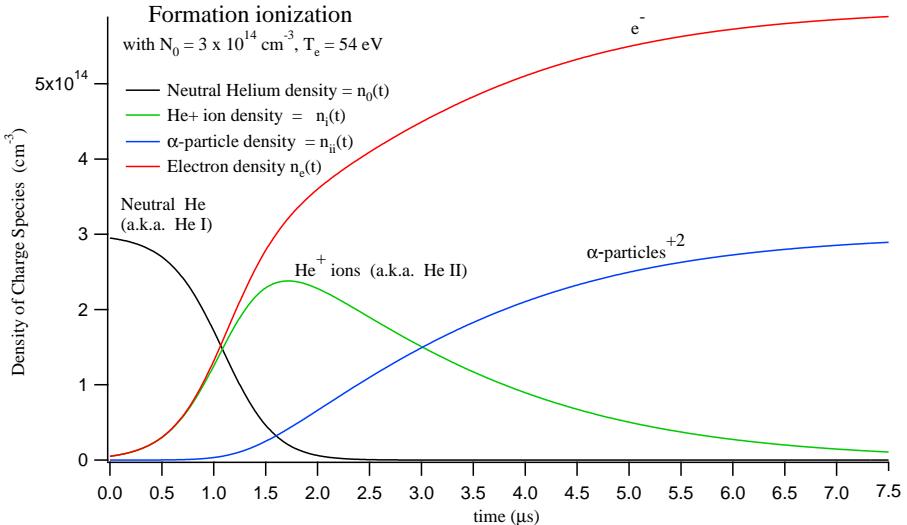
Figure 6.15: Time evolution of the density of charge states in the formation region for initial conditions N = 3.0 × 10^{14} cm^{-3}, and $\epsilon = 0.016$, with an electron temperature of 54 eV.

Accelerator Region Model Because the neutrals are not effected by the electromagnetic fields that accelerate the ions, the slow moving neutrals don't have enough time to make it into the accelerator section during the acceleration of the CT plasma. The absence of neutral helium simplifies the evolution equation for the singly charged ions while they are being accelerated.

We will now consider the evolution of the ion density with respect to a new time variable $t' = t - t_a$ where t_a is the time the fluid element has just entered the acceleration section. The initial condition is $n_i(t' = 0) = N_i$ which is the final ion density $n_i(t_a)$ using the formation region ionization model.

Because some doubly charged ions were created in the formation region, the accelerator initial condition for electron density is $n_e(t' = 0) = N_e = N_i + 2N_{ii}$, again using the formation model to find the doubly charged ion density at the time of entering the accelerator $N_{ii} = n_{ii}(t_a)$. The system evolves according to:

$$\frac{dn_i}{dt'} = -S_i n_e n_i \qquad n_e(t') = N_e + N_i - n_i(t')$$

which can be stated more compactly as

$$\frac{dn_i}{dt'} = -S_i n_i (2(N_i + N_{ii}) - n_i(t'))$$

Restated in terms of a few dimensionless variables,

$$\tau' = t' S_i N_i \qquad R = N_{ii}/N_i \qquad \beta(\tau') = n_i(t')/N_i$$

The evolution equation becomes a logistic equation:

$$\frac{d\beta}{d\tau'} = \beta^2 - 2(1+R)\beta \qquad \beta(0) = 1$$

This can be solved to give an exact solution of the ion density evolution in the accelerator region:

$$n_i(t') = 2N_i(1+R)[(2R+1)e^{2S_i(N_i+N_{ii})t'} + 1]^{-1} \tag{6.14}$$

6.7 Conclusions

We see from the ionization model that extinction time of the He II state is sufficiently rapid to account for the observed fall off of the spectroscopically determined average velocity. The PMT data also confirms that the spatial distribution of the intensity of the He II emission falls off rapidly with increasing axial position. This has been a cross-confirmation of several different physical effects, and as a result we have established several facts about the formation and acceleration process, as well as developed some sophisticated analysis tools that we can use again in future work.

As diagnostic, a Doppler spectrometer has some unique advantages, and certain limitations that are worthwhile to take into account when planning an experiment in this field. One key practical result is that the fast rate of ionization imposes a limitation to the size of the region where Doppler measurements can be made.

It happens that the $\lambda = 4686$ Å line of He II is one of the brighter lines in the plasma. Its brightness is good for visible spectroscopy because it allows short integration times, however the high magnitude of brightness also means that He II very rapidly becomes fully ionized long before the experiment is over, making it impossible to observe the maximum velocity of the CT via Doppler shifted line emission.

Unfortunately this effect also puts some constraints on the usefulness of higher Z impurities for visible spectroscopy with our plasma. For a plasma with a moderate electron temperature, there will be a highest charge state that can be obtained from electron impact ionization. For example, consider Ar V (Z=4) which is the most strongly charged argon ion that can be created in a $T_e = 100$ eV plasma. If recombination is negligible, then the Ar V will persist until the plasma discharge is complete. This terminal state has bound electrons, unlike fully ionized helium, and so can be made to emit visible light.

The difficulty is that because the excitation and ionization energies are comparable, Ar V only emits very dimly in the visible. If there is not enough energy to ionize, then there is not enough

energy to excite. Attempts were made to measure visible line emission of argon ions on the CTIX plasma with no real success so far. The best results were with helium, and in spite of its limitations, the data was very revealing about the basic plasma physics.

6.8 Future work

Plans are underway to improve these Doppler measurements with a new spectrometer [14], and allowing better optical access using periscopic mirrors placed within the ports on the accelerator section. The goal is to observe the red shifted light only from the plasma that has passed the port and is accelerating away from it.

We would also like to complete a Lagrangian interpolation of the PMT signals, which would allow us to compute v_{ave} using (6.3) directly. This could then be directly compared to the Doppler measurements. A similar comparison can be made with the results of the ion evolution model. The result of these comparisons will be included in a subsequent paper.

Chapter 7

Determination of

plasma Reynolds number,

hydrodynamic and magnetic

When it comes to the issue of turbulence in a plasma, there are two dimensionless quantities that most succinctly characterize the magnetofluid's behavior. These are the hydrodynamic and magnetic Reynolds numbers, defined below.

7.0.1 Definitions

Hydrodynamic Reynolds's number is defined as

$$\mathrm{Re} = \frac{L\mathrm{v}}{\nu} = \frac{\text{Inertial force}}{\text{Viscous force}},\tag{7.1}$$

where L is the length scale of the system under consideration, v is the fluid's average velocity, and ν is the fluid's kinematic viscosity. It can be interpreted as the ratio of the inertial forces exchanged between adjacent fluid elements over the viscous drag force on the fluid elements that ultimately

results in the irreversible conversion of mechanical energy to heat energy.

The dependence on length scale means that with every thing else held constant, large systems such as oceans, atmospheres, and astronomical plasmas will have a large Reynolds number, while any system examined on a microscale can be characterized by a very small Re.

Fluid velocity increases the value of Re, and it is through this velocity dependence that most of the effects of turbulence make their entrance. On CTIX we have relatively accurate measurements of average plasma velocity, which is large compared to most other laboratory plasmas. This is the primary reason why we have pursued work with turbulence on our accelerator.

Viscosity in a plasma is a more complex quantity than it is in a classical fluid, and we will make our estimates for its value based only on a relatively simple collisional model and standard formula [29], [58].

There is a related quantity called the magnetic Reynolds's number, defined as

$$R_m = \frac{\mu_0 L \mathrm{v}}{\eta} = \frac{\text{Flow velocity}}{\text{magnetic diffusion velocity}}, \tag{7.2}$$

where μ_0 is the magnetic permeability of free space, and η is the electrical resistivity of the plasma. Here, the viscosity has been replaced by η/μ_0 which also defines a rate of energy dissipation from the system (consider the evolution equation for the magnetic field from resistive MHD, equ (D.4)).

We can measure η with some confidence on our system, as described in chapter 3. We will use these measured values to estimate the magnetic Reynolds numbers that are attainable on CTIX.

In part, R_m determines the degree to which the magnetic field is effectively frozen into the fluid. Large values of R_m mean that resistivity small, and so the rate resistive diffusion of the magnetic field relative to the fluid will also be small.

In this way the magnetic Reynolds number is often used to model the rate of magnetic reconnection. For example in the Sweet-Parker model of reconnection, the reconnection velocity (the speed at which magnetofluid flows toward the reconnection layer) is related to the Alfven

velocity (magnetic wave speed) according to

$$\mathrm{v}_R = \mathrm{v}_A \cdot (R_m)^{-1/2}$$

However, we find that this is at odds with observation because the typically large values of R_m result in reconnection velocities many orders of magnitude slower than what is actually seen in real plasmas.

Reconnection effects are also important in MHD turbulence, because turbulent magnetic fields can be littered with reconnection layers that range in size from the microscale on up to the device length scale.

The notion of Reynolds numbers can also be useful for bridging gaps between seemingly different physical systems. If they have the same Re and R_m, they will have geometrically similar flow behavior that can be scaled to match each other under a suitable transformation of length and time units.

7.0.2 Onset of turbulence

Flows that have high Reynolds numbers typically exhibit turbulent behavior, while low values are indicative of simple laminar flows [59], [60], [61]. Fundamentally, turbulence is composed of large amplitude oscillatory fluctuations that occur over a broad spectrum of length and frequency scales, with certain statistical properties [62], [63], [64], [65]. The fact that these oscillations away from equilibrium occur when the Reynolds numbers are large, is essentially just a restatement of the fact that when the rate of energy dissipation is small, free energy in the velocity field (or magnetic field) can be converted into wave energy faster than the waves are being damped out. This results in growth of wave amplitude, and nonlinear interaction of the waves with each other.

In a way, it almost more reasonable to think of turbulence as being the more "natural" state, and smooth, laminar flow only occur when the addition of some energy dissipation mechanism is large enough to damp out any waves before they can grow into turbulence. And of course when

the energy dissipation is high (via a large resistivity or viscosity), we have correspondingly small values for the Reynolds numbers.[1]

Some insight can be gained from considering an analogy with a damped harmonic oscillator, which bears some resemblance to the motion of a fluid element within a turbulent flow [66]. Consider a one dimensional motion in the x-direction, of an object with mass m, acted on by a linear restoring force $-kx$ and a viscous damping force that depends on velocity $-c\dot{x}$. The equation of motion is

$$m\ddot{x} + c\dot{x} + kx = 0$$

and this has two basic modes of behavior (underdamped and overdamped) that can be characterized by a dimensionless constant called the damping number, similar to the Reynolds number, as well as a transitional mode (critcally damped). The damping number is given by $D = 4mk/c^2$, the different modes of behavior are determined by its value.

$$D < 1 \quad \rightarrow \quad \text{Overdamped case} \quad \rightarrow \quad \text{analogous to laminar flow, } Re < Re_{crit}$$

$$D = 1 \quad \rightarrow \quad \text{Critically damped case} \quad \rightarrow \quad \text{analogous to transition to turbulence, } Re = Re_{crit}$$

$$D > 1 \quad \rightarrow \quad \text{Underdamped case} \quad \rightarrow \quad \text{analogous to turbulent flow, } Re > Re_{crit}$$

Here Re_{crit} is the critical Reynolds number for the system, which divides turbulent behavior from laminar. The exact value of this point of transition is still subject to much uncertainty, both experimentally and theoretically, even for classical fluids obeying Navier-Stokes.

---

[1]This is reminiscent of the comparison between Newton's first law, and the Platonic concept that the natural state of all objects is a state of rest, v = 0. Newton's proposal that objects naturally maintain a constant velocity unless acted on by an external force seems downright counterintuitive to many people, who like Plato see every object in their world come "naturally" to rest when they stop pushing it along the ground. Of course, it is the much taken-for-granted force of friction that is ultimately responsible for de-accelerating any object toward a state of rest, which Plato was ignorant of. In analogy with this, there is some sense in thinking of laminar flow as being imposed upon a fluid by the addition of a dissipative force.

7.0.3   Range of accessible values

Here are the estimated values of Reynolds numbers, based on the full range of plausible parameters on our system.

$$100 < \text{ Fluid Reynolds number Re } = \; L\text{v}_{CT}/\nu \; < \; 2 \times 10^4$$

$$10 < \text{ Magnetic Reynolds number } R_m \; = \; \mu_0 L\text{v}_{CT}/\eta \; < \; 10^4$$

The lower end of these estimates corresponds to the coldest, slowest, and most dense possible plasmas we could create (10 eV, 1 cm/μs, 10^{15} cm^{-3}), while the high end represents the hottest, fastest, and most diffuse plasma we have seen (80 eV, 30 cm/μs, 10^{13} cm^{-3}). Typically, we have plasmas that fall closer to the high end of this range. Further work needs to be done to quantify the statistics of how the plasma shots are distributed within this range.

Chapter 8

Gas puff imaging technique

Gas puff imaging (GPI) is a relatively new plasma diagnostic technique that makes it possible to photograph fully ionized plasmas using very short exposure times (1 microsecond or less). The idea is to make the plasma pass through a cloud of neutral gas, thereby causing the plasma electrons to collisionally excite the neutral atoms, which then emit enough light to be imaged by high-speed high-sensitivity cameras. [67],[68]

As we discussed in chapter 6, by the end of the accelerator, the CT plasma is composed of fully ionized hydrogen (or helium) and emits visible light very dimly due to trace amounts of higher Z, partially ionized impurities. We have implemented neutral helium gas puff imaging systems, located on the transverse viewing chamber, as well as the z = 91 cm port of CTIX. The neutral gas is injected about a millisecond before the formation of the hydrogen CT plasma.

A target chamber with large windows (0.5 m by 0.2 m) was constructed that allows transverse imaging of a large volume of plasma. The gas puffing in the target region greatly enhances plasma brightness, and spatial variation of image brightness can be used to infer the spatial fluctuations of the plasma electron flux density [69]. These fluctuations have been observed with fast intensified and non-intensified cameras, with and without the use of narrow bandpass optical filters. In combination with existing diagnostics, wave phenomena and turbulent flow states have been

observed in a variety of experimental configurations.

8.1   Practical considerations

The primary piece of hardware in the gas puff system is a fast opening gas valve. We used electromechanical valves created for a previous experiment, but modified for this work to have an increased gas output. The valve is composed of an aluminum disk (poppet) that is pressed against a vacuum o-ring seal by a spring and the inlet gas pressure. The opening of the valve is achieved by driving the poppet away from the vacuum seal using a large inductive repulsion force created by rapidly switching a large current through a coil near the poppet. Because the electromagnetic force of repulsion between the coil and the poppet can be very large, the poppet-vacuum seal can be very rapidly opened (10 μs), allowing a uniform pulse of gas to flow from the input gas line, around the poppet and into the vacuum chamber.

Once open, however, the gas valve is slow to fully close because it is only using the mechanical force provide by the holding spring. Typically, the valve may stay open for several milliseconds, before gas flow completely halts. This means that gas will be flowing out of the gas puff nozzle for the entire duration of the CTIX discharge.

The gas value pulser circuit is shown in figure 8.1. It uses a silicon controlled rectifier (SCR) to hold off the high voltage of the capacitor bank (typically 700 VDC to 1200 VDC) before the pulse. The SCR is able to rapidly switch on the current to the coil (several kiloAmps) without burning out. A small bias pulse of about 10 V is applied to the gate to change the state of the SCR from OFF to ON. Once current starts flowing, the SCR effectively latches in the ON state until the voltage drops below some threshold value, reached after the capacitor bank has mostly discharged through the valve coil. Typically the current pulse to the coil has a duration of about 200 μs. This is not a problem for our system because the gas valve can't close faster than a few milliseconds anyway.
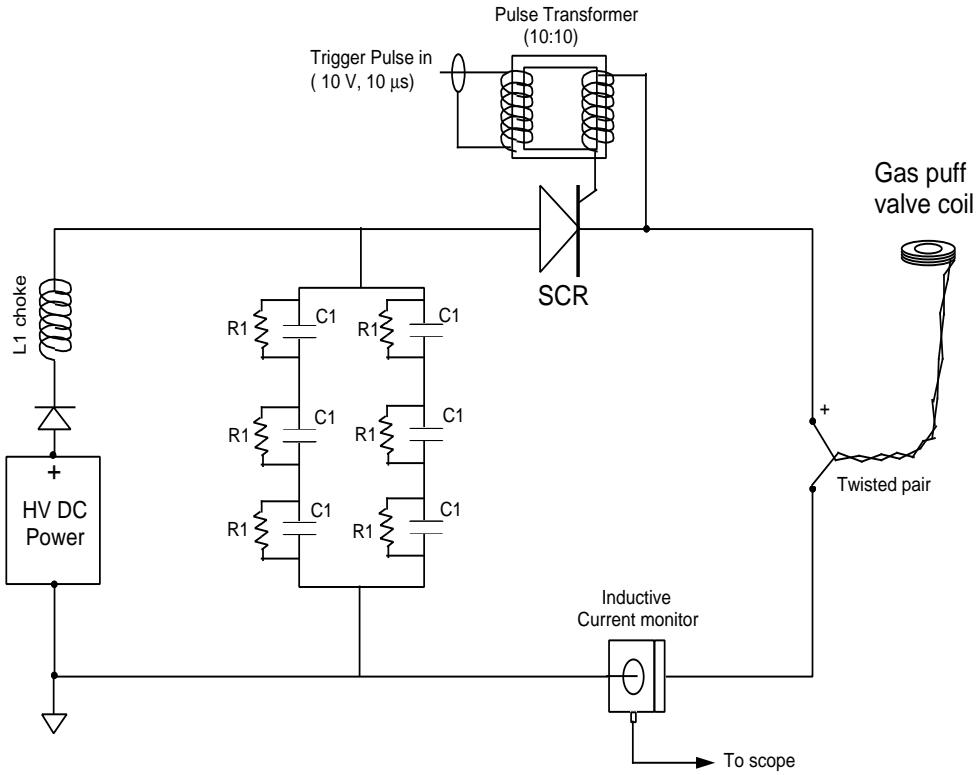
Figure 8.1: Circuit schematic for silicon controlled rectifier(SCR) switched gas valve pulser. The capacitor bank is composed of two parallel sets of three sequential capacitors (6 total), each having a capacitance of C1 = 470 μF, with a maximum voltage of 450 V. The bank as a whole has a capacitance of 313 μF and can be charged up to a maximum of 1350 V. For safety, R1 = 200 $k\Omega$ resistors are put across each capacitor to bleed off any stored charge when external power is not applied. We used an SCR model T960300903DE 9038PY.

The SCR is a nice device to work with, it is reliable, has high tolerances, and is solid-state so there are no direct environmental safety hazards, such as exist with mercury ignitrons, the main alternative switching element for comparable applications.

Because of the large dV/dt that occurs when the SCR turns on, we found that it was necessary to add a high voltage diode and iron core choke inductor to protect the external high voltage power supply from being damaged from high voltage pulses propagating backwards from the capacitor bank into the power supply. We lost several of the more lightweight power supplies

this way, at first not knowing why. This reverse voltage blocking is an important feature that I recommend to anyone trying to build a pulser of this type.

Further complications occur with the z= 91 cm gas valve. The difficulty is that the valve is directly attached to the outer electrode of the accelerator circuit, and so it becomes charged to a high potential before and during a shot. The solution to this requires us to send the driving pulse through an insulated isolation transformer. This allows the pulser circuit to be grounded, yet still inductively drive the current pulse in the valve coil which rests at high voltage.

Another important practical consideration comes about because the CTIX accelerator is passively switched. While this is not a problem for diagnostics that occur after the plasma discharge has begun (which can be triggered off of the rising edge of the formation current), it poses some difficulty to creating a trigger signal that comes a reproducible amount of time before the randomly initiated plasma breakdown event. This kind of pre-breakdown trigger is needed for the gas valve pulser circuit. In practice, we solve this problem by making a guess of how long the plasma breakdown will hold off after firing the formation gas valve, and then we set a long delay for the pulser relative to the early pre-defined timing triggers. This hopefully results in a properly timed trigger pulse to the helium gas puff valve. However, if the plasma breakdown happens significantly faster than your guess, then the gas puff could go off after the shot. Likewise, a very late breakdown would result in a gas puff that came far too early, and may result in a neutral density that is too low to make a good image. We found that the near optimal gas puff conditions occur if we can manage to fire the gas puff about .5 ms to 1 ms before the plasma breakdown event. Once the machine has warmed up the jitter in the breakdown timing does calm down to about $\pm 200 \mu s$, which allows a reasonable attainment of the desired gas puff conditions.

Overall, with some skill and patience, this scattter-shot approach does eventually pay off. The high repetition rate of CTIX also helps.

Pressure rise measurements were made using an ion vacuum gauge to estimate the gas output as a function of applied voltage. Using the total volume of the vacuum vessel it is possible

to estimate the neutral density, given a measured pressure rise as shown in figure 8.2.
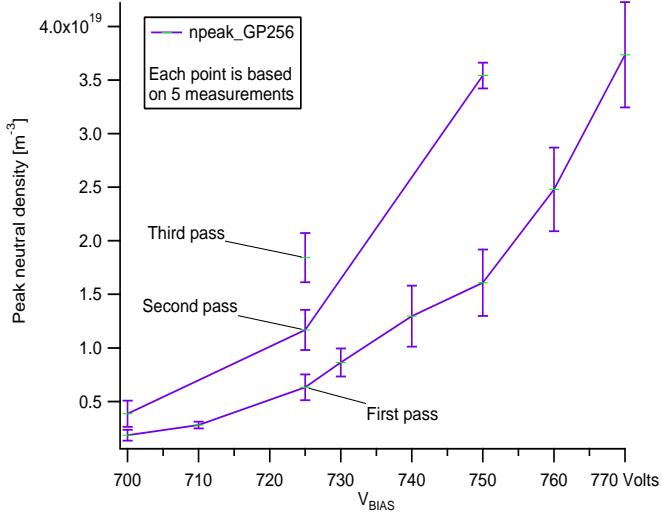
Figure 8.2: Peak gas puff neutral density in viewing chamber as a function of gas puff pulser voltage V_{BIAS} for a sequence of test shots.

We found that good GPI performance occured near $V_{BIAS} = 750V$, which according to this estimate resulted in between 1.5×10^{13} cm^{-3} and 3.5×10^{13} cm^{-3}, about a factor of 3 to 10 below peak plasma density. (For figure 8.2 note that 10^{13} $cm^{-3} = 10^{19}$ m^{-3}). In this dataset there is a noticeable amount of drift in total output from the gas valve. The data was taken in three scans of the the bias voltage, the second and third being only partial scans. We see that as time goes by the valve appears to open more, and lets in more gas. It would be worth making and improved series of measurements of this type to see how large this drift is, and to determine the limits of precision that are possible for a calibration of gas valve output.

A final practical matter, when imaging the plasma-gas puff interaction it can become difficult to distinquish the direct image of the luminous plasma, from its reflection off the stainless steel wall. To minimize these reflections, we added a second window on back side of the viewing chamber with black curtain located back about 10 cm from the window, collectively to act as an optical dump for plasma light. Reflections still occur off of the glass surface, but their intensity is lessened.

8.2   Implementations on CTIX
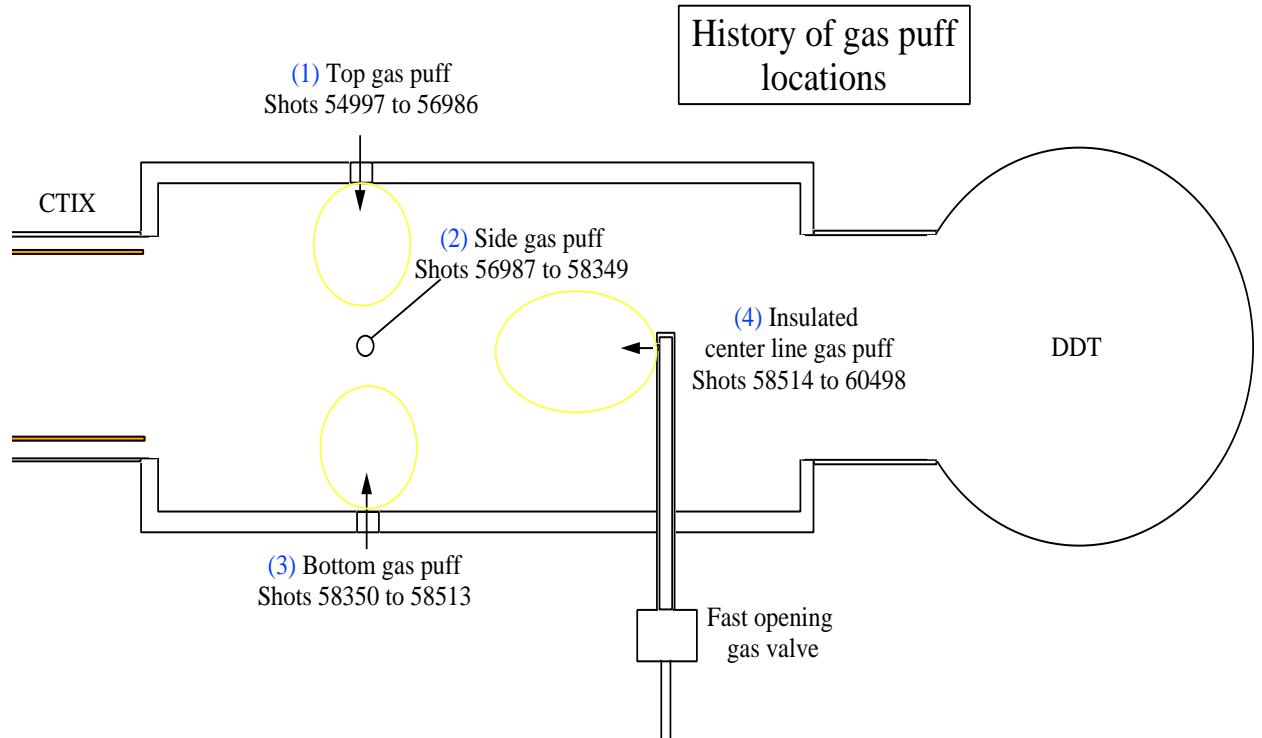
Figure 8.3: History of gas puff locations, summarized.

The gas puff valve was installed on a total of five different locations on the machine during these experimental runs. Four of these locations were on the drift section transverse viewing chamber, while a second gas valve was located at a fifth position on the $z = 91$ cm port on the accelerator section.

Early testing was done on with the valve mounted on a port on the top plate. During these runs we tested the performance of different cameras, as well as searched the parameter space to find an operating region for the gas puff. Too much gas injected at the wrong time typically resulted in an internal arc from the accelerator section to the pseudo-ground of the viewing chamber. This could occur in roughly two ways. There was a soft-fail mode, where the CT was formed and accelerated,

and the arc was triggered by the leading edge of the CT. All systems would still work, the problem was only that any interesting plasma-dynamic effects in the CT were complete obscured by a high luminosity arc. And then there was a hard-fail mode, where plasma breakdown occurs near the end of the accelerator section long before any CT can be formed. These arcs are worse because they have all the energy of the fully charged capacitor bank behind them when they go. These bad arcs almost always caused the data acquisition system to crash.

After some trial and error we found a reasonable slice of parameter space which provided enough luminosity for the GPI to work, yet did not result in bad arcs. However, it was effectively impossible to completely eliminate the soft-arcs when running the gas puff at the $z = 232$ cm position on the top plate. Part of the reason for this was the close proximity to the end of the high voltage accelerator section. The other problem was that by having the gas nozzle be the port hole in a conducting material, we set up conditions that made it possible for large currents to flow through the plasma-ionized gas puff between two conducting surfaces at a relative high voltage between them.

The gas valve was moved to a side port to allow the window to positioned on the top port for viewing the interaction of the CT with the magnetic field of DDT from above. This was compared to the standard side-view arrangement where we viewed a long a line of sight that was tangent to the DDT field, resulting in an image of the structure in the plane perpendicular to the DDT field. Overall, we found that we we able to observe more structure with the side view arrangement, while the plasma only had a near uniform absence of structure when viewed from above, imaging the plasma in a plane parallel to the DDT field.

When we returned to side viewing, we positioned the gas puff valve on the bottom plate to allow more diagnostic access on the top plate. We found similar soft-arcing problems in the side and bottom positions, as we did with the gas valve on the top plate.

Next we moved the original gas puff valve to the $z = 91$ cm port, to begin work with snow-plow type build up of plasma density. Later we used this as a way to do GPI work with co-moving luminous ions, that were ultimately useful for detecting turbulent flow structures.

Then we re-implemented the drift section gas puff with a second gas valve of the same type, but this time we tried to solve the soft-arc problems by positioning the gas puff source further away from the accelerator section, and by injecting the gas into the chamber using a long Pyrex (glass) tube with a small hole at near the tip (1/8 inch diam.) The insulating glass tube breaks the circuit between the ionized, high potential gas puff, and ground. The gas inside of the tube remains neutral, and therefore also works as an insulator. We found that these measures did in fact solve the arc problem. However, with a new valve, in a new location, with a different sized nozzle, we needed to conduct a second scan of parameter space to find the optimal running conditions for the gas puff imaging. We were able to use this final arrangement to observe what appeared to be coherent plane wave structures in the plasma, as discussed further in chapter 9.

8.3 Cameras

High quality image data has been made possible using a high-sensitivity non-intensified CCD camera that provided fast exposures and high resolution. The model we have used is the High Speed SensiCam by made by Cooke Corp. It has 1280 by 1024 pixels (6.7 μm by 6.7 μm per pixel), with a monochrome response of the CCD from $\lambda = 280$ nm to 1000 nm, although this is limited to above about ~ 350 nm due to the glass optics. It has a 12-bit dynamic range, and a maximum quantum efficiency of greater than 50%. We found that the image quality was generaly superior to microchanel plate image insensified cameras, under identical imaging conditions, primarily because it didn't have the intensifier plate getting in the way of the optics.

The SensiCam is able to gate down to 100 ns exposure time, although we usually had a better image quality at or above 500 ns, due to the finite luminosity of the plasma. It also had an adjustable delay for the start of the exposure period, however, we found that the true delay was always about 1.6 μs longer than what was programed. This extra delay was caused by some kind of overhead in the communication with the PC that was used to control the camera. The effect it had

for our experiment was that the very earliest times after the breakdown were inaccessible to being recorded. If the programmatic delay was set to zero, the plasma breakdown trigger signal would tell the camera to acquire at t = 0, but the SensiCam wouldn't actually begin its exposure until t = 1.6 μs. Once this was known we could account for the offset for most of the applications, where we would want to observe the plasma structure at a delay of 10 to 40 μs into the shot.

We also took some data with two microchannel plate intensified cameras, however it we are focusing on the SensiCam data in this thesis because of its higher quality.

The original plan was to use the Imacon framing camera (used in chapter 4) to track the evolution of plasma structures during these experiments. A sequence of malfunctions occurred with its internal power and triggering circuits, some of which we we able to repair, but others we were not able to fully diagnose. The primary imaging/framing tube itself seems to work fine, and so it is worth having it repaired. For this study, we only had time to take data with the working cameras.

8.4   PMT and LMP measurements

Two diagnostics are particularly helpful during an experimental run as basic indicators of the existence of the gas puff, and to use for deciding what the delay timing should be for the cameras. These are the collimated photomultiplier tube assemblies (PMT) and the Langmuir plasma probe (LMP).
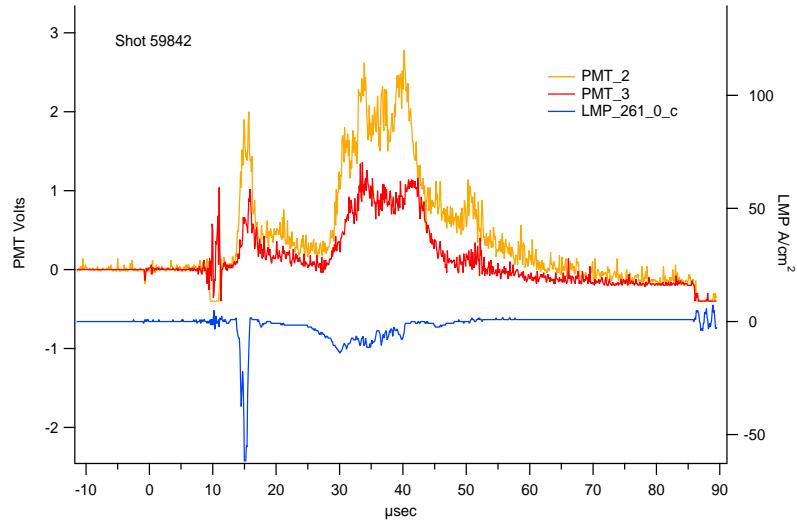
Figure 8.4: PMT luminosity and LMP (electron current) density measurements as function of time.

The top traces in figure 8.4 show the light emission measured along two different chords in the transverse viewing chamber (Left y-axis has units of volts, no calibration factors are applied). Photomultiplier tubes (PMT's) used with a pair of adjustable apertures in order to limit the input light to a narrow chord located near the $z = 250$ cm position, near the center of the flow. We see that light emission as a function of time correlates well with electron density as measured with Langmuir probes (LMP) at floating potential, drawing electron current. The first large peak in both graphs corresponds to the passage of the CT plasma through the drift section, while the second broader peak is the trailing plasma. In the future, we may calibrate these density and plasma luminosity measurements, as well as quantify their ratio, so that density may be inferred from non-perturbing visible luminosity measurements.

Chapter 9

Wire target experiments

9.1 Target design

The final set of experiments conducted on CTIX was motivated by an analogy with grid turbulence of a classical fluid in a wind tunnel. The idea is that we create a localized obstruction to the flow, that has a known k-value, and we watch the plasma's reaction to this perturbation as it
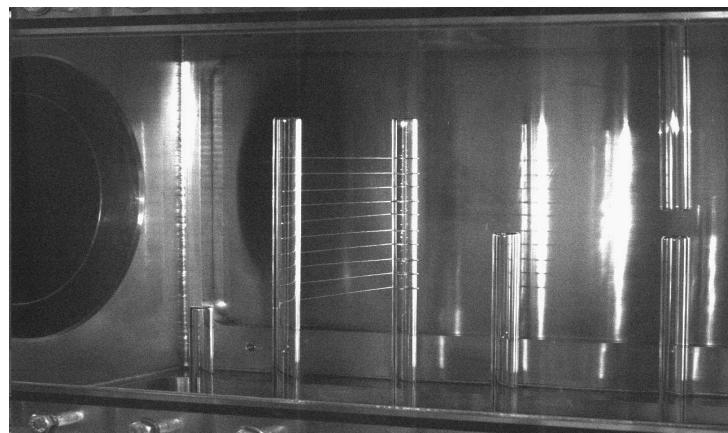
Figure 9.1: Photograph of wire target

flows downstream. The large-window transverse viewing chamber was designed with this experiment in mind.

We constructed a rotatable wire array composed of 1 mm diameter stainless steel wire mounted to an insulating Pyrex support tube. The wire array was designed to be rotated relative to the plasma flow, this was implemented without the need for a complete vessel opening by (very carefully) releasing most of the clamping pressure on the o-ring vacuum seal, and then rotating the end of the support tube with one hand while steadily increasing the o-ring clamping pressure again with the other hand. The target can be rotated between the angles of $-56°$ and $230°$, relative to the positive z axis (see figure 9.3). The support tube is hollow and allows a magnetic probe to be inserted along its entire depth.

A second Pyrex tube was positioned at the tips of the wires, in order to provide a symmetric configuration and also to allow magnetic measurements at a second location in the target region.
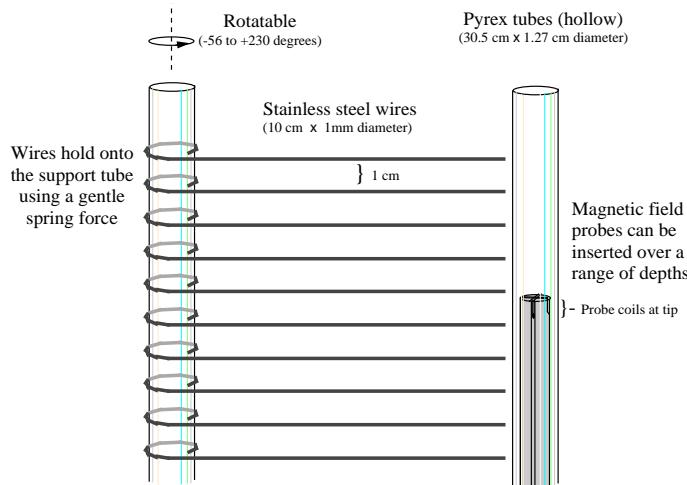
Figure 9.2: Drawing of wire target detail

The intended effect of wire array is to break up the plasma flow and its internal magnetic field. Each wire has a creates a low density wake in the flow, with a possible shock-like interface with the higher density flow in between the wires [70]. This effect on density can be seen in figure
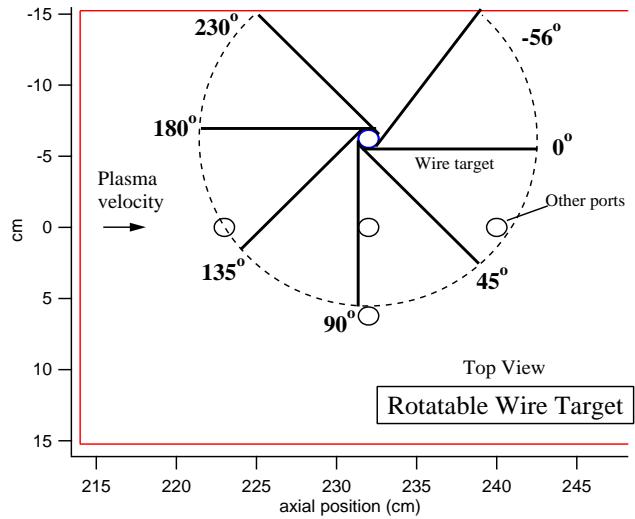
Figure 9.3: Angular positions of wire target

9.4. These images were taken with the target rotated into the $-56°$ position such that the tips of the wires are in contact with the surface of the back window.
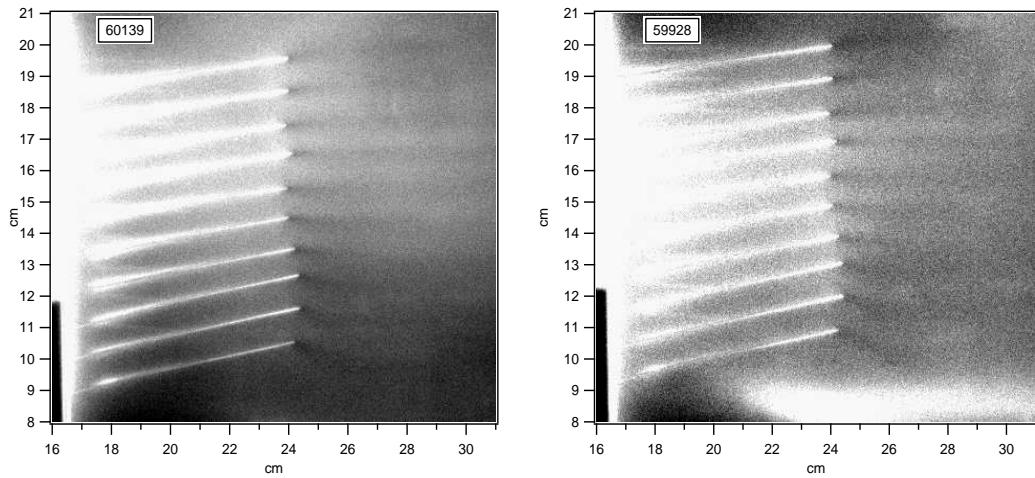
Figure 9.4: Images showing shadow effect of wire target on shots 59928 and 60139

There appears to be a boundary layer of plasma that is significantly brighter than the central flow. The conclusion that the region of luminous plasma is clinging to the back surface is

inferred from the very localized edge between the low density wake and the higher density background. The location of the wake edge corresponds to the near the tip of the wires, which is against the back wall. Because the wires are projected on the image plane of the camera at a non-horizontal angle, we can be sure that the luminous region does not extend throughout the volume because this would not result such a sharp wake only near the wire tips, instead it would have a more diffuse pattern of light and dark spread out in the vertical direction.

The wires also affect the magnetic field of the plasma. Field lines that lie parallel to the wires should be able to slip through unaffected, while transverse field components should get snagged by the conducting wires. The field lines will become stretched by the flow, and will ultimately reconnect with themselves resulting in a cluster of 1 cm scale magnetic islands that flow downstream.

Magnetic measurements have been made in the regions before and after the target along the central axis, and elsewhere in the viewing chamber. However the analysis is not sufficiently complete to determine the properties of these magnetic fluctuations caused by interaction with the target. It is a matter of further analysis of existing data to determine how these fluctuations grow or decay in the flow after the target interaction.

In addition to any controllable, intended effects during the interaction of the plasma with the wire target, there are always unintended effects which we have to understand in order to account for them while interpreting the data, or to try to minimize their role in future experiments.

One important effect is the hydrodynamic effect of the glass support tubes. While this was not intended, it was unavoidable given the constraints on the target design. Based on the later work with imaging the co-moving ions from the accelerator gas puff, it seems like the dominant fluctuations may be due to vortex shedding at the tips of the support tubes, and may not be due to wire array. This is the unconfirmed suspicion at the present.

Another unintended effect was the accumulation of a layer of residual gas on the surface of the target, most likely on the glass tubes. This layer of residual gas affected the imaging work by out-gassing during the shot, resulting in a bright luminous region being always present near the

target, as seen in figure 9.5.

This effect is mostly due to implantation of hydrogen from the CT plasma. It only took about 100 shots for the effect to become noticeable, and it leveled off at a maximum after about 1000 shots. The glow from the residual gas tends to be brighter on the side directly hit by the oncoming CT, and less bright on the downstream side.
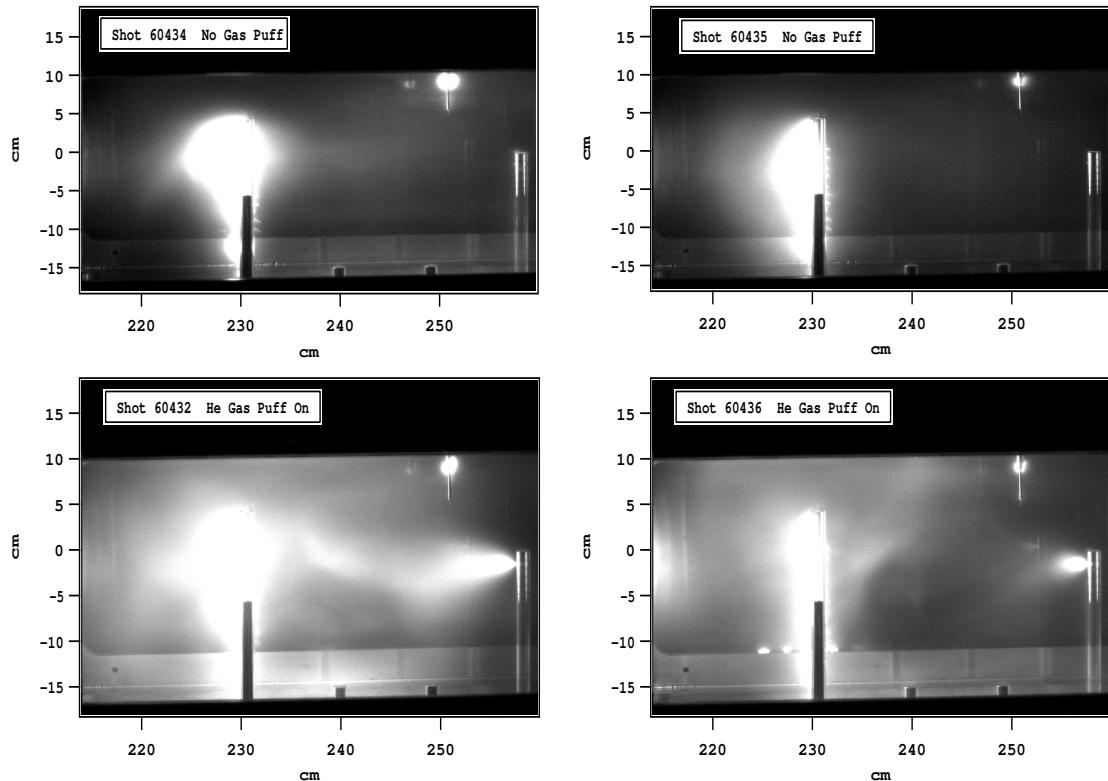
Figure 9.5: Images showing residual gas on target

After being removed from the vessel during our move to the new facility, we noticed that the glass support tubes had a very observable brownish discoloration due to atoms of something being implanted into its surface. On the areas of the tube that were covered by the wire loop wrapping around it, there was significantly less discoloration than the exposed areas.

To determine the composition of the residual gas (which is ejected off during a shot), we

performed a little experiment where we fired a few shots with the helium gas puff, then a few shots with the gas puff, and then a few more with the gas puff back on. We observed the visible emissions for all of these shots with the SensiCam camera, and the low resolution survey spectrometer. The images from this data set are shown in figure 9.5, the top two images were taken with no gas puff and the only light is clearly from the residual gas on the target. The bottom two images were taken with the helium gas puff on, immediately before and after the shots with no gas puff.
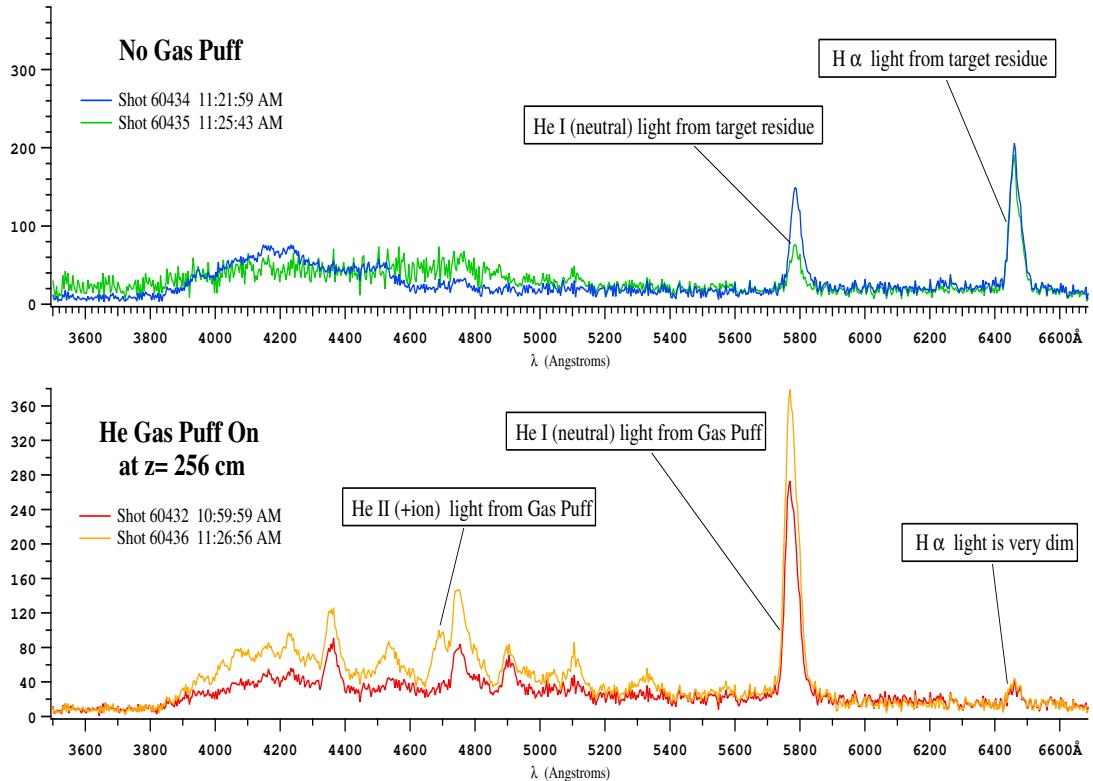
Figure 9.6: Spectra showing composition of residual gas on target

The survey spectra are shown in figure 9.6. The spectroscopic data showed that the light from the residual gas was mainly in the hydrogen H_α line, while all other helium and impurity emission was greatly reduced. The conclusion is that hydrogen from the CT has built up on the surface of the glass tubes and is later ejected when plasma washes over the target. This effect should

be considered when designing future gas puff experiments. Possibly, hydrogen absorption could be reduced with a different choice of materials for any support structures (ceramic perhaps).

We are also planing to have a surface analysis done on these tubes to quantify how much hydrogen was implanted, and how deep, and what other elements were implanted. It will be interesting to see the results.

Displayed in figure 9.7 is a top view of the layout of diagnostics in the drift section viewing chamber as it was during the experiments with the wire target. The colored circles indicate probe locations, either magnetic or Langmuir. The dotted lines trace out the lines of sight of two photomultiplier tubes, which were positioned on the side that is toward the bottom of the page.
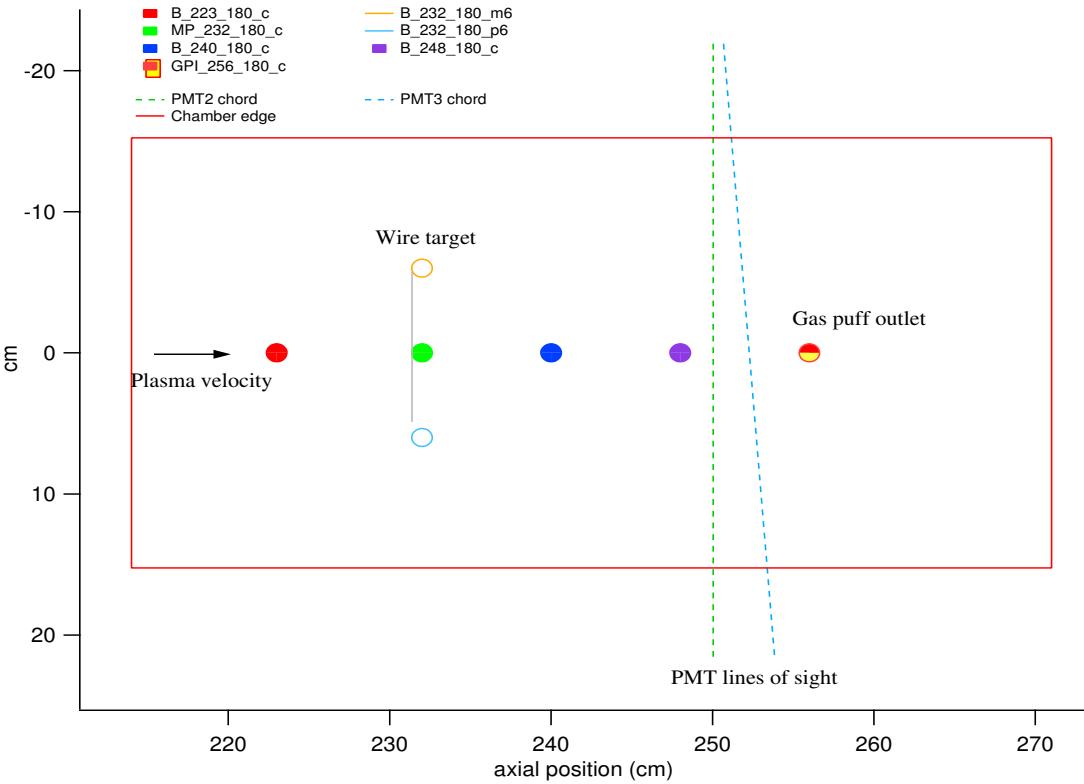
Figure 9.7: Top view of drift section arrangement

9.2 Observation of coherent density waves

The figure below shows the location of observed plane waves and their approximate wavelength λ and direction. For some shots distinct waves were observed in multiple locations and so are listed separately. There was a noticeable amount of reproducibility of waves occurring in the same location, implying that the waves do not form at random, but instead are caused by some identifiable mechanism.
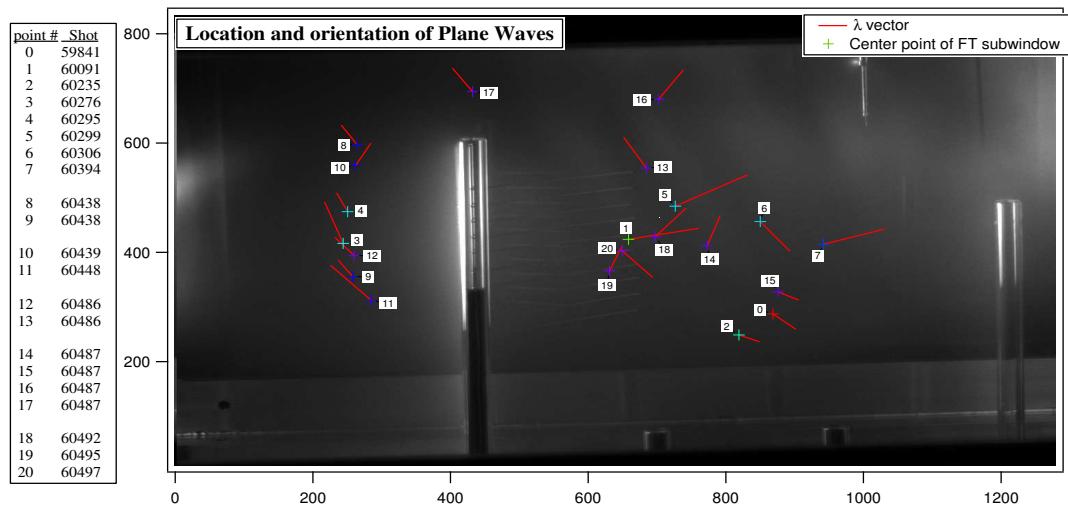
Figure 9.8: Plane wave locations with labels according to shot number.

Careful examination of these images gives some indication that the regions of highest luminosity are sometimes very close to the glass window. This was first demonstrated with the observation of sharp density wakes localized near the tips of the wires, which were touching the glass (as mentioned in the last section).

This makes it plausible that the waves are dominantly fluctuation near the surface. This might explain their apparent independence from the positioning of the wire array.
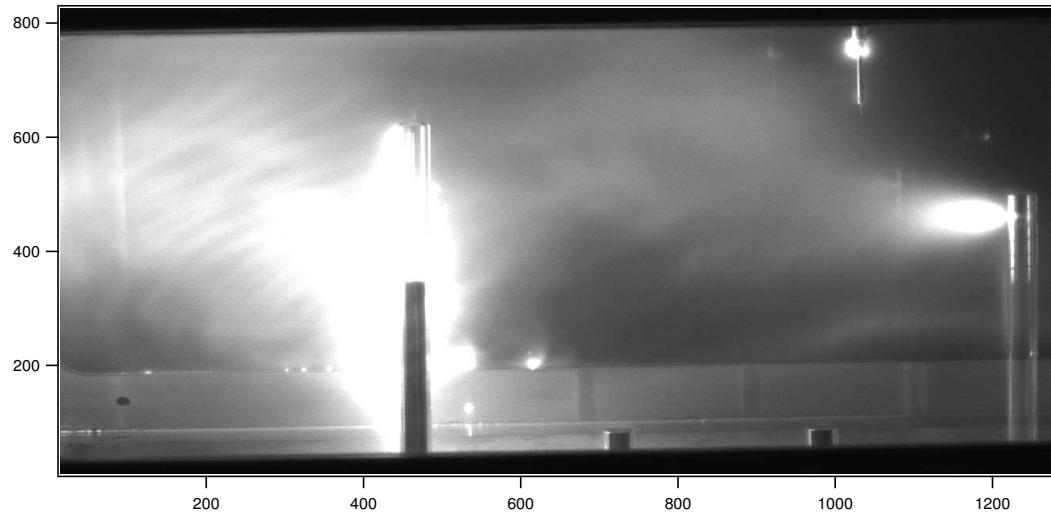
Figure 9.9: Coherent waves in plasma during shot 60438
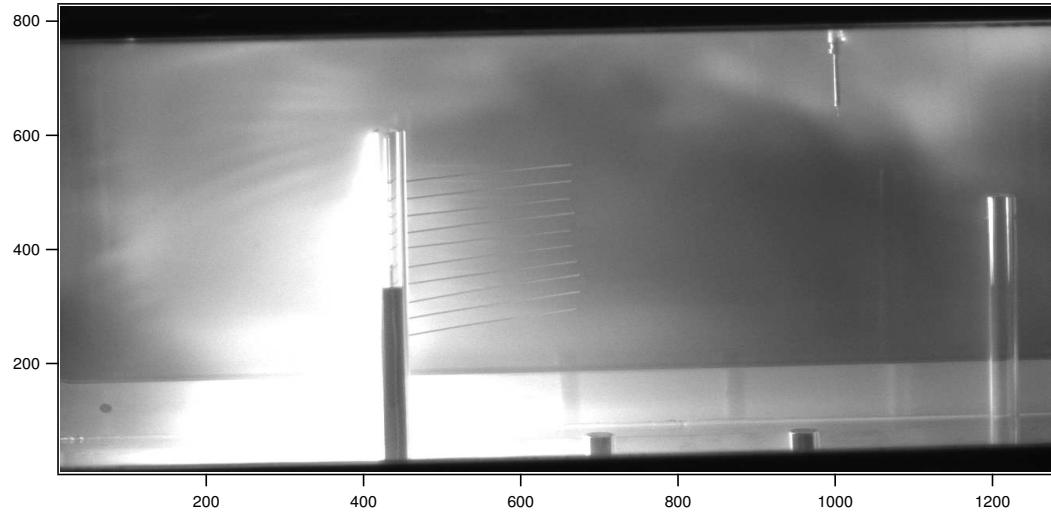
Figure 9.10: Coherent waves in plasma during shot 60295

A number of questions present themselves about these waves [71]. What are they? Ion acoustic waves? MHD waves? Current filaments? How do they evolve in time? What is their wave velocity? What physical mechanism created them? While the evidence needed to determine answers
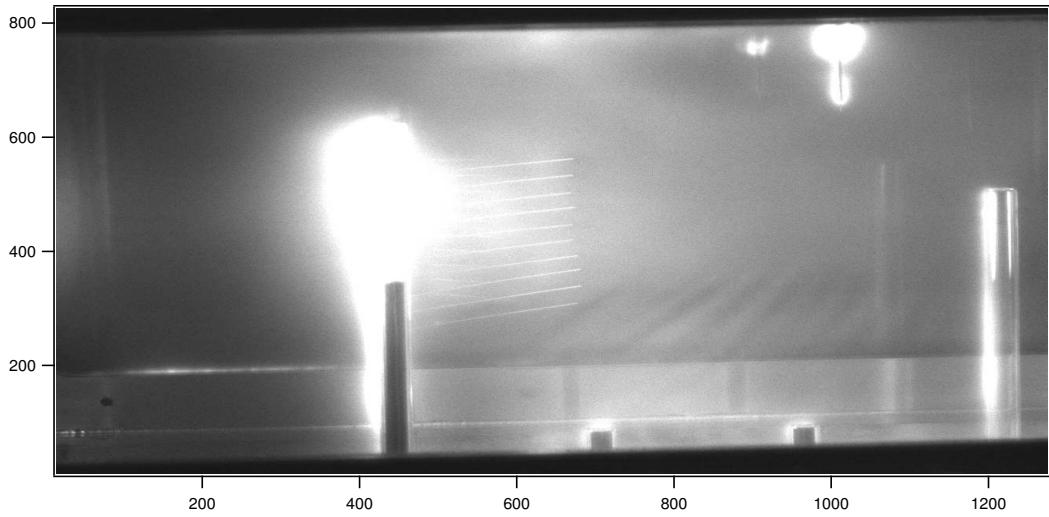
Figure 9.11: Coherent waves in plasma during shot 59841
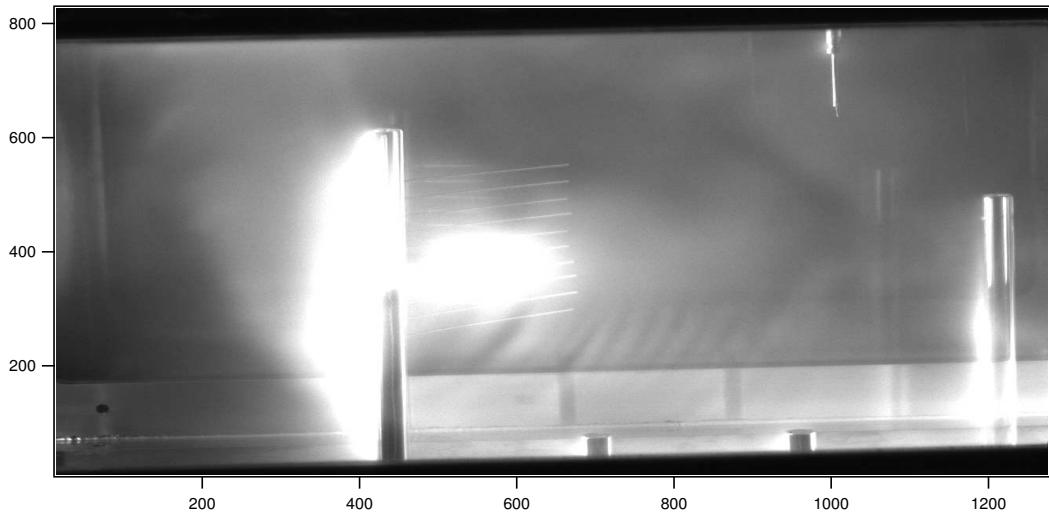
Figure 9.12: Coherent waves in plasma during shot 60235

to these questions is still incomplete, there are a few solid facts we have been able to glean from our data.

We have done Fourier analysis on the images containing wave patterns, and used this to find the wavelength λ and wavevector $\mathbf{k}$ of the dominant mode. Displayed in figures 9.9 - 9.12 are
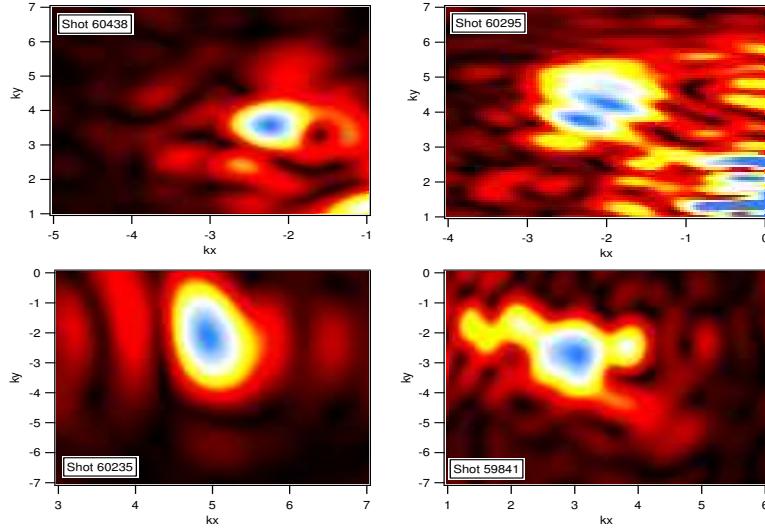
Figure 9.13: Localized Fourier modes of plane waves, in k_x, k_y Fourier space (color scale represents magnitude of FT)

some examples of very localized Fourier modes, which we visually identify as plane waves.
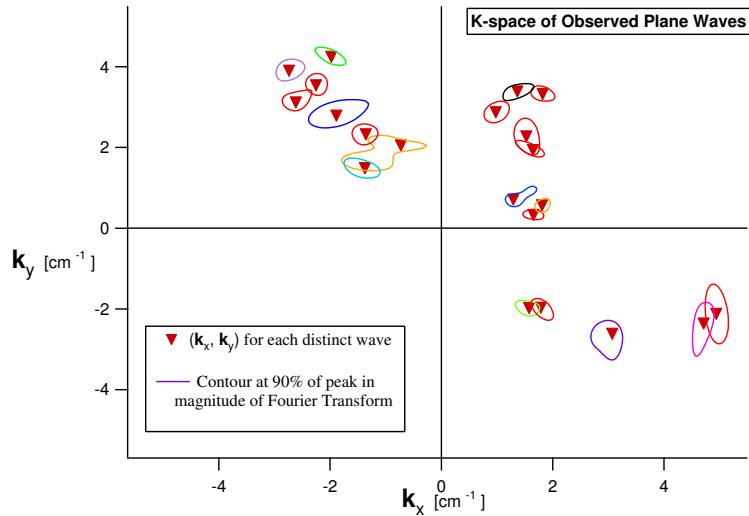
Figure 9.14: K-space distribution of Plane waves

A very important consideration comes about from considering the finite exposure time of these images given the extremely rapid motion of the plasma past the camera. The relevant quantity

is the exposure smear length, which is the distance the plasma should move during the camera exposure time (of 1 μs), based on time of flight measurements of plasma velocity ($L_{exp} = v_{CT}\ \tau_{exp}$). Here we compare this length to the wavelength of the plane waves.
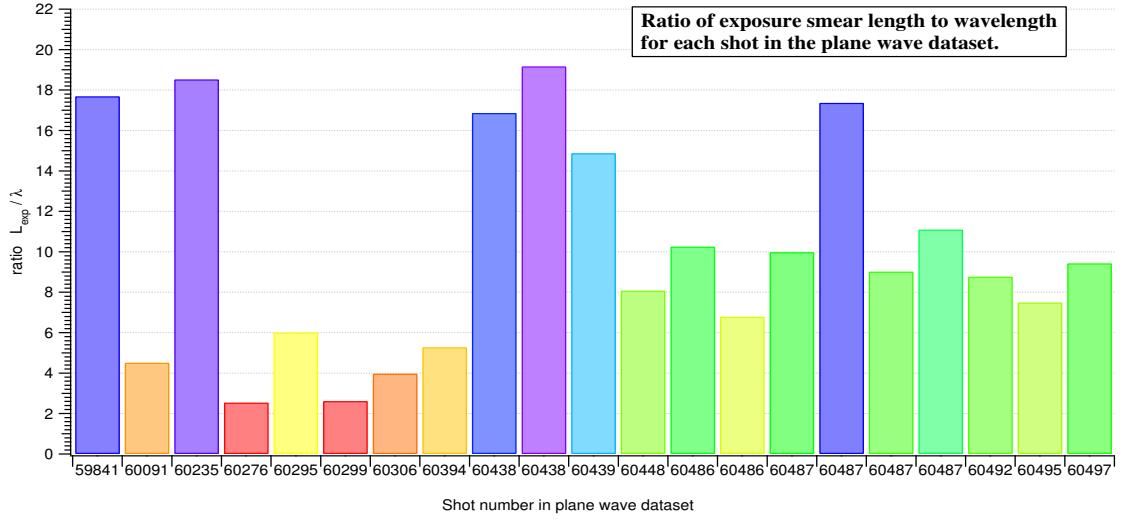
Figure 9.15: Ratio of expected exposure smear length to wavelength is displayed here vs shot number of data set ($L_{exp} = v_{CT}\ \tau_{exp}$).

The curious fact is that if these were plane waves were co-moving with the plasma at a velocity between 3 to 15 $cm/\mu s$, then for an exposure of 1 full μs, we would not be able to resolve the clear wave structures on the order of 1 cm that we do see. If these were co-moving plane waves, the images would be mostly a blur due to the relatively long exposure time, and the fast motion of the plasma. We also see (in fig. 9.16) that there is no apparent trend that relates wavelength and plasma flow velocity, such as might be expected from a simple traveling wave with $\lambda f = v_\phi$. This again implies that the wave speed is not the same as the plasma flow speed.

The only viable conclusion is that these waves are essentially standing waves in the laboratory frame of reference, with wave velocities of less than 1 $cm/\mu s$.

The mechanism that is responsible for generating these density waves is not fully understood. The problem here is an over abundance of candidates due to the many important interaction effects that are conceivable within our system.
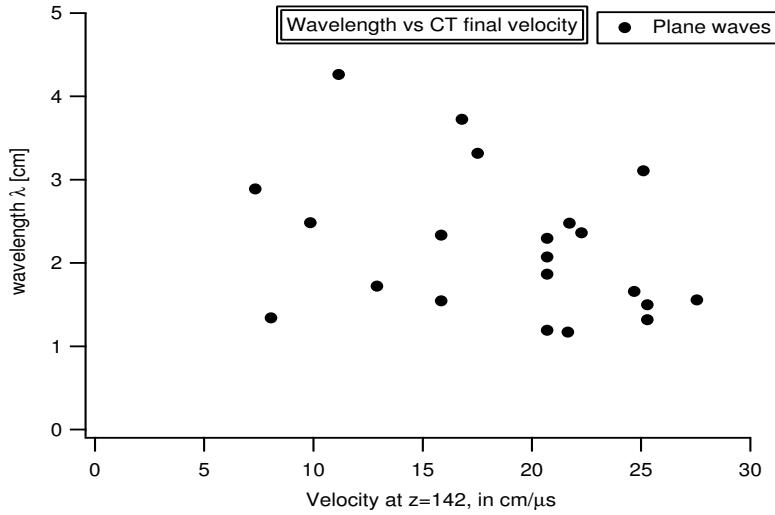
Figure 9.16: Wavelength vs plasma flow speed

One possibility is that the wire targets in the plasma did just what they were intended to do, and the result of this perturbation is that coherent, single-mode density waves are created if the plasma conditions are right [72]. However, the waves appear to occur with equal probability in the regions upstream and downstream of the target. They also occur with the target at any of the possible angles. Although this can't be ruled out, it is my current opinion that this is not a very good explanation of what we see.

An alternative hypothesis is that these waves could be generated by the two stream instability between the moving CT plasma and a stationary singly ionized helium plasma [71]. The specific of such a theory need to be worked out, but it should provide some testable predictions regarding the wavelength and velocity of any such waves generated by this kind of instability.

Along this same line of thought, it is conceivable that if there is a velocity sheer layer at the interface between the fast moving CT plasma and a relatively immobile but luminous boundary layer plasma, that this system might have some kind of flow instability (Kelvin-Helmoltz or Buneman perhaps [73],[74],[60],[75],[76],[77],[78],[72]), which gives rise to a displacement wave at the interface between the two fluids. The regions where the boundary layer becomes thinner due to the wave

motion, we would expect a darker area in the image. Brighter regions would correspond to the boundary layer becoming thicker due to the wave motion. This idea seems to have the most merit of any considered so far, and we could test it by imaging the same wave from two different vantage points (with two identical high speed cameras) to determine its spatial variation more precisely.

Further analysis on the existing data may also help to develop a better model of what causes these, and other wave phenomena in the CTIX plasma.

9.3   Observation of turbulent waves

One mode of operation was found to be especially useful for visualizing turbulent flow in the plasma. In this mode we used the accelerator gas puff to add helium to the flow of hydrogen plasma [79]. For example, the image taken on CTIX Shot 60062 (Fig 9.17) displays an apparent transition from laminar to turbulent flow as plasma passes wire target and support tubes, traveling from left to right.
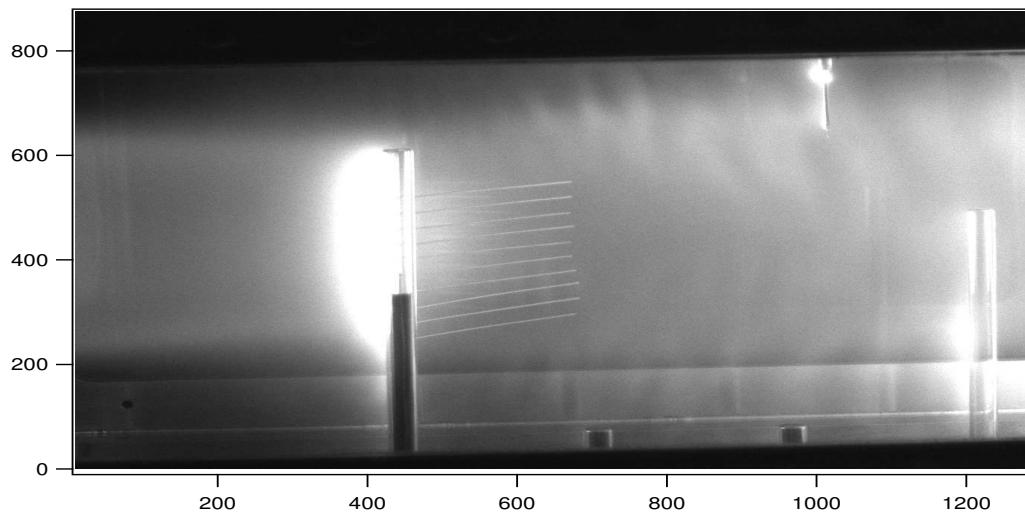
Figure 9.17: Transition to turbulent flow on shot 60062

The camera exposure for this shot was 1 μs, with a delay of 30 μs from the formation of the CT plasma. This image is of the relatively uniform B_θ pushing field plasma behind the CT, after the CT has already moved through the viewing chamber. The helium gas puff was injected into the z = 91 cm accelerator port at approximately 14 milliseconds before the shot, which primarily served to increase the plasma electron density by about a factor of 3 for this shot. The secondary effect of the gas puffing is that helium ions (which serve as the dominant source of light for fast imaging) have a chance to be captured and accelerated by the magnetic fields. By the time they enter the drift section they are co-moving with the plasma and therefore the light emission from these captured

ions is indicative of the structure of the flow, and evidence of density fluctuations. When gas puff conditions are just right, this mode of operation is ideal for flow visualization, roughly analogous to using smoke to trace streamlines in wind-tunnel experiments. Injection velocity of SCT for this shot was 3.35 cm/μs. The dominant wavelength of post-target fluctuations for this shot was 2.5 cm.
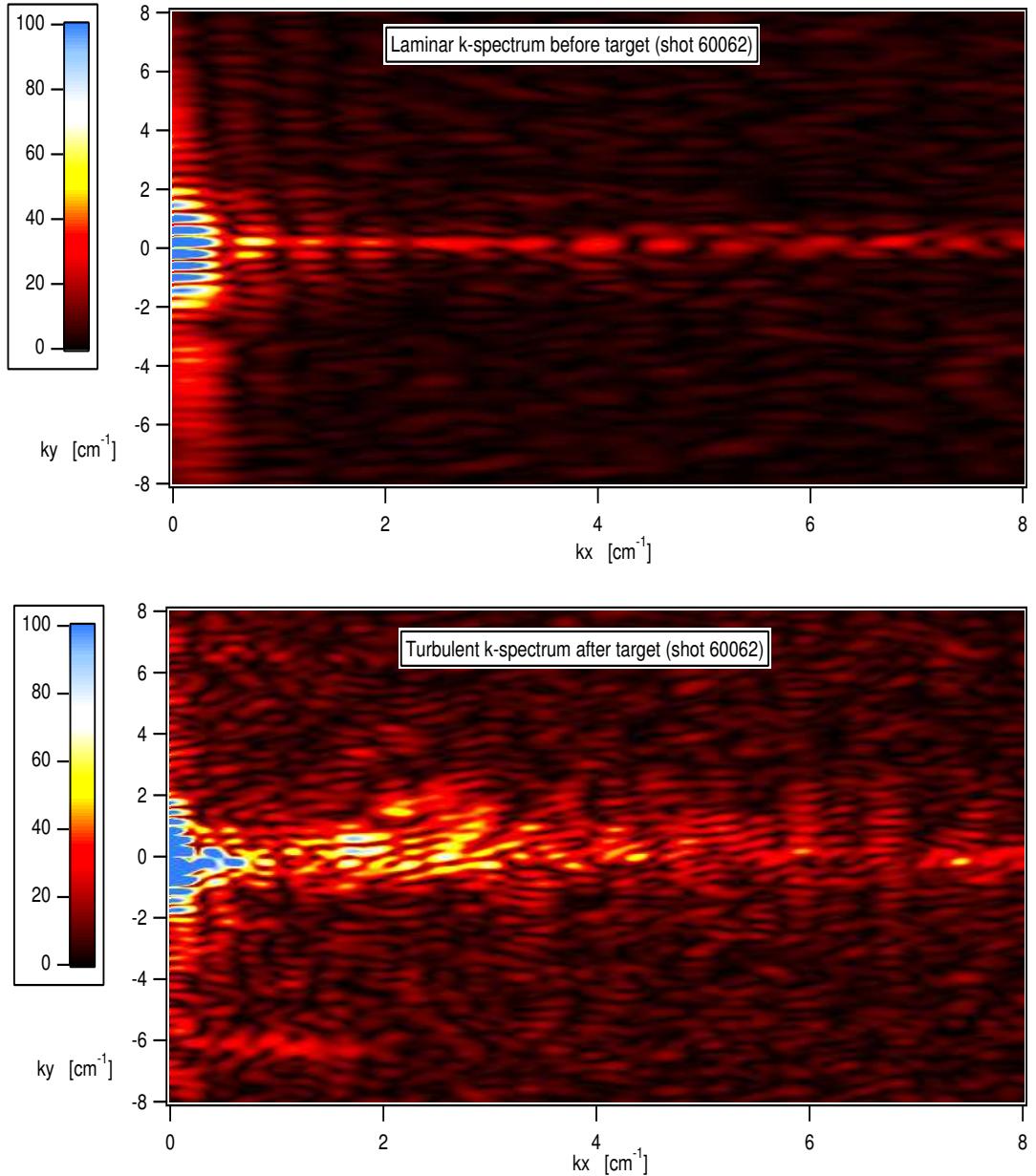
Figure 9.18: Fourier transforms of the image taken for shot 60062,(top) in laminar region before plasma has interacted with target, (bottom) turbulence after interaction.

The top graph in figure 9.18 is the 2-D Fourier transform of the plasma luminosity in the region before it has interacted with the target. The bottom graph is the FT of the plasma after it has interacted with the target. The color scale represents the magnitude of the FT for any given wavevector (k_x, k_y), and the units are arbitrary, but the same for both top and bottom graphs. A significant increase in fluctuation amplitude is observed, as well as wider distribution of waves in the k_y direction. Also the k-spectrum is noticeably more choppy and irregular for the turbulent flow than for the incoming laminar flow [80]. The dominant wave modes in the turbulent spectrum are localized near $k = (2.5, 0)$ [1/cm], where $k = 2\pi/\lambda$. A custom-made discrete Fourier transform algorithm was used instead of a prepackaged FFT algorithm in order to provide more precise control of the resulting resolution in k space.

The clear conclusion that we can make from this image and its Fourier transform (and the others from its data set) is that the plasma flow is significantly effected by its interaction with the target. However, it is less clear whether this effect is due to the wire array or simply the glass support tubes.
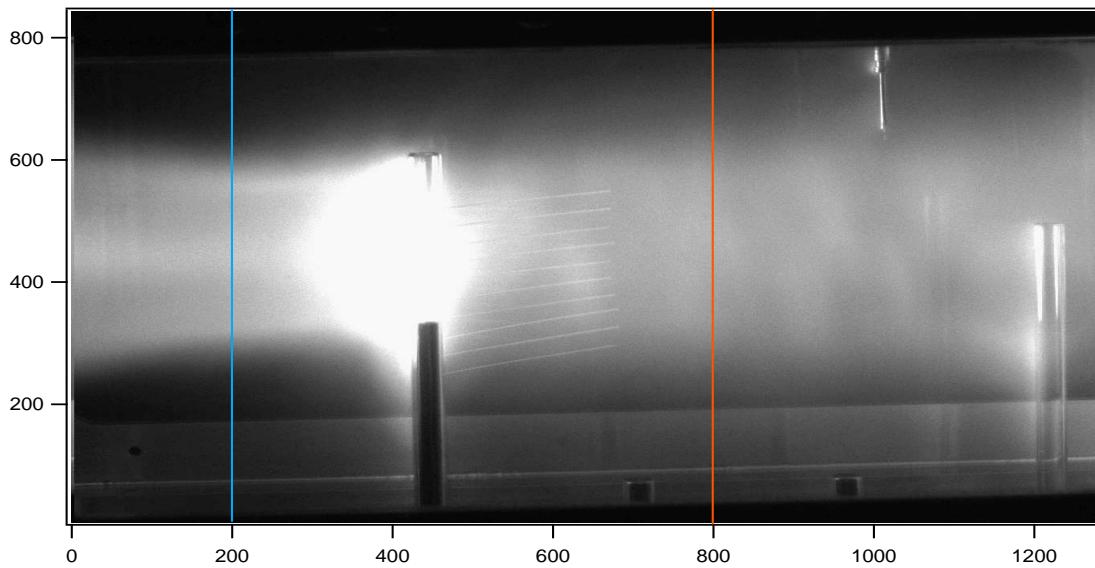
Figure 9.19: Image of shot 60055, showing vertical lines where sampling was done.

Another example of the apparent laminar-turbulent transition was observed during shot 60055 (image take at t = 30 μs). We examined the radial profile of this image at two axial positions, as shown in figure 9.19. The blue chord is before interaction with the target, while the red chord is after.

The resulting radial profiles are shown in figure 9.20. Before interaction we see that plasma leaves the accelerator relatively well collimated, with a symmetric and slightly hollow radial distribution that is consistent with the coaxial geometry of the accelerator. After it interacts with the target, significant radial diffusion has occurred. The x-axis of this graph is in units of pixels.
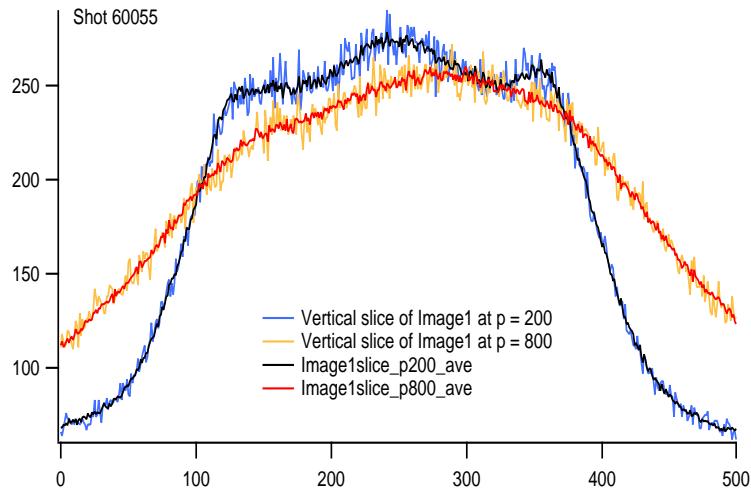
Figure 9.20: Radial profiles of luminous flow, before and after target for shot 60055.

We can also examine the exposure smear length as we did before with the coherent waves. Let us consider in detail the example of shot 60061 (image at t= 27 μs, 1 μs exposure), shown in figure 9.22. Compared to other shots in this data set, this had a relatively slow CT velocity of $v_{142} = 2.6947$ $cm/\mu s$ as inferred from the time of flight between the magnetic probes in the accelerator. We find that the dominant wavelength in the post-target fluctuation is $\lambda_{dominant} = 3.5$ cm. This results in an exposure smear ratio for this image is 0.76, which allows for direct imaging of waves co-moving with the fluid of $\lambda_{dominant} = 3.5$ cm that are at most 76% blurred due to fluid motion.

If the velocity decreases in the drift section below its original 2.6947 $cm/\mu s$ then there will be even less blurring. For this shot it is possible that the apparent wavefronts in luminosity are oriented transverse to the stream lines of the flow, and that the waves are co-moving with the fluid. Although this interpretation is possible given the data on this shot, it is not necessarily so.

In fact, most of the other shots in the data set have exposure smear ratios that are greater than unity, making it very unlikely that the wave structures are co-moving with the fluid given the crispness of the wave edges that we see in the images. In figure 9.21 we compare the scatter of wavelength versus velocity for the shots in the turbulence dataset, and the those of the coherent wave data set, previously displayed in figure 9.16. We see that with the accelerator gas puffing the final velocity of the CT could go slightly lower than it did with the drift section gas puff, which agrees with the fact that the accelerator puff causes a mass density increase due to the CT snow-plowing its way through the neutral cloud while being accelerated. However, there is about the same spread in dominant wavelength in both cases.
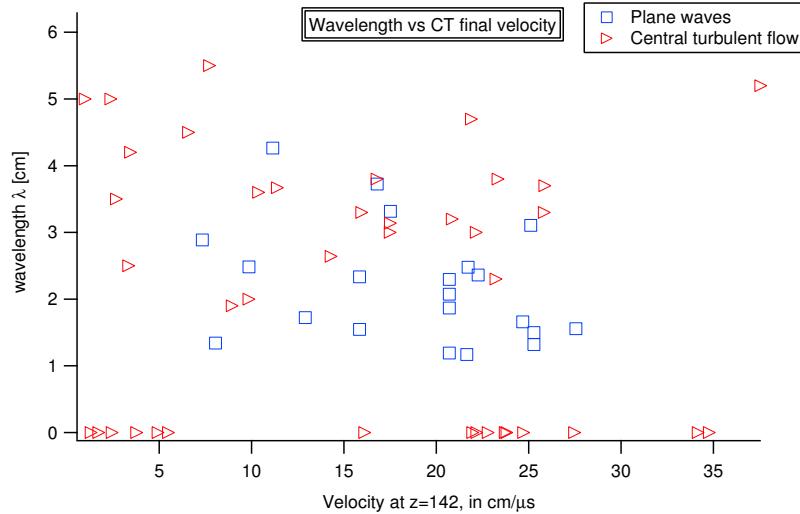
Figure 9.21: Wavelength vs. plasma flow speed for plane wave and turbulent cases

Now this all adds up in an unexpected way. Unlike the coherent waves in the drift section gas puff, we find that during shots with accelerator gas puffing the neutrals have enough time

to become ionized and accelerated by the fields. So the light emitting ions that we see in these accelerator gas puff shots must be co-moving with the rest of the CT plasma, without a doubt. Yet these shots also had large exposure smear ratios, implying that the wave structures are not co-moving with the fluid.

I propose an interpretation that may resolve this dilemma. If the ions happen to be flowing along streamlines that are twisted in space, possibly along some sort of helical, vortex-like path, then a side view of the edge of this structure would result in an image that had alternating light and dark areas in it. The light areas are where the ions at the edge of the central jet follow the streamlines out into the surrounding void, while the dark areas are the regions of void (or at least low density), that protrude into the negative space between the turns of the outermost helical streamlines.

In figure 9.22 I have draw some possible stream lines overlaid on the image, to illustrate the plausibility of such an interpretation.
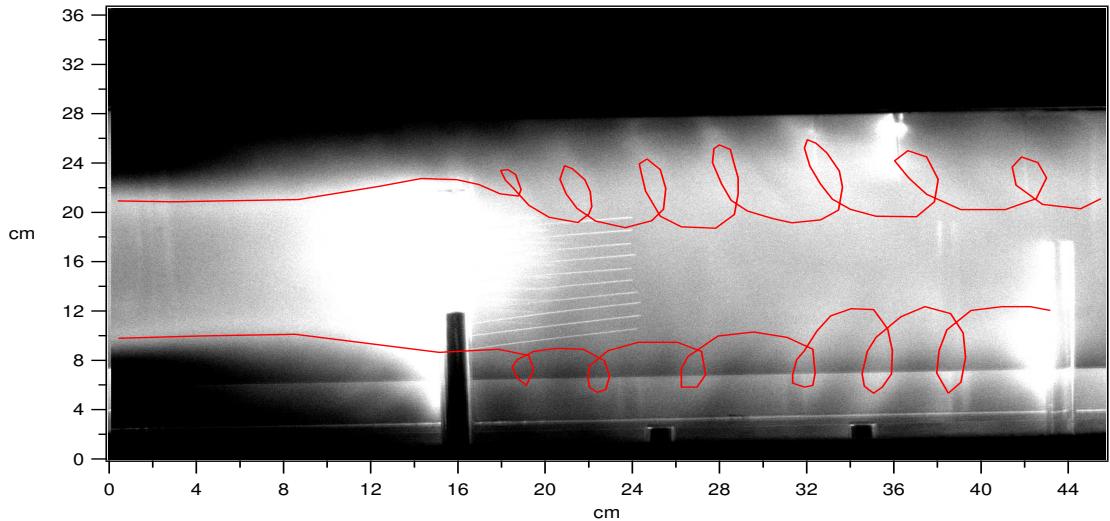
Figure 9.22: Possible long wavelength streamlines for shot 60061

Bibliography

[1] H. S. McLean, D. Q. Hwang, R.D. Horton, R. W. Evans, and S. D. Terry *et al*. Design and operation of a passively switched repetitive compact toroid plasma accelerator. *Fusion Technology*, 33:252–272, May 1998.

[2] R. D. Horton. Observation of poloidal field amplification in a passively switched coaxial compact toroid accelerator. In preparation, 2006.

[3] D. Q. Hwang, M. Ryutova, , and H. McLean. Penetration of a compressible magnetized plasma object into a low beta target plasma. *Physics of Plasmas*, 6(5):1515–1521, May 1999.

[4] D. Q. Hwang, H. S. McLean, K. L. Baker, R.D. Horton, R. W. Evans, S. D. Terry, S. Howard, and G. L. Schmidt. Interaction of a spheromak-like compact toroid with a high-beta spherical tokamak plasma. *Nuclear Fusion*, 40(5):897–905, 2000.

[5] H. Alfvèn, L. Lindberg, and P. Mitlid. Experiments with plasma rings. *Journal of Nuclear Energy Part C: Plasma Physics*, 1:116–120, 1960.

[6] Peter Beiersdorfer and Eugéne J. Clothiaux. High-frequency magnetic measurements using small inductive probes. *Am. J. Phys*, 51(11):1031–1036, November 1983.

[7] J. H. Rogers, J. S. De Groot, and D. Q. Hwang. Validating Cylindrical Langmuir Probe Techniques. *Rev. Sci. Instr.*, 63(1):31, January 1992.

[8] Stephen J. Howard. Preliminary Study of Compact Toroid Fuel Deposition in a Vacuum Magnetic Field. Bennington College, VT, December 1998. Undergraduate Thesis in Applied Mathematics.

[9] J. H. Rogers and D. Q. Hwang. Measurement of beat-wave accelerated electrons in a toroidal plasma. *Physical Review Letters*, 68(26):3877–3880, June 1992.

[10] S. J. Brockington, R.D. Horton, D. Q. Hwang, R. W. Evans, and S. Howard. Plasma density gradient measurement using laser deflection. *Rev. Sci. Instr.*, 76:063503, 2005.

[11] S. D. Terry, D. Q. Hwang, H. S. McLean, R. D. Horton, R. W. Evans, and K. L. Baker. The Compact Toroid Injection Experiment tomographic imaging system. *Rev. Sci. Instr.*, 71(11):4119–4126, November 2000.

[12] R. Burnham and D. Scarl. Photomultiplier dark pulses. *Applied Optics*, 24(2):293–295, January 1985.

[13] A. Graf, M. May, and P. Beiersdorfer *et al*. High resolution transimssion grating spectrometer for edge toroidal rotation measurements of tokamak plasmas. *Rev. Sci. Instr.*, 75(10):4165–4167, October 2004.

[14] S.B. Utter and P. Beiersdorfer *et al*. Implementation of a normal incidence spectrometer on an electron beam ion trap. *Rev. Sci. Instr.*, 70(1):288–291, January 1999.

[15] J. B. Taylor. Relaxation and magnetic reconnection in plasmas. *Reviews of Modern Physics*, 58(3):1139–1141, July 1986.

[16] S. Riyopoulos, A. Bondeson, and D. Montgomery. Relaxation toward states of minimum energy in a compact torus. *Physics of Fluids*, 25(1):107–115, January 1982.

[17] W. C. Turner *et al*. Investigations of the magnetic structure and the decay of a plasma-gun-generated compact torus. *Phys. Fluids*, 26(7):1965–1986, July 1983.

[18] James H. Hammer, C. W. Hartman, J. L. Eddleman, and H. S. McLean. Experimental demonstration of acceleration and focusing of magnetically confined plasma rings. *Physical Review Letters*, 61(25):2843–2846, December 1988. This is the RACE paper that talks about surface effect of SS electrodes. It also shows a nearly identical Bz magnetic field profile as seen on CTIX (for example compare Fig 2 with CTIX shot 52756, Bz 142).

[19] J. H. Degnan *et al*. Compact toroid formation, compression, and acceleration. *Phys. Fluids B*, 5(8):2938–2958, August 1993. This is the only known paper that includes the Bessel function solution to a force-free state in a coaxial geometry (with errors). It presents the experiments of the MARAUDER device.

[20] Tristan Needham. *Visual Complex Analysis*. Clarendon Press, Oxford, UK, 2000. See chapters 10, 11, and 12 regarding harmonic duality.

[21] John David Jackson. *Classical Electrodynamics*. John Wiley & Sons, Inc., New York, NY, 1999. Third Edition.

[22] G. W. Hart *et al*. Finite-pressure-gradient influences on ideal spheromak equilibrium. *Physical Review Letters*, 51(17):1558–1561, October 1983.

[23] Leaf Turner. Hall effects on magnetic relaxation. *IEEE Trans. Plasma. Sci.*, 14(6):849–857, December 1986.

[24] P. Geren and L. Steinhauer. Gyroscopic effect in compact toroidal plasmas. *Physics of Plasmas*, 11(7):3646–3652, July 2004.

[25] M. Iqbal. Minimization of field-aligned current and flow. *J. Plasma Physics*, 71(3):335–344, 2005.

[26] E. A. Witalis. Hall magnetohydrodynamics and its application to laboratory and cosmic plasma. *IEEE Trans. Plasma. Sci.*, 14(6):842–848, December 1986.

[27] L. Steinhauer and A. Ishida. Relaxation of a two-species magnetofluid and application to finite-β flowing plasmas. *Physics of Plasmas*, 5(7):2609–2622, July 1998.

[28] Francis F. Chen. *Introduction to Plasma Physics and Controlled Fusion*, volume 1: Plasma Physics. Plenum Press, New York, NY, 1984. Second Edition.

[29] J. D. Huba. NRL Plasma Formulary. Technical Report NRL/PU/6790–98-358, Naval Research Laboratory, Washington, DC, 1998.

[30] Roger Penrose. *The Road to Reality*. Alfred A. Knopf, New York, 2005. See chapters 12 and 14 regarding the mathematics of manifolds.

[31] G. Arfken. *Mathematical Methods for Physicists, 3rd ed.* Academic Press, Orlando, FL, 1985. pp. 198-200.

[32] H. Goldstein. *Classical Mechanics, 2rd ed.* Addison-Wesley Publishing Company, Reading, MA, 1980. See section 4-4 (pp. 143-148) and Appendix B (pp. 606-610).

[33] F. Trintchouk *et al*. Measurement of the transverse spitzer resistivity during collisional magnetic reconnection. *Physics of Plasmas*, 10(1):319–322, January 2003. This is the paper that motivated my resistivity analysis.

[34] Dieter Biskamp. *Magnetic reconnection in plasmas*. Cambridge University Press, Cambridge, UK, 2000.

[35] R. B. White. Resistive reconnection. *Reviews of Modern Physics*, 58(1):183–207, January 1986.

[36] S. Iizuka, Y. Minamitanim, H. Tanaca, and Y. Kiwamoto. Magnetic field-line reconnection in a toroidal plasma. *Physical Review Letters*, 53(9):918–921, August 1984.

[37] C. T. Dum *et al*. Anomalous resistivity of a turbulent plasma. *Plasma Physics*, 12:062902–1,8, 2005.

[38] I. Silin *et al*. Anomalous resistivity due to nonlinear lower-hybrid drift waves. *Physics of Plasmas*, 12:062902–1,8, 2005.

[39] H. L. Berk, J. H. Hammer, and J. W. Shearer. Reconnection conditions for a coaxial plasma gun. *Phys. Fluids*, 25(1):102–106, January 1982.

[40] K. L. Baker, R. D. Horton, D. Q. Hwang, R. W. Evans, and S. Howard. Simulation of the "Blowby" Effect in an Accelerating Compact Toroid. *IEEE Trans. Plasma Sci.*, 30(1):48–49, February 2002.

[41] L. J. Perkins, S. K. Ho, and J. H. Hammer. Deep penetration fueling of reactor-grade tokamak plasmas with accelerated compact toroids. *Nuclear Fusion*, 28(8):1365–1378, 1988.

[42] M. Nagata *et al*. Behaviour of compact toroid injected into an external magnetic field. *Nuclear Fusion*, 41(11):1687–1694, 2001.

[43] J. T. Slough and A. L. Hoffman. Penetration of a transverse magnetic field by an accelerated field-reversed configuration. *Physics of Plasmas*, 6(1):253–263, January 1999.

[44] R. Raman *et al*. Experimental Demonstration of Nondisruptive, Central Fueling of a Tokamak by Compact Toroid Injection. *Physical Review Letters*, 73(23):3101–3104, December 1994.

[45] D. W. Longcope and S. C. Cowley. Current sheet formation along three-dimensional magnetic separators. *Physics of Plasmas*, 3(8):2885–2897, August 1996.

[46] N. V. Erkaev *et al*. Rate of steady-state reconnection in an incompressible plasma. arXiv:physics/0111188 v1 26 Nov 2001.

[47] Saeed Ghahramani. *Fundamentals of Probability*. Prentice Hall, Upper Saddle River, NJ, 1996.

[48] Philip Morse. *Thermal Physics*. Perseus Books, 1969. 2nd edition.

[49] Arthur W. Molvik. Large acceptance angle retarding-potential analyzers. *Rev. Sci. Instr.*, 52(5):704–710, May 1981.

[50] R. J. Groebner *et al*. Measurement of plasma ion temperature and rotation velocity using the He II 4686-Å line produced by charge transfer. *Appl. Phys. Lett.*, 43(10):920–922, November 1983.

[51] R. J. Fonck, D. S. Darrow, and K. P. Jaehnig. Determination of plasma-ion velocity distribution via charge-exchange recombination spectroscopy. *Physical Review A*, 29(6):3288–3308, June 1984.

[52] R. Fischer and V. Dose. Electron energy distribution reconstruction in low-pressure helium plasmas from optical measurements. *Plasma Phys. Control. Fusion*, 41:1109–1123, 1999.

[53] Y-K. Kim and M. E. Rudd. Binary-encounter-dipole model for electron-impact ionization. *Physical Review A*, 50(5):3954–3967, November 1994.

[54] S. M. Younger. Electron-impact-ionization cross sections for highly ionized hydrogen- and lithium-like atoms. *Physical Review A*, 22(1):111–117, July 1980.

[55] S. M. Younger. Electron-impact-ionization cross sections for highly ionized heliumlike atoms. *Physical Review A*, 22(4):1109–1123, October 1980.

[56] R. G. Montague *et al*. A measurement of the cross section for the ionisation[*sic*] of helium by electron impact using a fast crossed beam technique. *J. Phys. B: At. Mol. Phys.*, 17:3295–3310, 1984.

[57] I. V. Kalagin *et al*. Modelling [*sic*] of ion accumulation processes in EBIS and EBIT. *Plasma Sources Sci. Technol.*, 7:441–457, 1998.

[58] R. V. Bravenec, H. L. Berk, and J. H. Hammer. An alternative derivation of the parallel ion viscosity. *Phys. Fluids*, 25(4):608–609, April 1982.

[59] Dieter Biskamp. *Magnetohydrodynamics Turbulence*. Cambridge University Press, Cambridge, UK, 2003.

[60] Stephen B. Pope. *Turbulent Flows*. Cambridge University Press, Cambridge, UK, 2003.

[61] X. Q. Xu *et al*. Transitions of turbulence in plasma density limits. *Physics of Plasmas*, 10(5):1773–1781, May 2003.

[62] J. A. Krommes. Fundamental statistical descriptions of plasma turbulence in magnetic fields. *Physics Reports*, 360:1–352, 2002.

[63] D. Biskamp and E. Schwarz. On two-dimensional magnetohydrodynamic turbulence. *Physics of Plasmas*, 8(7):3282–3292, July 2001.

[64] Wolf-Christian Müller, Dieter Biskamp, and Roland Grappin. Statistical anisotropy of magnetohydrodynamic turbulence. *Physical Review E*, 67(066302), June 2003.

[65] V. S. L'vov *et al*. Invariants for correlations of velocity differences in turbulent fields. *Physical Review Letters*, 79(11):2050–2052, September 1997.

[66] R. Kent Nagle and Edward B. Saff. *Fundamentals of Differential Equations*. Addison-Wesley Publishing Company, Reading, MA, 1993. Third Edition, See pages 204-206.

[67] R. J. Maqueda *et al*. Edge turbulence measurements in nstx by gas puff imaging. *Rev. Sci. Instr.*, 72(1):931–934, January 2001.

[68] J. L. Terry *et al*. Observation of the turbulence in the scrape-off-layer of Alcator C-Mod and comparisons with simulation. *Physics of Plasmas*, 10(5):1739–1747, May 2003.

[69] D. P. Stotler *et al*. Neutral transport simulation of gas puff imaging experiments. *J. Nuc. Mat.*, 313(316):1066–1070, 2003.

[70] B. S. Tanenbaum and D. Mintzer. Recent research in magneto-aerodynamics. *Progress in Aerospace Sciences*, 37:1–20, 2001. This has some nice results of shock effects in plasma flows interacting with blunt objects.

[71] Thomas Howard Stix. *Waves in Plasmas*. American Institute of Physics, New York, NY, 1992.

[72] W. A. Newcomb. Magnetohydrodynamic wave drag. *Phys. Fluids B*, 3(8):1818–1829, August 1991.

[73] Glenn Bateman. *MHD Instabilities.* The MIT Press, Cambridge, Massachusetts, 1980. Second Edition.

[74] Dieter Biskamp. *Nonlinear Magnetohydrodynamics.* Cambridge University Press, Cambridge, UK, 1993.

[75] K. Theilhaber and C. K. Birdsall. Kelvin-Helmholtz vortex formation and particle transport in a cross-field plasma sheath. I. Transient behavior. *Phys. Fluids B*, 1(11):2244–2259, November 1989.

[76] A. Bondson *et al.* Tilting instability of a cylindrical spheromak. *Physics of Fluids*, 24(9):1682–1688, September 1981.

[77] S. C. Hsu and P. M. Bellan. Experimental identification of the kink instability as a poloidal flux amplification mechanism for coaxial gun spheromak formation. *Physical Review Letters*, 90(21):215002–1, 4, May 2003.

[78] E. M. Marshall and K. L. Hall. Collisional drift instabilities in hollow and coaxial plasmas. *Plasma Physics and Controlled Fusion*, 28(12A):1867–1884, 1986.

[79] David Dietz. Coaxial plasma accelerator in the snowplow mode: Analytical solution in the weak coupling limit. *J. Appl. Phys.*, 62(7):2669–2674, October 1987.

[80] O. Ishihara and A. Hirose. Turbulent heating and anomalous k spectrum in the quasilinear evolution of current-driven ion-acoustic instability in a magnetic field. *Phys. Fluids*, 27(2):364–376, February 1984.

[81] Vladimir I. Arnold and Boris A. Khesin. *Topological Methods in Hydrodynamics.* Springer-Verlag, New York, 1998. See chapter III regarding helicity.

[82] Sergio Ortolani and Dalton D. Schnack. *Magnetohydrodynamics of Plasma Relaxation.* World Scientific, Singapore, 1993.

[83] F. M. Henderson. *Elliptic Functions with Complex Arguments.* The University of Michigan Press, 1960.

[84] K. L. Baker, D. Q. Hwang, R. W. Evans, R. D. Horton, H. S. McLean, S. D. Terry, S. Howard, and C. J. DiCaprio. Compact toroid dynamics in the compact toroid injection experiment. *Nucl. Fusion*, 42:94–99, 2002.

[85] K. L. Baker, D. Q. Hwang, R. W. Evans, R. D. Horton, H. S. McLean, and S. D. Terry. Observation of pinching in the compact toroid injection experiment:implication for a plasma opening switch. *App. Phys. Lett.*, 79(9):1237–1239, 2001.

[86] J. B. Taylor. Relaxation of toroidal plasma and generation of reverse magnetic fields. *Physical Review Letters*, 33(19):1139–1141, November 1974.

[87] C. D. Cothran *et al*. Spheromak merging and field reversed configuration formation at the swarthmore spheromak experiment. *Physics of Plasmas*, 10(5):1748–1754, May 2003.

[88] C. W. Barnes *et al*. Spheromak merging and field reversed configuration formation at the swarthmore spheromak experiment. *Physics of Fluids*, 29(10):3415–3432, October 1986.

[89] A.M. Dixon *et al*. A generalization of the Woltjer minimum-energy principle. *Astron. Astrophys.*, 225:156–166, 1989.

[90] John M. Finn, W. M. Manheimer, and E. Ott. Spheromak tilting instability in cylindrical geometry. *Physics of Fluids*, 24(7):1336–1341, July 1981.

[91] John M. Finn. Tilt and shift stability in a spheromak with a flux core. *Physics of Fluids*, 27(12):2973–2975, December 1984.

[92] P. M. Bellan. Why current-carrying magnetic flux tubes gobble up plasma and become thin as a result. *Physics of Plasmas*, 10(5):1999–2008, May 2003.

[93] M. Taguchi, T. Miyazaki, and S. Kaneko. Magnetohydrodynamic stability of spheromak plasma in toroidal flux conserver with rectangular cross section. *Journal of the Physical Society of Japan*, 54(6):2163–2167, June 1985.

[94] Yu. P. Emets and A. I. Zamidra. Bounded spherical force-free magnetic field configurations with an axial current. *Sov. Phys. Tech. Phys.*, 30(3):284–285, March 1985.

[95] Yasumasa Tsuji. Force-free magnetic field in the axisymmetric torus of arbitrary aspect ratio. *Phys. Fluids B*, 3(12):3379–3387, December 1991.

[96] James. H. Hammer *et al*. Experimental demonstration of compact torus compression and acceleration. *Phys. Fluids B*, 3(8):2236–2240, August 1991.

[97] S. K. Ho, L. J. Perkins, and J. H. Hammer. Potential High-Q, Noninductive Current Drive in Tokamak via Accelerated Compact Toroids. *Fusion Technology*, 17:658–670, 1990.

[98] M. R. Brown and P. M. Bellan. Current drive by spheromak injection into a tokamak. *Physical Review Letters*, 64(18):2144–2147, December 1990.

[99] T. Ogawa *et al*. Compact toroid injection experiment in JFT-2M. *Nuclear Fusion*, 39(11Y):1911–1915, 1999.

[100] C. Xiao, A. Hirose, and W. Zawalski. Trajectory of a compact toroid tangentially injected into an tokamak. *Nuclear Fusion*, 38(2):249–256, 1998.

[101] P. B. Parks. Refueling tokamak by injection of compact toroids. *Physical Review Letters*, 61(12):1364–1367, September 1988.

[102] A. I. Morozov and L. S. Solov'ev. On the acceleration of plasma in a coaxial system. *Sov. Phys. Tech. Phys.*, 5:1033–1038, 1960.

[103] A. I. Morozov. Equilibrium configurations of uniformly accelerated axially symmetric plasmoids. *Sov. Phys. Tech. Phys.*, 12(1):53–56, July 1967.

[104] D. M. Woodall and L. K. Len. Observation of current sheath transition from snowplow to deflagration. *J. Appl. Phys.*, 57(3):961–964, February 1985.

[105] Zhehui Wang and C. W. Barnes. Exact solutions to magnetized plasma flow. *Physics of Plasmas*, 8(3):957–963, March 2001.

[106] A. Fruchtman and Y. Maron. Fast magnetic-field penetration into plasmas due to the hall field. *Phys. Fluids B*, 3(7):1546–1551, July 1991.

[107] Hans C. Ohanian. On the approach to electro- and magneto-static equilibrium. *Am. J. Phys*, 51(11):1020–1022, November 1983.

[108] H. Bhuyan *et al.* Magnetic probe measurements of current sheet dynamics in a coaxial plasma accelerator. *Meas. Sci. Technol.*, 14:1769–1776, August 2003.

[109] M. Landreman *et al.* Rapid multiplexed data acquisition: Application to three-dimensional magnetic field measurements in a turbulent laboratory plasma. *Rev. Sci. Instrum.*, 74(4):2361–2368, April 2003.

[110] S. Galtier *et al.* Self-similar energy decay in magnetohydrodynamic turbulence. *Physical Review Letters*, 79(15):2807–2810, 1997.

[111] C. L. Rousculp and R. L. Stenzel. Helicity injection by knotted antennas into electron magnetohydrodynamical plasmas. *Physical Review Letters*, 79(5):837–840, August 1997.

[112] G. I. Barenblatt and A. J. Chorin. New perspectives in tubulence: Scaling laws, asymptotics, and intermittency. *SIAM Rev.*, 40(2):265–291, June 1998.

[113] F. Wagner *et al.* Regime of Improved Confinement and High Beta in Neutral-Beam-Heated

Divertor Discharges of the ASDEX Tokamak. *Physical Review Letters*, 49(19):1408–1412, November 1982.

[114] C. Riccardi *et al*. Turbulence generated by electrostatic fluctuations. *Physica Scripta*, T75:232, 1991.

[115] S. J. Zweben *et al*. Edge turbulence imaging in the Alcator C-Mod tokamak. *Physics of Plasmas*, 9(5):1981–1989, May 2002.

[116] C. E. Bush *et al*. H-mode threshold and dynamics in the national spherical torus experiment. *Physics of Plasmas*, 10(5):1755–1764, May 2003.

[117] R. P. Drake. The design of laboratory experiments to produce collisionless shocks of cosmic relevance. *Physics of Plasmas*, 7(11):4690–4698, November 2000.

[118] J. Cho and A. Lazarian. Compressible MHD Turbulence: Mode coupling, Scaling Relations, Anisotropy, New Regime, and Astrophysical Implications. *Mon. Not. R. Astron. Soc.*, 345:325, 2003. Can also be found at: arXiv:astro-ph/0301062 v2 11 Jan 2003.

[119] B. S. Tanenbaum and D. Mintzer. Energy transfer in a turbulent fluid. *Phys. Fluids*, 3(4):529–538, July 1960.

[120] F. Stefani and G. Gerbeth. Velocity reconstruction in conducting fluids from magnetic field and electric potential measurements. *Inverse Problems*, 15:771–786, 1999.

[121] G. R. McKee *et al*. Turbulence imaging and applications using beam emission spectroscopy on DIII-D (invited). *Rev. Sci. Instr.*, 74(3):2014–2019, March 2003.

[122] Michel Chahine. Motion-compensated interpolation using trajectories with acceleration. In *IS&T/SPIE Symposium on Electronic Imaging* , Digital Video Compression , volume 2419, San Jose , CA , Feb 5–10 1995.

[123] M. Kawasaki, S-I. Itoh, and K. Itoh. Statistics for transition of plasma turbulence with multiple characteristic scales. arXiv:physics/0302021 v1 7 Feb 2003.

[124] L. M. Malyshkin, T. Linde, and R. M. Kulsrud. Magnetic reconnection with anomalous resistivity in two-and-a-half dimensions I: Quasi-stationary case. arXiv:astro-ph/0508094 v1 3 Aug 2005.

Appendix A

Magnetic helicity of a compact toroid

The key idea in magnetic relaxation is that short timescale effects such as microturbulence and reconnection cause the magnetic fields to decay and become reconfigured in space in such a way as to find a state of minimum total energy. This minimum is non-zero because the total magnetic helicity of the plasma is a conserved quantity on the MHD timescales, and this provides a constraint on the system [74], [59], [81]. The magnetic field can only become reconfigured in ways that preserve the value of the magnetic helicity $\mathbf{A} \cdot \mathbf{B}$ integrated over the volume of the plasma. In order to measure this constant

$$H = \int_V \mathbf{A} \cdot \mathbf{B} \; dV \tag{A.1}$$

we need to determine the vector potential $\mathbf{A}$. The magnetic field is curl of the vector potential, and so $\mathbf{A}$ is determined only up to the gradient of a scalar function.

For the case of a force-free field it is sufficiently general to formulate A in terms of the magnetic field and two scalar functions $\gamma = \gamma(\mathbf{x})$ and $\psi = \psi(\mathbf{x})$ according to

$$\mathbf{A} = \gamma \mathbf{B} + \nabla \psi \tag{A.2}$$

The helicity is gauge invariant for a bounded plasma in a conducting vessel, and the helicity integral simplifies to

$$\int_V \mathbf{A} \cdot \mathbf{B} \ dV = \int_V \gamma B^2 \ dV$$

The $\nabla \psi$ term was dealt with by applying a vector identity in combination with $\nabla \cdot \mathbf{B} = 0$, followed by the use of the divergence theorem and the fact that $\mathbf{B} \cdot \mathbf{n} = 0$ at the walls of the conducting vessel. We see that the grad ψ term vanishes.

$$\int_V \nabla \psi \cdot \mathbf{B} \ dV = \int_V \nabla \cdot (\psi \mathbf{B}) \ dV = \int_{\partial V} \psi \mathbf{B} \cdot dA = 0$$

For a force free magnetic field configuration satisfying $\nabla \times \mathbf{B} = \lambda \mathbf{B}$ the multiplicative factor $\gamma(\mathbf{x})$ that determines $\mathbf{A}$ can be found by taking the curl of $\mathbf{A}$

$$\mathbf{B} = \nabla \times \mathbf{A} = \gamma \nabla \times \mathbf{B} + (\nabla \gamma) \times \mathbf{B}$$

so

$$\lambda \mathbf{B} = \frac{1}{\gamma} \mathbf{B} - \frac{\nabla \gamma}{\gamma} \times \mathbf{B}$$

Then taking the dot product with $\mathbf{B}$ eliminates the cross product term and we see that

$$\lambda B^2 = \frac{1}{\gamma(\mathbf{x})} B^2$$

so $\gamma(\mathbf{x}) = 1/\lambda$ which is a constant. So the vector potential is uniquely determined (up to a scalar gauge) by the magnetic field and the force free eigenvalue λ. The vector potential for a force free magnetic field is simply

$$\mathbf{A} = \frac{1}{\lambda} \mathbf{B} \tag{A.3}$$

The magnetic helicity is then directly proportional the total magnetic energy

$$H = \frac{1}{\lambda} \int_V B^2 \ dV \tag{A.4}$$

This result implies that once a plasma has reached a force-free state, the total magnetic energy cannot be reduced any further because it is constrained by the conservation of H. From then on, the magnetic field and the helicity can decay only at a much slower rate due to the bulk resistivity of the plasma. [89]

Appendix B

Magnetic computations

for probe calibration

In this appendix we present the details of a variety of approaches that were explored to tackle the problem of magnetic measurements in a finite conducting well. (See chapter 2 for application.)

B.1 Plane with circular hole

The simplest is to regard the probe well as simply a hole in the vessel wall which we can reasonably approximate as flat. The magnetostatic field near a circular hole in a thin flat conducting plate has a tractable analytic solution expressible as an integral that can be numerically evaluated [21]. The magnetic field $\mathbf{H}$ has the form $\mathbf{H} = -\nabla \phi_M$ where the magnetostatic potential ϕ_M is given by

$$\phi_M = \begin{cases} -H_0 y + \Phi^1(\vec{x}) & \text{if } z > 0 \\ -\Phi^1(\vec{x}) & \text{if } z < 0 \end{cases}$$

This form guarantees that $\mathbf{H} = -\nabla \phi_M$ will approach a constant vector of magnitude H_0 in the y-direction, as you move away from the hole in the upper half space, while the field goes to zero in the lower half plane. Thus, $\Phi^1(\vec{x})$ describes the localized variation away from complete uniformity. The solution of $\nabla^2 \Phi^1 = 0$ given the boundary conditions of a hole of radius a can be found by Bessel series expansion in cylindrical coordinates (ρ, ϕ, z)

$$\Phi^1(\vec{x}) = \frac{2H_0 a^2}{pi} \int_0^\infty dk j_1(ka) e^{-k|z|} J_1(k\rho) \sin\phi \tag{B.1}$$

where $j_1(x) = \frac{\sin x}{x^2} - \frac{\cos x}{x}$ is the spherical Bessel function of order 1, and $J_1(x)$ is just an ordinary Bessel function of the first kind, order 1.

This solution is attractive to work with because it is fully 3-dimensional, so the total flux through a coil oriented arbitrarily in space can be accurately calculated. However, the simplicity of the boundary geometry yields some quantitatively different effects than the actual, more complex, probe well geometry. The root cause of this discrepancy is that in the case of the simple hole, the field is allowed to expand out infinitely into to void beneath the plane, instead of just the finite sized well that we actually have. This means that more total flux enters the hole than would enter the opening of a well. Since more flux enters, the field beneath the plane is stronger for the hole geometry than the well (i.e., the field below the hole is diminished less than it would be inside the well). Then the calibration factor $\frac{H_0}{\langle H \rangle_p}$ due to field diminishment caused by expansion, would be somewhat less in the hole geometry than for a finite well.

Secondly, each field line that enters the hole will go deeper than it will in the case of a finite well. Thus for a given probe position, the resulting effective depth will be noticeably larger for the simple hole than it would be for the finite well.

Since we are primarily seeking an accurate estimate of the effective depth of the probe in order to compare measured field components to those predicted by theory, we need to do a better job of including the effects of the finite well geometry. So, let us consider a few more possible ways to approach the full magnetostatic problem for a finite well.
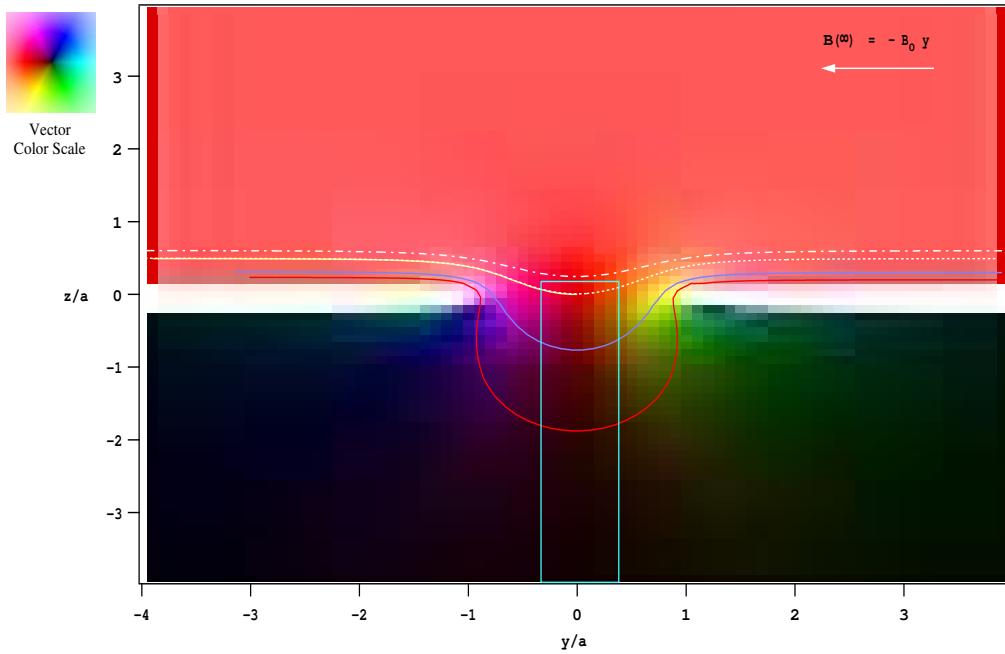
Figure B.1: Analytic result for magnetic field near a hole in a conducting plane. Here the field vectors are represented by a color-wheel type coloring of the complex plane, which corresponds to the (y, z) directions in physical space. Red indicates a vector pointing directly in the -y direction, while other colors represent vectors at other directions as indicated by the color legend in top left. Vector magnitude is represented by a color's brightness, with black for the zero vector. This color code avoids the "pick-up-sticks" effect that can occur with arrow-field representations. A sampling of field lines are also plotted to guide the eye.

B.2   Analytic approach to full problem

The most ambitious route would be to perform a similar Bessel series expansion of the potential as above. However, there is a significant complication that two distinct regions of space would need to be analyzed separately, and then a unique solution to the full problem could be found by matching series coefficients at the interface of the two regions.

The natural choice would be to set one region as the cylindrical volume inside the well, with conducting boundary conditions on the side and base, and the interface matching condition on the top surface. Then the second region would be the upper half space above the plane, with conducting boundary at the $z = 0$ plane, everywhere except for the circular disk where the field needs to match the other region. To implement this, first some analytic simplifications to the general Bessel

series would need to be made that take into account the different symmetries of the two regions. Then you would try to see how matching the coefficient at the interface would constrain the form of the solution. However, at this point, progress toward a purely analytic solution begins to fall into that grey unknown between difficult and impossible, and a numerical solution of the system of coupled integral Fourier-Bessel equations becomes the only tractable option. Then considering that the primary aim of my work was not to spend weeks or months to perfectly solve an advanced 3-D magnetostatic problem by numerical evaluation of Fourier-Bessel equations, I decided to find a simpler, quicker approach.

B.3   Conformal mapping approximation

Since the diameter of the probe coil is relatively small compared with the diameter of the port hole, a 2-D approximation can be made that should be quite accurate for the fields near the central plane of the probe port well. Field expansion effects should be more faithfully recreated by a 2-D solution of the right cross-section geometry than a 3-D solution of the wrong cross-section geometry.

Essentially, the problem in 2-D is equivalent to a field above a conducting plate with an infinitely long trench cut into it, with a rectangular cross-section. If the trench runs in the x-direction, then the solution of the field will be independent of x, it will only vary in the 2-D (y,z) plane. This 2-D solution would correspond to the x = 0 plane in the full 3-D problem.

One standard analytic method for dealing with this 2-D problem is the use of conformal mapping, [83] (pg 10). In general it is possible to transform the upper half of the complex plane into the interior of a polygon, by a conformal map according to a straight-forward formula.

For the case at hand, the resulting polygon would be the "upside-down top hat" shape of the vacuum-conductor boundary. It would have four vertices, and interior angles of $\{\frac{3\pi}{2}, \frac{\pi}{2}, \frac{\pi}{2}, \frac{3\pi}{2}\}$. The original untransformed plane is the z-plane, and the transformed plane is the w-plane; the

mapping function is $w = w(z)$, which is formulated implicitly through a differential relation:

$$\frac{dw}{dz} = G\frac{(z-c)^{\frac{1}{2}}(z+c)^{\frac{1}{2}}}{(z-1)^{\frac{1}{2}}(z+1)^{\frac{1}{2}}} = G\sqrt{\frac{z^2-c^2}{z^2-1}} \tag{B.2}$$
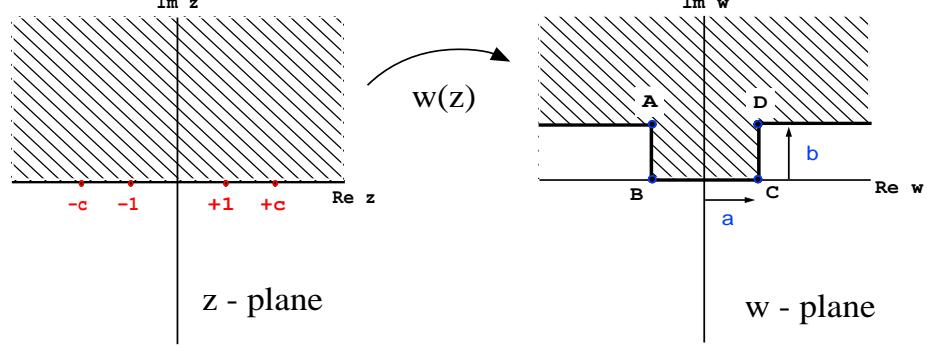
Figure B.2: Conformal mapping method for 2-D approximation

Here, G is a complex constant that accounts for overall scale and orientation of the resulting polygon, and c is a positive real number, where the points $z = \pm c$ get mapped to the vertices at the opening of the well $w = \pm a + bi$, which are labeled points D and A, respectively (see Fig 5). To solve for $w(z)$ we need to take the indefinite path integral, where the integration dummy variable u takes a path from $u = -\infty$ to $u = z$, which is route-independent as long as no branch cuts (along Im $z = 0$) are crossed. The integral is

$$w(z) = G\int_{-\infty}^{z}\sqrt{\frac{u^2-c^2}{u^2-1}}\,du = Gc\int_{-\infty}^{z}\sqrt{\frac{1-(\frac{u^2}{c^2})}{1-u^2}}\,du \tag{B.3}$$

This integral is not possible to evaluate "analytically" in terms of elementary functions, and does not appear in any standard table of integrals. This is because it corresponds to a combination of elliptic integrals of the second kind, usually notated by $\mathrm{E}(k, z)$, here taking a complex argument.

Some formal progress can be made from this realization,

$$w(z) = Gc[\mathrm{E}(1/c, z) - \mathrm{E}(1/c, \infty)] \tag{B.4}$$

and the resulting dimensions of the well radius $= a$, depth $= b$, are determined from G and c according to

$$a = Gc \left[\tilde{E}(1/c) - \mathrm{E}(1/c, \infty) \right], \qquad b = Gc \left[\tilde{K} \left(\sqrt{1 - (1/c)^2} \right) - \tilde{E} \left(\sqrt{1 - (1/c)^2} \right) \right] \tag{B.5}$$

where $\tilde{K}(k)$ and $\tilde{E}(k)$ are complete elliptic integrals of the first and second kind, respectively. The shape of the well (i.e., the ratio b/a) is then independent of G and has the form

$$\frac{b}{a} = \frac{\tilde{K} \left(\sqrt{1 - (1/c)^2} \right) - \tilde{E} \left(\sqrt{1 - (1/c)^2} \right)}{\tilde{E}(1/c) - \mathrm{E}(1/c, \infty)} \tag{B.6}$$

It was not too difficult to implement a direct numerical evaluation of the path integral $(B.3)$, and some qualitatively good initial results were obtained.

Once you have the mathematical mechanics set up, it is very easy to find the shape of field lines in the vicinity of the well. You just sequentially evaluate $w_p = w(z_p)$ N times, where $z_p = (x_0 + p \cdot \Delta x) + iy$ for point index taking values of $p \in \{0, 1, 2, \ldots, N\}$. This just maps the horizontal line Im $z = y = $ constant to the corresponding field line. The resulting array of complex numbers w_p can be plotted to visualize the field line in space.

Furthermore, the effective depth can be found by tracking field lines away from the well and then finding how high above the wall they are after going several hole-radii away from the well. Field expansion ratios can be calculated by comparing the distance between two neighboring field lines, when they are far from the well, vs. when they are at the center of the well.

Since the magnitude of the magnetic field is proportional to the density of flux lines, in this way we can get the ratio of the far field to its corresponding value of the distorted near field. To measure the average flux through the probe coil, we just choose one field line that passes through the upper tip of the coil, and a second that passes through the lower tip of the coil. If the distance between these two field lines far from the probe well is δz and the height of the probe coil is Δz_{coil} then the calibration factor due to field expansion is $C_{exp} = \frac{\Delta z_{coil}}{\delta z}$.

The one stumbling block that prevented the full application of this method to solve the problem at hand is that, for reasons not yet understood, the ratio of b/a was not precisely controllable

with the algorithms I have implemented. Essentially, only a single value of $b/a \sim 1$ was achievable, regardless of the choice of c and G. An intrinsic part of the problem is that my algorithm was divergent for points close to the real axis in the z-plane. This prevented me from making an accurate determination of what the real b/a ratio was for any particular instance of the mapping. There is some hope that after some further work with elliptic integrals, the increased insight and experience may lead to a resolution of the bugs in my code. But for the sake of time management, I abandoned this semi-analytic approach and switched to an even simpler fully numeric 2-D iterative relaxation method.

B.4   Gauss-Seidel iterative relaxation

We begin this final (successful) approach with a significant practical simplification. The magnetic field vectors themselves are not really important to find the effective depth and expansion factor, especially if we are only considering a 2-D case. Really we just need to know the shape of the flux surfaces on which the magnetic field lines reside. The simplifications arises from the fact that the magnetostatic potential ϕ_M is what we call the *harmonic dual* of the electrostatic potential ϕ_E. [20]

The concept of harmonic duality is that if two scalar functions satisfy the Laplace equation ($\nabla^2 \phi = 0$, which is the definition of harmonic here) on the same boundary geometry, we say that the functions are dual to each other if one function satisfies Dirichlet boundary conditions ($\phi_1 = $ constant), while the second function satisfies Neumann boundary conditions ($\frac{\partial \phi_2}{\partial n} = $ constant). The result is that equipotential surfaces of ϕ_1 correspond to flux surfaces of ϕ_2, and vice versa. This is due in part to the fact that equipotential surfaces and the flux surfaces for the same potential function are locally orthogonal to each other. To go from a potential function to its harmonic dual, we just have to interchange the role of equipotentials and flux surfaces, and the resulting potential will still satisfy the Laplace equation, but with the dual boundary condition.

The magnetostatic potential satisfies the Neumann boundary condition at the surface of the conductor, while the electrostatic potential for the same conductor geometry satisfies the Dirichlet boundary condition. Therefore, we can find the flux surfaces of the magnetic field by actually computing the equipotential surfaces of the dual electrostatic potential problem. This is an advantage because Dirchelet boundary conditions are intrinsically simpler in that you don't have to evaluate derivatives to apply them, and they lend themselves to numerical solution by iterative relaxation methods.

I have implemented a simple Gauss-Seidel method using a 2-step iteration on two inter-leaved square meshes. [21, pp. 47-50]
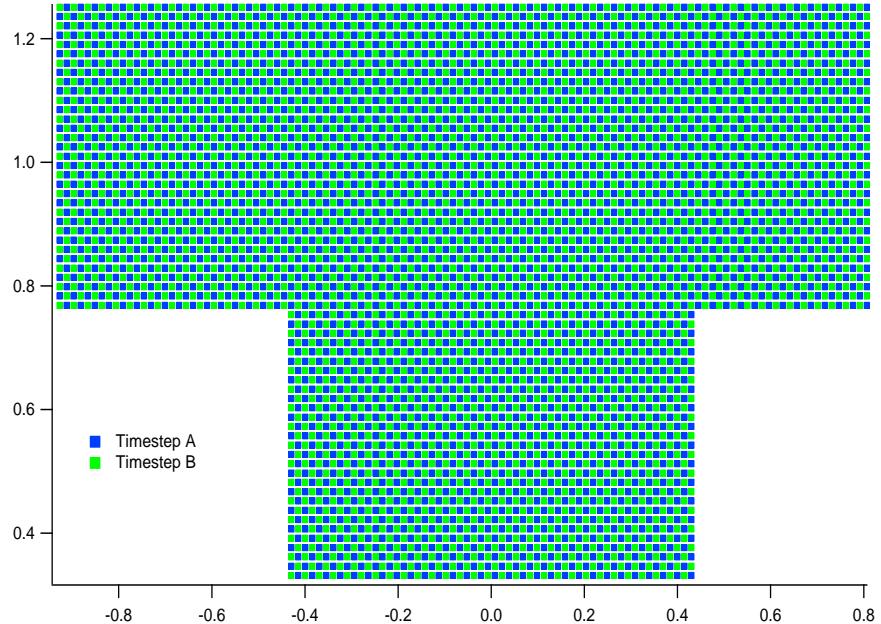
Figure B.3: Two interleaved meshes, one for each timestep, used for calculating magnetic field near probe port

The iteration scheme divides the mesh into two lists of coordinates, corresponding to pair of interleaved meshes depicted in fig B.3. First, using list A of coordinates $L_A = \{(x_0, y_0), (x_1, y_1), \ldots\}$, which correspond to the blue squares in fig B.3, we evaluate a new value for ϕ that is equal to the average of its neighboring values, including newly modified values on the same list. Then we repeat

using list B (corresponding to the green squares in fig B.3).

$$Step\ A: \quad \phi_{new}(x,y) = \frac{4}{5}\langle\phi_{old\ B}\rangle_c + \frac{1}{5}\langle\phi_{new\ A}\rangle_s \quad \forall(x,y) \in L_A$$

$$Step\ B: \quad \phi_{new}(x,y) = \frac{4}{5}\langle\phi_{old\ A}\rangle_c + \frac{1}{5}\langle\phi_{new\ B}\rangle_s \quad \forall(x,y) \in L_B$$

where $\langle\phi\rangle_c$ is the "cross" average of neighboring values in the opposite list, and $\langle\phi\rangle_s$ is the "square" average of neighboring values in the same list that is being currently updated,

$$\langle\phi(x,y)\rangle_c = \tfrac{1}{4}[\phi(x+\delta,y) + \phi(x,y+\delta) + \phi(x-\delta,y) + \phi(x,y-\delta)]$$

$$\langle\phi(x,y)\rangle_s = \tfrac{1}{4}[\phi(x+\delta,y+\delta) + \phi(x+\delta,y-\delta) + \phi(x-\delta,y+\delta) + \phi(x-\delta,y-\delta)]$$

where δ is the pixel size of the mesh.

The initial configuration at timestep 0 was such that $\phi_M = 0$ inside the well and along the walls, while a constant upward gradient in ϕ_M existed in the upper half plane. As the iterations progress the field steadily expands into the well and relaxes into a solution of Laplace's equation. The program halts after a preset number of iterations (stop when $i = N$). We tried different values of N and recorded how the Laplacian error asymptotically leveled off toward a stable minimum. For a mesh of 200×200 pixels, after about $N \sim 1500$ iterations the largest error in the system was less than 10^{-2} (see fig B.5).

A quantitative analysis of the results are discussed in chaper 2.
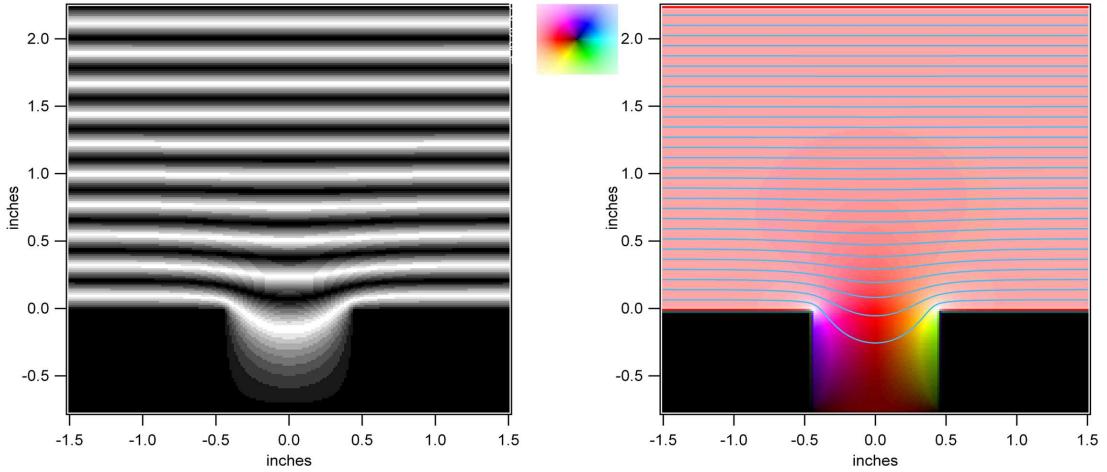
Figure B.4: 2-D Relaxation simulation result of magnetic field near a conducting port well. Image on left uses a cyclic greyscale to visualize flux surfaces. Image on right represents the magnetic field vectors using a color-wheel type coloring of the complex plane, which corresponds to the (y, z) directions in physical space. Red indicates a vector pointing directly in the -y direction, while other colors represent vectors at other directions as indicated by the color legend in top left. Vector magnitude is represented by a color's brightness, with black for the zero vector.
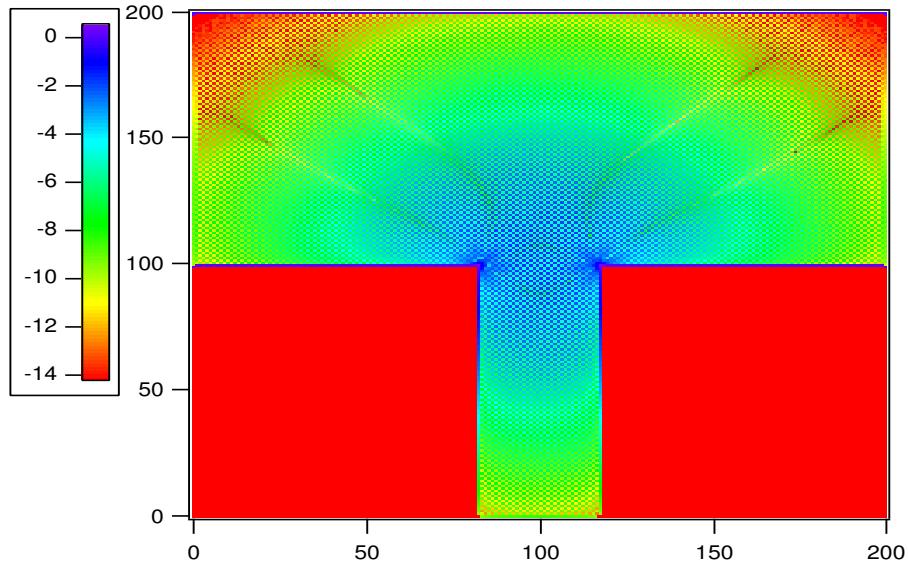
Figure B.5: The log (base 10) of the value of the Laplacian of the magnetostatic potential near a conducting port well. Since the goal is $\nabla^2 \phi = 0$, this graph indicates the order of magnitude of the error in the calculation.
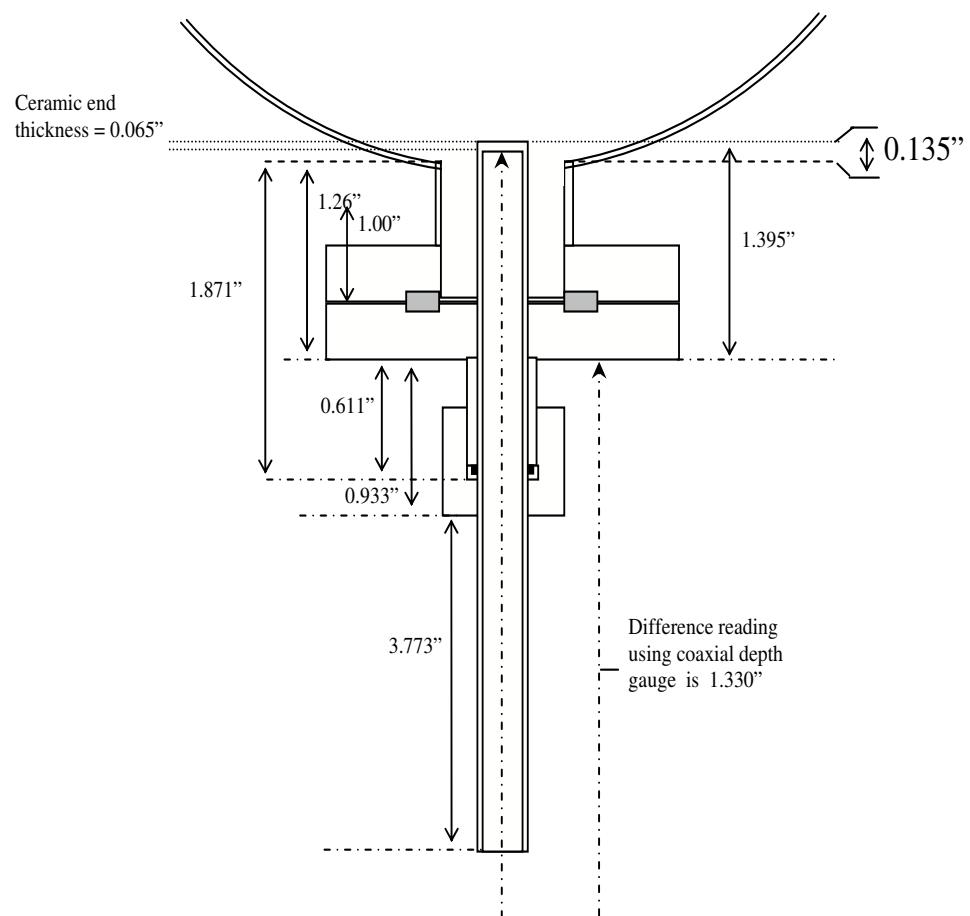
Figure B.6: Mechanical drawing of probe port at z = 142 cm showing measured dimensions.

Appendix C

Method of reconstructing

a moving pulse

In the following discussion we present a general purpose method of analyzing a set of N time signals $F_i(t)$, $i \in \{1, 2, \ldots, N\}$ that consist of local measurements of the same physical observable taken at the N sequential diagnostic port locations of a linear accelerator device, with i being the port index (e.g. 57, 91, 142 for CTIX). We describe an algorithm that can reconstruct an accurate approximation of the true space and time dependence of the given observable $F(z, t)$ in the regions between the points of measurement where diagnostic access is possible. This method has many conceptual parallels with the method of characteristics used in analyzing nonlinear wave motion, however we are looking at the problem from a vantage point that deals more with experimentally relevant issues of applied mathematics, and not at all with the issues involved in a theoretical analysis of some set of differential equations. We also explore the conditions needed for this approximation to hold, and we test the algorithm under a variety of circumstances.

C.1 Sequential measurements of a moving pulse

The motivation for developing this type of interpolation originates with the daily task of trying to interpret time-domain data from a set of spatially distributed diagnostic signals, on the fly as the data comes in during an experimental run. After some experience with the raw signals, a sort of mental-interchange of space and time coordinates is possible to visualize; resulting in an intuitive appreciation of the accelerator dynamics and an approximate understanding of how a given observable varies in space. Of course, it is often difficult to fully communicate this understanding to others who are less familiar with the nuances of the particular system under consideration. In this appendix we present the details of an algorithm that produces a quantitative result that makes the accelerator dynamics easy to interpret. (Compare to [104], [108]).

Some sample data is presented below in fig.C.1. It shows the time dependence of the magnetic field measured by probes on the CTIX accelerator section.
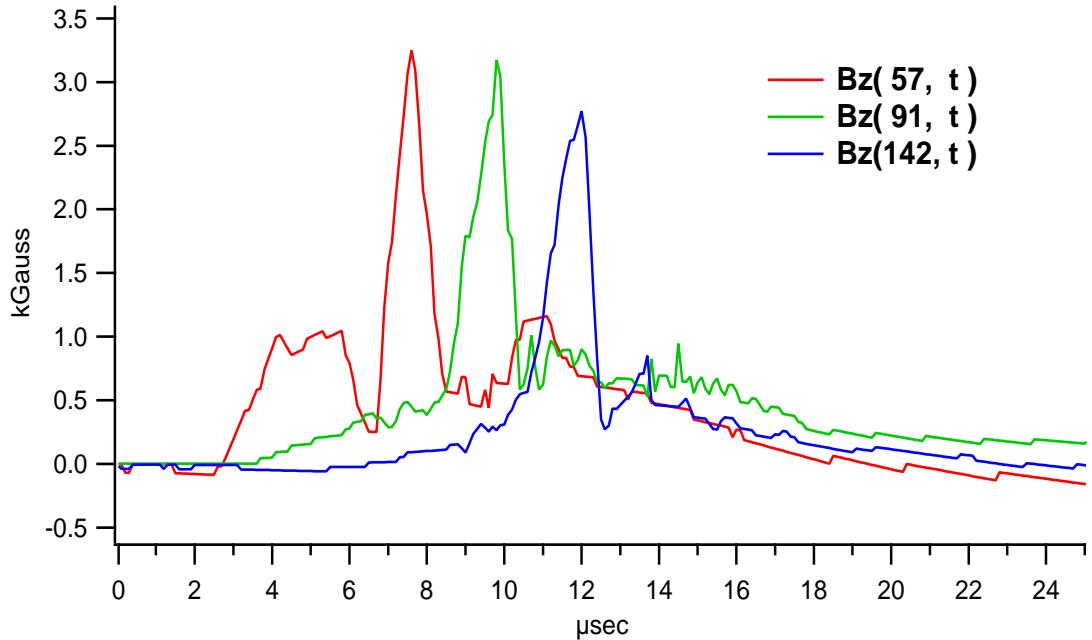
Figure C.1: Example of time-signals from axially distributed probes. These are the three measurements of $B_z(t)$ taken within the CTIX accelerator at positions z = 57, 91, 142 cm.

This work has been primarily motivated by signals like this and the desire to use them to determine the true magnetic geometry of the compact toroid plasma. Essentially, we would like to know what is the function $B(z,t)$ that describes the magnetic field as a function of axial position and time (see chapter 2). Additionally, a variety of other experimental observables are also measured at sequential positions and can benefit from this interpolation analysis. For example, these signals could be the average electron density, visible light emission, or plasma probe current at several axial positions as a function of time. In chapter 6 we used this reconstruction method on a sequence of visible emission measurements to determine plasma luminosity as a function of space and time.

It is interesting to note that a similar algorithm is used in video decompression schemes when trying to interpolate in time between actual frames of a video image, in order to reconstruct a better video at a higher frame rate [122]. The motion of distinct features within an image can be taken into account to predict where each feature will be at any intermediate time t, according to a quadratic model of its trajectory. In this problem the observables are vectors, and the details of any practical solution ultimately rely on some advanced image analysis.

While the problem of one dimensional flow considered in our work is in some sense a lower-dimensional special case of the motion-compensated interpolation used in video analysis (where the analogy requires an interchange of the space and time coordinates used in the two problems) it is worth formulating this application on its own in a coherent and more directly usable way.

The algorithm we have developed can be broken down into two distinct sub-processes. The goal of the first process is to estimate the fluid velocity field for all (z,t) in the system, by any means necessary. The method used to make this estimation will need to rely on specific physical properties of the dynamical system under consideration. What are the basic constraints on the velocity field? Can "fluid/wave" elements pass through each other with several different velocities at the same point, such as would happen with a superposition of traveling waves in a dispersive medium? If this is the case, then an accurate reconstruction of the field observable and its wave phenomena would need to begin with a good characterization of all of different wave velocities present.

This kind of complication is far beyond what has been considered so far; we will only deal with the much simpler case of fluid elements that never interpenetrate along the axis of motion (i.e., a single valued and continuous velocity field). This seems to be sufficient to describe the experimental observations of magnetohydrodynamics on the CTIX accelerator, moreover, the assumption of single valued velocity is consistent with basic intuitive reasoning about the evolution of a magnetic field that is frozen into a moving fluid.

The second process takes this estimated velocity field and uses it to create fluid element trajectories, and finally computes a unitary-weighted superposition of the adjacent real data to determine the interpolated value of the observable at intermediate positions along each trajectory.

C.2   Estimation of flow field

On the most fundamental level, everything will depend on some incarnation of a mapping function that defines a correspondence between points on one probe signal with points on the signals of neighboring probes. This kind of mapping function is essentially a way to label the fluid elements in some unique way so that they all can be tracked. This tracking information enters our awareness in terms of measurements of the time at which each fluid element passes by each probe location.

The criteria that defines which pairs of points correspond to each other is really a very system-specific issue. To do a good job with this, some consideration of the physical dynamics will be needed. And each distinct physical system may need its own bag of tricks. Overall, there are two basic varieties of possible point-matching criteria, which can be classified as being either point-wise in nature, or having a dependence on the collective properties of some subset of the data points in the signals.

We will now list a number of important examples of *point-wise* matching criteria.

1) Peak-to-peak   This is a discrete valued map that only tracks a single fluid element through the system. This criterion defines the *fluid element of peak amplitude*, and we measure the time it

crosses each successive probe position by finding the time at which each probe signal reached its maximum value. We can generalize this to track the fluid elements that ride along with any of the local extrema in the field.

2) Level set labeling   This is a continuous method that might be useful in certain non-dissipative systems, where we identify two points on adjacent probe signals if they have the same amplitude, and exist within corresponding "regions", which is an additional constraint needed to prevent the labeling from being many-to-one. It is often reasonable to partition the domain into regions that fall between successive local extrema in the signal. In this way we ensure that every point is labeled in a unique way. This type of labeling can be extended to dissipative systems if we can normalize all of the probe signal to give them the same range of values, yet still preserve the correct kinematic behavior of the system.

3) Differential labeling   The simplest instance of this type would be to make a correspondence between points of maximum ($\pm$) slope in the probe signals. Clearly, this could be extended in a variety of ways similar to those already mentioned.

The second category of matching criteria, *collective correspondence maps*, define relations between groups of points in one probe signal to corresponding groups of points in the neighboring probe signals, often with no explicit relation between pairs of individual points, instead it is implicitly determined via the collective relation. There are two important examples relevant to our work.

1) Correlation methods   Ideally we want to find the time-of-flight of each distinct fluid element as it travels between adjacent probes. We can begin to do this by calculating the correlation function between adjacent probe signals.

$$C_i(\Delta t) = \int_{-\infty}^{\infty} F_i(t)F_{(i+1)}(t + \Delta t)dt$$

The global maximum of $C_i(\Delta t)$ occurs when Δt results in the optimum translational correspondence between the two signals.

For a moving pulse that does not change shape very rapidly as it travels, this method has certain advantages over point-wise maps, such as the peak-to-peak method, which can produce erroneous results due to any moderately high frequency noise occurring near the peak of the pulse. Instead, the correlation averages out any noise and finds the best overall fit between the signals.

For any real system in which acceleration is occurring, this is not enough to properly estimate the velocity field. One conceptually attractive approach is to make a first order approximation using the global correlation to match the peaks of the signals, then go back and make a second order correction, again using correlation integrals to calculate the optimal translation, but this time locally, over a sequence of subwindows that progress away from the peak toward $(t = \pm\infty)$. The result is a time-shift function $\Delta t_{ij}(t)$ that defines the correspondence between points in adjacent probe signals F_i, and F_j, according to $F_i(t + \Delta t_{ij}(t)) \simeq F_j(t)$. The time-shift function depends on the first and second order correlations in a straight-forward way, $\Delta t_{ij}(t) = \Delta t^{[1]} + \Delta t^{[2]}(t)$. Overall, this method would find the optimal (non-uniform) stretch to make one function fit another.

However, there are a number of difficult pitfalls involved in actually calculating this second-order correction. One problem is that any overall slope in the signals across the length of the subwindow will lead to the maximum value on a boundary point always being optimally correlated with the largest neighboring peak in the second signal, regardless of any real coincidence between the ups and downs of the two signals. To make this idea work requires some sophistication, possibly fitting smooth curves to the signals in the subwindows, and then only correlating the residuals from this fit. An added complication is the question of how to iteratively evaluate and then apply the local time-shift function, as the subwindow moves away from the peak.

A more important issue with this method is that not all moving pulses will leave time-signals that can be used to reconstruct the original pulse via correlation methods. The primary pathological examples are dispersive pulses consisting of several distinct wave components, each traveling at a different phase velocity. Even the case of two wave components can lead to serious errors in estimation of wavelength of the individual components, and the overall shape of the pulse.

This error is simply due to the correlation method incorrectly matching wave crests. Basically, this method uses the overall group velocity of the pulse, when it should be finding distinct phase velocities.
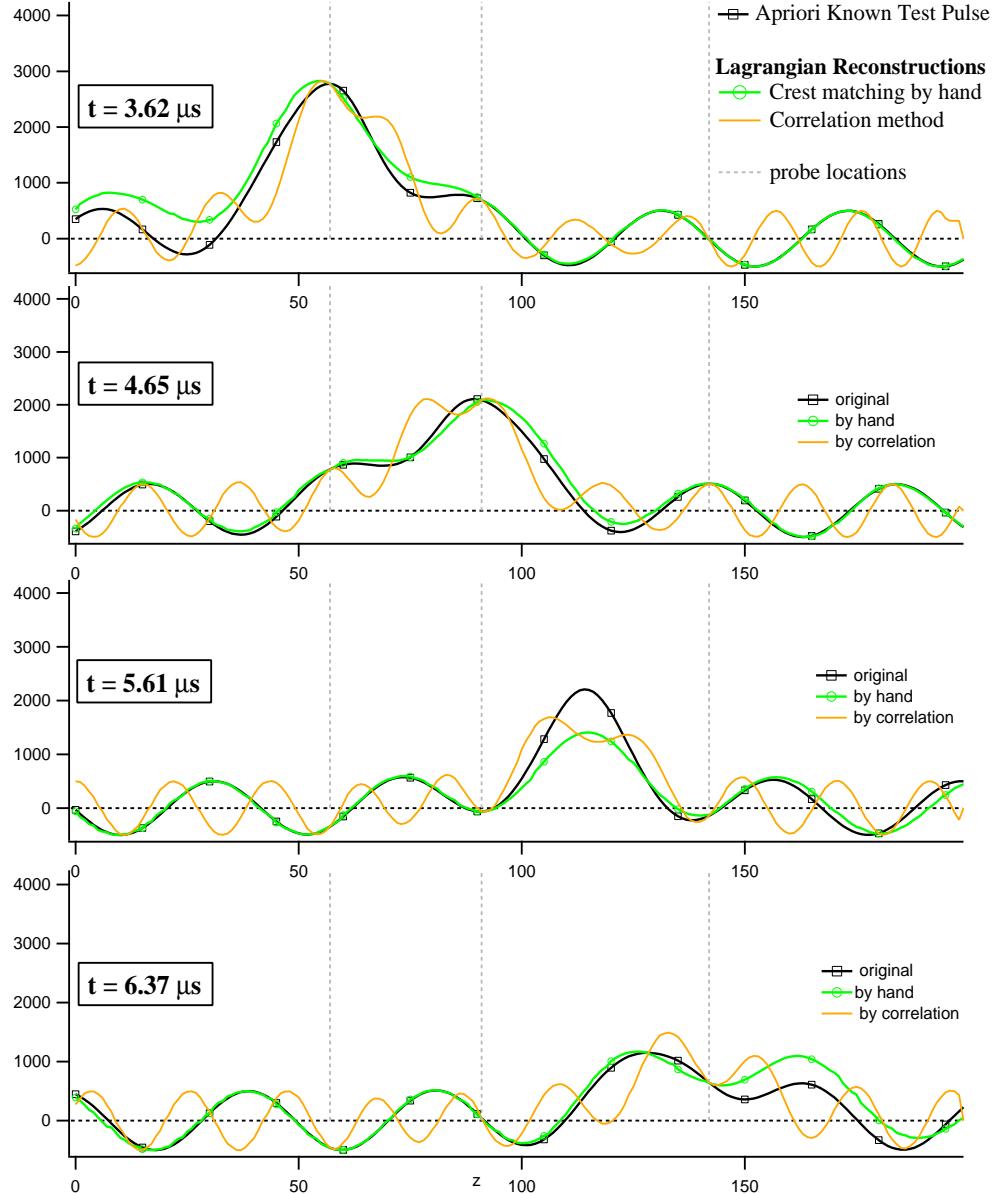
Figure C.2: Example of waveform that causes problems with the correlation method (orange curve). A simple remedy exists (green curve), but this example shows the limitation of the correlation method.

The error in this reconstruction occurred because we were simply using the wrong velocity field. If we carefully match wave crests correctly by hand, and then simply use piecewise linear extrapolations to estimate the velocity, we do significantly better in our reconstruction.

This goes back to my point about the importance of including your best understanding of a system's dynamics to make the velocity estimation. Correlation methods should not be used when they are in disagreement with the basic physics of the system. However, when multi-wave effects are unimportant, successfully implemented correlation methods can be robust and elegant.

2) Kinematic modeling When some kinematic property of a dynamical system is well established, it can be used to directly estimate the velocity field [120]. The correspondence between points in neighboring probe signals will be entirely implicit in this method, but could be found by calculating trajectories from the estimated velocity field.

Implementation specific to CTIX Consideration of the acceleration dynamics leads to a relatively simple model of the velocity field defined in a piece-wise fashion.

$$\text{v}(z,t) = \begin{cases} \sqrt{2 \ \bar{\text{a}} \ (z - z_{min})} & \text{if } z > z_{fit} \\ \sqrt{2 \ \bar{\text{a}} \ (z_{fit} - z_{min})} & \text{if } z \leq z_{fit} \end{cases} \tag{C.1}$$

which has previously discussed in section 2.3

C.3   Lagrangian interpolation algorithm

This method can be simply described by the following general formula for the interpolated value of the observable $F(z,t)$ at position z between the ith and $(i+1)th$ real probes, which involves a unitary superposition of neighboring probe signals, evaluated at retarded and advanced times:

$$F(z,t) = w_i(z,t)F_i(t + \Delta t_i(z,t)) + (1 - w_i(z,t))F_{(i+1)}(t + \Delta t_{i+1}(z,t)) \tag{C.2}$$

where w_i is a weighting factor (≤ 1) dependent on the fractional distance between the position z of

and the positions of the real probes. Although w_i can in general depend on z and t, the simplest

good implementation is actually independent of time, $w_i(z) = (z - Z_i)/(Z_{i+1} - Z_i)$ where Z_i is the

position of the *ith* real probe, $i \in \{1, 2, ...(N-1)\}$. The function $F_i(t)$ is the time signal of the

ith real probe, and $\Delta t_i(z, t)$, $\Delta t_{i+1}(z, t)$ are some delay functions that will need to be optimized

for best agreement with the approximately measured flow dynamics inferred from the time of flight

between sequential probes. For fluid that is moving in the positive z direction, a given fluid element

first passes by the lower probe at Z_i, then it passes through the value of z under consideration for

interpolation, and lastly it passes the upper probe at Z_{i+1}. And so with the sign convention used

in (C.2) we see that $\Delta t_i(z, t)$ will have negative values, while $\Delta t_{i+1}(z, t)$ will have positive values.

Examples of the application of this method to actual data from CTIX have been presented

in chapters 2, 4, and 6.

C.4   Trajectory calculations

Once the velocity field is known, it is straightforward to calculate the time shifts $\Delta t_i(z, t)$

used in the Lagrangian interpolation itself. The algorithm simply loops through every (z, t) in the

domain, at each point it creates two trajectory waveforms, one going forward in time, and the other

backward in time. Each trajectory waveform is really a pair of dynamically redimensioned 1D arrays,

one contains the calculated position of a fluid element along the trajectory, while the second contains

the time coordinates at which the position measurements have been made. The zeroth element in

the trajectory waveform corresponds to the starting position that lies on the domain grid, however

as subsequent timesteps have been taken along the trajectory, the array coordinates will not match

up with any discrete valued (z, t) grid coordinate. At each timestep in the trajectory calculation,

the fluid velocity is evaluated at the current trajectory point, and the next point in the trajectory

waveform is added by going some small fractional distance $ds/|v|$ in the direction of the spacetime

velocity vector $(v_z, 1)$, where the time-component of this vector representation of a 1D velocity is unity. In this way the $(i+1)th$ trajectory point (z_{i+1}, t_{i+1}) depends on the ith point according to:

$$z_{i+1} = z_i + ds \cdot \frac{v_z}{|v|} \qquad (C.3)$$

$$t_{i+1} = t_i + ds \cdot \frac{1}{|v|} \qquad (C.4)$$

And the trajectory points are only added to the waveform until the nearest neighboring probe location has been crossed. We find the crossing time t_{xing} by interpolating across the transitional interval where $z_j < z_{probe} < z_{j+1}$, such that $t_{xing} \in [t_j, t_{j+1}]$

Finally, we find the timeshift for the Lagrangian interpolation simply by $\Delta t_i(z, t) = t_{xing} - t$.

C.5   Validity of approximation

First the good news. If carefully implemented, this interpolation is 100% accurate at all of the locations where the real measurements have been made. Of course, this must be so for any kind of interpolation, and formula (C.2) is no different.

In the following subsections we examine two fundamental categories of errors in this algorithm. The first kind of error can occur in the estimate of the velocity field. This is the most important practical concern because if the velocity field is wrong then the final reconstruction will probably suffer from a variety of serious errors. The second kind of error can occur even if you have a perfect formulation of the velocity field, and we will explore the hypothetical worst case that is mathematical allowable, in which transient pulses appear and disappear in the physically real field variable, but do so in the regions between probe measurement and thereby go undetected.

C.5.1   First order velocity error

Here we will examine in some detail the errors produced in a certain formulation of a pointwise velocity estimation method that has been particularly useful on CTIX data. We need to find the error in the velocity curve of the CT/pushing-field interface (CT back edge), since any error at

this stage will have an effect on the entire reconstruction. The key idea is that there will be some time error Δt in the measurement of the time that the CT back passes each probe position, and this error is dependent on the random fluctuation of the signal level, and inversely proportional to the slope of the signal at the crossing time. $\Delta t = \frac{1}{m} \Delta B_z$.

First we need to estimate the signal fluctuation level. Here we will investigate the high frequency noise in the B_z signal as being the source of any errors in computing the velocity of the CT as a function of time. We will define the signal fluctuation to be the maximum absolute value of the residual of the B_z signal after subtracting off a smoothed version $S_i(t)$ of the original signal.

$$\Delta B_z = \max \left| B_z(t) \; - \; \lim_{\xi_i \leq \xi_{stop}} S_i(t) \right|$$

However, the result of this is dependent on exactly how much smoothing is done. The parameters of the limit, ξ_i and ξ_{stop}, simply represent a stopping condition for the smoothing process, and will be defined shortly. To provide an objective criterion for sufficient smoothing, and thereby yield uniform results in this analysis, we will adopt the following procedure to implement the smoothing. The primary concern of this procedure is that it smooths enough, but not too much. The fluctuations that we identify as noise in our B_z signals typically exhibit a rapid change from positive to negative slope over a short interval of time. And so the "true" signals (as we conceptualize them) that lie underneath the noise will not have this "jumpy" character to them. As a reasonable measure of this "jumpiness" factor we can consider the first time derivative of the partially smoothed signal S_i, and then multiply it by a weighting factor determined by the duration that the signal is near that value of time-slope. The result is a function of time

$$jump(t) = \frac{1}{Duration(slope)} \cdot \frac{dS_i(t)}{dt}$$

Here, the term $Duration(slope)$ is simply the time between zero crossings of the time derivative, and it measures (in a piecewise fashion) the duration that the signal has either positive or negative slope. The reason for dividing by the duration of same-sign slope is that the physically real signal may have large slopes, but it will typically maintain this slope for some extended period

of time; whereas noise will change the sign of its slope every few digitization steps.

As the original signal is iteratively smoothed, the noise will be removed, and the maximum absolute value of $jump(t)$ of the ith partially smoothed signal S_i , will fall monotonically. Let us call this jumpiness parameter $\xi = \max |jump(t)|$. The smoothing process should stop when ξ falls below some small predetermined value ξ_{stop}, which represents the goal for smoothness of the noise-free signal. It can also be thought of as corresponding to the fraction of total noise that has been removed from the signal, $(1 - \xi_{stop}) \sim (removed\ noise)/(total\ noise)$. The reason for following this procedure, is that we can make a single subjective choice for a reasonable value of ξ_{stop}, and then use the same value across the board when analyzing all of the magnetic data; yet each signal will yield a different value of fluctuation level ΔB_z depending on its noise properties. This is far more objective than estimating ΔB_z by eye every time you do this analysis.

For example, here is the Bz 57, 91, and 142 signals for shot ?. With a value for the smoothing limit of $\xi_{stop} = 0.01$ we will tabulate the estimated signal error ΔB_z, and a corresponding arrival-time error $\pm \Delta t$ for each probe. Lastly we list the relative error of the final velocity of the CT, derived from the maximum possible error considering all possible sign combinations for each of the arrival time errors.

Note that if you had a set of three new arrival times that were all shifted in the same direction (either + or -) by the same amount Δt, then the calculated final velocity with these "errors" would be exactly the same as the true final velocity. Only if there is some asymmetric distribution of positive or negative errors, will the resulting error of the final velocity reach its maximum value.

Using the value of $\xi_{stop} = 0.01$ in this analysis, for shot 59842, we find that worst case velocity error is 7.86% of the original estimate for the velocity.

C.5.2 Constraints on the amplitude of undetectable transient pulses

In order to estimate the reliability of this reconstruction method we need to carefully consider the worst possible errors that could exist in the space between consecutive probes. We will consider errors that are as large as the mathematics of the algorithm allow, with no concern initially for the physical limitations on such errors. The end result of this analysis is a constraint in the form of an uncertainty relation between the duration and spatial extent of any undetected transient pulse-like modulations of the field occurring in the unmeasured region between the probes. This will provide a solid upper limit to the total error of the reconstruction.

Since the probes themselves yield extremely accurate and reproducible measurements of the field quantities in the immediate vicinity of the probe locations, there is very little error due to global fluctuations of the real field, since these would be detected simultaneously by multiple probes. Instead, the real cause for concern are *transient fluctuations*, that cause error because they are short enough in duration and spatial extent, and happen to occur deep enough into the empty space between probes so that they go undetected, and consequently the algorithm has no ability to include their existence in the reconstructed waveform.

It is tractable and informative to consider transient pulses that have a Gaussian form in space and time (z, t) such as

$$\mathcal{F}(z, t) = A \, e^{-\left(\frac{t - t_p}{\tau}\right)^2} e^{-\left(\frac{z - vt}{L}\right)^2},\tag{C.5}$$

here, A is the amplitude of the pulse, τ is the characteristic rise/decay time of the pulse (i.e., its duration), L is the characteristic spatial extent, t_p is the time at which the pulse reaches its peak value, and v is the pulse group velocity, which we will assume is approximately the average fluid velocity. To measure the damage this pulse could do to our reconstruction, we need the envelope of the pulse as a function of position z, which is the maximum value of the pulse at a fixed z, over all values of time.

First we find, for each z, the value of t maximizes $\mathcal{F}(z, t)$. For positive-valued Gaussians
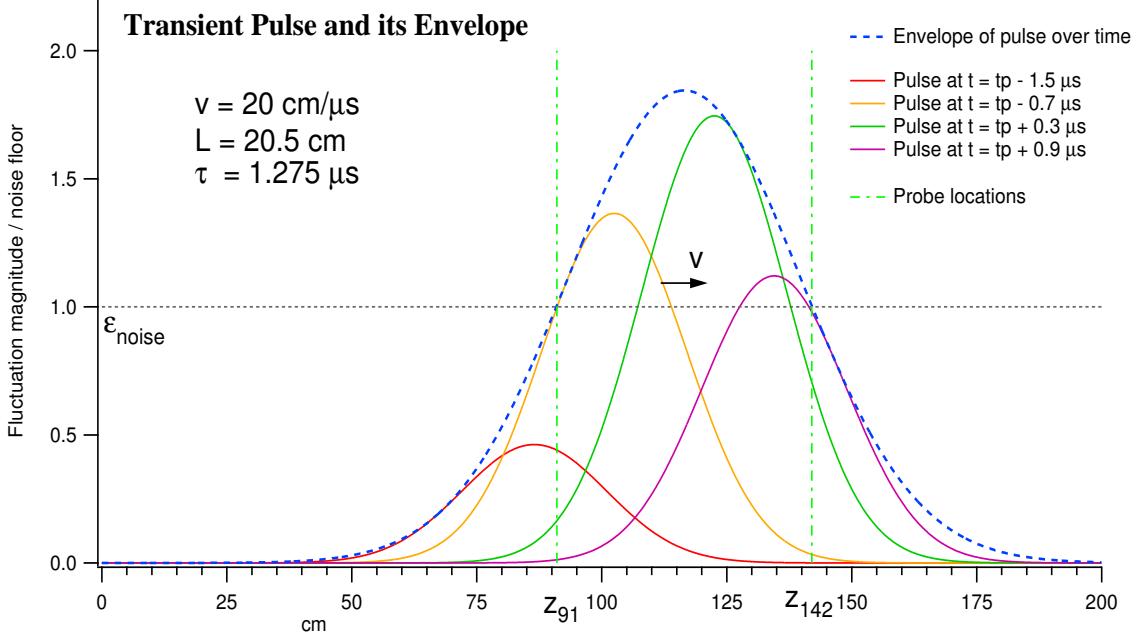
Figure C.3: Transient pulse at various times and its time-envelope as a function of axial position.

like we are considering, there is a finite maximum value but no minimum value for finite (z, t). The maximum occurs when $\partial \mathcal{F} / \partial t = 0$,

$$\frac{\partial \mathcal{F}}{\partial t} = -\mathcal{F}(z, t) \left(\frac{2}{\tau} \left(\frac{t - t_p}{\tau} \right) - \frac{2v}{L} \left(\frac{z - vt}{L} \right) \right)$$

And so the maximum occurs when

$$\frac{t - t_p}{\tau^2} - \frac{v(z - vt)}{L^2} = 0$$

$$\text{or} \quad t \left(1 + \frac{v^2 \tau^2}{L^2} \right) = t_p + \frac{v^2 \tau^2 z}{L^2}$$

Now, to clarify the algebra, let us define a dimensionless parameter $\kappa = v\tau/L$, and we see that for a fixed z the pulse reaches a maximum value at time

$$t = t_{max}(z) = \frac{t_p + \frac{\kappa^2 z}{v}}{(1 + \kappa^2)}$$

The envelope is given by $\mathcal{F}_{env}(z) = \mathcal{F}(z, t_{max}(z))$, which simplifies to

$$\mathcal{F}_{env}(z) = A\; e^{-\left(\frac{z\;-\;vt_p}{L\sqrt{1+\kappa^2}}\right)^2}.$$

Restated in terms of of τ, (using $L\sqrt{1+\kappa^2} = \sqrt{L^2 + v^2\tau^2}$), this is

$$\mathcal{F}_{env}(z) = A\; e^{-\left(\frac{z\;-\;vt_p}{\sqrt{L^2+v^2\tau^2)}}\right)^2}. \tag{C.6}$$

In order for this pulse to be undetected by neighboring probes located at z_A and z_B we would need the pulse envelope to be less than some noise floor ϵ_{noise}

$$\mathcal{F}_{env}(z_A) < \epsilon_{noise} \qquad \text{and} \qquad \mathcal{F}_{env}(z_B) < \epsilon_{noise} \tag{C.7}$$

where ϵ_{noise} is determined by the statistical fluctuations that are present in an ensemble of measured signals under equivalent experimental circumstances. It does not have to be restricted to just the electrical noise present in the probe diagnostics, but could include actual MHD modes in the plasma that constitute random deviations away from the average waveform of the probe signals. It is at least conceptually possible that occasionally these real fluctuations would occur at a larger than normal amplitude and in a transient fashion between the probes, and thus go undetected. In the worst case scenario the peak of the transient pulse would occur at exactly the half-way point between consecutive probes, thereby allowing the largest possible amplitude allowable by $(C.7)$. From this (unlikely) situation, we could make the most conservative estimate for the accuracy of this reconstruction method. The true accuracy should only be better than what we find here. The worst case is when $vt_p = z_{mid} = \frac{1}{2}(z_A + z_B)$, and so let $\Delta L_{probe} = 2(z_B - z_{mid})$. Then condition for nondetection is

$$A\; e^{-\left(\frac{\Delta L_{probe}}{2\sqrt{L^2+v^2\tau^2)}}\right)^2} \;<\; \epsilon_{noise} \tag{C.8}$$

And the maximum possible undetectable amplitude is constrained by

$$A < \epsilon_{noise}\; e^{\frac{\Delta L_{probe}^2}{4(L^2+v^2\tau^2)}} \tag{C.9}$$

This maximum possible amplitude is plotted in fig $(C.4)$ as a function of fluctuation duration and spatial extent (τ, L) using parameters typical for the CTIX experiment. Using this result
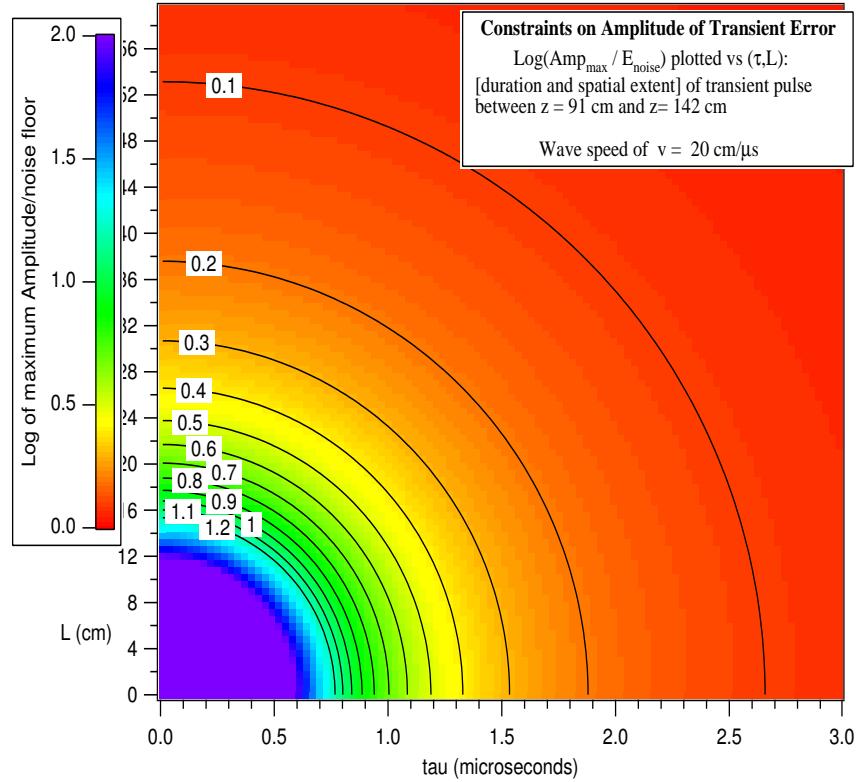
Figure C.4: Log (base 10) of the maximum possible amplitude of undetected transient pulses, plotted as a function of pulse duration and spatial extent.

we can make statements regarding an upper bound of the error of the reconstruction method, such as:

> For an average fluid velocity of $v = 20\ cm/\mu s$ we can say that in the region between $z_A = 91$ cm and $z_B = 142$ cm, if there exists an undetected transient pulse that spans the space between the probes, and it exists for at least the transit time between probes $[2L = 51\ cm, \Rightarrow L = 20.5\ cm$ and $2\tau = (51/20)\mu s, \Rightarrow \tau = 1.275\mu s]$, (see fig $C.3$) then the amplitude of the pulse can be no larger than

$$A_{max} = 1.84493 \cdot \epsilon_{noise}$$

For pulses that are significantly shorter in duration and extent, the upper limit on amplitude becomes much larger than this example. In fact, formula $(C.9)$ goes to ∞ in the limit of zero pulse length and duration. Ultimately however, this does not cause any serious problems if our goal is to reconstruct the average waveform of the field moving past a set of probes, where we care about a spatial resolution of several cm, and temporal resolution of a few μs.

Also, there is a mitigating factor involving the probability of these hypothetical high-amplitude events. If we take the noise floor to be the expectation value of the natural fluctuations $\mathcal{F}$ that occur with the plasma, $\epsilon_{noise} = \langle \mathcal{F} \rangle$, then we can use Markov's inequality [47] to bound the probability that a high-amplitude event will occur during any given shot. Let $\mathcal{F}$ be a nonnegative random variable; then for any amplitude of fluctuation $A > 0$, the probability that $\mathcal{F}$ will exceed A is bounded according to

$$P(\mathcal{F} > A) \ \leq \ \frac{\langle \mathcal{F} \rangle}{A}$$

For example, the probability that a fluctuation will exceed 100 times ϵ_{noise}, is at the very most 1/100. And so, although high amplitude errors are possible, they are constrained by basic probability laws to be correspondingly rare occurrences. Alternatively, if there is some physical reason for some finite upper bound on A, such as conservation of energy perhaps, then we can restate equation $(C.9)$ in the form of an uncertainty relation

$$L^2 + v^2\tau^2 < \frac{\Delta L_{probe}{}^2}{4\ln\left(\frac{A}{\epsilon_{noise}}\right)} \tag{C.10}$$

We see that if $A < \epsilon_{noise}$ then L and τ are unconstrained, which agrees with the fact that small amplitude fluctuations have already been included in our definition of ϵ_{noise}. But as A becomes larger, the region of spacetime with a significant reconstruction error must become smaller and smaller, and its occurrence becomes increasingly improbable. Lastly, for some fixed $A > \epsilon_{noise}$, we see that there is a trade-off between the spatial extent and the duration of undetectable pulses, and that this relationship depends on the fluid velocity and the distance between consecutive probes. The best reconstruction occurs when consecutive probes are closely spaced, and there is a high flow velocity.

Appendix D

Equations of incompressible

resistive MHD

The equations of magnetohydrodynamics (MHD) describe the evolution of the velocity field, $\mathbf{v}(\vec{x}, t)$ and magnetic field, $\mathbf{B}(\vec{x}, t)$ within a conducting fluid, and also how they couple to each other. We call this description *ideal* MHD if we consider case of infinite electrical conductivity, while it is called *resistive* MHD when we take into the effects of more practical, finite values of the conductivity.

There exist certain symmetries between the two fields that is worth notice. Both $\mathbf{v}$ and $\mathbf{B}$ are solenoidal

$$\nabla \cdot \mathbf{v} = 0, \qquad \nabla \cdot \mathbf{B} = 0 \tag{D.1}$$

Also, the definition of fluid vorticity closely parallels that of current density via Ampere's Law

$$\omega = \nabla \times \mathbf{v}, \quad \mathbf{j} = \nabla \times \mathbf{B} \tag{D.2}$$

The vorticity evolves in time according to a Navier-Stokes equation that includes the effect

of the Lorentz force term (j x B). The dissipative term can be generalized in a variety of ways.

$$\partial_t \omega - \nabla\times(\mathbf{v}\times\omega + \mathbf{j}\times\mathbf{B}) = (-1)^{\nu-1}\mu_\nu\Delta^\nu\omega \tag{D.3}$$

Here μ_ν is the fluid viscosity and the exponent ν determines the type of diffusion operator that is used. $\nu = 1$ gives the usual Navier-Stokes diffusion according to the Laplacian of ω, while $\nu = 2$ gives "hyperdiffusion".

The magnetic field also evolves in time according to a convection-diffusion equation:

$$\partial_t \mathbf{B} - \nabla\times(\mathbf{v}\times\mathbf{B}) = (-1)^{\nu-1}\frac{\eta_\nu}{\mu_0}\Delta^\nu\mathbf{B} \tag{D.4}$$

Where η_ν is the electrical resistivity of the fluid. Be aware that equations (D.3) and (D.4) are nonlinearly coupled through the convection terms.

One subtle point, although the above equations give an accurate and deterministic description of the evolution of the vector fields $\mathbf{v}(\vec{x},t)$ and $\mathbf{B}(\vec{x},t)$, there is not an absolute meaning to the evolution of any particular *field line* [73]. At any particular instant in time (t_1), we can correctly trace out a field line that is locally parallel to the magnetic vector field at every point along its length. However, we can not uniquely identify the future version that field line at some later time (t_2). It could correspond to any possible field line that exists at time t_2. This is true even if the fluid velocity field is known, and the resistivity is low enough to consider that the field is "frozen" into the fluid. The mathematical argument for this non-uniqueness goes a bit like this:

Given that any magnetic field can be expressed in terms of two scalar functions $\alpha(\vec{x},t)$, and $\beta(\vec{x},t)$ by

$$\mathbf{B}(\vec{x},t) = \nabla\alpha\times\nabla\beta$$

then any field line at a fixed time is uniquely delineated by a pair of coordinates $\alpha = constant$, $\beta = constant$. In other words, any magnetic field line is the curve of intersection between some surface of constant α, and some surface of constant β. If we apply this formulation for $\mathbf{B}$ to its evolution equation (D.4), and consider the perfectly conducting case ($\eta = 0$) to ensure that the field

is frozen-into the fluid,

$$\partial_t \mathbf{B} - \nabla \times (\mathbf{v} \times \mathbf{B}) = 0$$

we find that the fluid velocity cancels out and we have,

$$\nabla \times \left[\frac{d\alpha}{dt} \nabla \beta - \frac{d\beta}{dt} \nabla \alpha \right] = 0$$

Due to the curl operation, this relation for the evolution of $\alpha(\vec{x}, t)$, and $\beta(\vec{x}, t)$ is only determined up to the gradient of a some arbitrary scalar potential $\phi(\vec{x}, t)$,

$$\frac{d\alpha}{dt} \nabla \beta - \frac{d\beta}{dt} \nabla \alpha = \nabla \phi.$$

Thus, depending on your choice for ϕ, an initial set of scalar fields $\alpha(\vec{x}, t_1)$, $\beta(\vec{x}, t_1)$ will evolve into any other possible scalar fields $\alpha(\vec{x}, t_2)$, $\beta(\vec{x}, t_2)$, with the intersections between level surfaces also changing in an arbitrary manner. In the case of $\phi \equiv 0$, we find that the field lines do indeed flow with the fluid elements. But for any other $\phi(\vec{x}, t)$ with a non-zero gradient, this will not be the case and the field lines will have a relative motion to the fluid elements.

Overall, the moral of this story is that the equations of MHD describe the vector fields $\mathbf{v}(\vec{x}, t)$ and $\mathbf{B}(\vec{x}, t)$, but they say nothing about the evolution of *magnetic field lines*. And we must adjust our intuitions accordingly.

Appendix E

Discussion of CT Fueling

We would like to be able to use accelerated compact toroids to deposit the fuel within the innermost 20% of a reactor plasma. We are aiming for the core because confinement times are not infinitely long and so all of the particles in the plasma eventually work their way out of themagnetic field. Depositing fuel at the core gives the fuel particles the greatest number of collisional opportunities to fuse before they escape confinement,thus maximizing the burn fraction. [41],[3],[4],[97],[98],[42],[100],[43],[101]

A good deal of work has gone into studying compact toroids, for the purpose of developing a technique for deep fueling. Some of the early projects have been CTX at Los Alamos [17], RACE at LLNL [18], MARAUDER at the Phillips Laboratory [19], and more present experiments include CTIX at LLNL [1], TdeV [44] and JFT-2M [99]. Achievable velocities are high enough to allow a CT to penetrate deeply within a reactor field, where the CT can come to rest, reconnect to the reactor field and deposit its fuel.

Because of the large forces a CT can sustain an injection accelerator ends up being just a few meters in length rather than the few hundred meters necessary for a pellet injector. This means that it is possible to use high velocity CTs fired from a set of relatively small, easy to maintain injection railguns to fuel a functional fusion reactor. This body of experimental work shows that

CT deep fueling is feasible. The one final condition is fuel injection rate.

An injection system, possibly composed of a set of several guns, needs to match the fuel injection rate with the fuel consumption rate of the reactor. Projected from feasible CT mass sizes, (milligram range),along with a practical range for number of injectors per reactor, (6 to 10), we could say that each injector would need to fire reliably at a rate of 1 to 10 CTs per second.

Now that fuel penetration has been demonstrated on devices with acceptable accelerator efficiencies, the task now shifts to the development of finer control of CT injection. For a working reactor the injection system would need to be able to control the density profile of the tokamak plasma. This would involve a three-fold control of CT mass, injection rep rate, and final depth of CT deposition.

There are presently programs underway to develop the first two of these criteria, (see references), this thesis addresses the third task of depth control in a preliminary way. To control the depth at which the fuel is deposited we first need to have a clear understanding of the physics of the deposition process.

This is a comprehensive task that can be broken down into smaller steps. The ultimate goal is to understand the physics of CT-field interaction, and CT-plasma interactions, to properly model pre-reconnection stopping mechanisms, the process of reconnection, and post-reconnection effects of thermalization and dispersion.

Appendix F

Vector field visualization

using a complex color code

In order to visualize the vector fields that were considered in this project I developed a method to create a color image that is determined by vector field's direction and magnitude at each position. I found that this had some advantages over conventional vector plotting techniques.

The representation is accomplished in a multi-step process, representing a two-dimensional vector at each point by a color determined by a combination of hue, saturation, and value (h, s, v), and then finally by a corresponding combination of red, green and blue (r, g, b). Clearly any such a mapping is underdetermined and we will have to add a parameter, and choose its value to make the final product look good. This parameter will take the form of a "maximum radius of magnitude", $R_{\max}$ that should be chosen to make the final brightness range match the full extent of vector magnitudes that exist within the domain of interest.

The first step is to convert the vector field $\vec{V}(x, y)$ to a complex-valued scalar field in the obvious way,

$$z(x, y) \equiv V_x(x, y) + iV_y(x, y)$$

this will allow us to use the convenience of complex numbers when formulating our algorithm.

The core of the algorithm is a 1-1 correspondence between the complex plane and a color-wheel. The hue is simply the angle of a point on the color wheel (0 to 360°), equal to the angle of the complex representation of the vector.

$$h = 180 + \frac{180}{\pi}\arg(z)$$

Then we will determine the saturation and value of the color based on the relative magnitude of the vector $R = |z| = \sqrt{V_x^2 + V_y^2}$ compared to our choice for $R_{\max}$. We use the following formulas because they give nice results.

$$s = \begin{cases} 1 & \text{if } R \leq R_{\max} \\ e^{(1-R/R_{\max})} & \text{if } R > R_{\max} \end{cases} \qquad v = \begin{cases} \sqrt{R/R_{\max}} & \text{if } R \leq R_{\max} \\ 1 & \text{if } R > R_{\max} \end{cases} \qquad (\text{F.1})$$

The tricky part is actually to convert to this (h, s, v) color to a more standard (r, g, b) color. It can be done by introducing a few intermediate variables, the integer part of h, $\text{ip} = \lfloor \frac{h}{60} \rfloor$, and the fractional part of h, $\text{fp} = \frac{h}{60} - \text{ip}$, which defines $m = v(1 - s)$, and $n = v(1 - s \cdot \text{fp})$. Then the conversion can be completed using permutations of $[v, m, n]$ according to the diagram shown in figure F.1.

This results in a coloring of the complex plane, with black at the origin, going to a maximum brighness as $R \to R_{\max}$, and then loosing all color information by desaturation $(s \to 0)$ as $R \to \infty$ resulting in white.
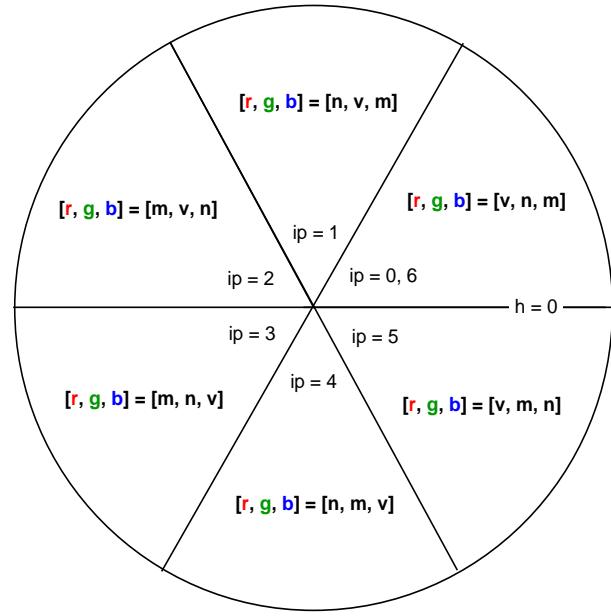
Figure F.1: Color conversion from (h, s, v) to (r, g, b). The variables ip, m and n are determined by the values of (h, s, v).
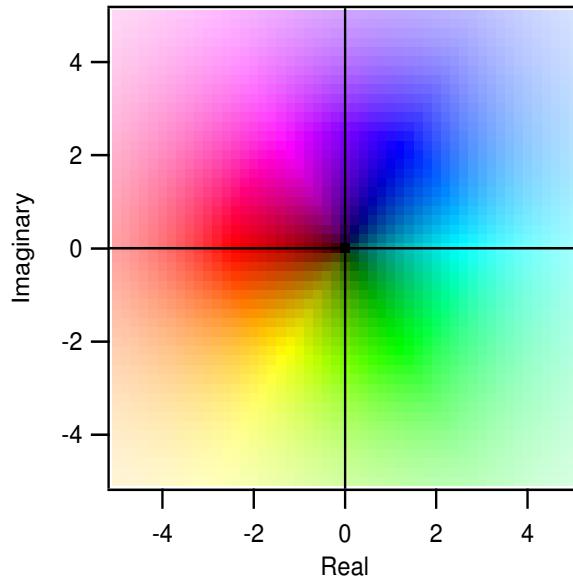
Figure F.2: Complex color code. A vector of zero magnitude is represented by black $(r,g,b) = (0,0,0)$; the color gains brightness as a vector increases magnitude, with the hue of the color determined by vector direction

Here we have an example of a vector field that shows the problem with an arrow representation, and the advantage of a color code.

$$\vec{V}(x,y) = (\sin(xy), y\cos(xy)) \qquad (x,y) \in [0,\pi] \times [0,\pi] \tag{F.2}$$
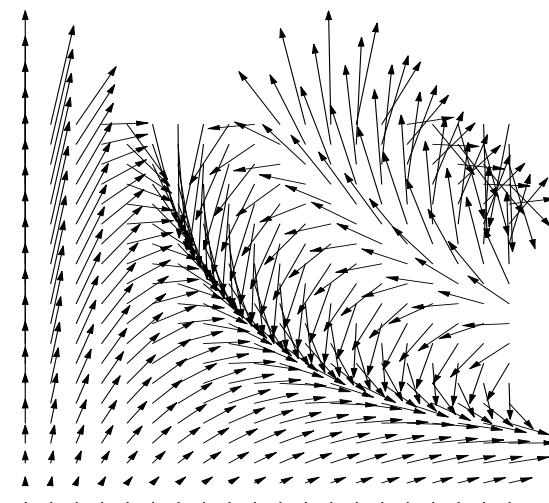
Figure F.3: Example of problem with "pick-up-sticks" effect.
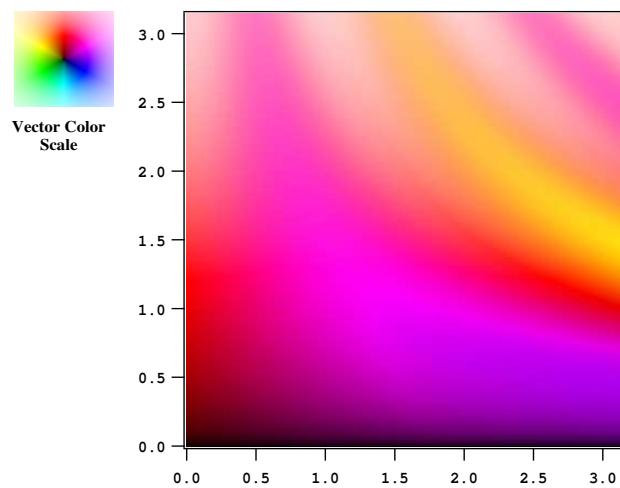
Figure F.4: The same vector field in color code.

Appendix G

Direction of future research

1. Make improved measurement of the effective depth of accelerator region magnetic probes. Possibly make new probes whose position and orientation are controllable in a more accurate way. New probes could also include a third coil to measure B_r. Effective depth could be calculated from actual measurements of a known sinusoidally varying field taken over a range of probe depths

2. A major avenue of research that would advance our understanding in a variety of ways, would be to perfect Doppler measurements of ion velocity. It would be of great theoretic value to known the velocity field down to a cm, $\text{sub} - \mu s$ scale. If it was possible to simultaneously measure this at several locations fluctuations in velocity could be examined, in principle. A new high resolution VUV spectrometer is planned to be installed on CTIX in 2006.

3. Conduct improved measurements of CT magnetic geometry, in a variety of situations. Improve estimates of resisitvity. Develop a real time resistivity computation that can be displayed during an experimental run. Measure the radial dependence of fields to compare with theory. Work out equilibrium with inclusion of Hall term invariants.

4. Turbulence work . Get fast framing camera repaired, and repeat the GPI experiment under the optimal conditions previously found in this study. Especially for the configuration with accelerator gas puffing, we would like to use the framing camera to watch the plasma structures evolve in time. We would of course use the other single frame cameras to take images along adjacent lines of sight, providing higher resolution images at certain key moments. Top on the list would be measurements of the wave velocity of the plane-wave and turbulent structures observed in this study. This would test out the idea that many of these structures are standing wave patterns relative to the lab frame.

A separate line of advancement might come from developing a much more localized neutral gas jet that could be injected at a specific location. This would allow some diffusion and transport measurements to be made by watching how the injected gas jet disperses as the plasma interacts with it. This would be not allow the detection of global structures like those found with a diffuse gas puff, instead a gas jet would work as a finer scale measurement of structure and dynamics. Only very repeatable effect could be explored in this way, because you would have to know how to position the gas jet in a location that reliably corresponded to some particular plasma structure of effect.

We have a proposal to NSF currently under review (2/25/2006), in which a sequence of further experiments will be conducted to study turbulence induced by two distinct types of turbulence-inducing targets:

1. Flow preserving targets (similar to the wire array target used so far)

2. Stagnation/compression targets (flat, concave, or corrugated plates)

The two target schemes induce different perturbations to the plasma, and explore distinct regions of the space of turbulent states. Additionally, for both types of target it is possible to include an externally generated magnetic or electric field in the vicinity of the target.

In the first set of proposed experiments we would begin simply, using a single cylindrical target oriented perpendicular to the flow. The diameter of the cylinder would be varied over a sequence of experiments from 1 mm to 10 cm. For sufficiently large diameters (¿1cm) magnetic

probes can be embedded inside the cylinder. Fast imaging of the plasma flow around the cylinder will be done from a transverse viewpoint that allows simultaneous observation of the upstream laminar flow and downstream turbulent flow.

Based on preliminary work with wire targets, we expect to be able to measure the size and shape of the resulting bow shock, as well as any turbulent structures as the plasma fills in the void behind the target. The goal of this first experimental sequence is to determine how these observables scale with target diameter and plasma flow parameters.

In a second set of experiments, targets that yield plasma stagnation and compression will be used. These will be initially implemented by colliding the CT into a flat plate which can be oriented at an adjustable angle. When oriented perpendicular to the flow, the plate will sharply reduce the bulk velocity of plasma during the collision and cause the plasma density to significantly increase during the stagnation process. The ion kinetic energy is expected to be thermalized by a variety of possible mechanisms, such as shock heating, microturbulence cascade to thermal scales, and collisional processes. One of the primary goals of this configuration is to obtain data which constrain the amount each mechanism contributes to the thermalization process.

When the target plate is oriented at oblique angles to the flow, the reflected particles and waves may interact differently with the incoming plasma, which may result in observably different effects in the evolution of the turbulent state, and of structures such as shocks or jets. Additional phenomena are expected to occur if the surface geometry of the target plate is not flat. Designs with periodic concavities are of interest, as well as a single concave focusing structure.

For these later experiments the Acton high-resolution spectrometer will be used to measure Doppler shifting and broadening of plasma lines to determine the velocity field and thermalization of ions. Energy analyzer probes will be used to measure electron thermal energy. Laser deflection measurements will be used to measure fast fluctuations in plasma electron density along multiple chords; this method is especially suitable to measure small-scale structures with high gradients which other methods cannot resolve. Langmuir probes will measure edge density, while fast cameras will

be used to get a global picture of the spatial variation at key moments during the shot. We will also install electromagnetic and electrostatic RF probes to diagnose turbulent processes such as excitation of plasma waves. The data will be analyzed using a wideband RF spectrum analyzer.

Appendix H

Image gallery of coherent waves
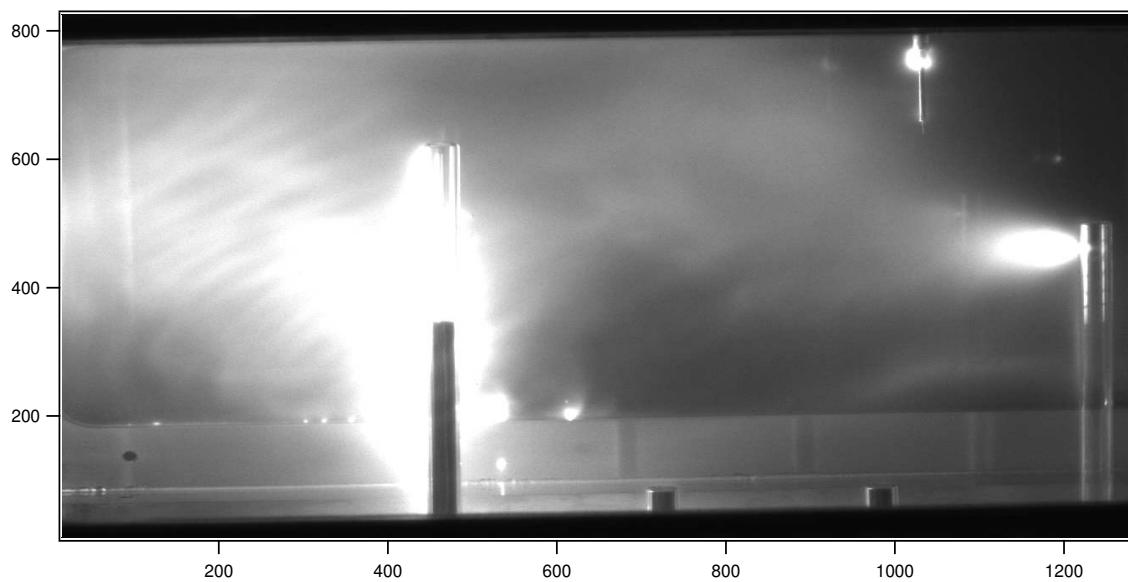
Figure H.1: Coherent waves in plasma, shot 60438
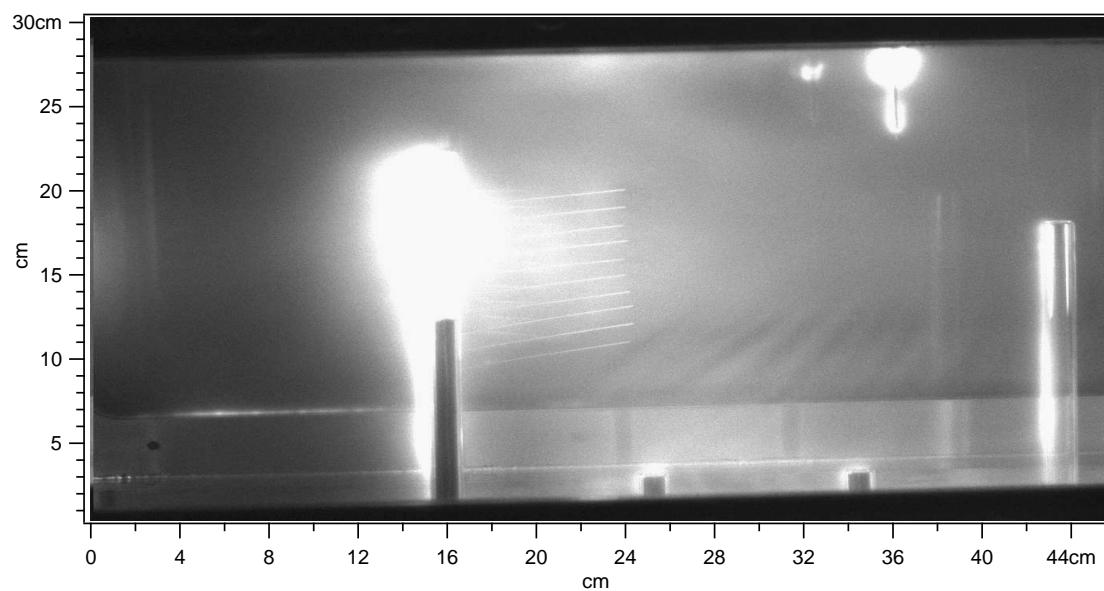
Figure H.2: Coherent waves in plasma, shot 59841
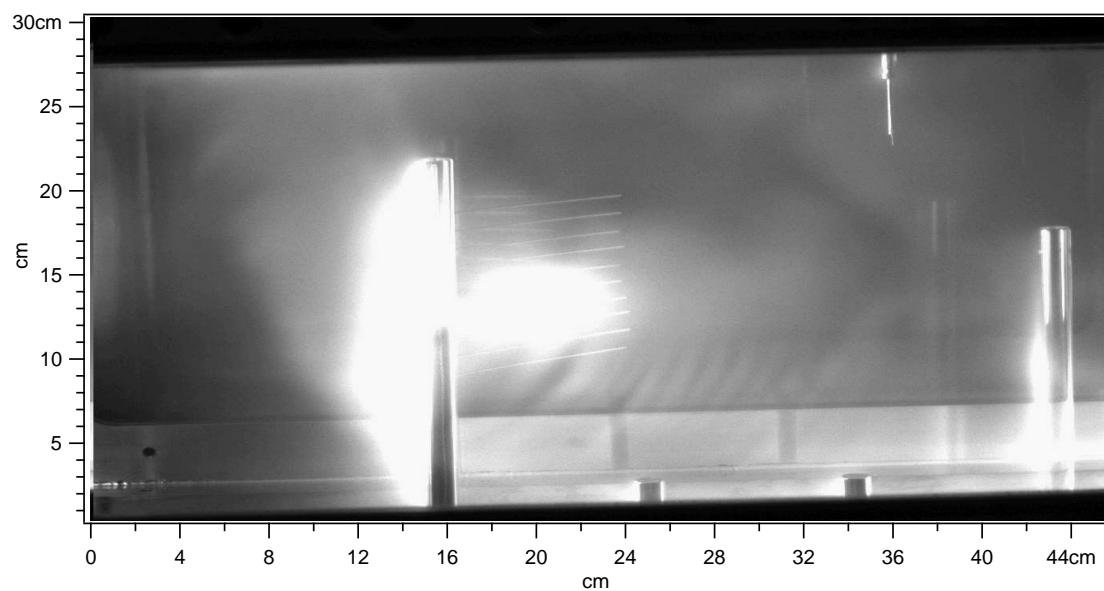
Figure H.3: Coherent waves in plasma, shot 60235
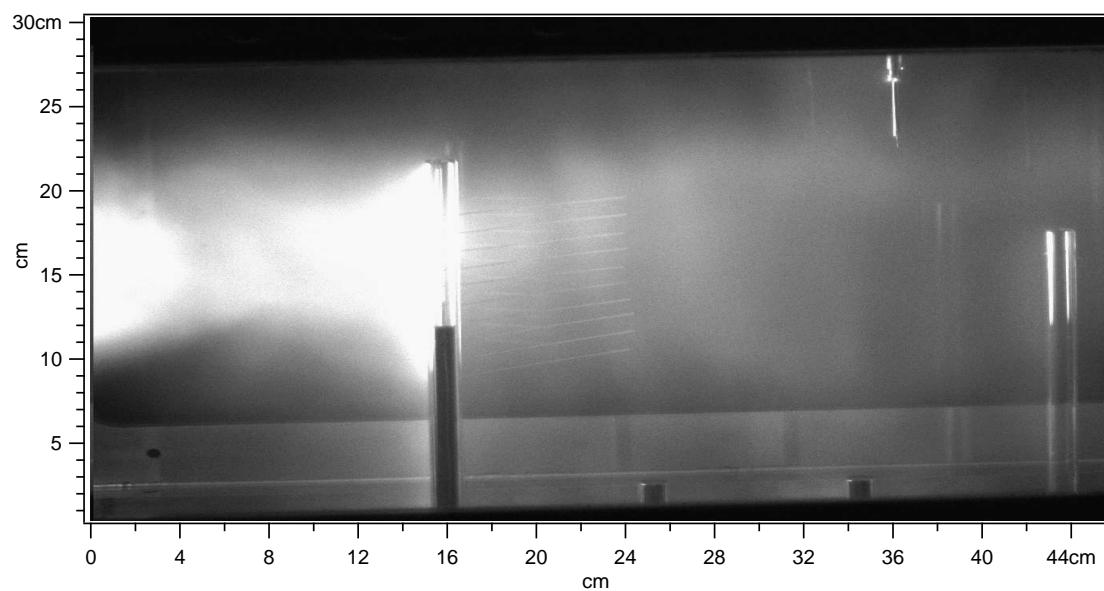
Figure H.4: Coherent waves in plasma, shot 60091
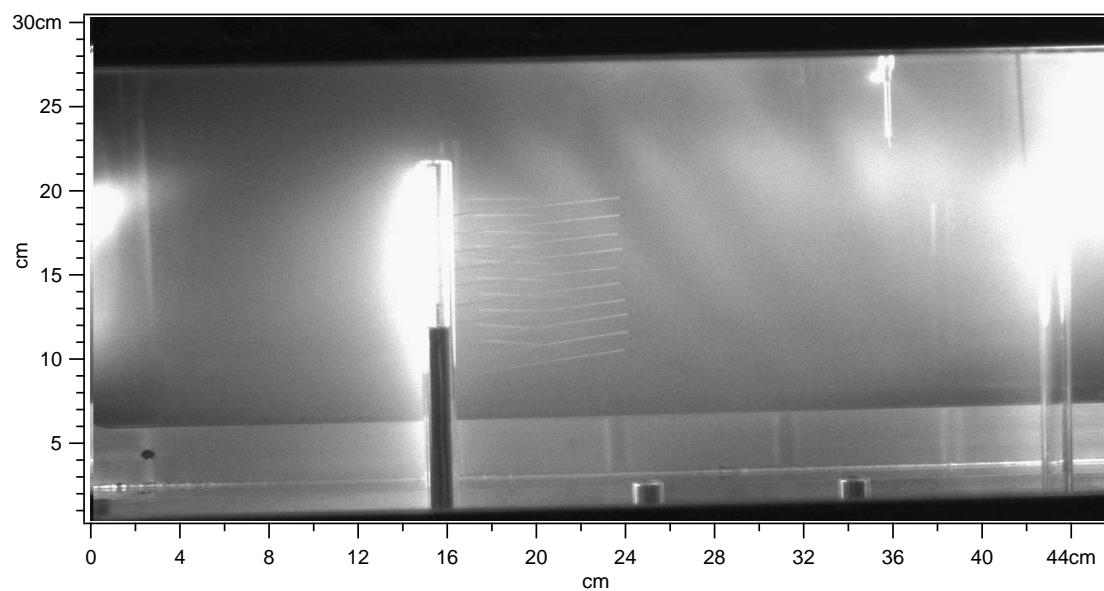
Figure H.5: Coherent waves in plasma, shot 60299
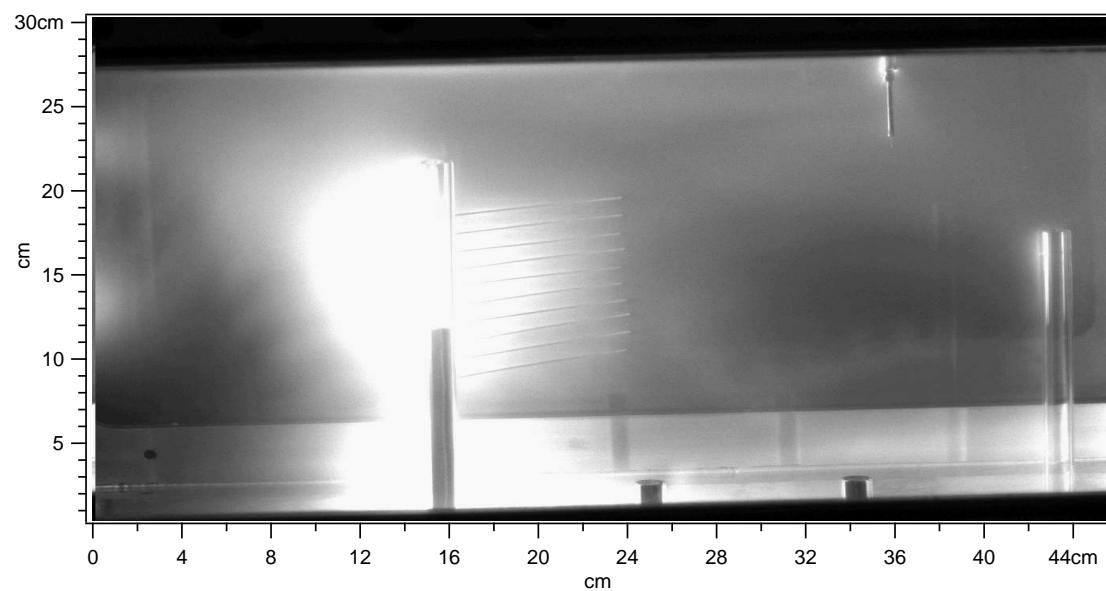
Figure H.6: Coherent waves in plasma, shot 60276
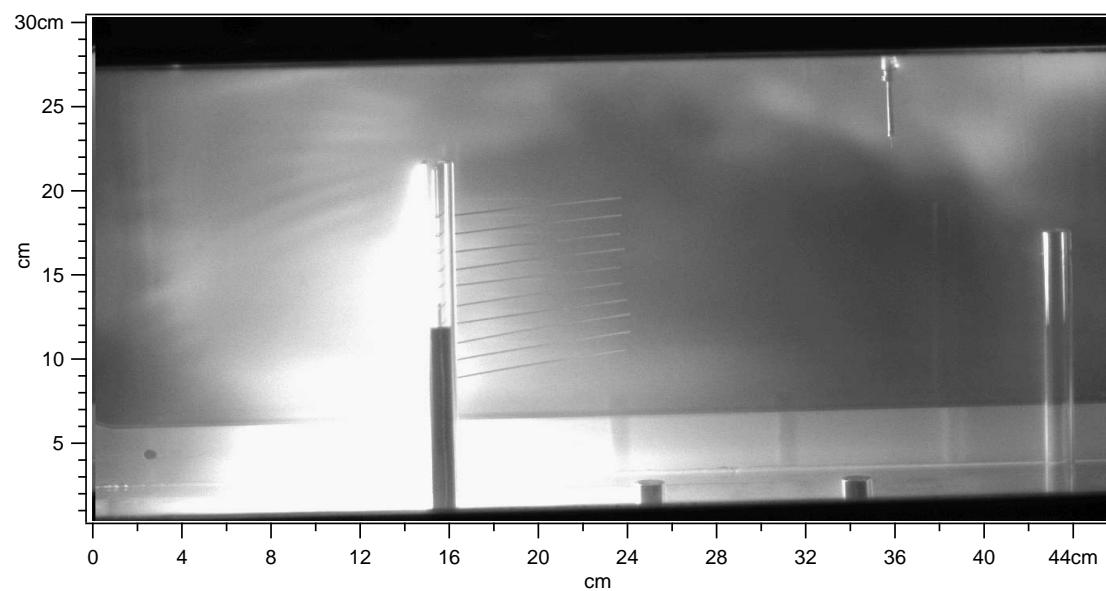
Figure H.7: Coherent waves in plasma, shot 60295
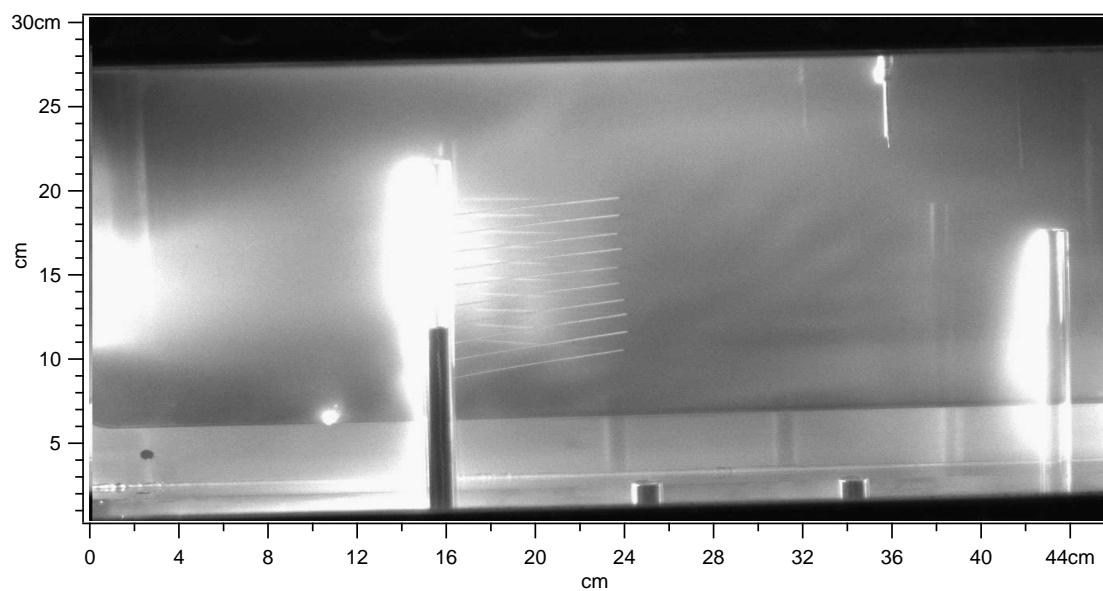
Figure H.8: Coherent waves in plasma, shot 60306
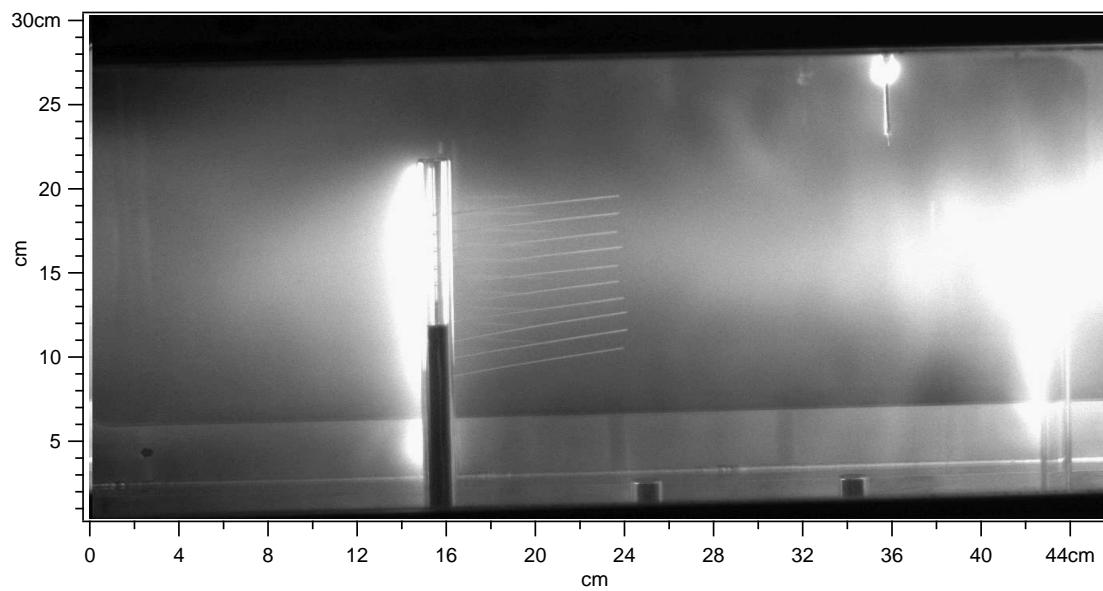
Figure H.9: Coherent waves in plasma, shot 60394
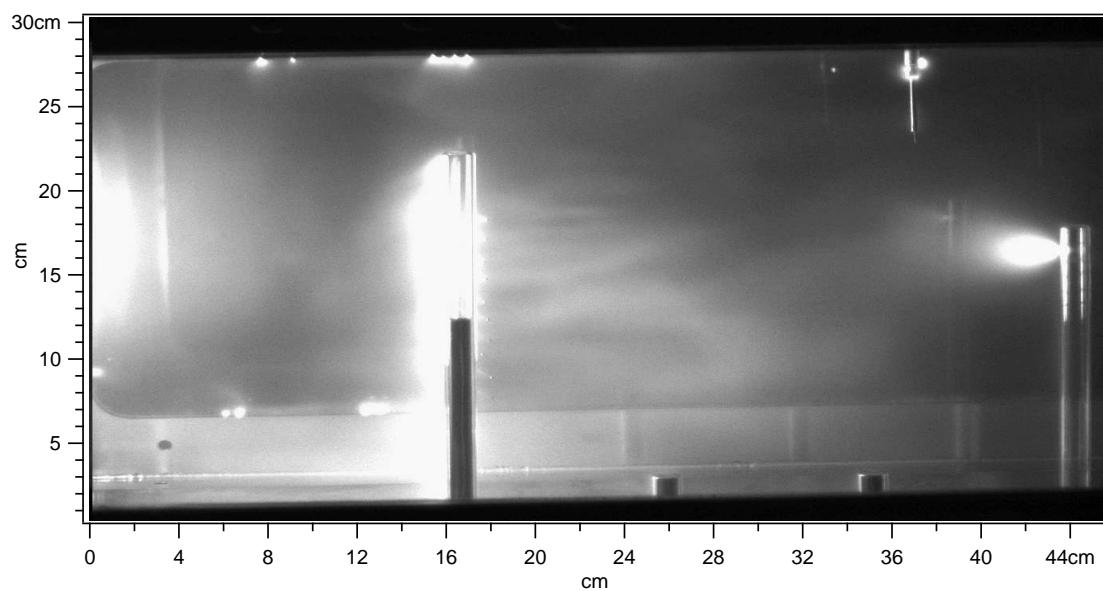
Figure H.10: Coherent waves in plasma, shot 60480
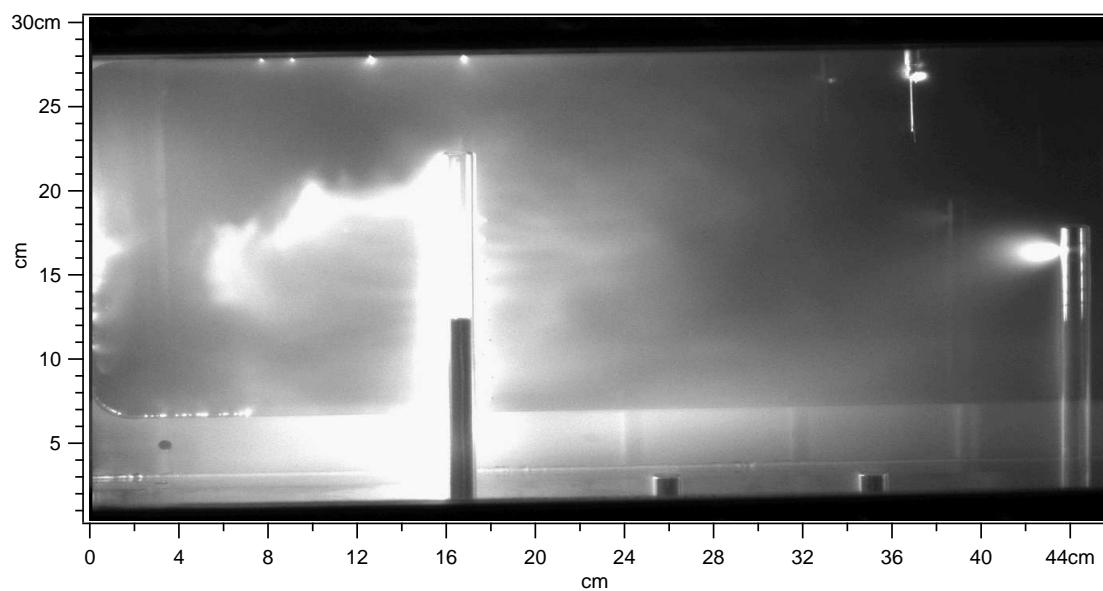
Figure H.11: Coherent waves in plasma, shot 60485
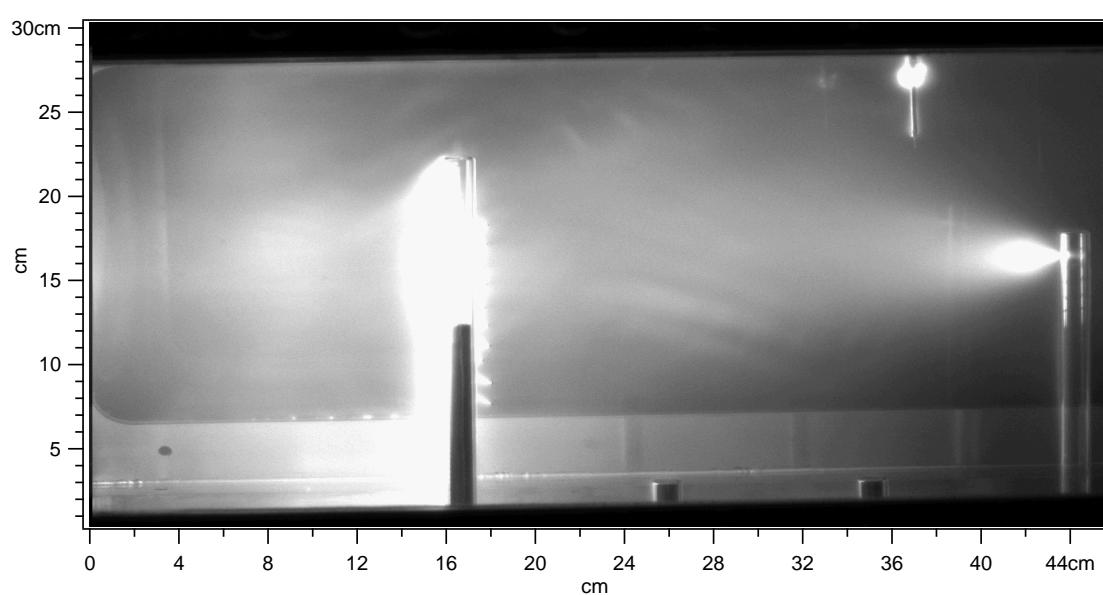
Figure H.12: Coherent waves in plasma, shot 60487

Appendix I

Image gallery of

turbulent flow effects
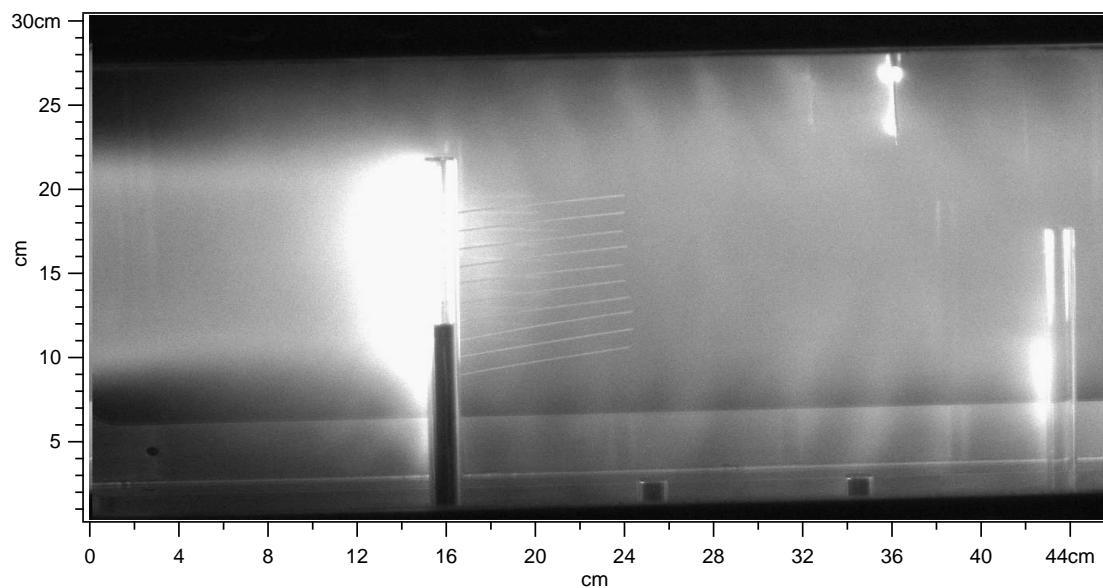
Figure I.1: Transition from laminar to turbulent flow, shot 60061
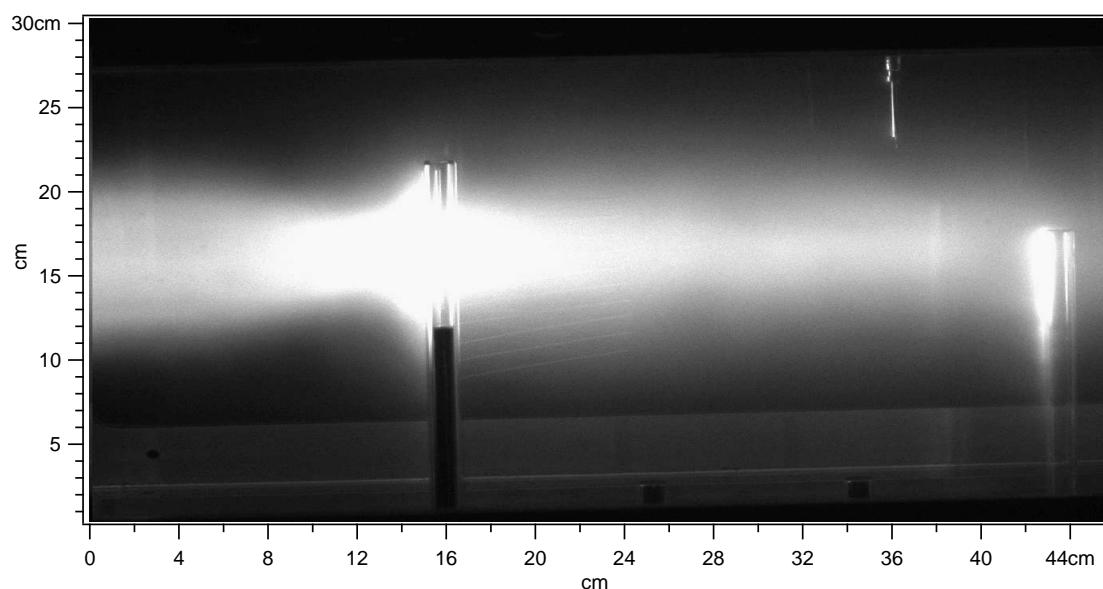
Figure I.2: Interaction with target changes the flow, but with no detectable increase in wave activity , shot 60054
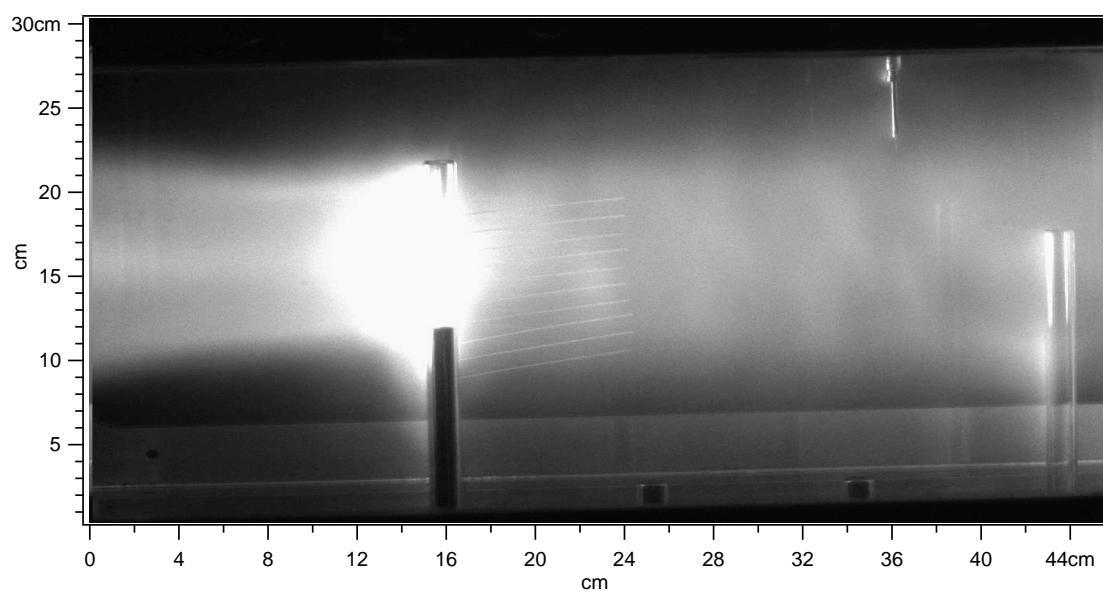
Figure I.3: Transition from laminar to turbulent flow, shot 60055
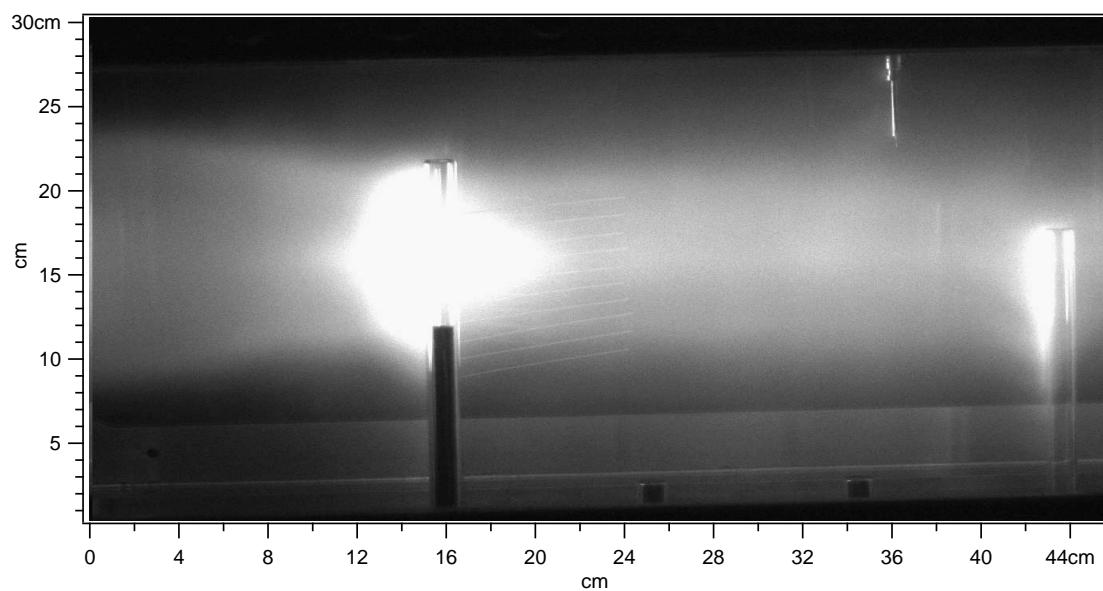
Figure I.4: Interaction with target changes the flow, but with no detectable increase in wave activity, shot 60056
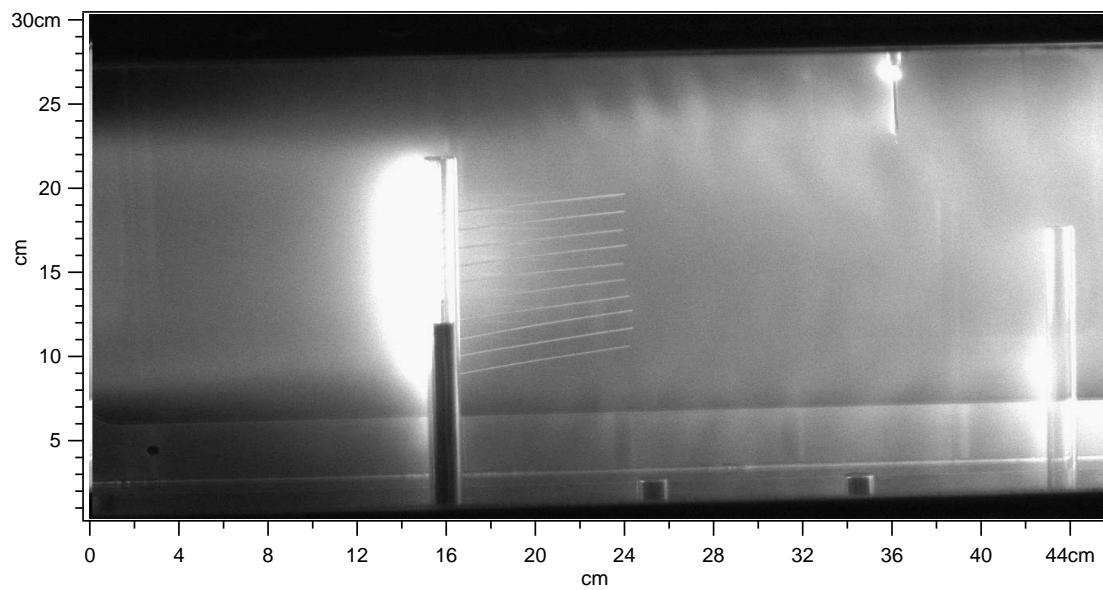
Figure I.5: Transition from laminar to turbulent flow, shot 60062
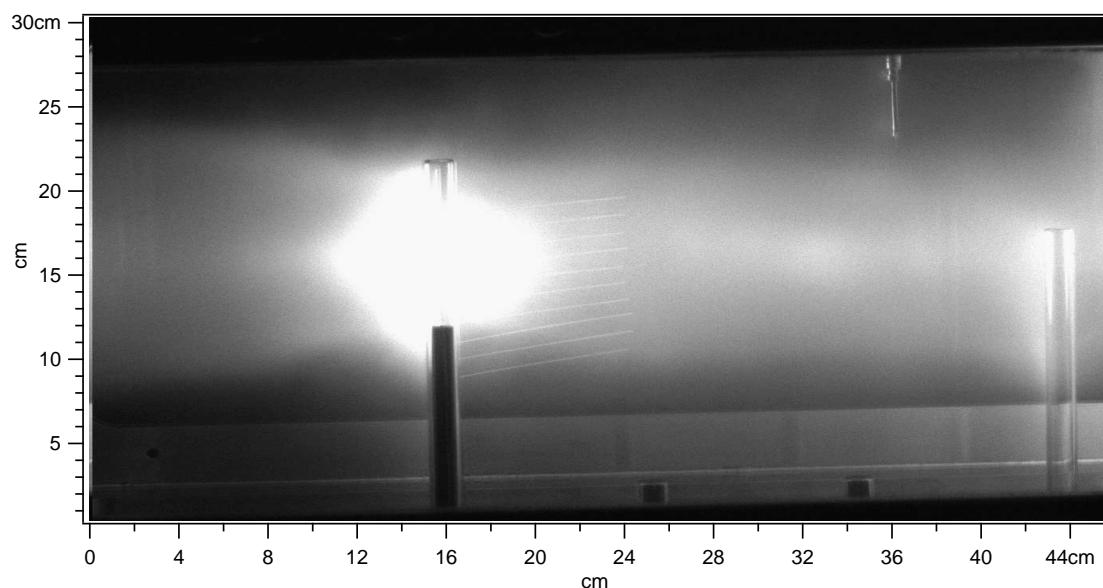
Figure I.6: Transition from laminar to turbulent flow, but with only a small increase in wave activity, shot 60063
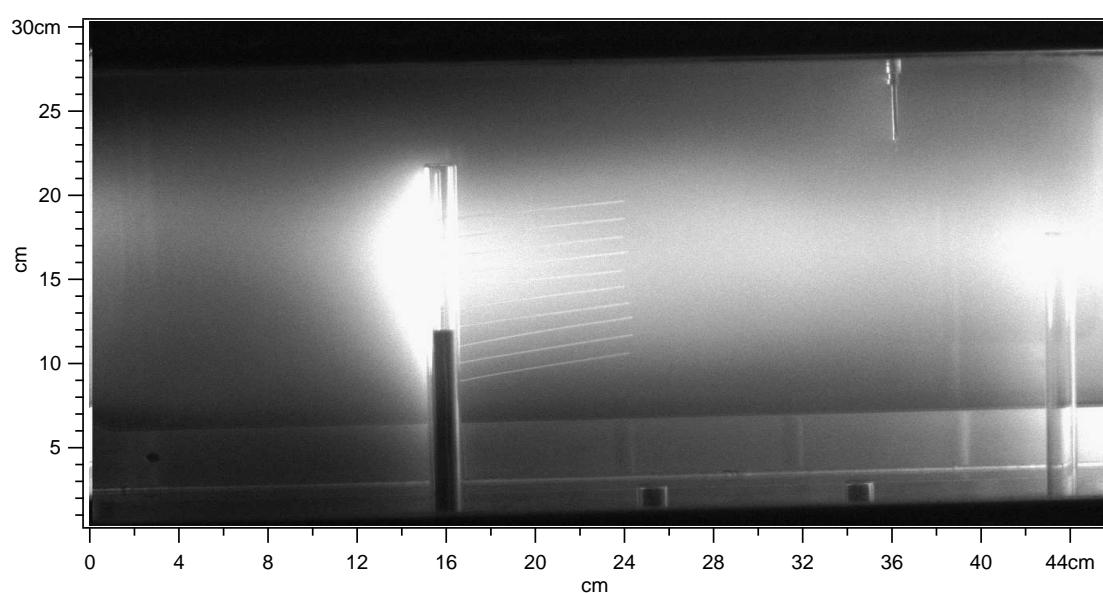
Figure I.7: Interaction with target changes the flow, but with no detectable increase in wave activity, shot 60064
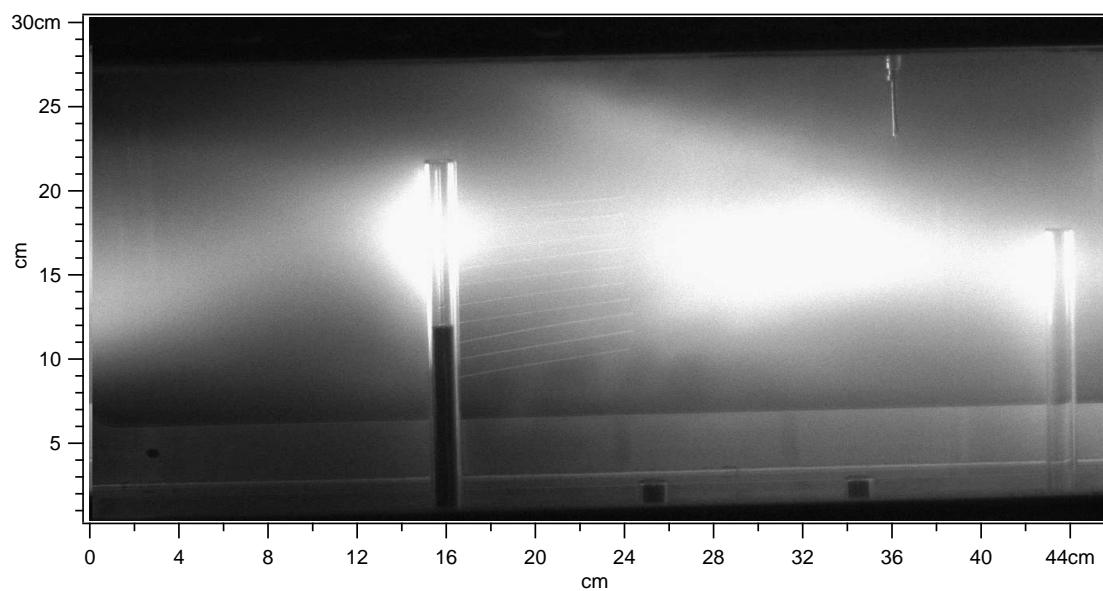
Figure I.8: Transition from laminar to turbulent flow, shot 60065
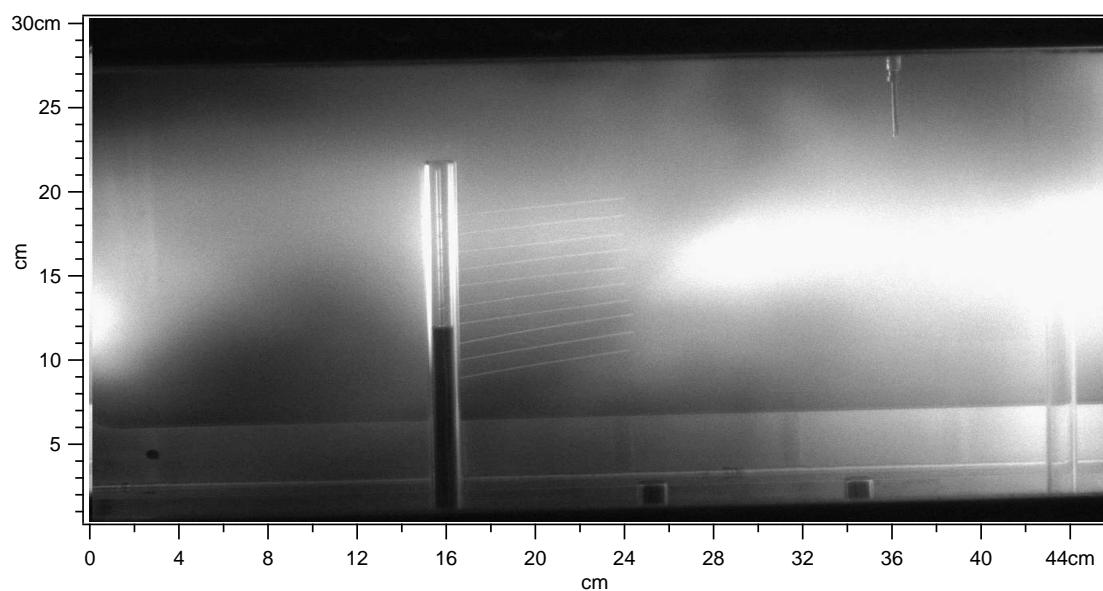
Figure I.9: Central flow interacting with target, shot 60066
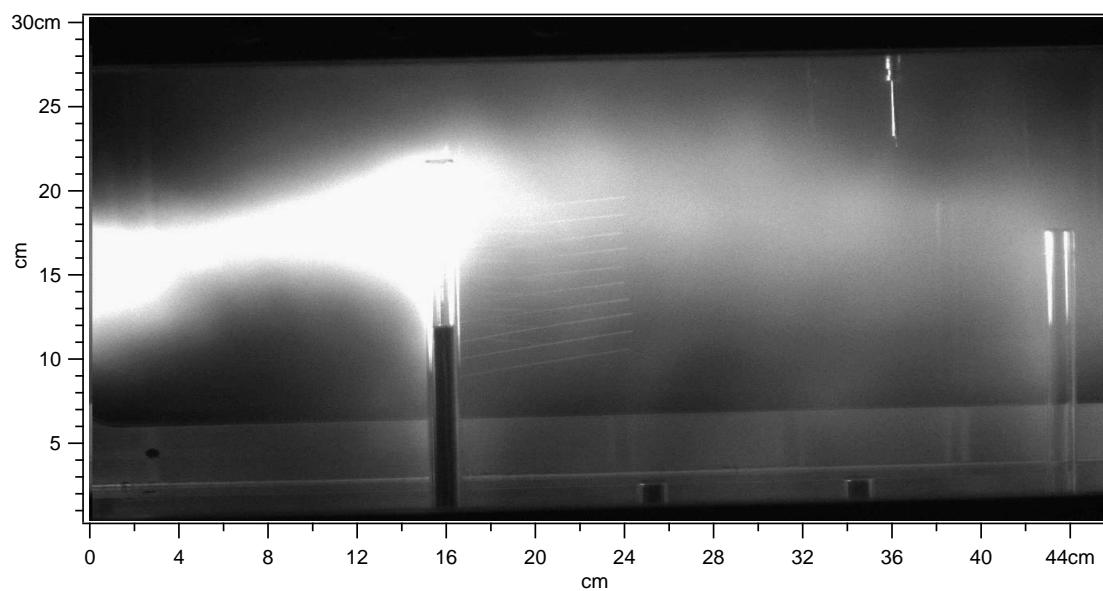
Figure I.10: Transition from laminar to turbulent flow, shot 60071
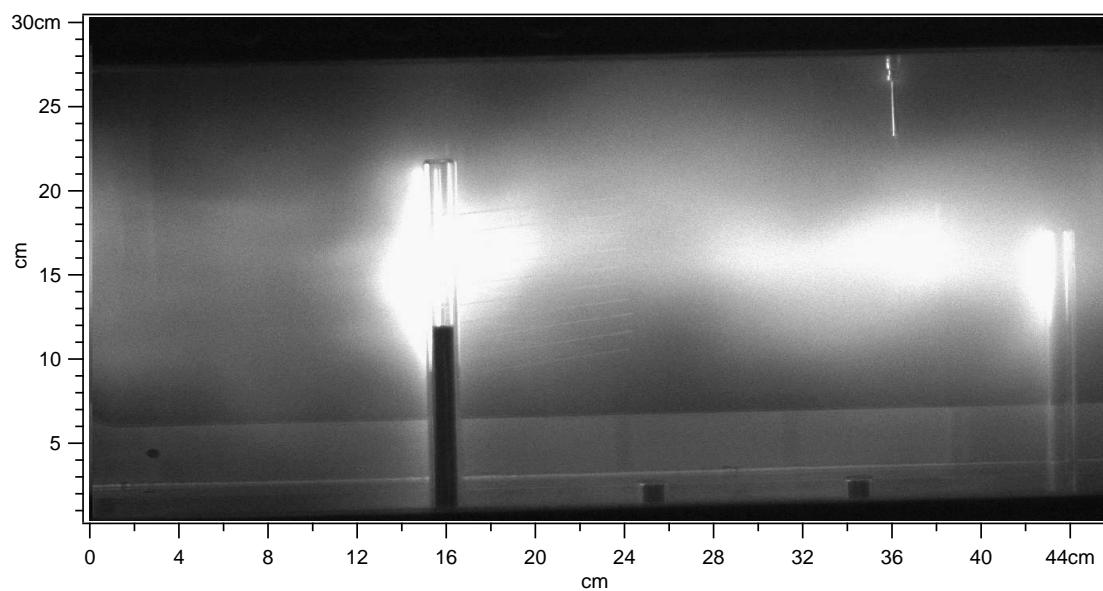
Figure I.11: Central flow interacting with target, shot 60073
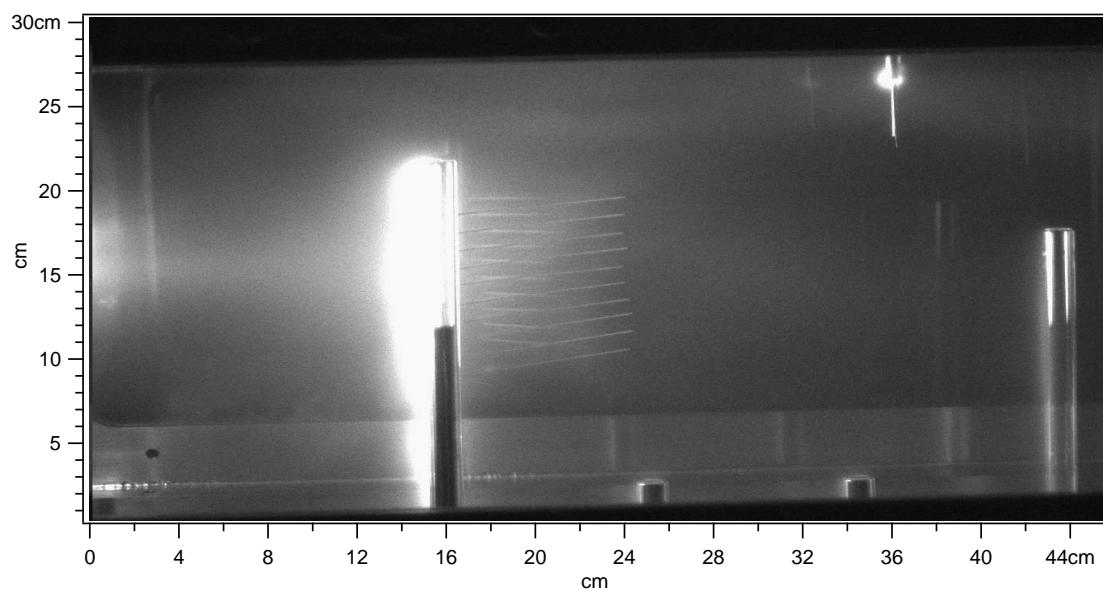
Figure I.12: Central flow interacting with target, shot 60087
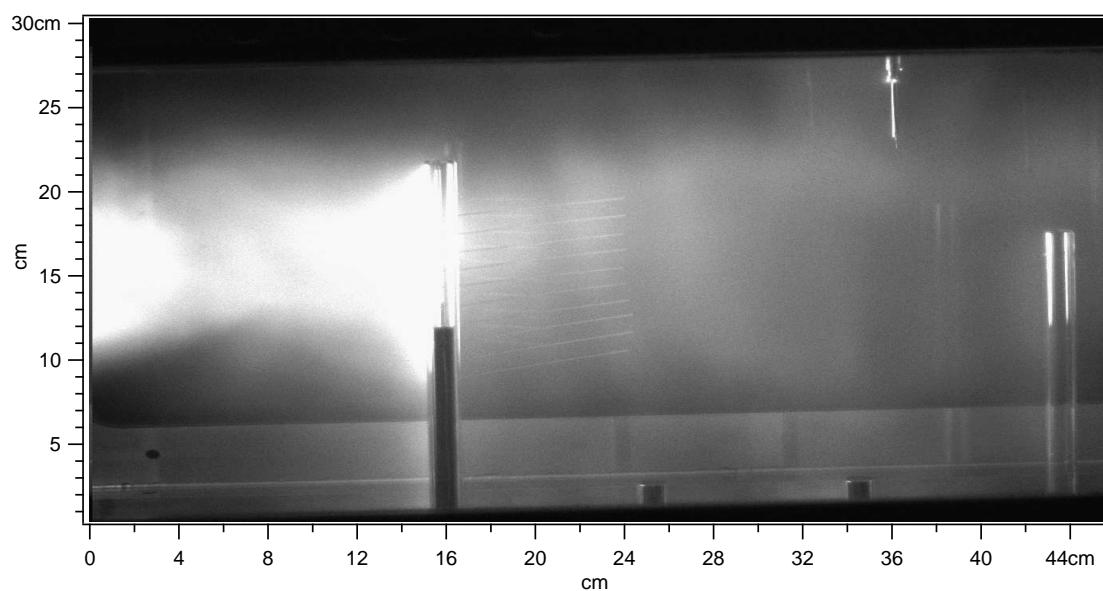
Figure I.13: Transition from laminar to turbulent flow, shot 60091
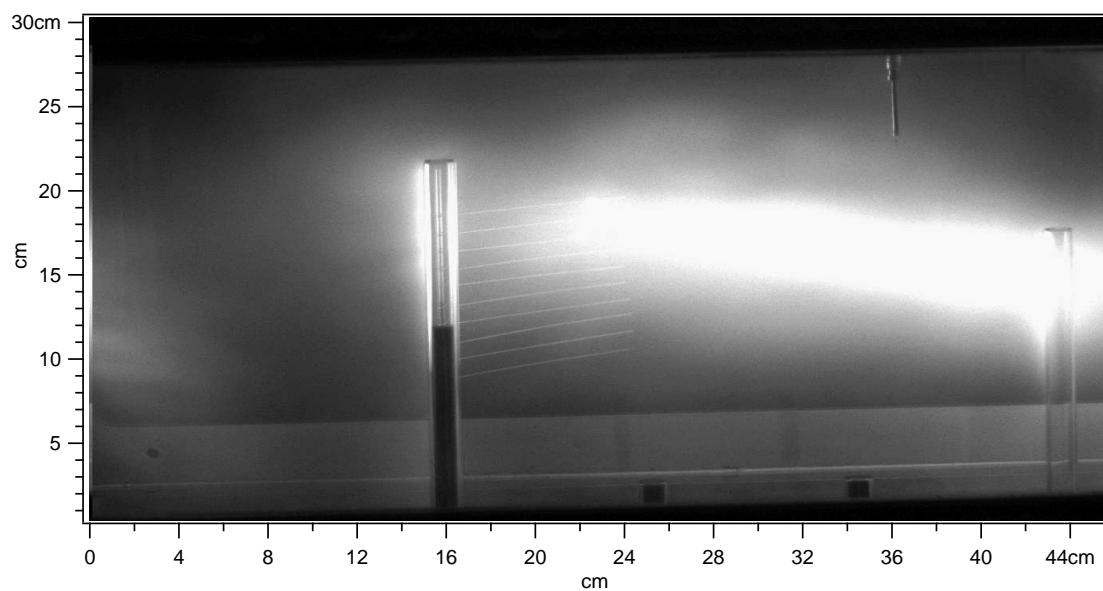
Figure I.14: Central flow interacting with target, shot 60093
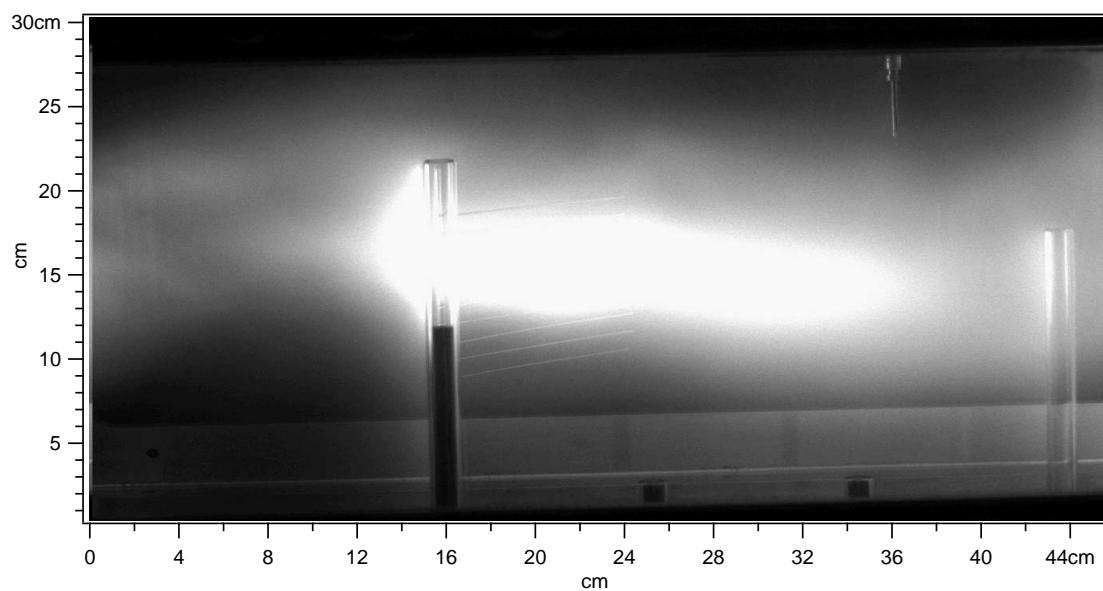
Figure I.15: Central flow interacting with target, shot 60104
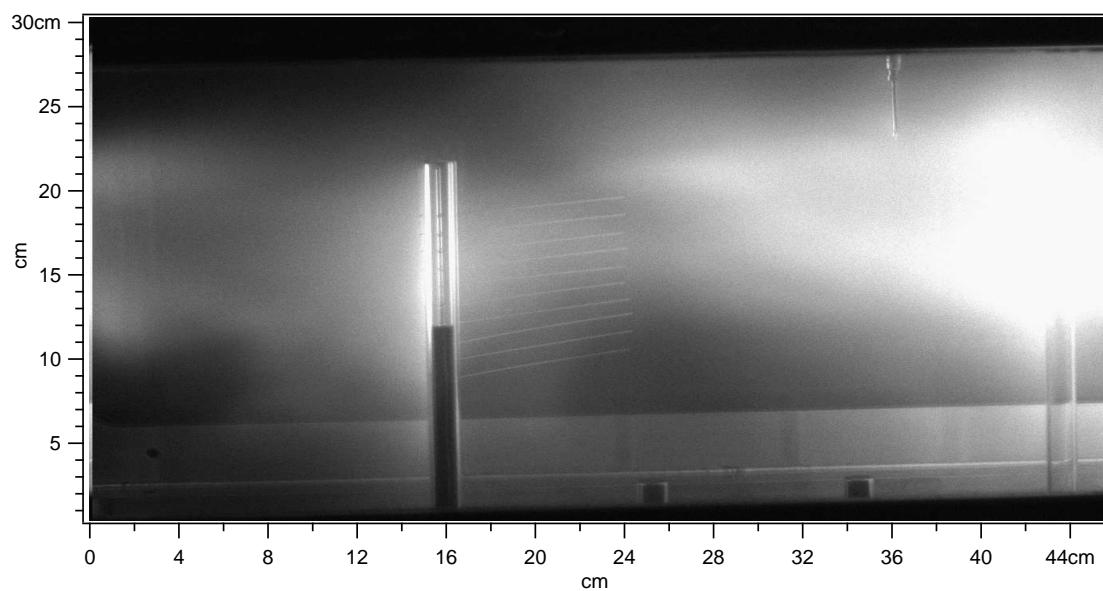
Figure I.16: Central flow interacting with target, shot 60106
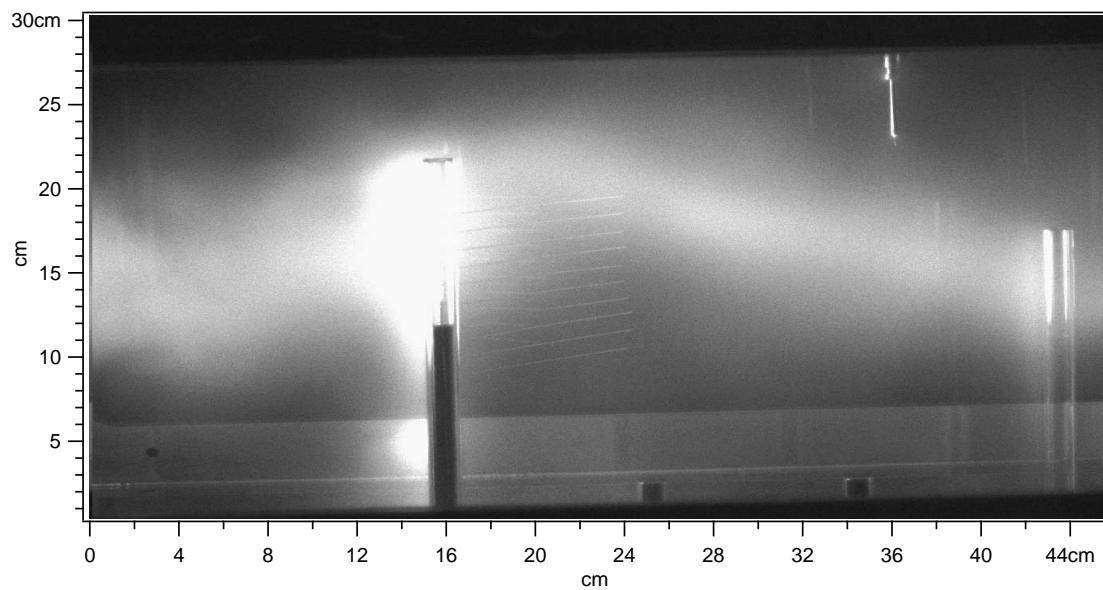
Figure I.17: Central flow interacting with target, shot 60145
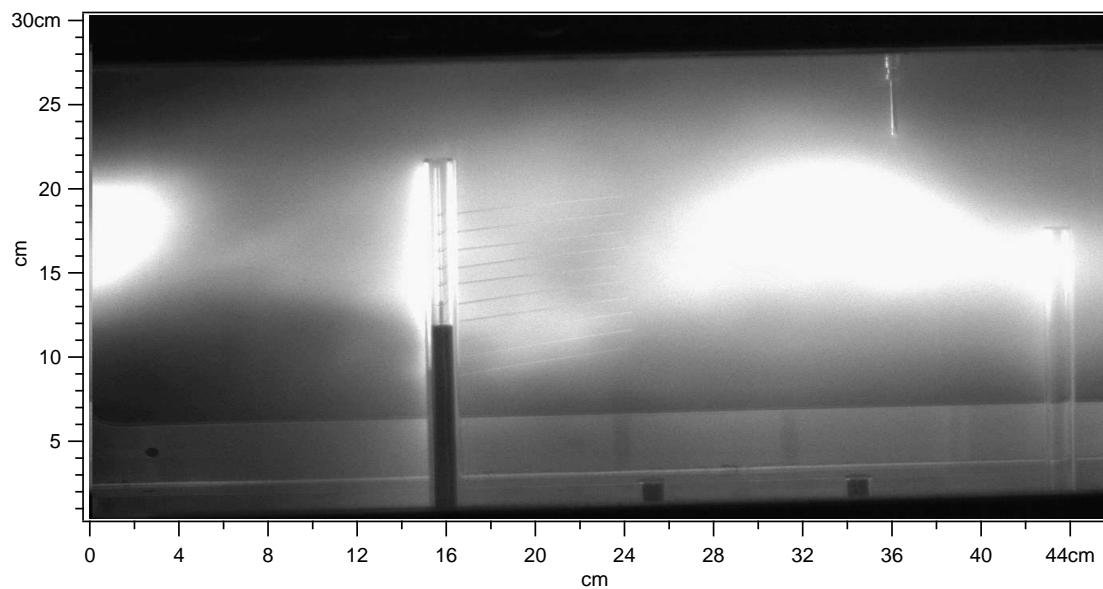
Figure I.18: Central flow interacting with target, shot 60149
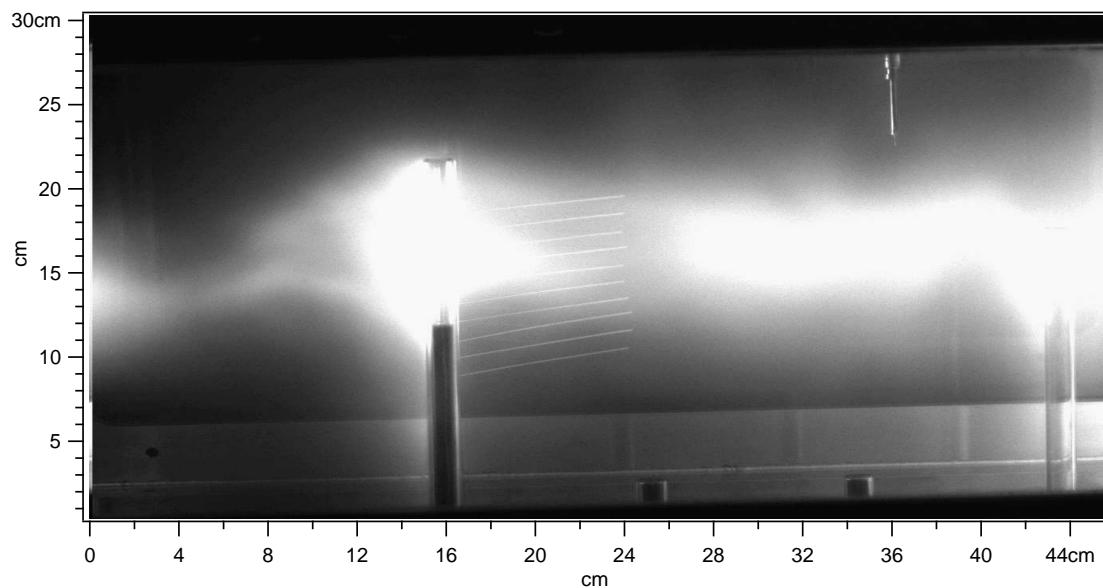
Figure I.19: Transition from laminar to turbulent flow, shot 60157
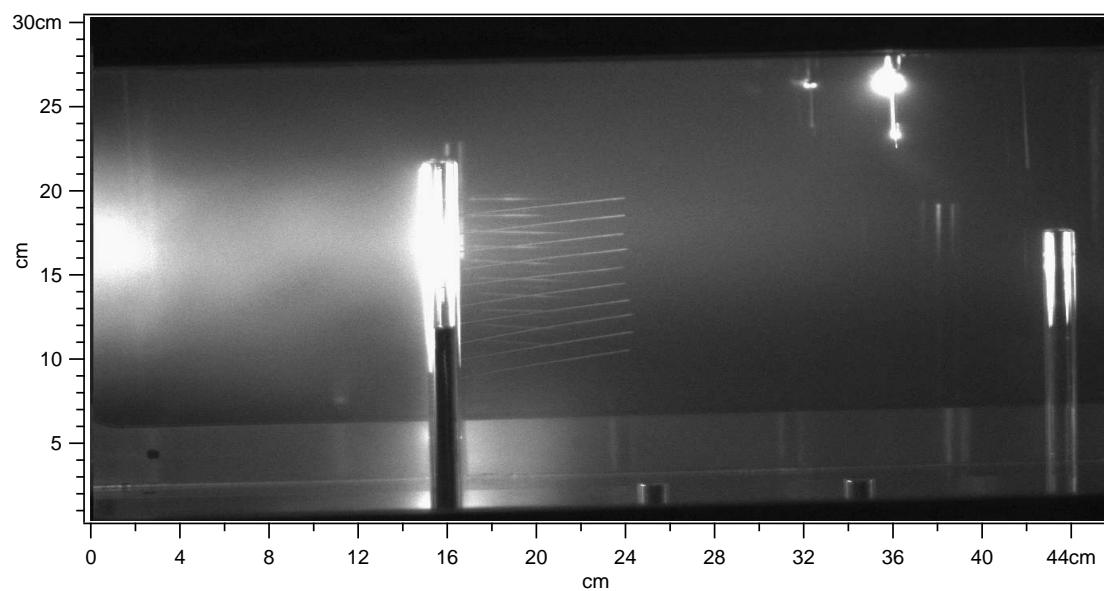
Figure I.20: Central flow interacting with target, shot 60166
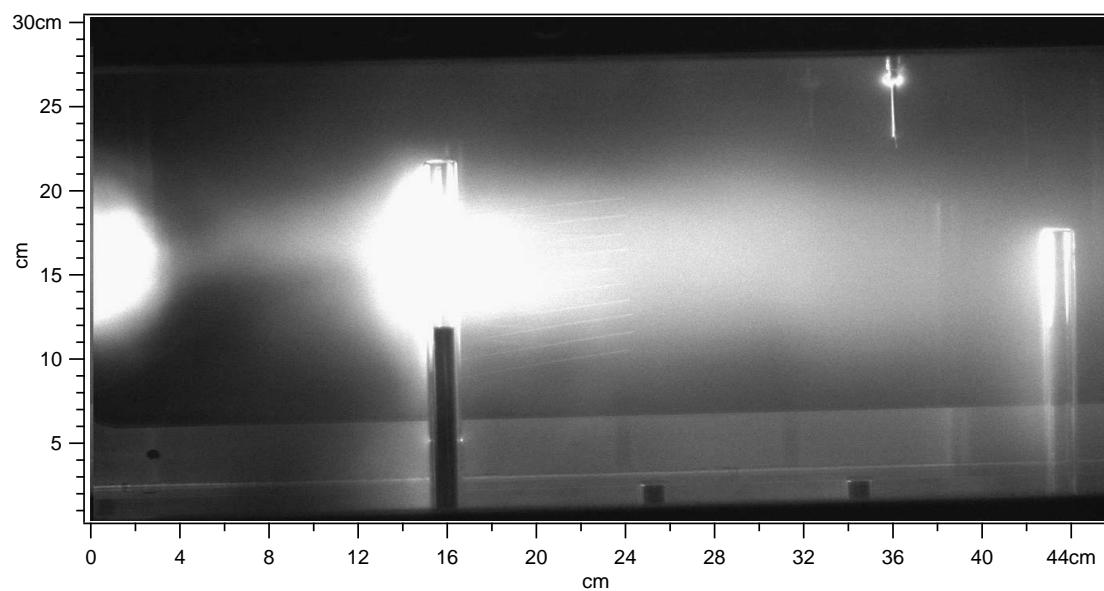
Figure I.21: Central flow interacting with target, shot 60167
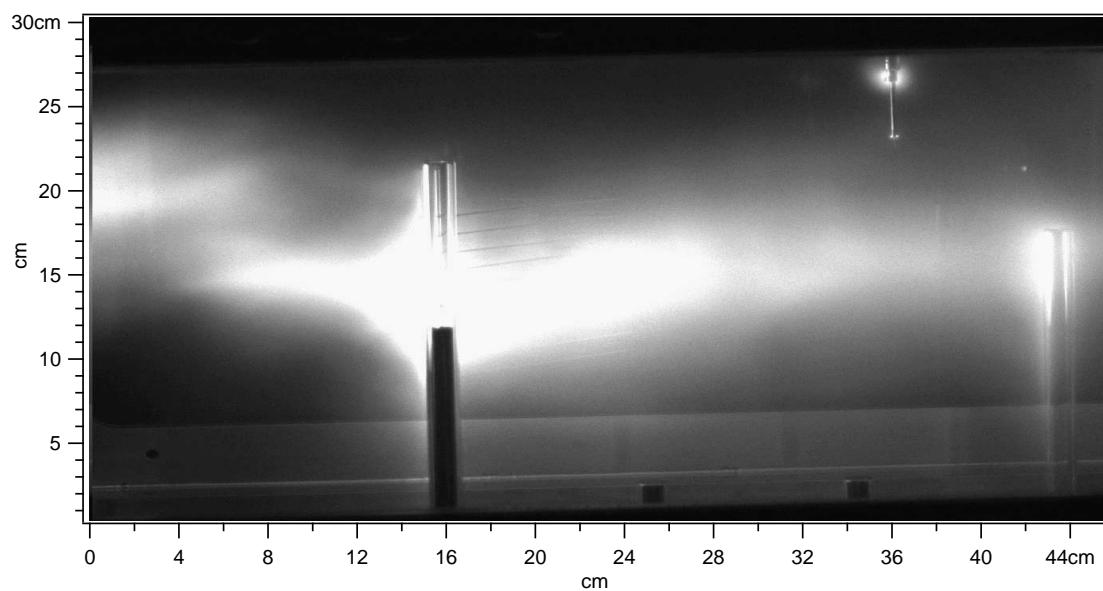
Figure I.22: Central flow interacting with target, shot 60168
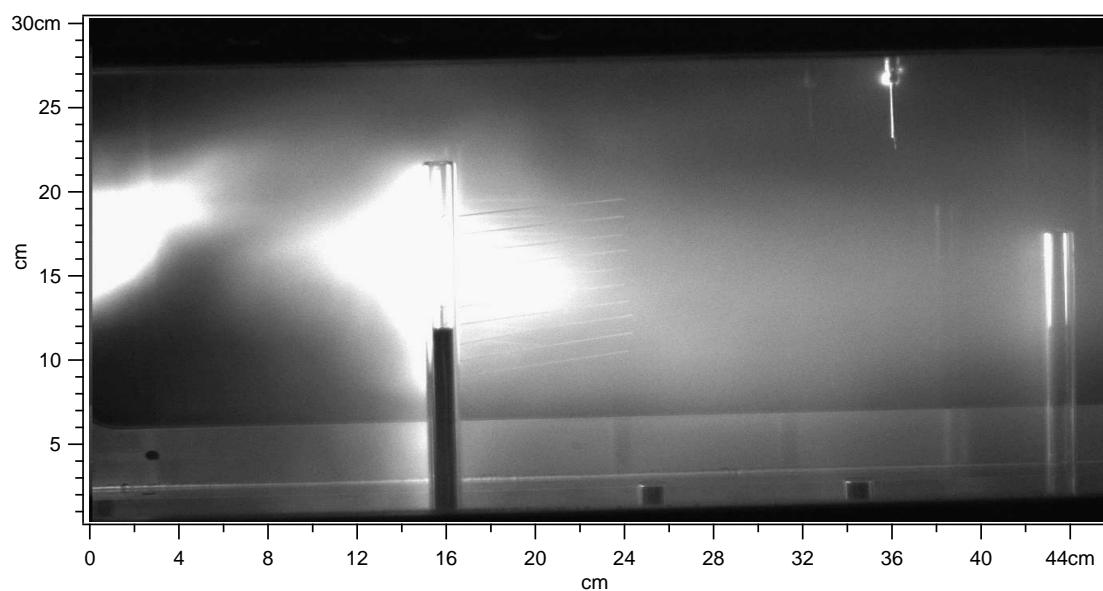
Figure I.23: Central flow interacting with target, shot 60178
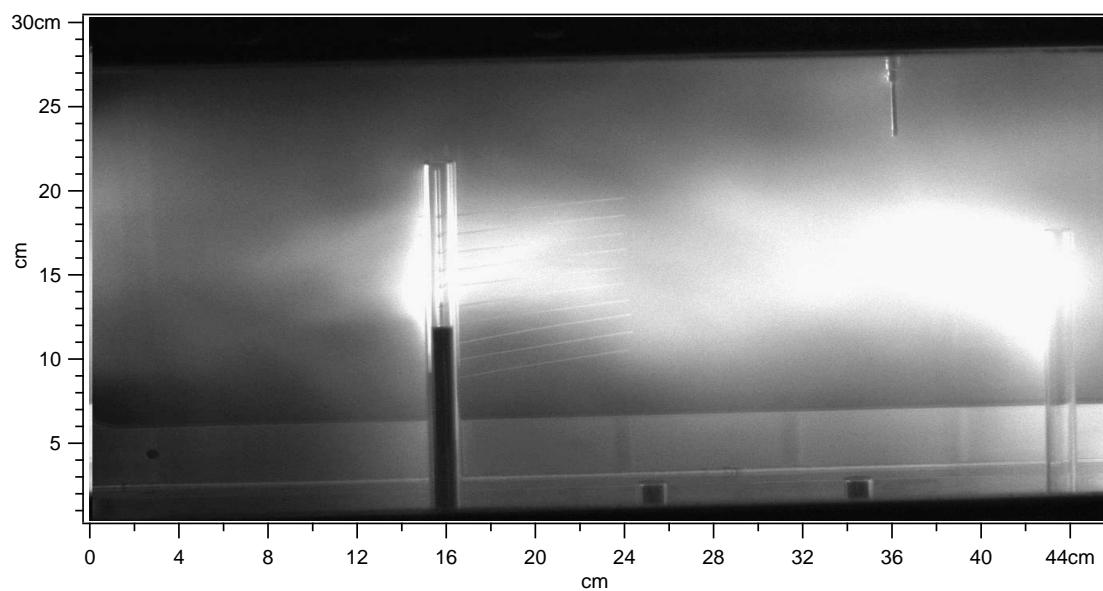
Figure I.24: Transition from laminar to turbulent flow, shot 60180
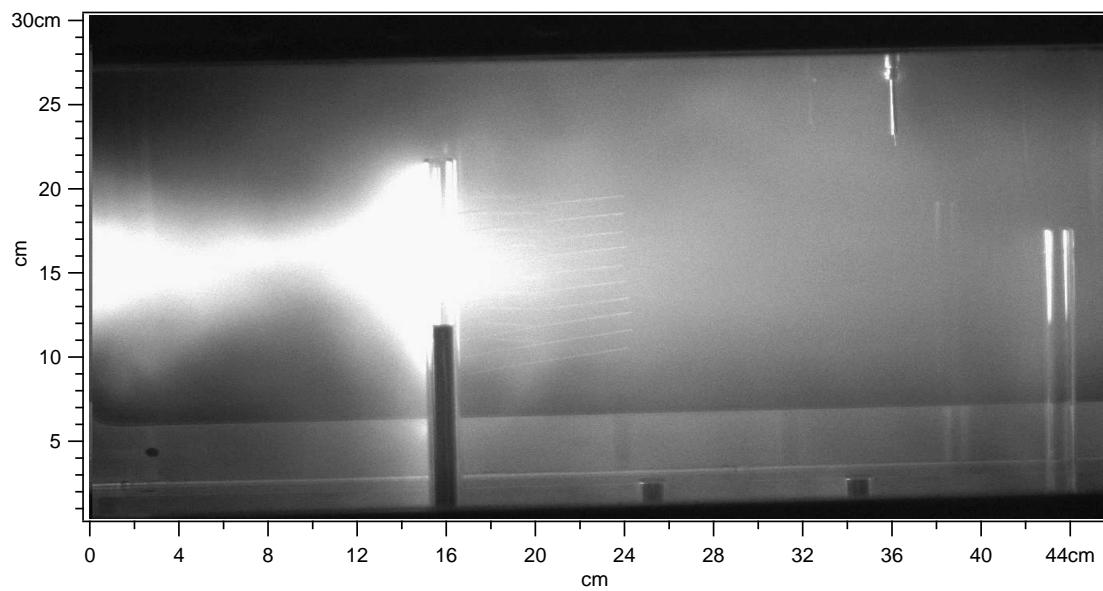
Figure I.25: Central flow interacting with target, shot 60216
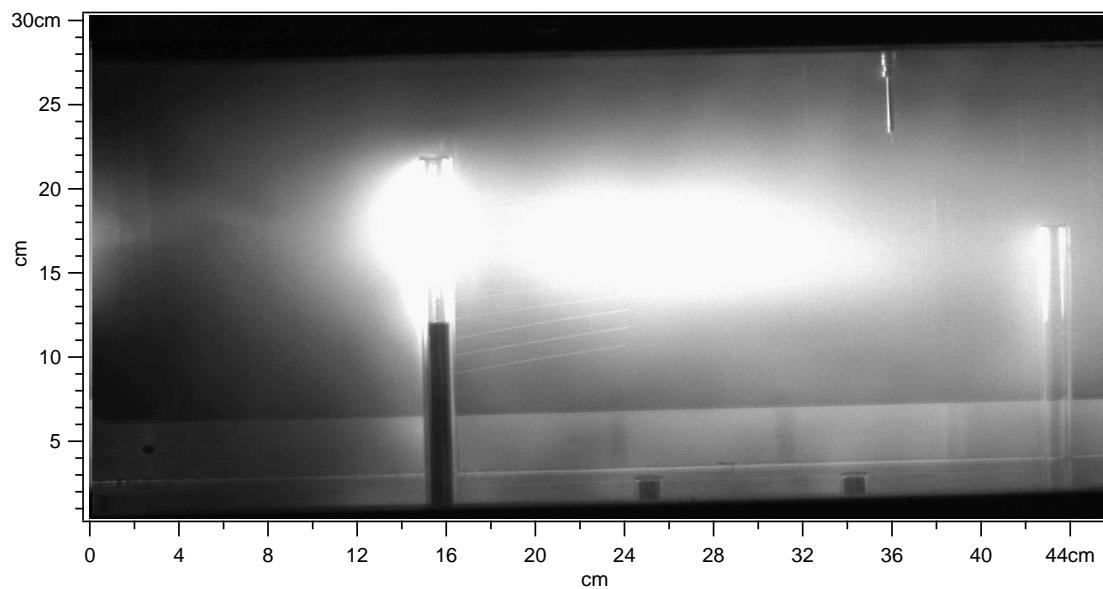
Figure I.26: Transition from laminar to turbulent flow, shot 60226
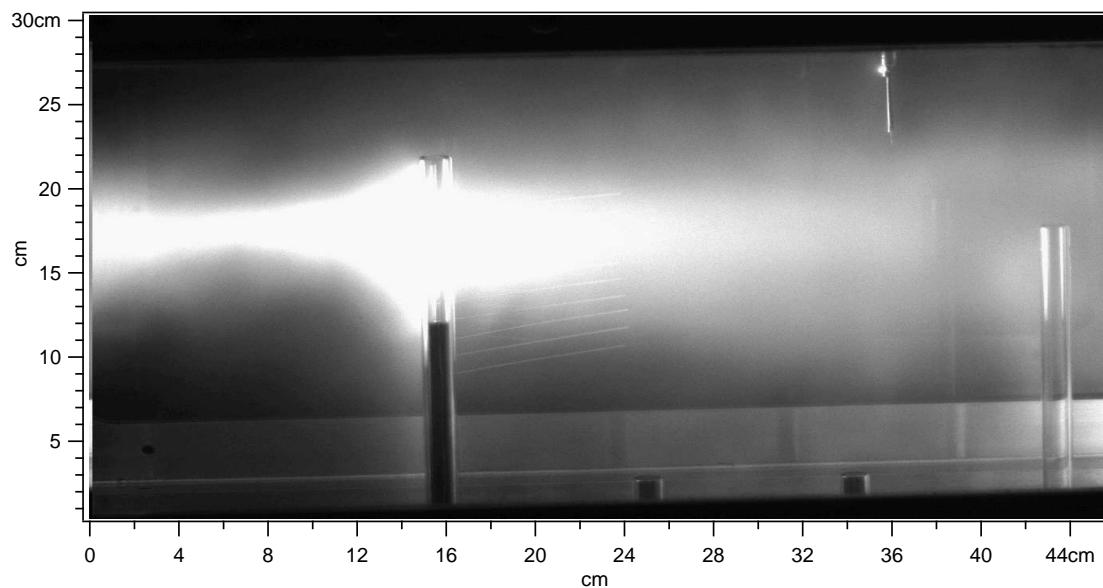
Figure I.27: Transition from laminar to turbulent flow, shot 60227
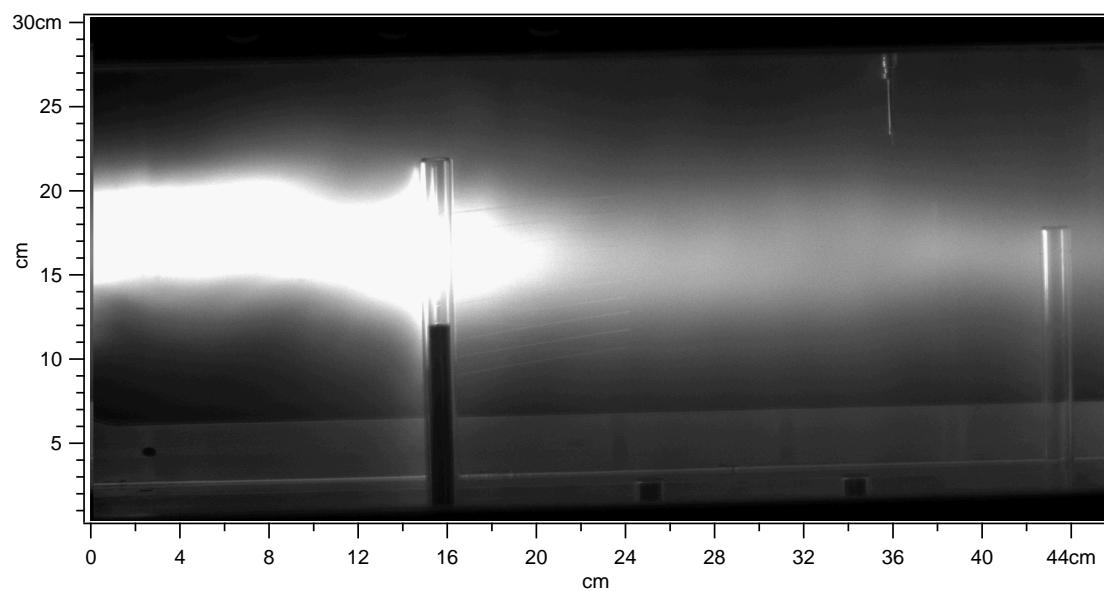
Figure I.28: Central flow interacting with target, shot 60229
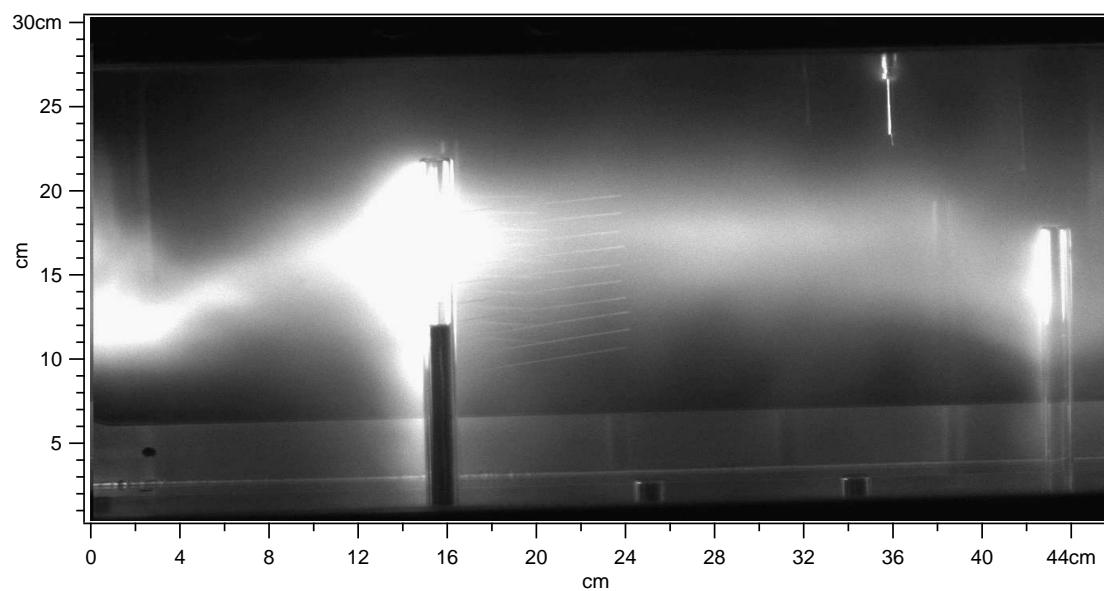
Figure I.29: Central flow interacting with target, shot 60244
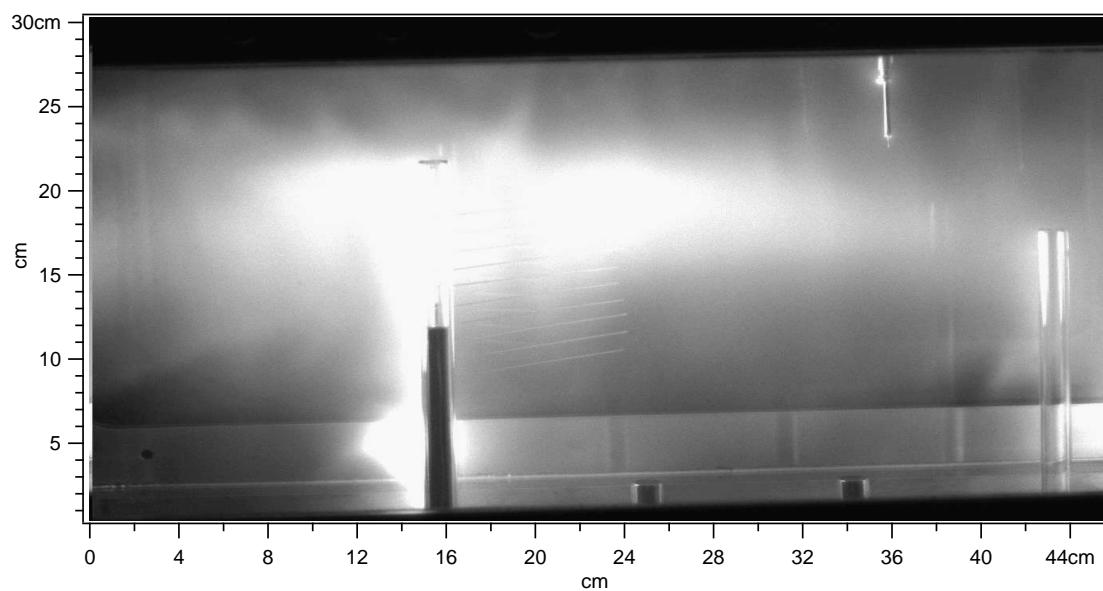
Figure I.30: Transition from laminar to turbulent flow, shot 60253
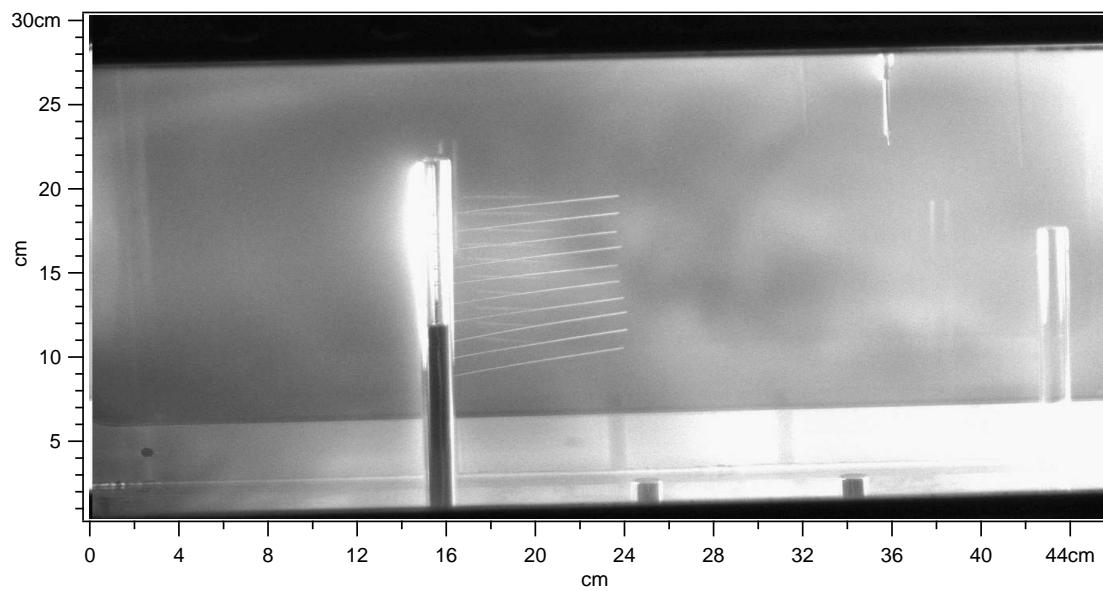
Figure I.31: Transition from laminar to turbulent flow, shot 60258
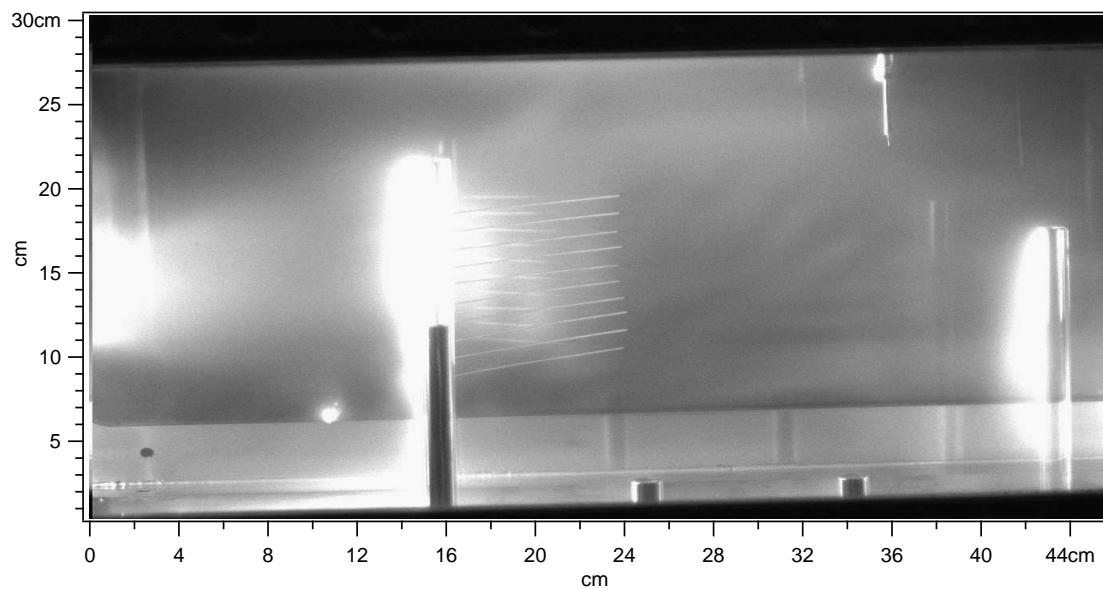
Figure I.32: Transition from laminar to turbulent flow, shot 60306
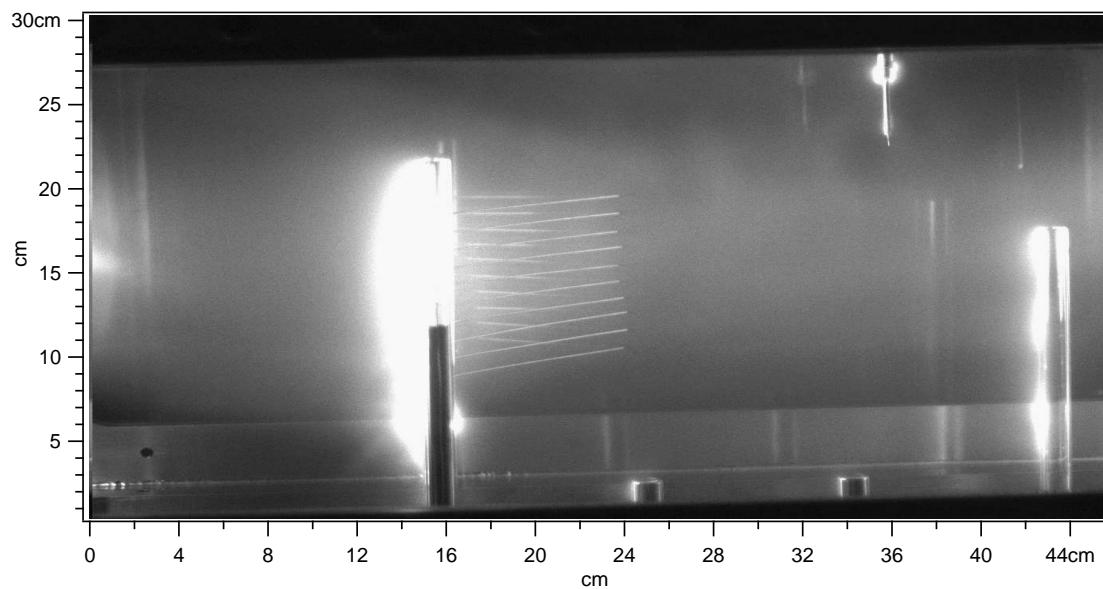
Figure I.33: Central flow interacting with target, shot 60307
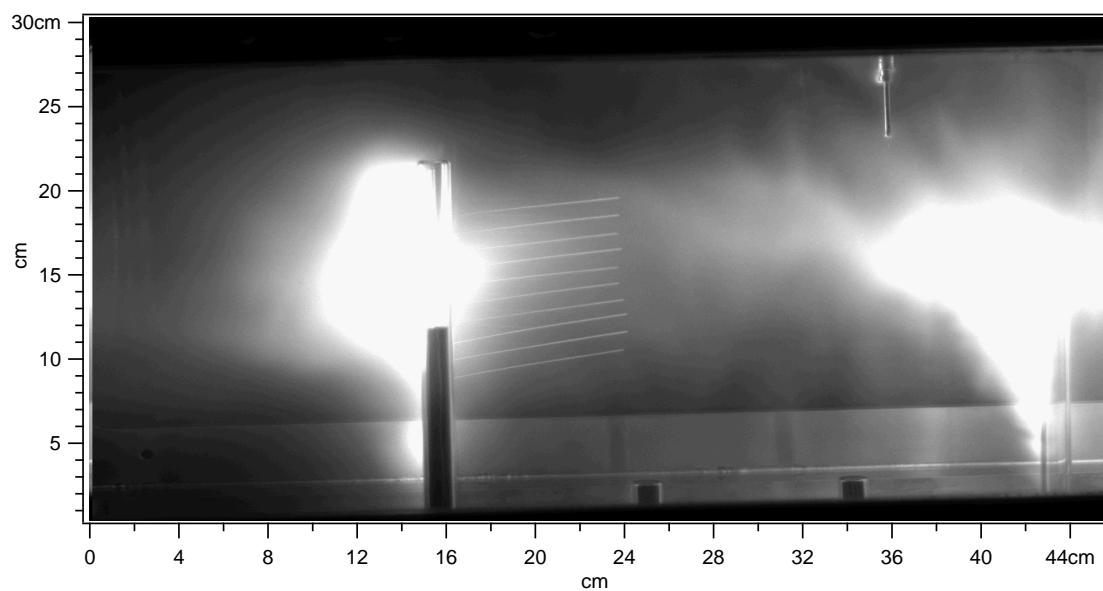
Figure I.34: Transition from laminar to turbulent flow, shot 60317
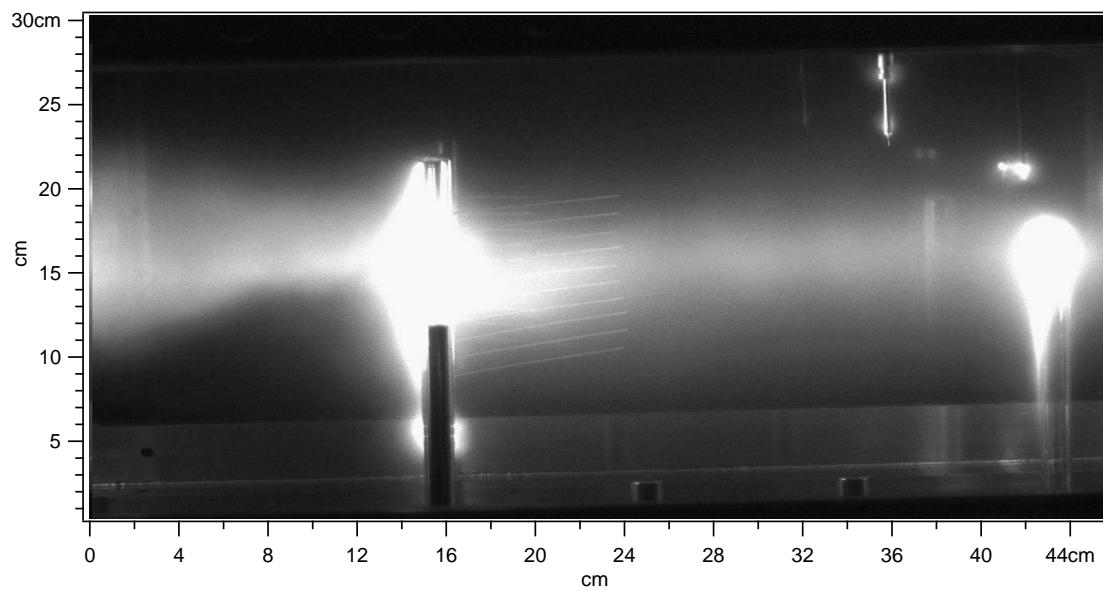
Figure I.35: Central flow interacting with target, shot 60318
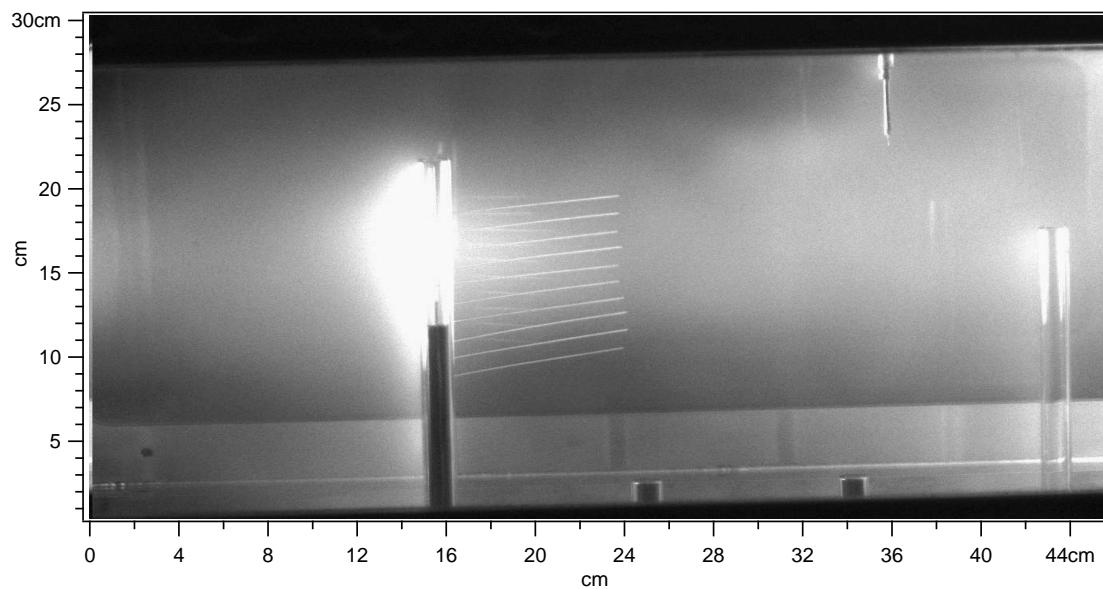
Figure I.36: Central flow interacting with target, shot 60350
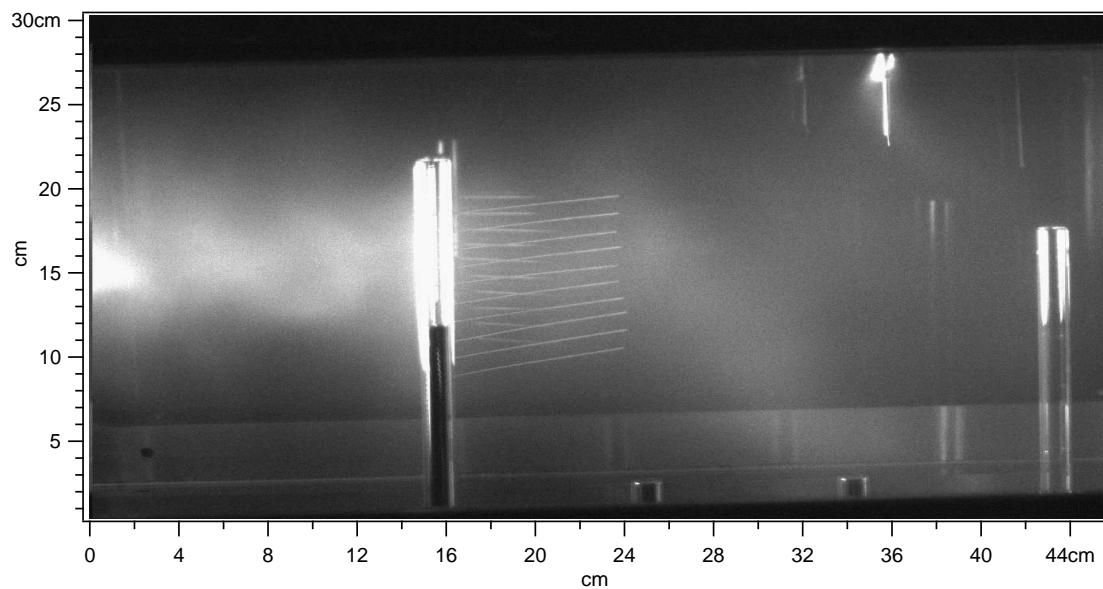
Figure I.37: Central flow interacting with target, shot 60368
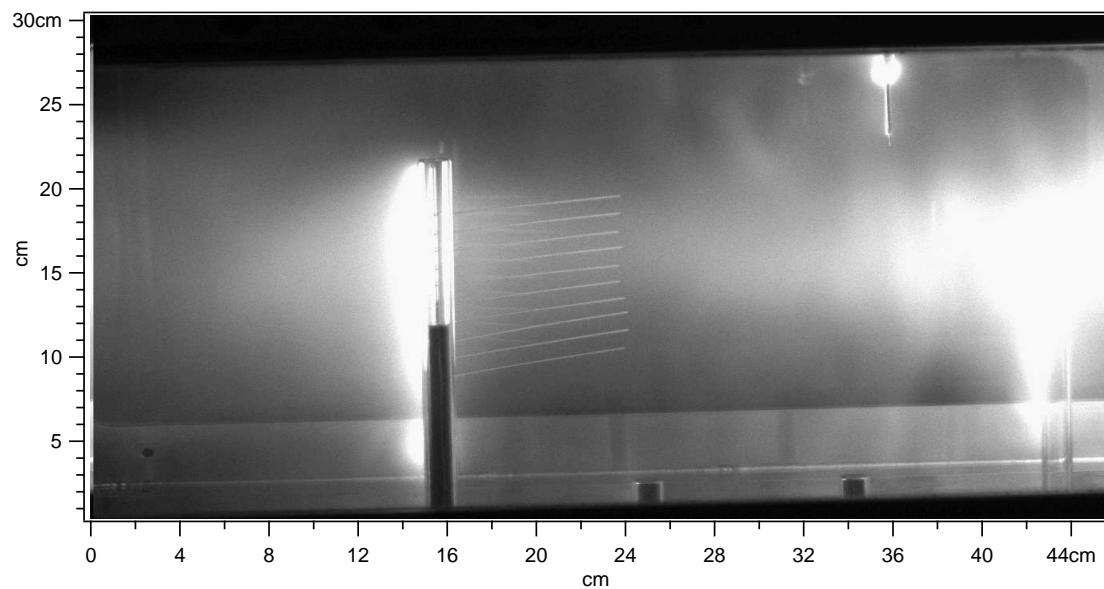
Figure I.38: Transition from laminar to turbulent flow, shot 60394
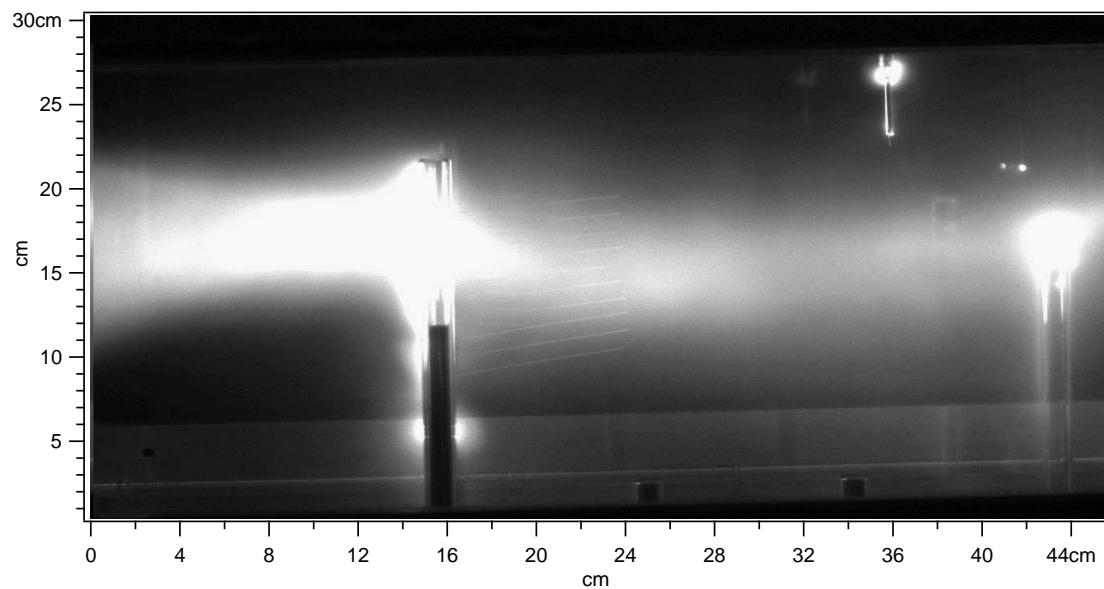
Figure I.39: Transition from laminar to turbulent flow, shot 60398

Appendix J

Image gallery of

unexplained flow observations
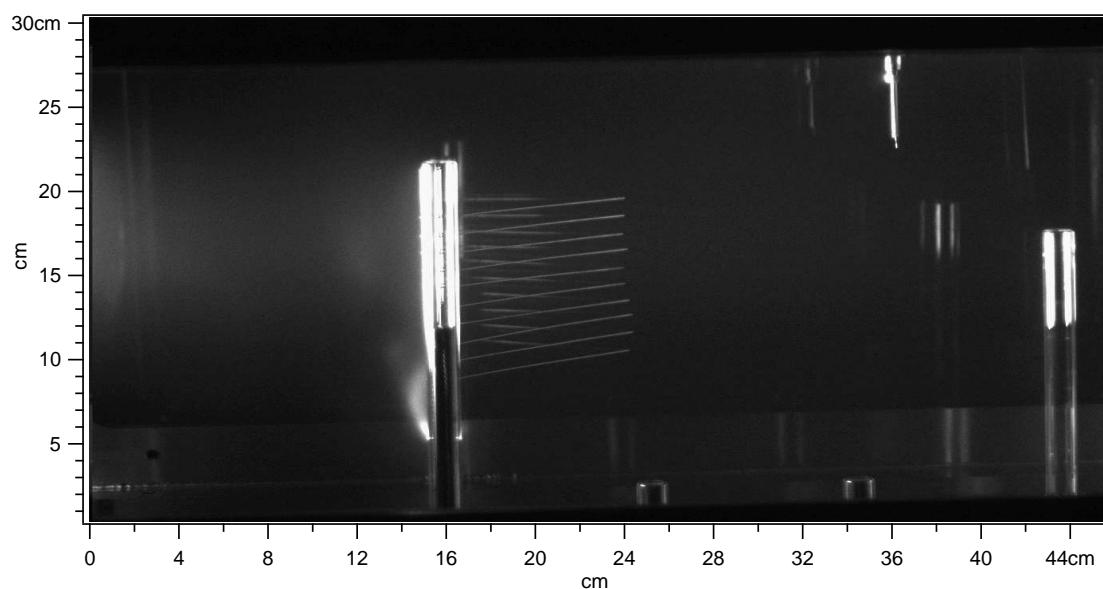
Figure J.1: Unusual shot 60018
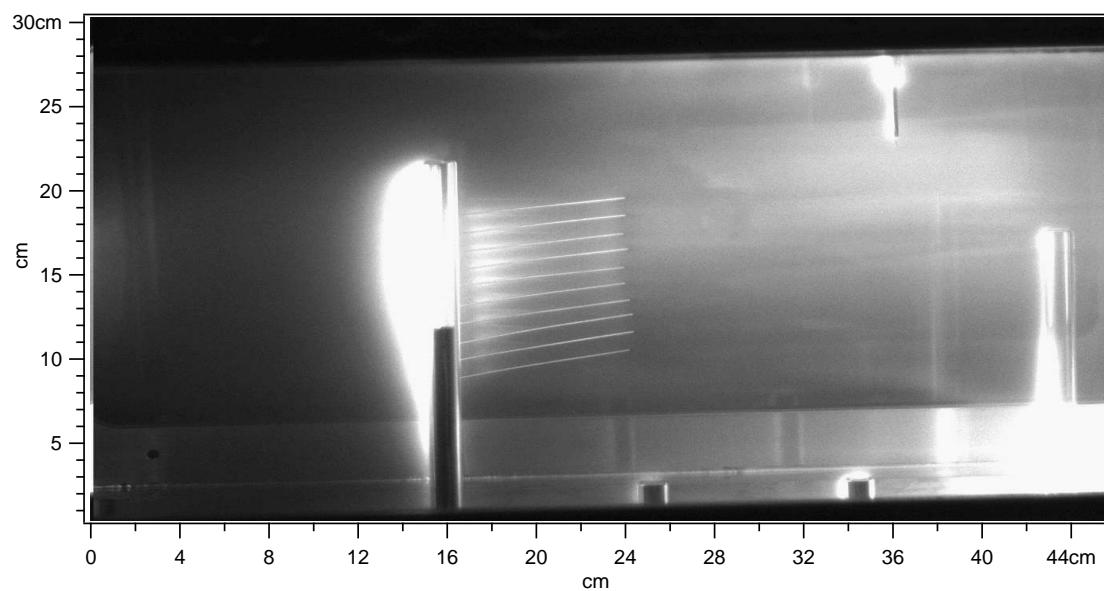
Figure J.2: Unusual shot 60152
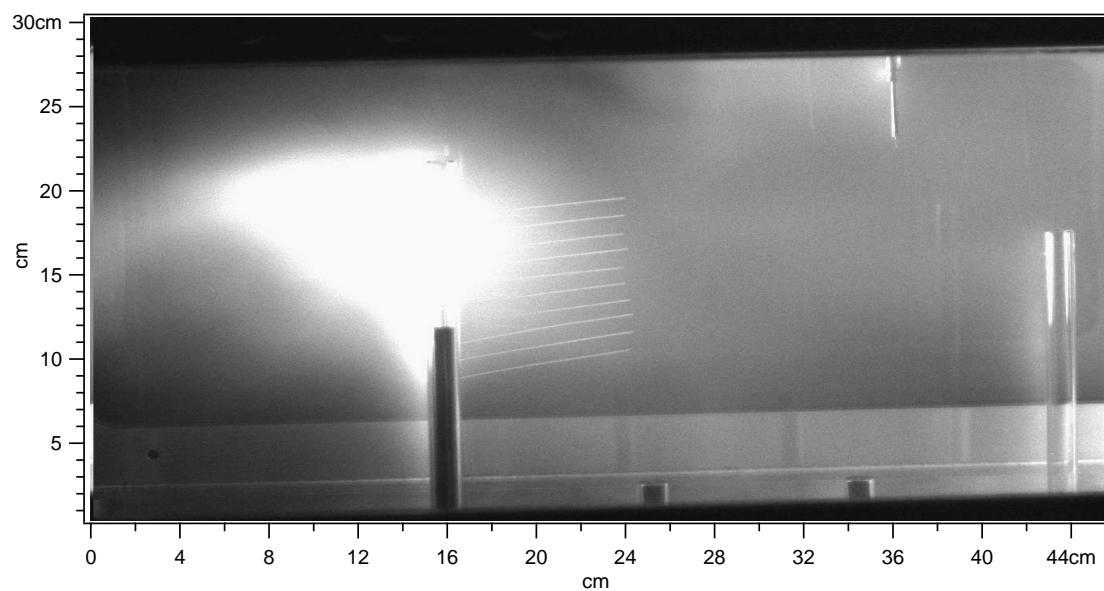
Figure J.3: Unusual shot 60155
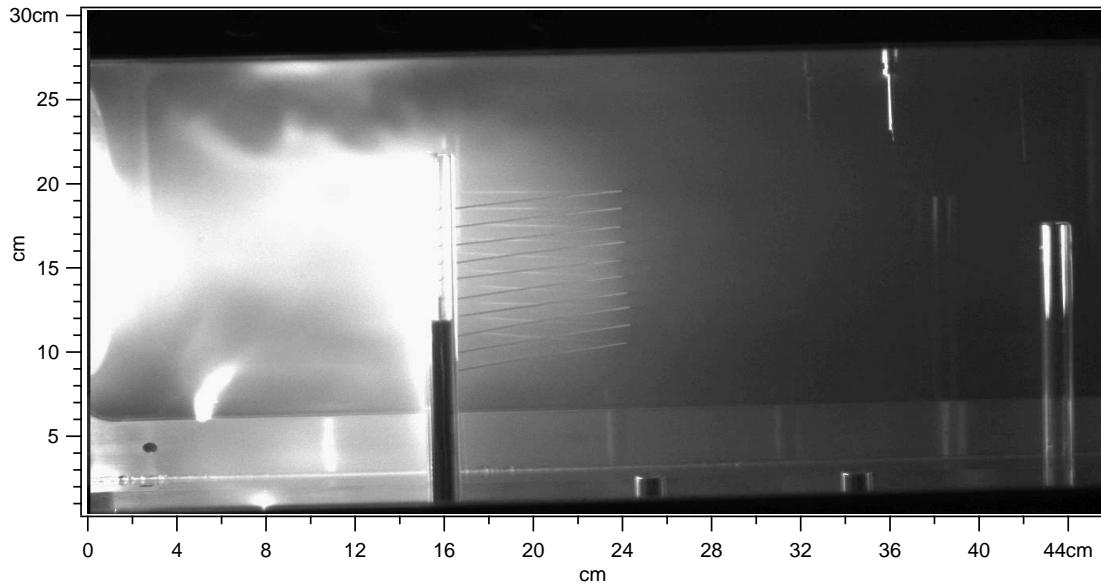
Figure J.4: Unusual discharge during arc, shot 60162. Sensicam exposure = 1 μs, delay = 20.6 μs. Magnetic data implies that breakdown began at z= 91 cm gas valve position and maintained a large arc at that position. GP 91 driving voltage = 575 V, delay = 65 ms.
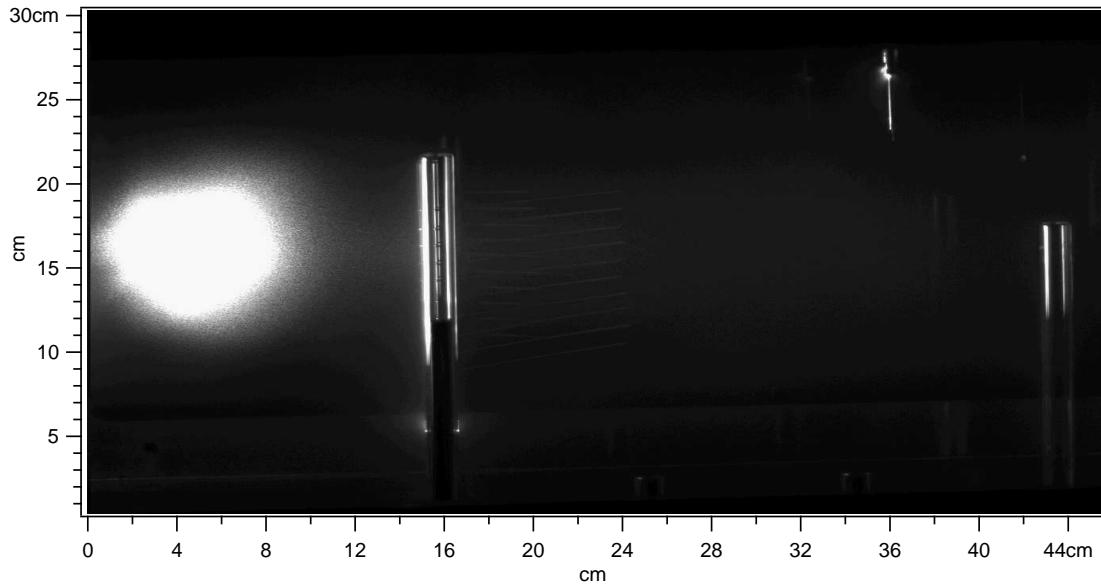
Figure J.5: Unidentified bright blob during arc, shot 60163. Sensicam exposure = 1 μs, delay = 22.6 μs, saturation of CCD occurred within area of blob. Magnetic data implies that breakdown began at z= 91 cm gas valve position and maintained a large arc at that position. GP 91 driving voltage = 575 V, delay = 65 ms.
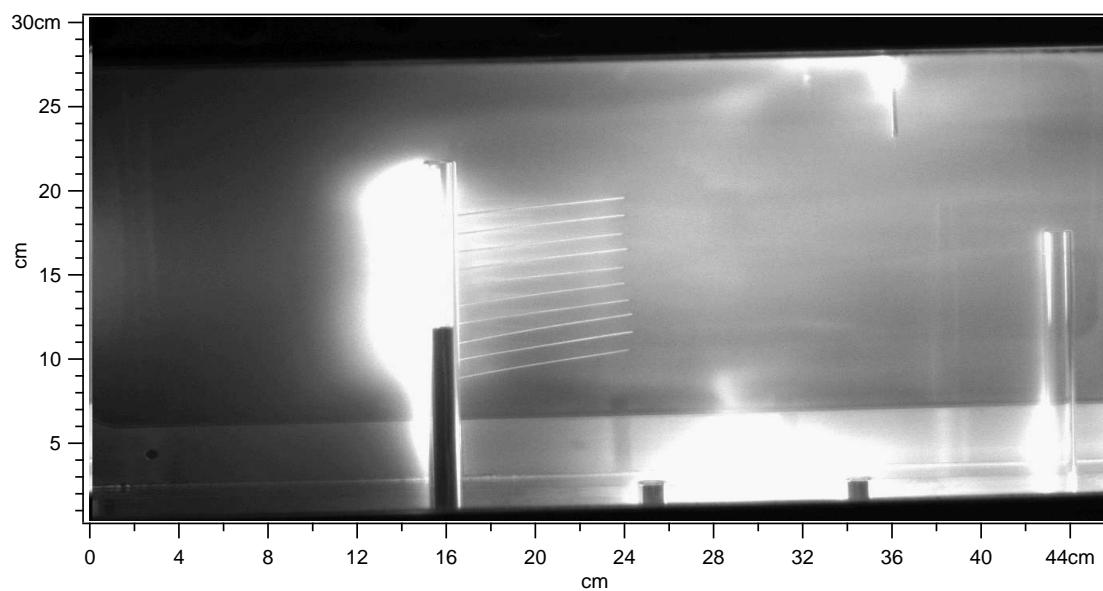
Figure J.6: Unusual shot 60222
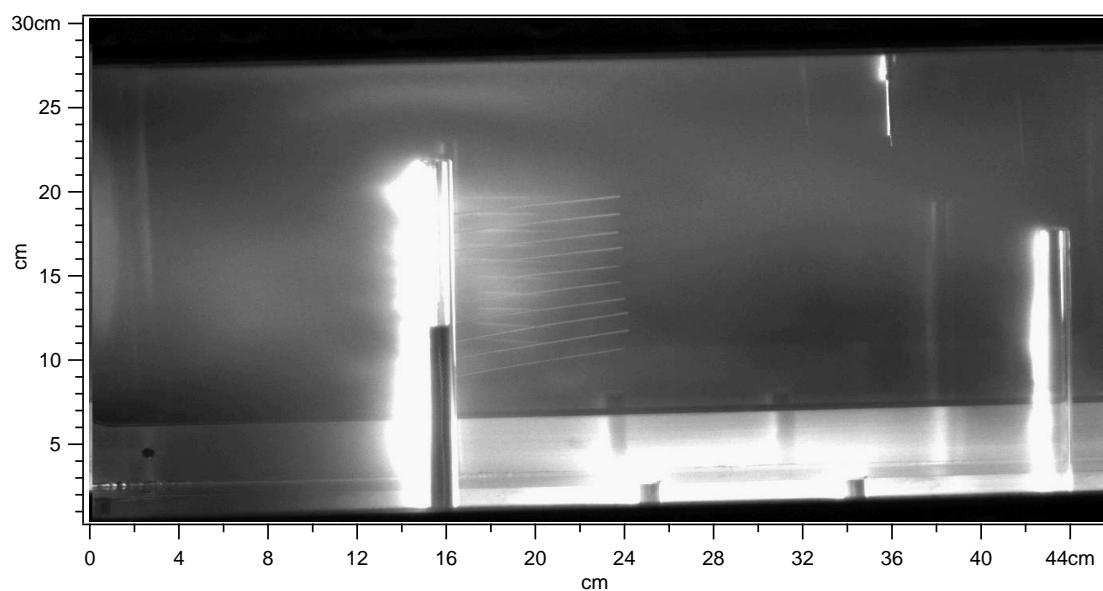
Figure J.7: Unusual shot 60243
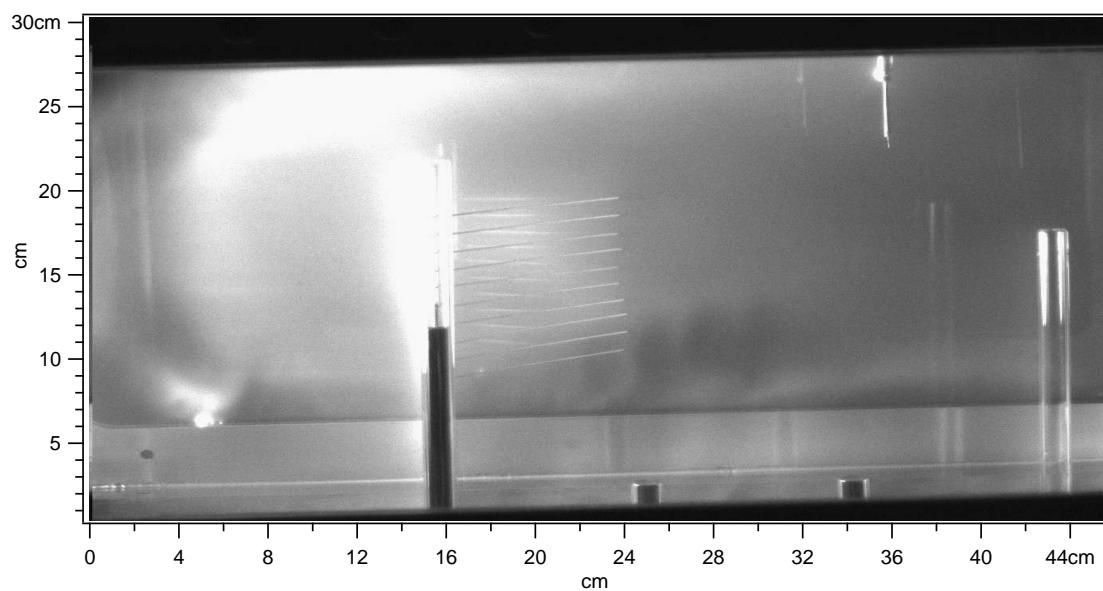
Figure J.8: Unusual shot 60251
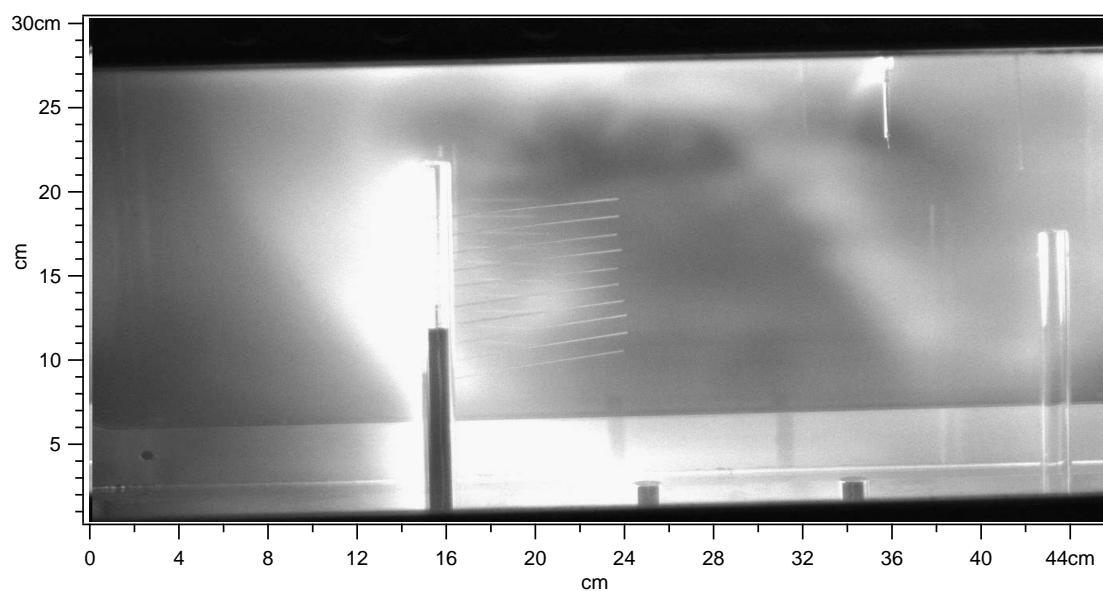
Figure J.9: Unusual shot 60252
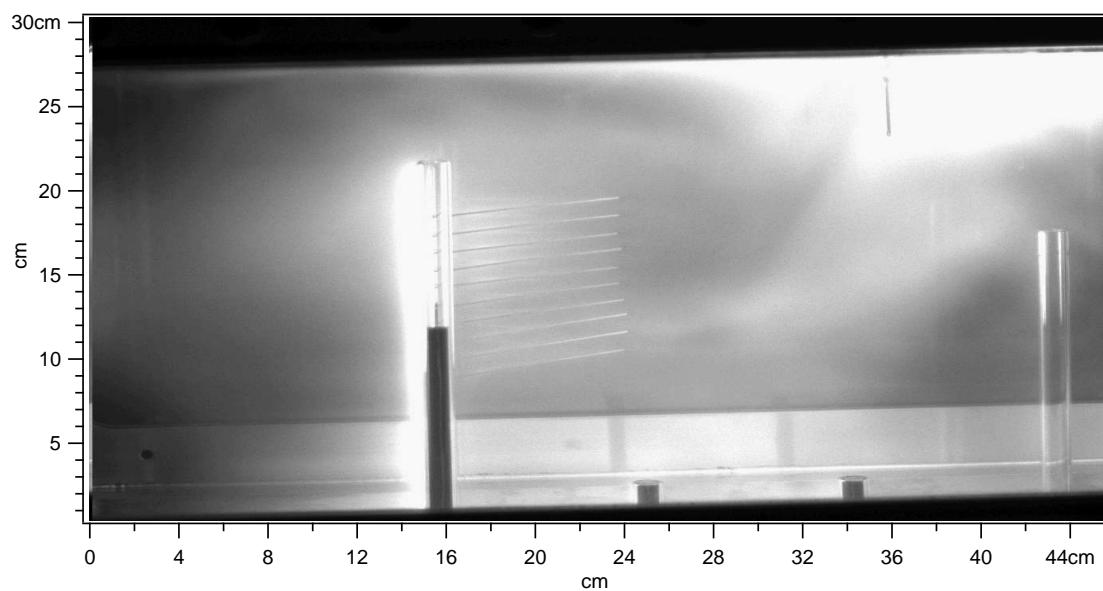
Figure J.10: Unusual shot 60264
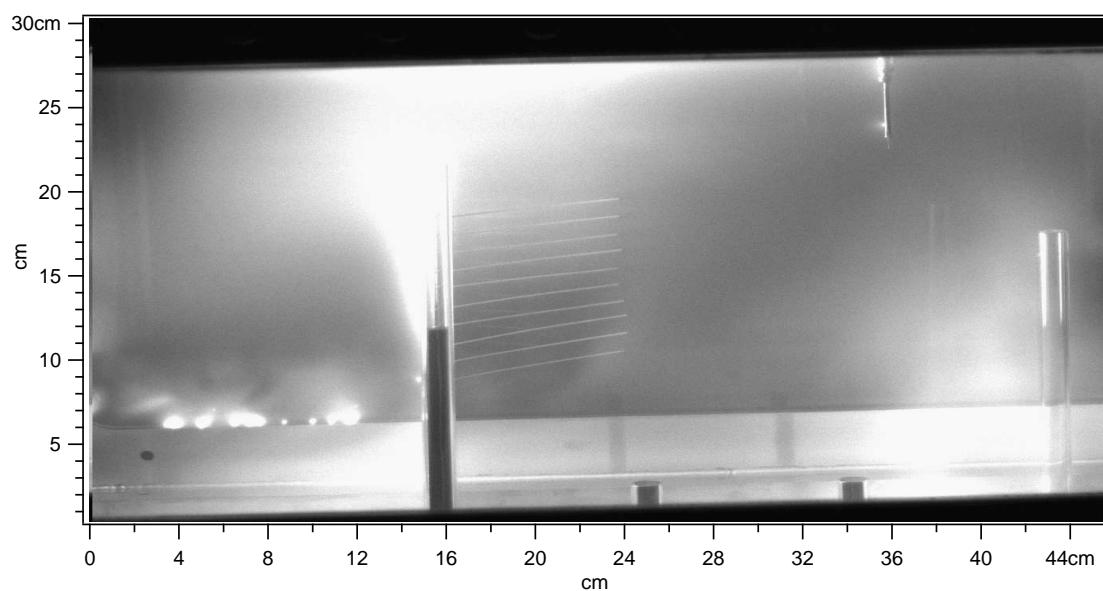
Figure J.11: Unusual shot 60266
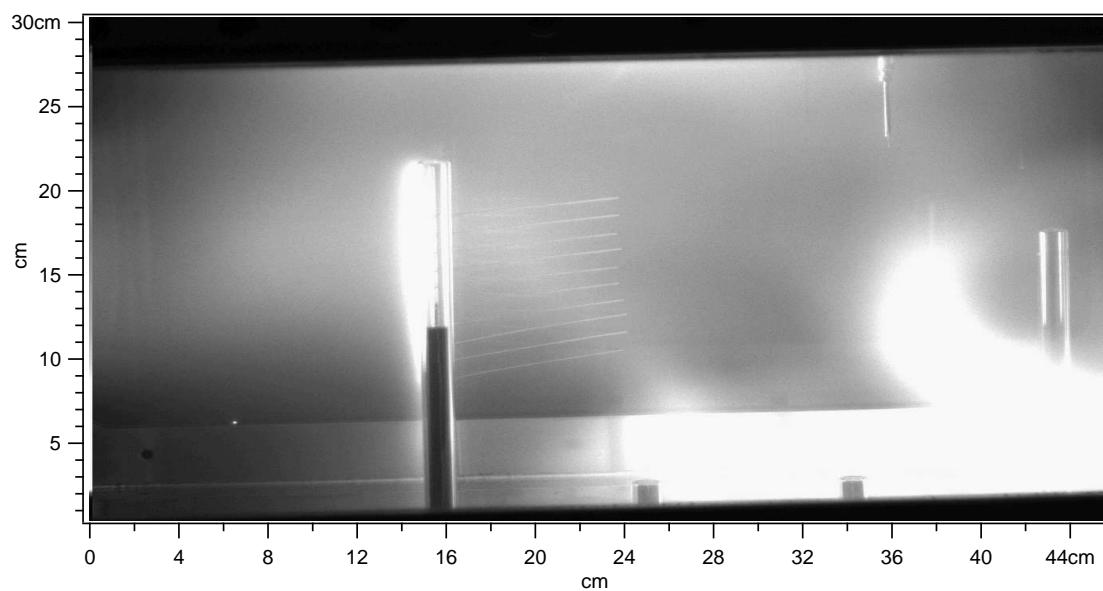
Figure J.12: Unusual shot 60267
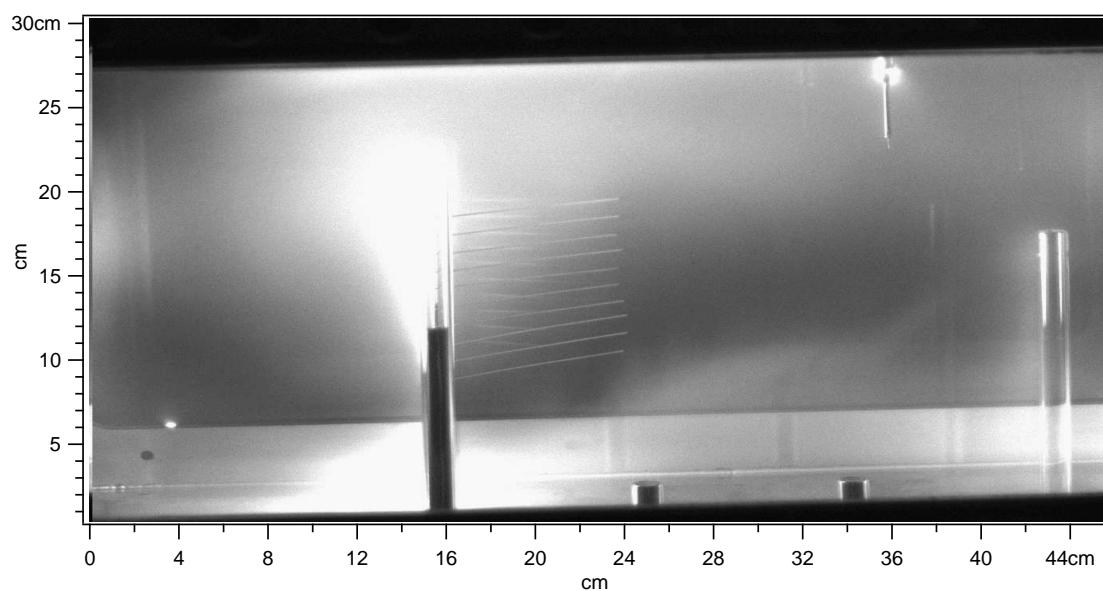
Figure J.13: Unusual shot 60275
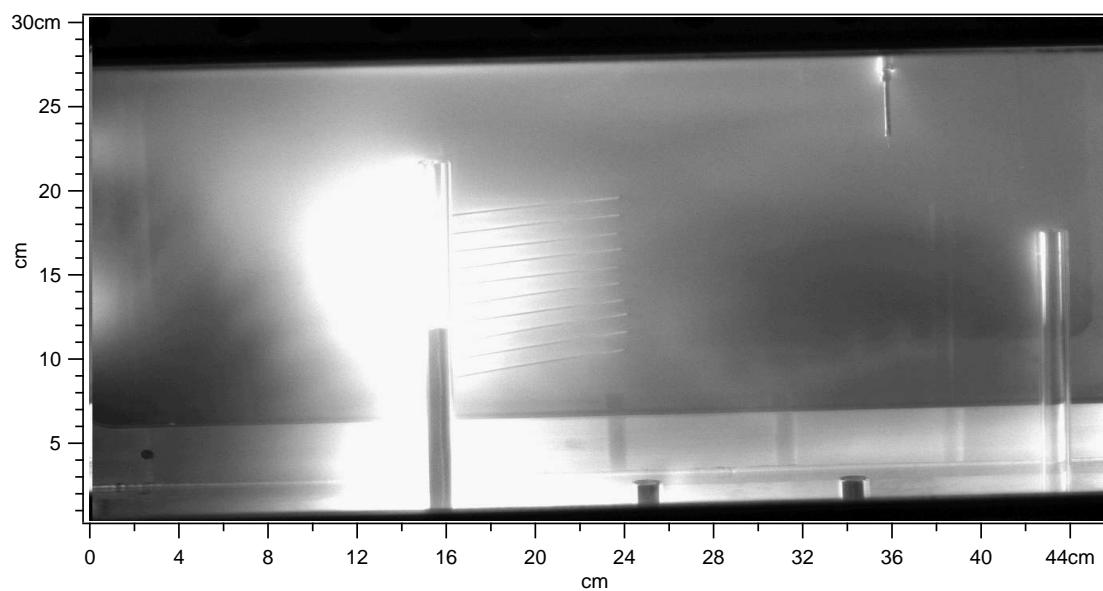
Figure J.14: Unusual shot 60276
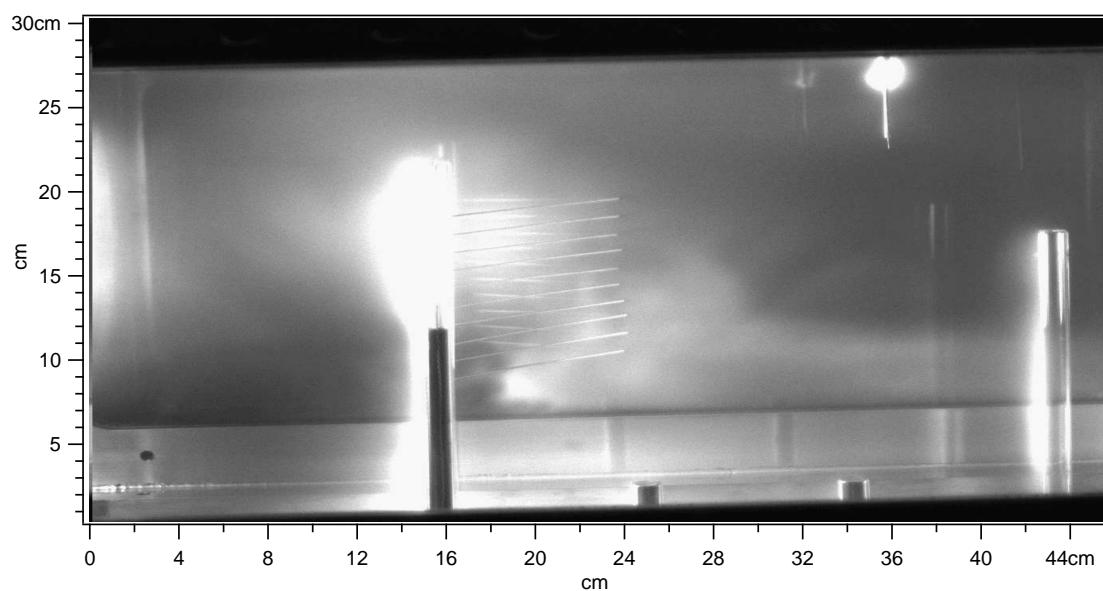
Figure J.15: Unusual shot 60308
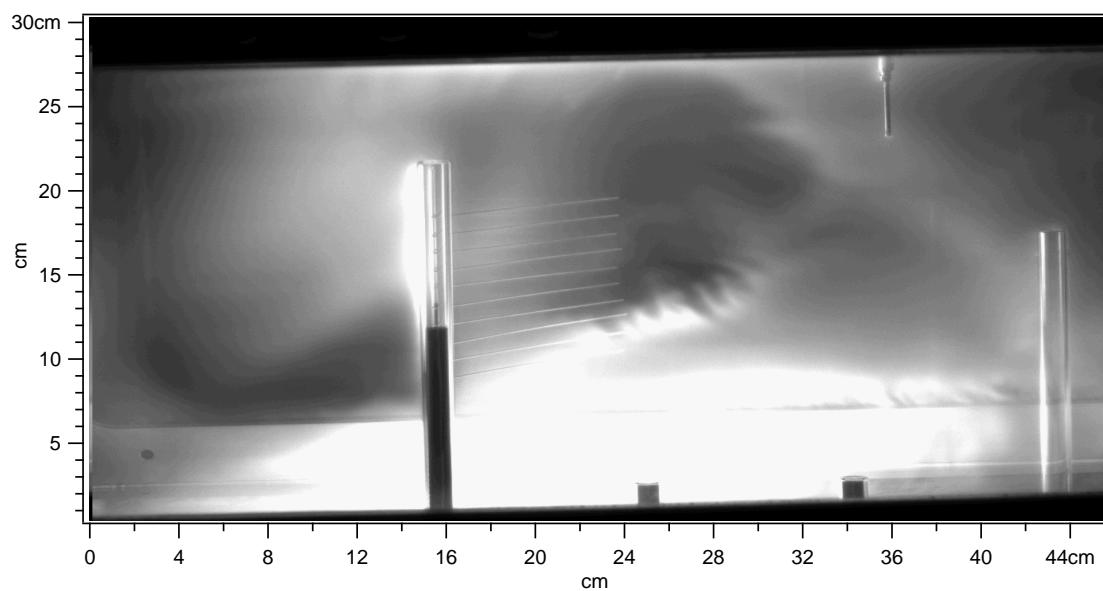
Figure J.16: Unusual shot 60309
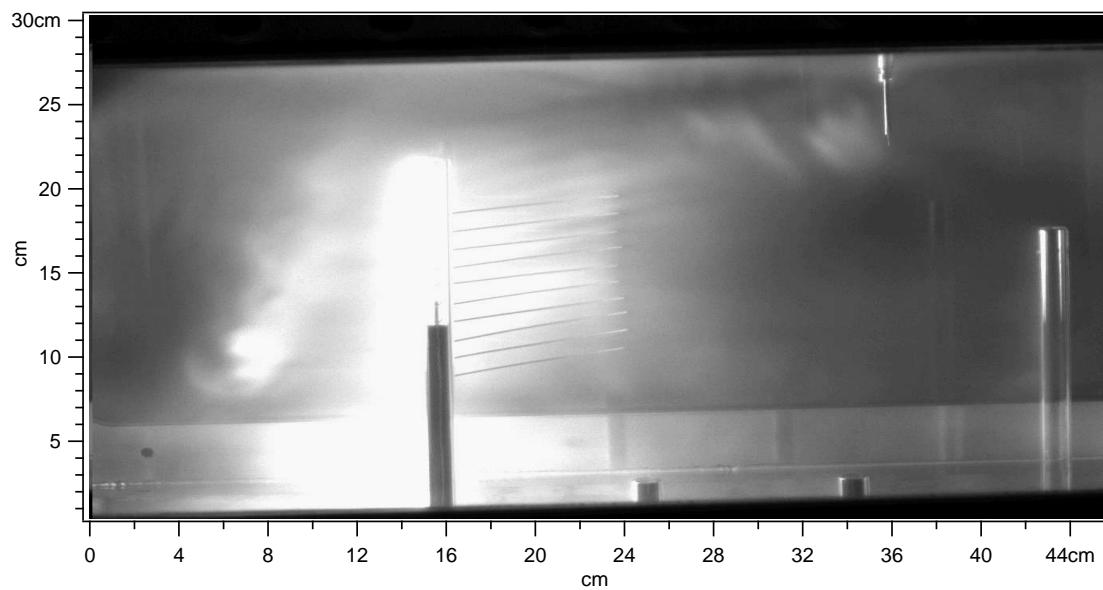
Figure J.17: Unusual shot 60311
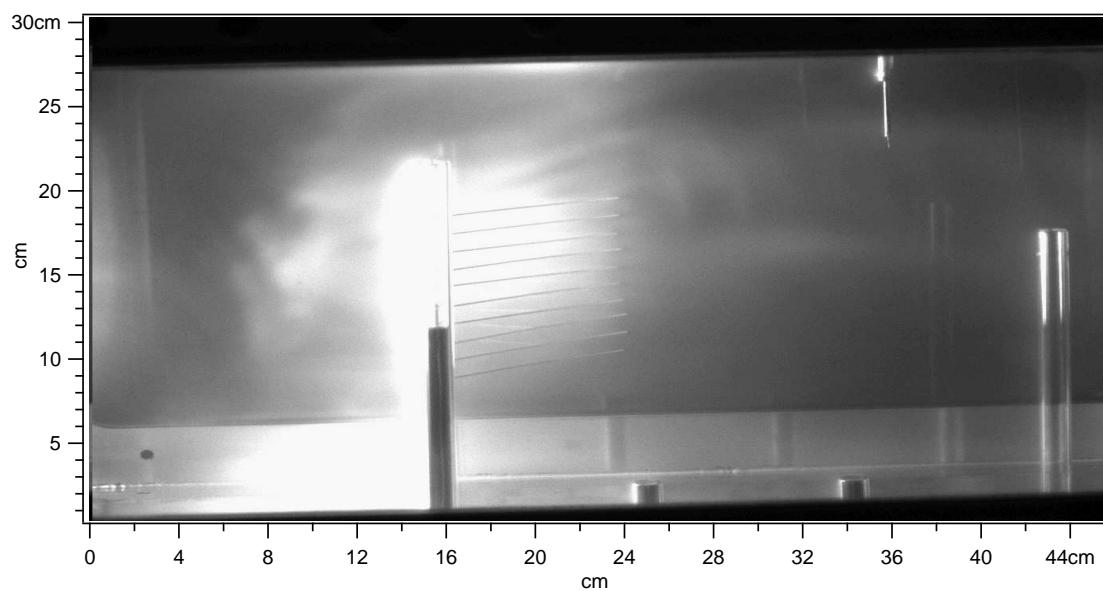
Figure J.18: Unusual shot 60313
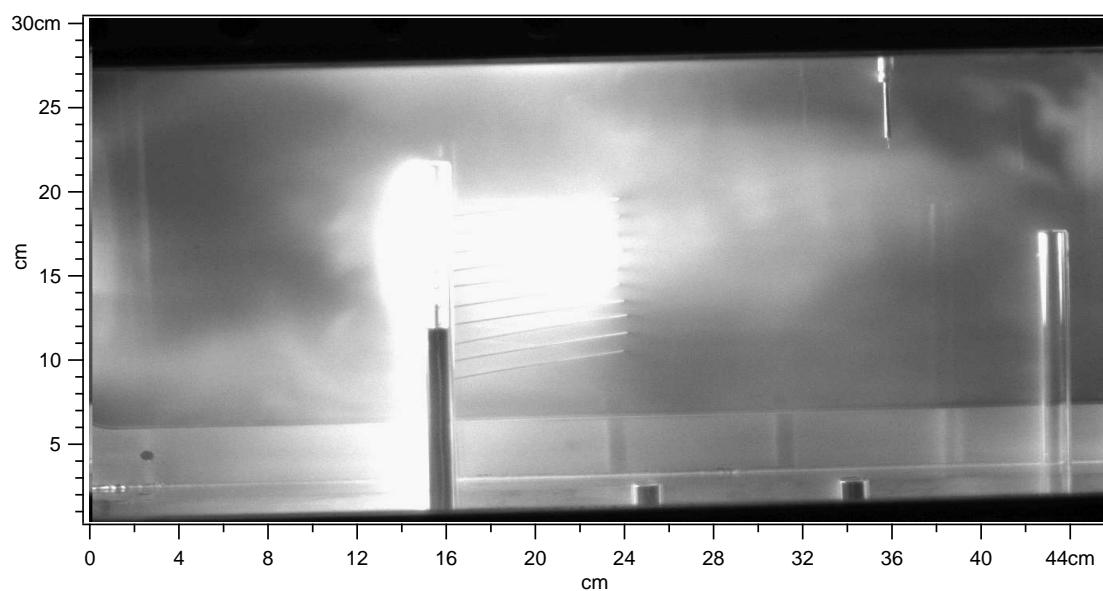
Figure J.19: Unusual shot 60314
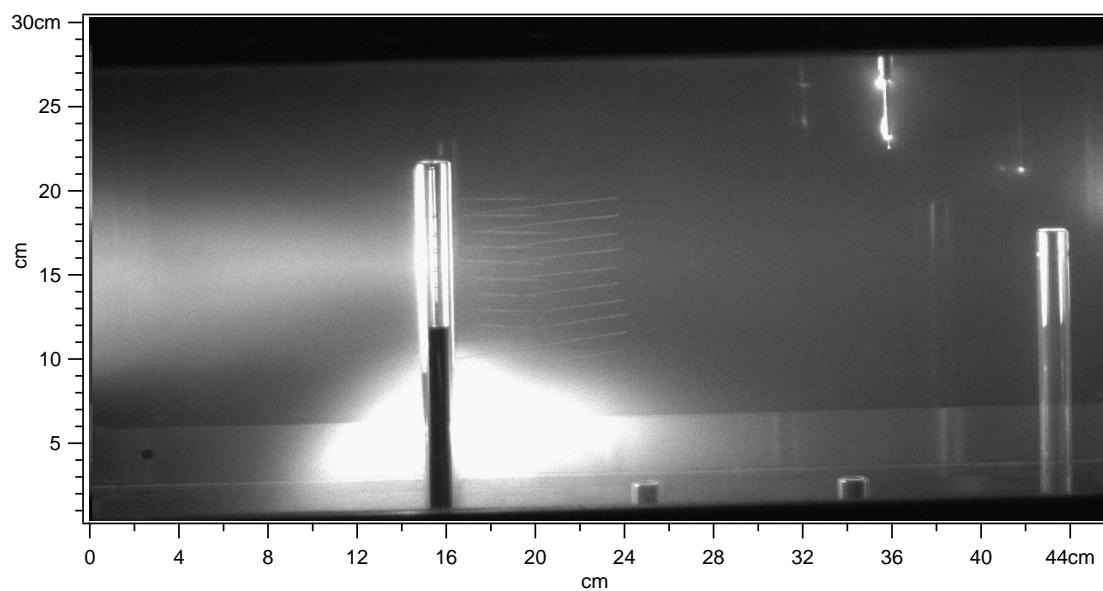
Figure J.20: Unusual shot 60357
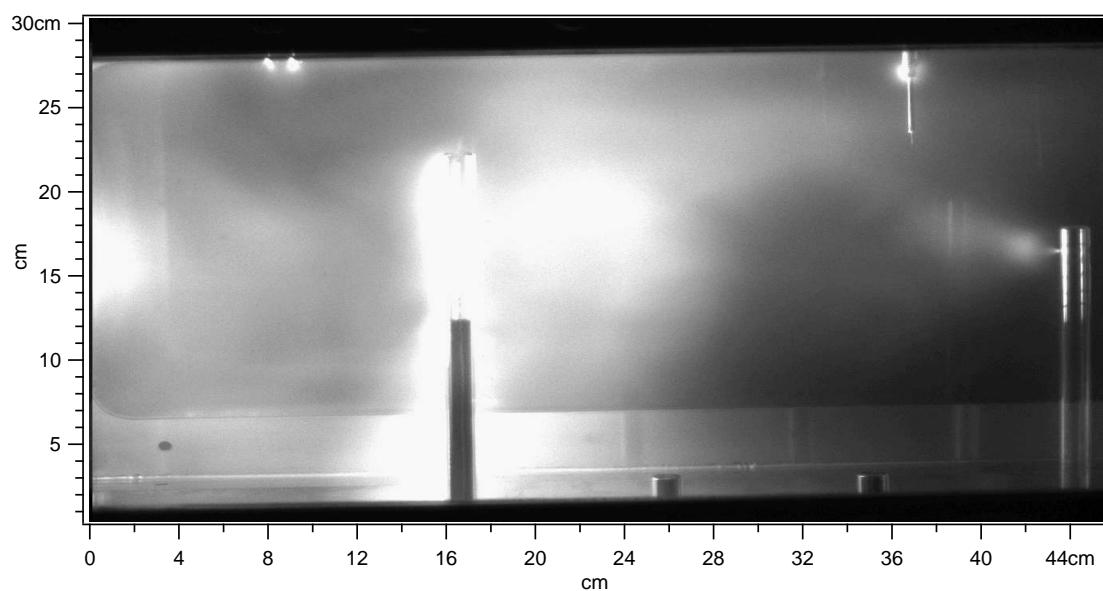
Figure J.21: Unusual shot 60456
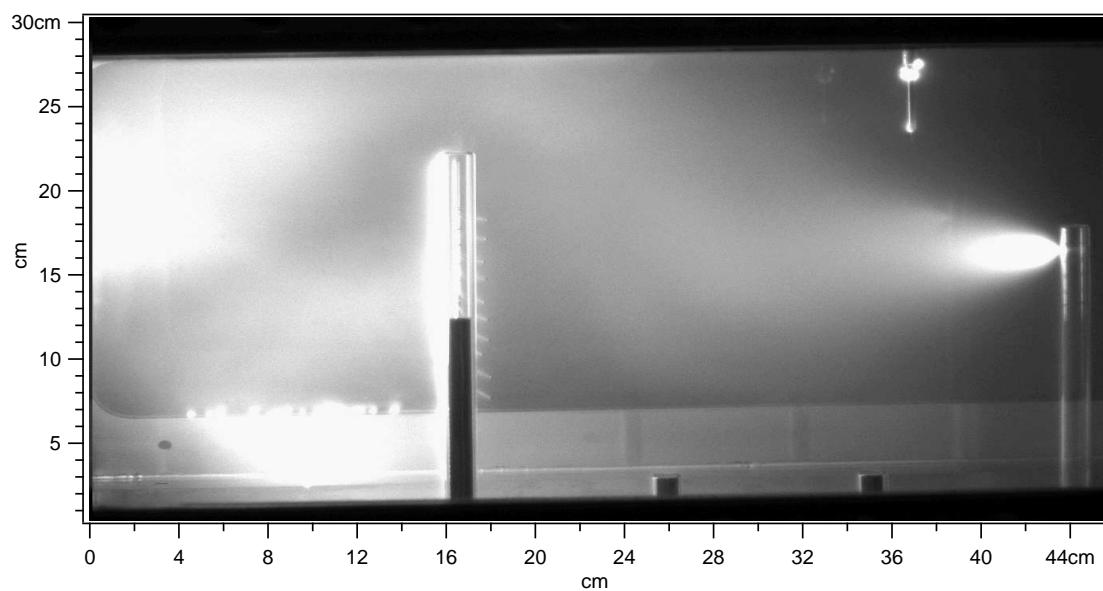
Figure J.22: Unusual shot 60469
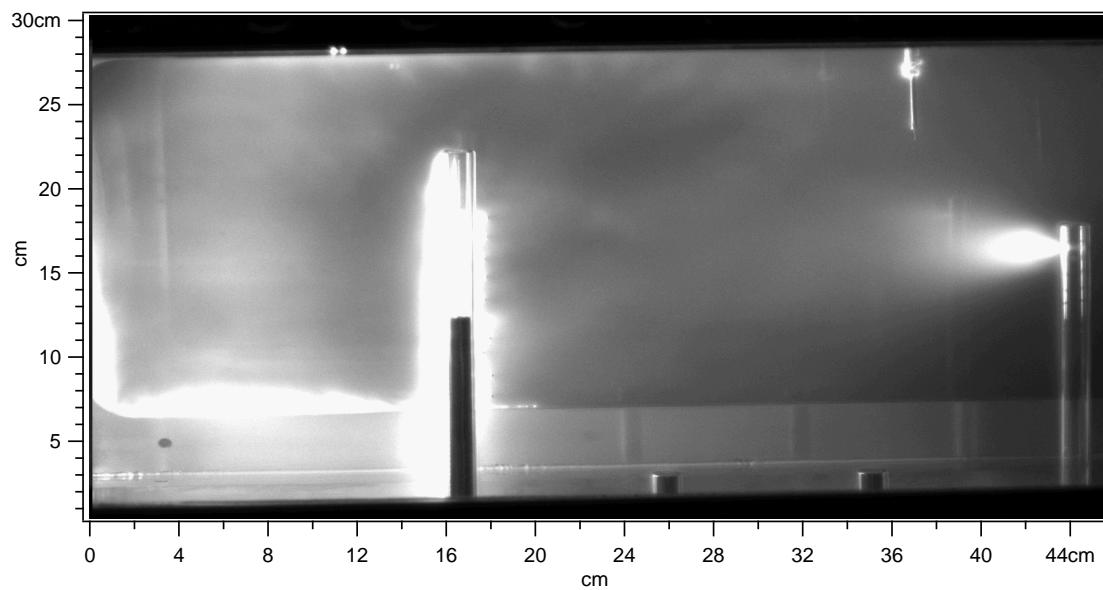

Figure J.23: Unusual shot 60482
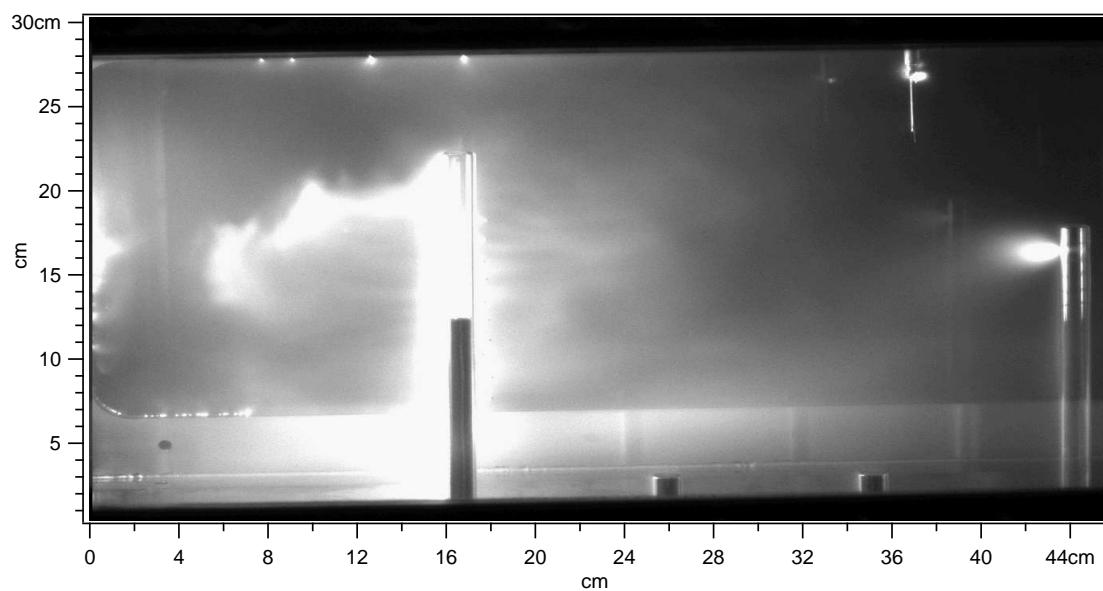
Figure J.24: Unusual shot 60485
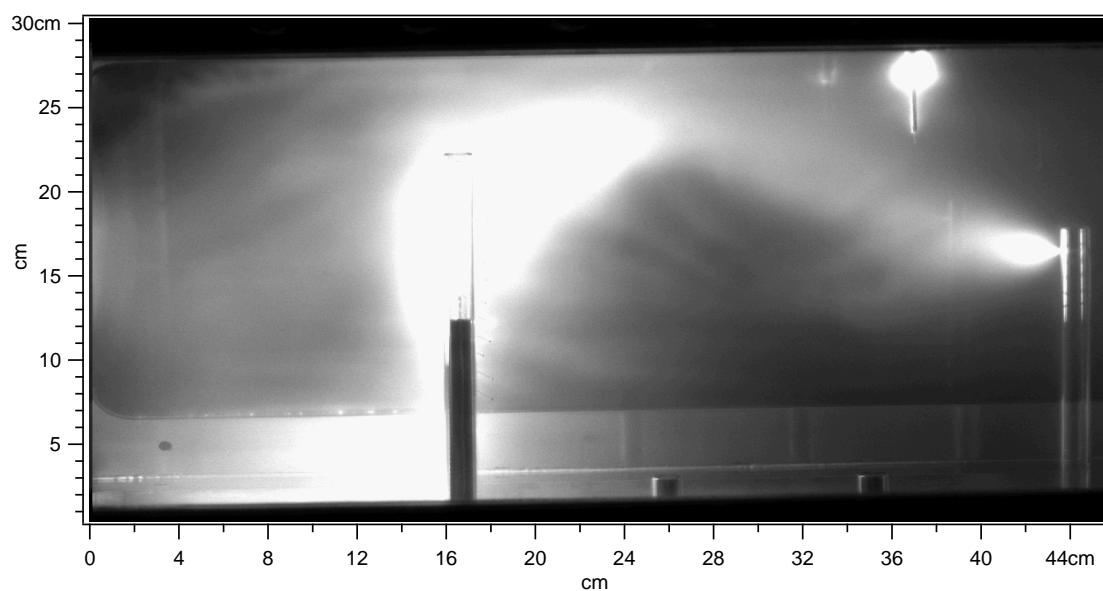
Figure J.25: Unusual shot 60492
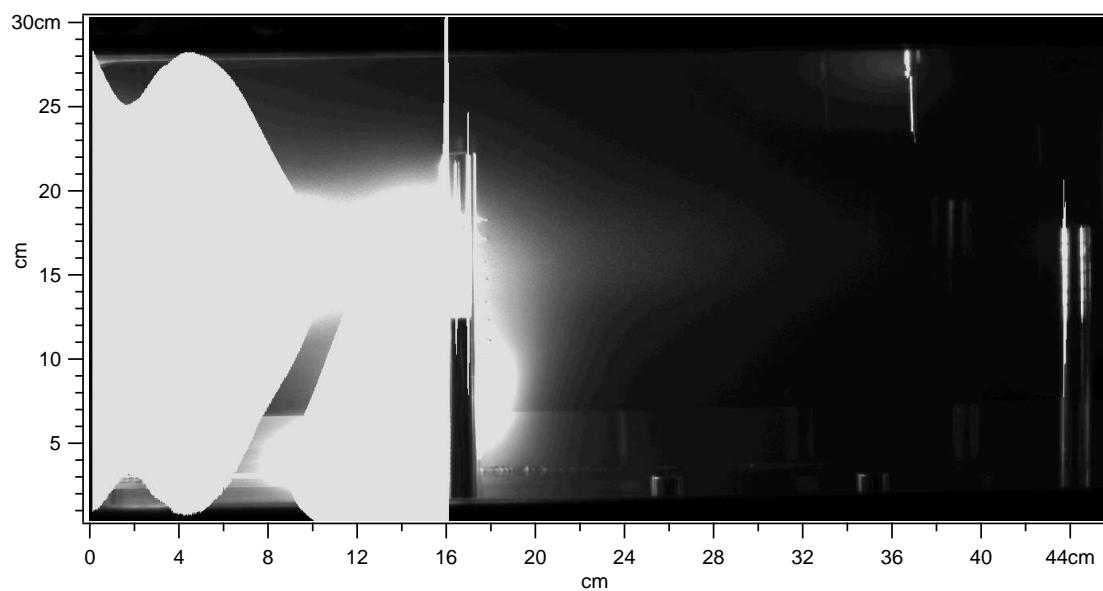
Figure J.26: Arc caused by pinhole fracture in tip of ceramic probe case at $z = 142$ cm, this occurred during the charging cycle prior to what would have been 60498. Arc originated at the 142 port several seconds before the formation gas valve would have fired. Detector saturation and spill-over between CCD pixels is responsible for unusual shape.